

All-Carbon Molecular Electronics: From Flexible Fabrication to Multi-Step  
Transport and Molecular Optoelectronics

by

Amin Morteza Najarian

A thesis submitted in partial fulfillment of the requirements for the degree of

Doctor of Philosophy

Department of Chemistry

University of Alberta

© Amin Morteza Najarian, 2018

## Abstract

The central idea of molecular electronics is to incorporate individual or ensemble molecules into the electronic circuit units in the hope of creating miniaturized functional devices with unique properties. This dissertation aims to present my efforts to pursue this ultimate goal, covering the fabrication of reliable all-carbon molecular junctions, and realization of structure-function characteristics in thick molecular layer (>4 nm). In addition, interaction of UV-Vis light with molecular layer and consequential photo-response in molecular junction is discussed.

Chapter 2 demonstrates the fabrication of large area molecular junctions on electron-beam deposited carbon (eC) surfaces with molecular layers in the range of 2 - 5.5 nm between conducting, amorphous carbon contacts. Incorporating eC as an interconnect between Au and the molecular layer improves substrate roughness, prevents electromigration and uses well-known electrochemistry to form a covalent C-C bond to the molecular layer. Au/eC/anthraquinone/eC/Au junctions were fabricated on Si/SiO<sub>x</sub> with high yield and reproducibility, and were unchanged by  $10^7$  current-voltage cycles and temperatures between 80 and 450 K. Au/eC/AQ/eC/Au devices fabricated on plastic films were unchanged by  $10^7$  *JV* cycles and repeated bending of the entire assembled junction. The low sheet resistance of Au/eC substrates permitted junctions with sufficiently transparent electrodes to conduct Raman or UV-Vis absorption spectroscopy in either reflection or transmission geometries. Collectively, eC on Au provides a platform for fabrication and operation of chemically stable, optically and electrically functional molecules on rigid or flexible materials. The relative ease of processing and the robustness of molecular junctions incorporating eC layers

should help address the challenge of economic fabrication of practical, flexible molecular junctions for a potentially wide range of applications.

Chapter 3 discusses that how carbon-based molecular junctions consisting of aromatic oligomers exhibit structure dependent current densities ( $J$ ) when the molecular layer thickness ( $d$ ) exceeds  $\sim 5$  nm. All four of the molecular structures examined exhibit an unusual, nonlinear  $\ln J$  vs bias voltage ( $V$ ) dependence which is not expected for conventional coherent tunneling or activated hopping mechanisms. All molecules exhibit a weak temperature dependence, with  $J$  increasing typically a factor of two over the range of 200-440 K. The observed current densities for four examined molecules with  $d = 7-10$  nm show no correlation with occupied (HOMO) or unoccupied (LUMO) molecular orbital energies, contrary to expectations for transport mechanisms based on the offset between orbital energies and the electrode Fermi level. UV-Vis absorption spectroscopy of molecular layers bonded to carbon electrodes revealed internal energy levels of the chemisorbed films, and also indicated limited delocalization in the film interior. The observed current densities correlate well with the observed UV-Vis absorption maxima for the molecular layers, implying a transport mechanism determined by the HOMO-LUMO energy gap. We concluded that transport in carbon-based aromatic molecular junctions is consistent with multistep tunneling through a barrier defined by the HOMO-LUMO gap, and not by charge transport at the electrode interfaces. In effect, interfacial “injection” at the molecule/electrode interfaces is not rate limiting due to relatively strong electronic coupling, and transport is controlled by the “bulk” properties of the molecular layer interior.

In Chapter 4, photocurrent generated by illumination of carbon-based molecular junctions were investigated as diagnostics of how molecular structure and orbital energies

control electronic behavior. Illumination through either the top or bottom partially transparent electrodes produced both an open circuit potential (OCP) and a photocurrent (PC), and the polarity and spectrum of the photocurrent depended directly on the relative positions of the frontier orbitals and the electrode Fermi level ( $E_F$ ). Electron donors with relatively high HOMO energies yielded positive OCP and PC, and electron acceptors with LUMO energies closer to  $E_F$  than the HOMO energy produced negative OCP and PC. In all cases, the PC spectrum and the absorption spectrum of the oligomer in the molecular junction had very similar shapes and wavelength maxima. Asymmetry of electronic coupling at the top and bottom electrodes due to differences in bonding and contact area cause an internal potential gradient which controls PC and OCP polarities. The results provide a direct indication of which orbital energies are closest to  $E_F$  and also indicate that transport in molecular junctions thicker than 5 nm is controlled by the difference in energy of the HOMO and LUMO orbitals.

## Preface

Chapter 2 of this thesis has been published as Morteza Najarian A., Szeto B., Tefashe U. M., McCreery R. L. “Robust all-carbon molecular junctions on flexible or semi-transparent substrates using "process-friendly" fabrication” *ACS Nano* **10** (2016) 8918–8928. Also part of the characterization of eC shown in this chapter has been published as Morteza Najarian, A., Chen, R., Balla, R. J., Amemiya, S., McCreery, R. L. “Ultra-flat, Pristine and Robust Carbon Electrode for Fast Electron Transfer Kinetics” *Analytical chemistry* **89** (2017) 13532–13540. U. Tefashe and B. Szeto contributed in wafer scale lithography for eC junction. I was responsible for all remaining experiments, data collection, analysis as well as the manuscript composition. R.L. McCreery was supervisory author and was involved in manuscript composition, preparation and writing.

Chapter 3 of this thesis has been published as Morteza Najarian A., McCreery R. L. “Structure controlled long-range sequential tunneling in carbon-based molecular junctions” *ACS Nano* **11** (2017) 3542–3552. I was responsible for designing the experiments, data collection, analysis as well as the manuscript composition. R.L. McCreery was supervisory author and was involved in manuscript composition, preparation and writing.

Chapter 4 of this thesis has been published as Morteza Najarian A., Bayat A., McCreery R. L. “Orbital Control of Photocurrents in Large Area All-Carbon Molecular Junctions” *J. Am. Chem. Soc.* **140** (2018) 1900–1909. A. Bayat contributed to molecular layer grafting. I was responsible for all remaining experiments, data collection, analysis as well as the manuscript composition. R.L. McCreery was supervisory author and was involved in manuscript composition, preparation and writing.

## **Dedication**

**To my beloved parents**

**Father**, Abasali Morteza Najarian

**Mother**, Parvin Amirali

## Acknowledgements

First of all, I would like to thank my supervisor, Prof. Richard L. McCreery for accepting me to his research group. I really appreciate his help and support to handle my projects in the right way and showing me how to shape my perception and thoughts and then transform them into the valuable scientific documents. He was always available to listen and discuss the science and also personal issues. I know he had a hard time in dealing with me in years; however, he always did it patiently. With teaching me the necessity of diplomacy in life, he provided influence on my future career also. Collectively, I will be forever grateful for all that he has done for me.

I was fortunate to work in such a friendly environment and I would like to thank all RLM group members who overlapped with me in time. In particular, I would like to express my gratitude to Bryan Szeto for his help, friendship and technical support in years. Special thanks to Dr. Akhtar Bayat for being a patient listener for scientific and non-scientific discussions. Furthermore, I would like to thank Dr. Jerry Fereiro for his friendly help and support through the fabrication and measurements of my first molecular junction. I cannot forget to mention my close friend Mohammadali Tabatabaei for his appreciated support and help when I just came to Canada in 2013, thank you.

Finally, and most importantly, I would like to give my sincere thanks to my parents and brother, for their inspiration, encouragement and endless love. Words can neither qualify nor quantify how I am grateful to have such this kind and supportive parents. They mean the whole world to me.

I know that was all you, and I believe you will be the only one, Thanks God!

## Table of content

|  |           |
|--|-----------|
| <b>CHAPTER 1 - INTRODUCTION .....</b>  | <b>1</b>  |
| <b>1.1 OVERVIEW OF MOLECULAR ELECTRONICS .....</b>                           | <b>2</b>  |
| <b>1.2 HOW TO FABRICATE MOLECULAR JUNCTION? .....</b>                        | <b>3</b>  |
| 1.2.1 Ensemble type of the molecular junction fabrication .....              | 4         |
| 1.2.2 Diazonium chemistry for grafting ensembles of molecular layer .....    | 6         |
| 1.2.3 Possible factors affecting the performance of MJs .....                | 17        |
| 1.2.4 Interlayer buffer in fabrication of cross-bar molecular junction ..... | 18        |
| <b>1.3 HOW DO THE ELECTRONS MOVE THROUGH MOLECULES? .....</b>                | <b>19</b> |
| 1.3.1 Transport diagnostics .....  | 20        |
| 1.3.1.1 Attenuation slope, beta ( $\beta$ ).....                             | 20        |
| 1.3.1.2 Functional form of the Current-Voltage curve .....                   | 22        |
| 1.3.1.3 Independent measurement.....   | 23        |
| 1.3.1.4 Temperature dependence .....   | 24        |
| 1.3.1.5 Structure correlations .....   | 24        |
| 1.3.1.6 Physical stimuli.....  | 25        |
| 1.3.2 Energy level alignment .....   | 25        |
| 1.3.2.1 Vacuum level shift.....  | 26        |
| 1.3.2.2 Band bending .....   | 27        |
| 1.3.3 Coherent vs incoherent transport .....                                 | 30        |
| 1.3.4 General remarks on conduction properties in disordered materials ..... | 33        |
| 1.3.5 Thermally assisted tunneling .....                                     | 36        |
| 1.3.6 Multistep tunneling .....  | 37        |
| <b>1.4 BEYOND ELECTRONIC CHARGE TRANSPORT .....</b>                          | <b>37</b> |
| 1.4.1 Thermoelectric studies .....   | 38        |



|   |           |
|---|-----------|
| 1.4.2 Molecular plasmonics .....  | 39        |
| 1.4.3 Molecular spintronic.....   | 41        |
| 1.4.4 Molecular Optoelectronics .....   | 42        |
| 1.4.4.1 <i>Photo-gating in conductance for molecular junction</i> .....   | 42        |
| 1.4.4.2 <i>Live Raman measurement during transport</i> .....  | 43        |
| <b>1.5 REAL WORLD APPLICATIONS OF MOLECULAR ELECTRONICS .....</b>   | <b>44</b> |
| <b>1.6 SCOPE OF THESIS.....</b>   | <b>46</b> |
| <b>CHAPTER 2 - ROBUST ALL-CARBON MOLECULAR JUNCTIONS ON FLEXIBLE OR SEMI-TRANSPARENT<br/>SUBSTRATES USING PROCESS-FRIENDLY FABRICATION.....</b> | <b>48</b> |
| <b>2.1 INTRODUCTION.....</b>  | <b>49</b> |
| <b>2.2 EXPERIMENTAL SECTION .....</b>   | <b>51</b> |
| 2.2.1 Fabrication of molecular junction.....  | 51        |
| 2.2.1.1 <i>Bottom contact deposition</i> .....  | 51        |
| 2.2.1.2 <i>Molecular layer grafting</i> .....   | 52        |
| 2.2.1.3 <i>Top contact deposition</i> .....   | 57        |
| 2.2.2. Wafer scale lithography for eC junction .....  | 57        |
| <b>2.3 RESULTS AND DISCUSSION .....</b>   | <b>62</b> |
| 2.3.1 Characterization of eC electrode .....  | 62        |
| 2.3.1.1 <i>Spectroscopic characterization of eC electrode</i> .....   | 62        |
| 2.3.1.2 <i>Surface coverage of eC layer</i> .....   | 68        |
| 2.3.1.3 <i>Surface roughness of eC electrode</i> .....  | 71        |
| 2.3.1.4 <i>Sheet resistance of eC electrode</i> .....   | 72        |
| 2.3.2 Molecular layer grafting on eC electrode .....  | 74        |
| 2.3.3 Electronic behavior of eC/molecule/eC junctions .....   | 76        |
| 2.3.3.1 <i>Comparison of two- and four-wire mode measurements</i> .....   | 79        |
| 2.3.4 Statistics of the fabricated eC junction.....   | 80        |

|   |            |
|---|------------|
| 2.3.5 Stability of junctions fabricated by eC electrode.....                            | 82         |
| 2.3.6 Flexibility of eC junctions.....  | 84         |
| 2.3.7 Transparency of eC junctions.....   | 86         |
| 2.3.8 Wafer scale lithography for eC molecular junctions.....                           | 89         |
| <b>2.4 CONCLUSION.....</b>  | <b>91</b>  |
| <b>CHAPTER 3 - STRUCTURE CONTROLLED LONG-RANGE SEQUENTIAL TUNNELING IN CARBON-BASED</b> |            |
| <b>MOLECULAR JUNCTIONS.....</b>   | <b>93</b>  |
| <b>3.1 INTRODUCTION.....</b>  | <b>94</b>  |
| <b>3.2 EXPERIMENTAL SECTION.....</b>  | <b>97</b>  |
| 3.2.1 Fabrication of bottom contact (PPF).....  | 97         |
| 3.2.2 Molecular layer grafting and thickness measurement.....                           | 98         |
| 3.2.3 Top contact deposition to complete junction.....                                  | 101        |
| 3.2.4 Electrical measurement.....   | 101        |
| 3.2.5 UV-Vis measurement on grafted molecular layer.....                                | 102        |
| 3.2.6 Statistics of fabricated junctions.....   | 104        |
| <b>3.3 RESULTS.....</b>   | <b>105</b> |
| 3.3.1 Electrical behavior of molecular junctions.....                                   | 106        |
| 3.3.2 Temperature dependent conductivity.....   | 111        |
| 3.3.3 Optical Absorption by Molecular Layers.....                                       | 117        |
| 3.3.4 Structural Effects on Junction Behavior.....                                      | 121        |
| <b>3.4 DISCUSSION.....</b>  | <b>124</b> |
| 3.4.1 Discussion about relevance of Pool-Frankel and Schottky mechanism.....            | 127        |
| 3.4.2 Proposed multistep tunneling mechanism.....                                       | 132        |
| <b>3.5 CONCLUSION.....</b>  | <b>135</b> |

## CHAPTER 4 - ORBITAL CONTROL OF PHOTOCURRENTS IN LARGE AREA ALL-CARBON MOLECULAR JUNCTIONS

|  |            |
|--|------------|
| .....  | 136        |
| <b>4.1 INTRODUCTION</b> .....  | <b>137</b> |
| <b>4.2 EXPERIMENTAL SECTION</b> .....                                | <b>139</b> |
| 4.2.1 Molecular layer grafting and thickness measurement .....       | 140        |
| 4.2.2 Completing the junction and electrical measurements.....       | 146        |
| 4.2.3 AC Photocurrent measurements .....                             | 147        |
| 4.2.4 External quantum efficiency calculation .....                  | 148        |
| 4.2.5 OCP and photocurrent under the bias measurements.....          | 150        |
| 4.2.6 UV-Vis absorbance spectroscopy.....                            | 151        |
| <b>4.3 RESULTS</b> .....   | <b>151</b> |
| 4.3.1 UV-Vis Absorption of molecular layer in different medium ..... | 151        |
| 4.3.2 Correlation of photocurrent with absorbance .....              | 153        |
| 4.3.3 Open-circuit potential and photocurrent polarity.....          | 155        |
| 4.3.4 Effect of the thickness .....                                  | 157        |
| 4.3.5 Heat-related photocurrent .....                                | 160        |
| 4.3.6 Back illumination of the junctions .....                       | 162        |
| <b>4.4 DISCUSSION</b> .....  | <b>163</b> |
| 4.4.1 Orbital control of the photocurrent polarity .....             | 163        |
| 4.4.2 Molecule in contact with electrode.....                        | 166        |
| 4.4.3 Molecular layer in contact with two interface .....            | 168        |
| 4.4.4 Photocurrent mechanism in thick molecular junction .....       | 170        |
| <b>4.5 CONCLUSION</b> .....  | <b>172</b> |
| <b>CHAPTER 5</b> .....   | <b>174</b> |
| <b>5.1 SUMMARY AND FINAL THOUGHTS</b> .....                          | <b>175</b> |

|                         |            |
|-------------------------|------------|
| <b>5.2 OUTLOOK.....</b> | <b>178</b> |
| <b>REFERENCES.....</b>  | <b>180</b> |

## List of Tables

|   |     |
|---|-----|
| <b>Table 1.1</b> Comparison of different approaches for molecular junction fabrication.....   | 4   |
| <b>Table 1.2</b> Comparison of fabrication techniques for ensemble fabrication of molecular junction. ....  | 6   |
| <b>Table 1.3</b> Structure of the molecule grafted on the surface of GC and further analyzed by TOF-SIMS.....   | 9   |
| <b>Table 1.4</b> Mass (m/z) and counts of the mass fragments from the surface of modified GC. .   | 10  |
| <b>Table 1.5</b> Comparison of $\beta$ for variety of molecular layers in different fabrication paradigm. ....  | 22  |
| <b>Table 2.1</b> Electrochemical parameters for grafting Anthraquinone molecular layer on the surface of PPF.....                                     | 53  |
| <b>Table 2.2</b> Anthraquinone grafting parameters for Cr <sub>3</sub> /Au <sub>15</sub> /eC <sub>10</sub> .....                                      | 55  |
| <b>Table 2.3</b> Anthraquinone grafting parameters on Cr <sub>3</sub> /Au <sub>15</sub> surfaces .....  | 56  |
| <b>Table 2.4</b> Electrochemical grafting parameters for NAB on integrated chips.....   | 59  |
| <b>Table 2.5</b> Statistics of integrated Cr <sub>4</sub> /Au <sub>30</sub> /eC <sub>10</sub> /NAB/eC <sub>10</sub> /Au <sub>20</sub> junctions ..... | 61  |
| <b>Table 2.6</b> 4-Point probe resistances of eC and Au films on Quartz (Q) and SiOx .....  | 74  |
| <b>Table 2.7</b> <i>JV</i> Statistics of SiOx/Cr/Au/eC/AQ/eC/Au junctions .....   | 81  |
| <b>Table 3.1</b> Electrochemical parameters for grafting of molecule on the surface of PPF .....  | 99  |
| <b>Table 3.2</b> R <sup>2</sup> for Fluorene data shown in Figure 3.8b of the main text, following least square fit to the abscissa indicated.....    | 109 |
| <b>Table 3.3</b> Slopes and intercepts for plots of ln <i>J</i> vs <i>V</i> <sup>1/2</sup> for Fluorene MJs.....                                      | 110 |
| <b>Table 3.4</b> Calculated apparent activation energies for Fluorene junctions .....   | 116 |
| <b>Table 3.5</b> Orbital Energies, UV-Vis absorption and Current Densities.....   | 122 |

|  |     |
|--|-----|
| <b>Table 3.6</b> Parameters obtained by fitting of Pool-Frankel mechanism to experimental data.<br>.....     | 129 |
| <b>Table 3.7</b> Parameters obtained by fitting of Schottky mechanism to experimental data.....              | 130 |
| <b>Table 4.1</b> Summary of photocurrent results and DFT predicted energy levels of examined molecules ..... | 155 |
| <b>Table 4.2</b> Scan ranges, PC statistics and number of samples for each junction type. ....               | 159 |

## List of Figures

|   |    |
|---|----|
| <b>Figure 1.1</b> Four important issues in Molecular electronics .....  | 3  |
| <b>Figure 1.2</b> Typical surface modification with approximate surface bond energy. ....   | 5  |
| <b>Figure 1.3</b> Examples of ensemble molecular junction platforms. <b>(a)</b> Nanopore, <b>(b)</b> Microscale via hole, <b>(c)</b> Nanoparticles bridged, <b>(d)</b> Crosswire, <b>(e)</b> Hg liquid metal, <b>(f)</b> Eutectic gallium-indium based. ....  | 6  |
| <b>Figure 1.4</b> (A) Raman spectrum of solid Diazonium Nitrobenzene (NB) (Red) and SERS spectra of diazonium NB-modified 40 nm AuNPs (Black line), 40 nm Au nanoparticles (NP) reacted with NB (Blue), and unmodified 40 nm AuNPs (Green). (B) Expanded Raman and SERS spectra of the samples in section (A). Figure reproduced with permission from ref [41]9 |    |
| <b>Figure 1.5</b> Proposed mechanism for multilayer formation through diazonium grafting.....   | 11 |
| <b>Figure 1.6</b> Representative Cyclic Voltammogram (CV) for grafting of AQ on the surface of carbon electrode.....  | 12 |
| <b>Figure 1.7</b> Suggested schematics of formation of AQ-based films obtained from electroreduction of AQ at three different potentials.....   | 13 |
| <b>Figure 1.8</b> Representative cyclic voltammograms recorded at a gold-covered QCM crystal on 2 mM AQD, and E (sweeping) = (A) $-0.145$ or (B) $-1.445$ V vs SCE in MeCN.....   | 14 |
| <b>Figure 1.9</b> IRRAS spectra of Au-Anthraquinone plates prepared from 2 mM AQD with increasing thickness.....  | 15 |
| <b>Figure 1.10</b> Raman spectra of Anthraquinone (AQ) multilayers on eC (A) and on eC/Ag (B), and simulated Raman spectra of the monomer (C), linear trimer (D), and branched trimer (E) of anthraquinone. Dihedral angles between AQ units are assumed to be $\sim 38^\circ$ in optimized oligomers.....  | 16 |

**Figure 1.11** Schematic illustration of the possible damage and defects in molecular layers.

**(A)** Stars represent the interaction of molecular end group with deposited metal (formation of a top chemi-contact). Labels: 1) molecular fracture, 2) formation of double-bonds, and 3) cross-linking. **(C)** Labels: 1) grain boundary in a crystalline SAM, 2) gauche kinks and looping, and 3) missing sites. **(D)** Digits: 1) a hot spot of shorter gap and 2) a cold spot of extra voids. .... 17

**Figure 1.12** Several examples of high-yield ensemble molecular junctions; based on the conducting buffer interlayer: **(A)** Conducting polymer PEDOT:PSS, **(B)** Conducting polymer Aedotron P, **(C)** Graphene, **(D)** Reduced graphene oxide, **(E)** Electron-beam deposited carbon. .... 19

**Figure 1.13** Six main steps in understanding of the transport mechanism in a molecular junction. .... 20

**Figure 1.14 a)** Collection of data from several studies of nanometer-scale contact area molecular junctions. Current densities ( $A/nm^2$ ) at 0.1 V is plotted as a function of molecular layer thickness. .... 21

**Figure 1.15 a)** Several scenarios for environments of a single molecule: **1)** molecule in gas phase, **2)** isolated molecule on a metal surface, **3)** one complete molecular layer on a metal surface, **4)** first molecular layer on metal surface, beneath a molecular film, **5)** bulk molecular film, away from both the metal interface and the film surface, and **6)** surface of a molecular film. **b)** Changes in HOMO and LUMO levels depending on the molecular environments shown in panel a. .... 26

**Figure 1.16** Several possible factors that affect formation of an interfacial dipole layer at an organic/metal interface: **a)** Charge transfer across the interface, **b)** Concentration of electrons



in the adsorbate leading to positive charging of the vacuum side, **c)** Rearrangement of electron cloud at the metal surface, with the reduction of tailing into vacuum, **d)** Strong chemical interaction between the surface and the adsorbate leading to the rearrangement of the electronic cloud and also the molecular and surface geometries (both directions of dipoles possible), **e)** Existence of interface state serving as a buffer of charge carriers, and **f)** Orientation of polar molecules or functional groups.....27

**Figure 1.17** Two common scenarios for energy band diagrams (upward and downward shift) of metal and n-type semiconductor contacts in different stages.  $E_{vac}$ : vacuum energy;  $E_c$ : the energy of conduction band minimum;  $E_v$ , the energy of valence band maximum;  $\phi_m$ : metal work function;  $\phi_s$ : semiconductor work function;  $\chi_s$ , electron affinity of the semiconductor. ....28

**Figure 1.18 a)** Electronic structure of a metal and an organic solid at an infinite distance.  $\Phi Bn$  and  $\Phi Bp$  denote the injection barriers for electron and hole. **b)** Contact of a metal and a thin organic solid layer. Interfacial energy diagram with a shift of VL at the interface due to dipole layer formation. In this figure, the organic side is charged positive, making this side more stable (low energy) for an electron, and making the sign of shift negative. **(c)** Interfacial energy diagram with band bending. The energy levels are bent by the charge redistribution in the organic layer to achieve electrical equilibrium with the alignment of the Fermi levels of the two sides.  $V_{bi}$  : built-in potential,  $W$ : diffusion layer of thickness. **(d)** Same bending scenario as the panel c with considering the vacuum level shift. ....30

**Figure 1.19** Simple schematics of the difference between coherent and incoherent transport. ....31

|   |    |
|---|----|
| <b>Figure 1.20</b> Coherent vs incoherent transport diagram. Green color indicates weakly temperature dependent transport mechanism. ....   | 32 |
| <b>Figure 1.21</b> Schematics of indicated transport mechanisms with their effective barriers and charge movement pathway. <b>(A)</b> Direct tunneling across a rectangular barrier. <b>(B)</b> Fowler-Nordheim tunneling across the triangular top part of a trapezoidal insulating barrier between two metallic electrodes, and Simmons tunneling through the lower rectangular part. <b>(C)</b> Schottky emission. <b>(D)</b> Poole-Frenkel conduction. <b>(E)</b> Hopping conduction through defects (slow) or virtual states (superexchange, fast). .... | 33 |
| <b>Figure 1.22</b> Schematics of the hopping transition between two localized $i$ and $j$ state along the contributing factors. Gaussian-like lines depicts carries wave function at each site.....   | 34 |
| <b>Figure 1.23</b> Two possible hopping transition between filled and unoccupied states: 1) nearest neighbor hopping, 2) Variable range hopping. Dashed line depicts the position of Fermi-level .....  | 35 |
| <b>Figure 1.24</b> Schematic representation of the energy bands of a metal-insulator-metal for thermally assisted tunneling compared to the Fermi-level tunneling.....  | 37 |
| <b>Figure 1.25</b> Histograms of Seebeck coefficient and fitting with Gaussian distribution for five indicated molecules. 1 and 2 exhibit positive $S$ while 4 and 5 exhibit negative $S$ . The Seebeck coefficient for 3 is close to zero.....   | 39 |
| <b>Figure 1.26 a)</b> Real plane images ( $x$ - $y$ plane) plotted as a function of time $t$ ( $z$ -axis). Images were recorded at intervals of 0.5 second and obtained from a junction with self-assembled monolayer film at a bias of $-1.8$ V. <b>b)</b> Schematics of the tested junctions in panel a. ....   | 40 |
| <b>Figure 1.27</b> Typical $dI/dV$ spectra (differential conductance) taken on parallel and antiparallel oriented cobalt islands clearly reveal the spin-polarized density of states below  |    |

the Fermi edge and effect of the magnetic field orientation on electronic behavior of junction.  
.....41

**Figure 1.28 (a)** Conductance heat-map plot for AminoPyr without illumination (dark condition). The colors correspond to the frequencies of the histograms; lighter colors indicate higher frequencies. **(b)** conductance heat-map plot under illumination for the same junction shown in panel a. The colored circles correspond to data in the dark (grey) and under illumination (cyan). **(c)** Plots of  $\log J$  vs  $V$  for AminoPyr from a single device showing three traces each from dark–light cycle. The dashed lines show the slight asymmetry of the device in both the dark (black squares) and light (cyan circles) states. **(d)** The plot of conductance cycling of AminoPyr. The values of  $\log J$  at 0.5 V as a function of light/dark cycles for a range of 100 consecutive cycles. The time between each cycle is on the order of 60 s. These data show a clear, statistical difference between AminoPyr-dark and AminoPyr-light.....43

**Figure 1.29 (a)** The Raman band of bipyridine at  $1609\text{ cm}^{-1}$  at the elevated applied voltage across the junction. Inset: current-voltage curve for the examined junction. Tip enhanced Raman spectroscopy setup is used to make a connection with single molecule of bipyridine and Raman measurement **(b)** The schematic for a possible explanation of band splitting at  $1609\text{ cm}^{-1}$  due to the applied voltage.....44

**Figure 1.30 (a)** Cross-sectional schematic of an idealized molecular junction structure and a photograph of the molecular junctions with a SIM-card format to simplify testing and integration into analog circuits. **(b)** Simplified schematic of the clipping amplifier section of the circuit employed in the prototype for the op-amp clipping gain stage. **(c)** Output waveforms for sine-wave input. **(d)** The power spectra for the Si and MJ waveforms with odd and even harmonics labeled.....46

|  |    |
|--|----|
| <b>Figure 2.1</b> Cyclic voltammogram of reduction of AQ diazonium ion on PPF.Cyclic voltammogram of reduction of AQ diazonium ion on PPF. ....  | 54 |
| <b>Figure 2.2</b> Cyclic voltammogram grafting of anthraquinone on the surface of Cr <sub>3</sub> /Au <sub>15</sub> /eC <sub>10</sub> . ....   | 55 |
| <b>Figure 2.3</b> Cyclic voltammogram grafting of anthraquinone on the surface of Cr <sub>3</sub> /Au <sub>15</sub> . ....   | 56 |
| <b>Figure 2.4</b> Schematic illustrations Au/eC/molecule/eC/Au molecular junctions using electron-beam deposited carbon adjacent to molecular layer. Each chip is 1.8 x 1.2 cm. Final dimension of each junction is 250 x 250 μm. ....   | 57 |
| <b>Figure 2.5</b> Cyclic voltammograms for grafting different thicknesses of Nitro-azobenzene (NAB) on the surface of integrated Cr <sub>4</sub> /Au <sub>30</sub> /eC <sub>10</sub> chips in acetonitrile solution of 1 mM NAB and 0.1 M TBAPF <sub>6</sub> . ....  | 60 |
| <b>Figure 2.6</b> Raman spectrum of electron-beam deposited carbon (eC). ....  | 63 |
| <b>Figure 2.7</b> Raman spectra of eC after 3 Hours annealing at 1000 °C in forming gas. ....  | 64 |
| <b>Figure 2.8</b> Raman spectra of pyrolyzed photoresist (PPF). ....   | 64 |
| <b>Figure 2.9</b> Raman spectra of glassy carbon (GC). ....  | 65 |
| <b>Figure 2.10</b> XPS C 1s region of electron beam deposited carbon (eC). ....  | 66 |
| <b>Figure 2.11</b> XPS C 1s region of eC after 3 hours annealing at 1000 °C. ....  | 66 |
| <b>Figure 2.12</b> UPS spectra of eC, Al, Al/eC, Cr/Au and Au/TiC/eC surfaces. The substrate for all cases was Si/SiOx. ....   | 68 |
| <b>Figure 2.13 (a)</b> Auger electron spectra of Si/SiOx/Cr <sub>3</sub> /Au <sub>30</sub> /TiC <sub>3</sub> /eC <sub>10</sub> before and after 30 second sputtering. The inset is the magnification of the oxygen peak at 505 eV. <b>(b)</b> Auger surface mapping of selected peak of oxygen at 505 eV and carbon at 260 eV for the surface of Au <sub>30</sub> /TiC <sub>3</sub> /eC <sub>10</sub> without sputtering. Ti and Au are undetectable by either a survey scan or elemental maps. .... | 69 |

**Figure 2.14 (a)** CV for the Si/SiO<sub>x</sub>/Cr<sub>3</sub>/Cu<sub>40</sub> and Si/SiO<sub>x</sub>/Cr<sub>3</sub>/Cu<sub>40</sub> /TiC<sub>3</sub>/eC<sub>10</sub> surface in alkaline solution (NaOH 0.1M) at 0.1 V/s. **(b)** Magnification of voltammograms shown in panel A for the region of Cu oxidation. **(c)** CV obtained for Si/SiO<sub>x</sub>/Cr<sub>3</sub>/Ni<sub>30</sub> and Si/SiO<sub>x</sub>/Cr<sub>3</sub>/Ni<sub>30</sub> /TiC<sub>3</sub>/eC<sub>10</sub> in alkaline solution (NaOH 0.1M) at 0.1 V/sec. **(d)** Magnification of voltammograms shown in panel C for the region of Ni oxidation. The area of the exposed electrode was 0.28 cm<sup>2</sup> for all cases..... 70

**Figure 2.15 (a)** AFM images of e-beam deposited Au and Au/eC surfaces on Si/SiO<sub>x</sub> substrate. Subscripts indicate thicknesses of each deposited layer in nm. Ra and Rq are average and root mean square roughness, respectively. **(b)** AFM images of the surface of e-beam deposited Cr/Au and Cr/Au/eC surfaces on Si/SiO<sub>x</sub> substrate. **(c)** AFM line scan profiles of surfaces shown in panel (a). **(d)** AFM line scan profiles of surfaces shown in panel (b). ..... 72

**Figure 2.16** Cyclic voltammograms of Anthraquinone diazonium solution on PPF, Cr/Au, and Cr/Au/eC surfaces. The solution was contained 1 mM AQ diazonium fluoroborate in acetonitrile with 0.1 M tetrabutylammonium hexafluorophosphate (TBAPF<sub>6</sub>) as supporting electrolyte, and scan rate was 50 mV/s for all cases. Detailed grafting conditions and cyclic voltammograms are shown in section 2.2.1.2. .... 76

**Figure 2.17 (a)** Current density vs bias voltage (*JV*) curves for junctions fabricated by Cr/Au/eC electrode as bottom contact, determined with a Keithley 2602A sourcemeter. AFM thicknesses of anthraquinone molecular layer are indicated in nm. Yield for tested junctions was 100% (non-shorter junctions) and error bars represent ± standard deviation for 8 junctions of each thickness. **(b)** Semi-logarithmic scale of *JV* curves shown in panel (a). Right side inset: schematics of tested junctions (Cr layer under the Au is not shown in

schematics). **(c)** Semi-logarithmic scale of  $JV$  curves for junctions fabricated by Cr/Au electrode as a bottom contact. Yield for tested junction was lower than 50% (non-shortcd) and error bars represent  $\pm$  standard deviation for non-shortcd junctions. **(d)** Corresponding attenuation plot at 0.1 V for different bottom electrodes.  $\beta$  is the slope of observed for SiOx/Au<sub>15</sub>/eC<sub>10</sub>/AQ<sub>x</sub>/eC<sub>10</sub>/Au<sub>15</sub> devices..... 78

**Figure 2.18** Comparison of two- and four-wire mode measurement for PPF/ NAB /eC<sub>10</sub>/Au<sub>20</sub>. ..... 79

**Figure 2.19** Comparison of two- and four-wire mode measurement for Cr<sub>3</sub>/Au<sub>30</sub>/eC<sub>10</sub>/ NAB/eC<sub>10</sub>/Au<sub>20</sub>..... 80

**Figure 2.20** Statistics for Cr<sub>3</sub>/Au<sub>15</sub>/eC<sub>10</sub>/AQ<sub>3.8</sub> /eC<sub>10</sub>/Au<sub>15</sub> junctions **a)** Overlay of eight measured  $I$  versus voltage **b)** Average of eight  $I$  versus voltage  $\pm$  standard deviation **c)** Overlay of eight  $\ln(I)$  versus voltage **d)** Average of eight  $\ln(I)$  versus voltage  $\pm$  standard deviation. .... 82

**Figure 2.21 (a)** Overlay of  $JV$  curves for fresh Au/eC/AQ/eC/Au junction before and after being stored in ambient air for 85 days. AQ thickness  $\approx$  3.6 nm. **(b)** Overlay of  $JV$  curve of a Au/eC/AQ/eC/Au junction before and after 10 million  $JV$  cycles to  $\pm$  1.3 V in air at 1000 V/sec. AQ thickness  $\approx$  4.4 nm. **(c)**  $JV$  curves for a single Au/eC/AQ/eC/Au junction at four temperatures from 77 to 450 K in vacuum. AQ thickness  $\approx$  4.4 nm. Corresponding Arrhenius plot is shown in Figure 2.22. Junctions were deposited on a Si/SiOx substrate with 3 nm Cr adhesion layer in all cases. .... 83

**Figure 2.22** Arrhenius plot for Cr<sub>3</sub>/Au<sub>15</sub>/eC<sub>10</sub>/AQ<sub>4.5</sub>/eC<sub>10</sub>/Au<sub>15</sub> molecular junction. Approximate activation energies in different ranges of temperature are indicated..... 84

**Figure 2.23 (a)** Optical image of PET/Cr<sub>3</sub>/Au<sub>15</sub>/ eC<sub>10</sub>/AQ/eC<sub>10</sub>/Au<sub>15</sub> devices deposited on transparency film (PET). Magnification shows an individual junction. **(b)** Optical image of

the fabricated device on PET substrate while bent. **(c)**  $JV$  curves of junctions fabricated on flexible PET substrate before (lines) and after (points) being bent 100 times to the degree shown in panel (b), which reduced the 1.8 cm dimension in panel (a) to  $\sim 1.4$  cm. Three AQ thicknesses were deposited electrochemically but were not be verified by AFM. **(d)** Overlay of  $JV$  curve of freshly fabricated AQ junction on flexible PET substrate before (blue) and after (red) 10 million JV cycles to  $\pm 1.3$  V in air.....86

**Figure 2.24 (a)** Optical absorbance of Quartz/Cr<sub>3</sub>/Au<sub>15</sub>/eC<sub>10</sub>/AQ relative to an air reference. Three different thicknesses of AQ molecular layer are shown. **(b)** Absorbance spectra of panel (a) following subtraction of the unmodified Q/Cr<sub>3</sub>/Au<sub>15</sub>/eC<sub>10</sub> spectrum, to yield the absorbance due to the AQ molecular layers. **(c)** Absorbance spectrum of complete Quartz/Cr<sub>3</sub>/Au<sub>15</sub>/eC<sub>10</sub>/AQ/eC<sub>10</sub>/Au<sub>15</sub> junction relative to an air reference, for three different thicknesses of Anthraquinone. **(d)** Absorbance from panel (c) following subtraction of the spectrum of a “blank” Q/Cr<sub>3</sub>/Au<sub>15</sub>/eC<sub>20</sub>/Au<sub>15</sub> sample.....88

**Figure 2.25 (a)** Image and enlargement of 100 mm diameter wafer of integrated chip design after dicing but before molecular layer deposition. **(b)** Completed chip with 25 Si/SiO<sub>x</sub>/Cr<sub>3</sub>/Au<sub>30</sub>/eC<sub>10</sub>/NAB/eC<sub>10</sub>/Au<sub>20</sub> after molecular layer and top contact deposition. NAB= nitroazobenzene oligomers. Magnification shows individual junction with the position of four probes for electrical contact to Au surfaces. **(c)** Overlay of  $JV$  curves for 8 junctions selected randomly on a chip with a 4.1 nm thick layer of NAB. **(d)** Average  $JV$  curves for integrated junctions with four different NAB thicknesses. Yield for tested junction was 100% of non-shortcd junctions and error bars represent  $\pm$  standard deviation for 6-8 junctions of each thickness. Statistics were given in Table 2.6.....90

**Figure 3.1** Cyclic voltammograms during grafting of Anthraquinone on the surface of PPF, with a variation of negative potential limit causing AQ layers with different thicknesses. ....98

**Figure 3.2 (a)** AFM Tapping mode 5 x 5  $\mu\text{m}$  tapping mode image of a 1 x 1  $\mu\text{m}$  “trench” made in a PPF/FL layer using contact mode AFM. **(b)** Histogram of heights determined within the white rectangle of the AFM image. Uncertainty in thickness is the quadrature addition of the two Gaussian  $\sigma$  values..... 100

**Figure 3.3** Schematics of fabricated complete chips. Bottom contact consists of four patterned parallel PPF lines. Top contact consists of eC (10 nm) and Au (20 nm). ..... 101

**Figure 3.4 (a)** Schematics of 4-wire mode electrical connection. **(b)** Schematics of 4-wire mode electrical measurement setup. ADC1 stands for the analog-to-digital channel for current and ADC0 monitors voltage that has a differential input..... 102

**Figure 3.5 (a)** UV-Vis absorption spectra for optically transparent PPF (black) and OTPPF modified with a BTB layer (red). **(b)** OTPPF/BTB spectrum after subtraction of unmodified OTPPF spectrum. .... 103

**Figure 3.6 (a)**  $JV$  curves for different FL thicknesses, with each curve representing the average of four junctions on a single sample. Yield for tested junctions was 100% of non-shortened junctions and error bars represent  $\pm$  standard deviation for four junctions of each thickness. **(b)** Semilogarithmic plot of  $JV$  curves shown in panel a..... 104

**Figure 3.7 (a)** Schematic illustration of PPF/fluorene/eC<sub>10</sub>/Au<sub>20</sub> molecular junction.  $n$  is a number of repeating units of oligomer which determine final thickness of molecular layer. **(b)** Structures and frontier orbital energy diagram for FL, AQ, NAB and BTB, relative to a vacuum reference. Orbital energies were calculated by Density Functional Theory (DFT) B3LYP 6-31G(d), in Gaussian 09. Fermi level of PPF and eC is -4.8 V vs vacuum..... 105



**Figure 3.8** (a) Current density vs bias voltage ( $JV$ ) curves for PPF/FL $_d$ /eC $_{10}$ /Au $_{20}$ .  $d$  is a thickness of fluorene molecular layer:  $d = 2.3, 3.0, 3.4, 3.8, 4.1, 4.5, 5.0, 5.5, 6.1, 7.1, 7.6, 8.0, 8.6$  nm in the order indicated. Each curve is an average of four independent junctions, with a typical deviation shown for  $d = 6.1$  nm junction. (b) Semilogarithmic plot of  $JV$  curves shown in panel a. (c) Corresponding attenuation plot for  $V = 0.3, 1.0$  and  $2.0$  V, with the slopes ( $\beta$ ) indicated. (d) Overlay of normalized semilogarithmic  $JV$  curves shown in panel b. Current density of each thickness was normalized to  $J = 1$  A/cm $^2$  at  $0.3$  V..... 107

**Figure 3.9**  $JV$  curves in semilogarithmic scale for different thicknesses of (a) NAB, (b) AQ ..... 108

**Figure 3.10** Natural log of current density vs square root of bias voltage for the same series of fluorene junctions shown in Figure 3.8, for positive bias. Order of thickness is the same as in Figure 3.8a..... 109

**Figure 3.11**  $\ln J$  vs  $V^{1/2}$  for indicated thicknesses of (a) BTB, (b) NAB, (c) AQ, (d) FL..... 111

**Figure 3.12** (a)  $JV$  curves for PPF/FL $_{5.5}$ /eC $_{10}$ /Au $_{20}$  junction at four temperatures from 200 to 440 K in vacuum. (b)  $\ln J$  vs  $V^{1/2}$  plots for curves in panel a. (c) Arrhenius plots at 0.1 and 0.3 V, with apparent activation energies for high and low  $T$  segments. (d)  $\ln J$  vs  $T$  at 0.1, 0.3 and 0.5 V.  $R^2$  for linear fits of the lines are indicated..... 112

**Figure 3.13** (a)  $JV$  curves for PPF/FL $_{3.8}$ /eC $_{10}$ /Au $_{20}$  junction at four temperatures from 200 to 440 K in vacuum. (b)  $\ln J$  vs  $V^{1/2}$  plots for curves in panel a. (c) Arrhenius plots at 0.1, with apparent activation energies for high and low  $T$  segments. (d)  $\ln J$  vs  $T$  at 0.1 V.  $R^2$  for linear fits of the lines are indicated..... 113

**Figure 3.14** (a)  $JV$  curves for PPF/FL $_{7.6}$ /eC $_{10}$ /Au $_{20}$  junction at four temperatures from 200 to 440 K in vacuum. (b)  $\ln J$  vs  $V^{1/2}$  plots for curves in panel a. (c) Arrhenius plots at 0.1, with

|   |     |
|---|-----|
| apparent activation energies for high and low $T$ segments. <b>(d)</b> $\ln J$ vs $T$ at 0.1 V. $R^2$ for linear fits of the lines are indicated.....   | 114 |
| <b>Figure 3.15</b> $\ln J$ vs $T$ at 0.1 V for fluorene junction at different thickness. Slopes and intercepts for linear fits of the lines are indicated. ....   | 115 |
| <b>Figure 3.16 (a)</b> $\ln J$ vs $T$ for AQ junctions at indicated thickness and voltage <b>(b)</b> $\ln J$ vs $T$ for BTB at indicated thickness and voltage. ....  | 117 |
| <b>Figure 3.17 (a)</b> Optical absorbance spectrum of fluorene monomer in acetonitrile (red) and fluorene multilayer bonded to the surface of OTPPF (Blue), after subtraction of unmodified OTPPF spectrum. TD-DFT prediction of fluorene monomer spectrum is dashed green line. <b>(b)</b> Optical absorbance of four thicknesses of fluorene on OTPPF in the range of $\sim 2$ to 9 nm. Inset: normalized spectra for different fluorene thicknesses..... | 118 |
| <b>Figure 3.18</b> Overlays of UV-Vis spectra of molecule's monomer in solution (ACN), multilayer on OTPPF, and TD-DFT (B3LYP 6-31G) spectra for <b>(a)</b> AQ, <b>(c)</b> BTB, and <b>(e)</b> NAB. The optical absorbance of the grafted molecules on the surface of OTPPF with increasing molecular layer thickness for <b>(b)</b> AQ, <b>(d)</b> BTB, and <b>(f)</b> NAB.....  | 120 |
| <b>Figure 3.19 (a)</b> UV-Vis absorption spectra for the indicated monomeric molecules in acetonitrile solution, with concentrations near $1 \times 10^{-4}$ M. Spectra were normalized to their absorbance maxima to permit comparison. <b>(b)</b> Absorbance spectra for FL, AQ, NAB and BTB multilayers bonded to OTPPF, all following subtraction of unmodified OTPPF spectrum. ....  | 121 |
| <b>Figure 3.20 (a)</b> $JV$ curves of BTB, NAB, FL and AQ with thicknesses close to 8 nm. <b>(b)</b> $\ln  J $ vs $V^{1/2}$ plots for curves in panel <b>a</b> .....  | 123 |

**Figure 3.21** (a) Attenuation plots for BTB, NAB, FL, AQ, all obtained at 0.5 V. (b)  $\ln J$  for  $V=0.5$  V and  $d=8$  nm for the four molecules plotted vs the energy of the main UV-Vis absorption peak of the molecular layer.  $R^2$  is the correlation coefficient for the linear fit shown. (c) The same  $\ln J$  plotted vs the DFT determined LUMO energy of the free molecules (d)  $\ln J$  vs free molecule HOMO energy from DFT. (e)  $\ln J$  vs the DFT determined HOMO-LUMO gap..... 124

**Figure 3.22** (a)  $\ln J$  vs  $E^{1/2}$  plots for curves for Fluorene junctions with thickness indicated in nm. (b) Attenuation plot at the constant field for the line shown in panel a at  $E = 0.25, 1$  and  $2$  V/nm, with the slopes ( $\beta$ ) indicated..... 128

**Figure 3.23** Dielectric constant measured by impedance spectroscopy for Fluorene junctions versus thickness of Fluorene molecular layer..... 131

**Figure 3.24** (a) Energy level diagram at zero bias for a fluorene junction with six pair of localized HOMO and LUMO states, using free molecule DFT energies and a PPF Fermi level of  $-4.8$  eV. (b) Magnification of three paired H-L states.  $\alpha$  and  $r_{ij}$  are the localization length and tunneling distance between two neighboring states. (c) The same diagram as panel a for  $V = -2$  V bias (PPF negative), assuming a linear potential profile through the molecular layer. (d) Magnification of panel c, with inset showing the tunneling barrier with height  $\phi_o$  at zero bias and  $\phi$  with bias applied. Arrows indicate possible tunneling paths for electrons. . 134

**Figure 4.1** Scheme of the electro-reduction and grafting of diazonium species on the surface: (a) diazonium species in the solution near to the surface of the electrode accept the electron and release  $N_2$  as a gas (b) Resulted radical medium approaches the surface (c) The radical react with the surface and make the covalent bond (d) With applying more negative potential

to the electrode, electron from the electrode reaches the diazonium species and makes more radicals. These radicals react with the underlayer molecules to make multilayer. .... 141

**Figure 4.2** Structure of amine precursor of eight examined molecules. .... 142

**Figure 4.3 (a)** Electrochemical parameters used for grafting Anthraquinone molecular layer **(b)** Electrochemical parameters used for grafting Fluorene molecular layer **(c)** Corresponding cyclic voltammetry for AQ grafting **(d)** Corresponding cyclic voltammetry for FL grafting. .... 143

**Figure 4.4 (a)** Tapping mode AFM image on the surface of FL multilayer grafted on Cr/Au/eC electrode **(b)** Tapping mode AFM image on the same position as panel **a** after scratching the molecular layer **(c)** histogram of the from the height data in the shown area and fitted Gaussian distribution **(d)** line profile scan for the indicated position **(e)** Thickness of the molecular layer with associated uncertainty. .... 145

**Figure 4.5 (a)** Optical picture of the completed chips. Each dotted circle shows individual cross-bar junction. **(b)** Schematic illustration of Quartz/Cr<sub>3</sub>/Au<sub>20</sub>/eC<sub>10</sub>/Anthraquinone/eC<sub>10</sub>/Au<sub>20</sub> molecular junction. *n* is a number of repeating units of oligomer which determine final thickness of molecular layer. .... 146

**Figure 4.6 (a)** Apparatus used for the PC measurement with continuum source, modulation by on optical chopper and detection with lock-in amplifier. Pie chart indicates the relationship between the measured phase shift from the lock-in amplifier and the PC polarity. **(b)** Optical image of the junction under illumination. .... 148

**Figure 4.7 . a)** Overlay of Photocurrent spectrum for NDI MJ and illuminated light intensity of Xe arc lamp measured at the sample. **b)** Corresponding PC yield and phase shift spectra for NDI MJ shown in panel a. .... 150

**Figure 4.8** **a)** Overlay of optical absorbance of Quartz/Cr<sub>3</sub>/Au<sub>20</sub>/eC<sub>10</sub> (black curve) and the same electrode after NDI grafting on the surface (blue curve). Subtraction of the substrate spectrum yields the absorbance due to the NDI molecular layer shown as the red curve. **b)** Overlay of absorbance spectrum of “blank” Quartz/Cr<sub>3</sub>/Au<sub>20</sub>/eC<sub>10</sub>/eC<sub>10</sub>/Au<sub>15</sub> electrode (black curve) and complete junction *viz* Quartz/Cr<sub>3</sub>/Au<sub>20</sub>/eC<sub>10</sub>/NDI/eC<sub>10</sub>/Au<sub>15</sub> (blue curve). Subtraction of the “blank: spectrum from the MJ spectrum yields absorbance due to the NDI molecular layer in the full MJ stack (red curve). **c)** Schematic of the bottom contact electrode structure modified with NDI molecular layer. **d)** Schematic of the complete NDI MJ consisting of top contact. .... 152

**Figure 4.9** Correlation of absorbance and photocurrent yield of molecules. Overlay of PC yield and absorption spectra for four molecules: **a** FL, **b** AQ, **c** NDI, **d** NAB. Absorption spectra of each molecule in different medium are shown: i) isolated monomer in solution, ii) Multilayer grafted on the surface of bottom contact (Cr/Au/eC/molecular layer), iii) Multilayer grafted on the surface in complete junction including top contact (Cr/Au/eC/molecular layer/eC/Au). All spectrums are corrected for the blank electrode absorption like the NDI shown in Figure 4.8 and normalized to the maximum peak of 1. PCs are shown in the secondary axis at the right side of the graphs with positive sign regardless of the actual measured polarity. .... 154

**Figure 4.10** Polarity of the photocurrent and OCP measurement. **a)** Overlay of the PC yield for six indicated molecules, with the sign of the yield indicating PC polarity. Maximum PC yield normalized to ±1.0 for comparison. **b)** Observed OCP for three on/off light cycles for FL and NAB MJs. **c)** Schematic of OCP apparatus. **d)** Observed current for light on/off

cycles with bias applied to a NAB MJ. Dark current is not subtracted; however, it is much smaller than the PC..... 156

**Figure 4.11 (a)** Current vs bias voltage ( $IV$ ) curves for Cr/Au/eC/AQ<sub>d</sub>/eC/Au.  $d$  is a thickness of Anthraquinone molecular layer:  $d = 4.1 \rightarrow 10.5$  nm. **(b)**  $IV$  curves for Cr/Au/eC/FL<sub>d</sub>/eC/Au.  $d = 4.6 \rightarrow 8.1$  nm. **(c)** Corresponding photocurrent spectrum for the AQ junctions shown in panel a. **(d)** Corresponding photocurrent spectrum for the FL junctions shown in panel b. .... 158

**Figure 4.12 (a)** Measured photocurrent by lock-in amplifier vs frequency of the optical chopper at three different energy of incident light for BTB molecular junction **(b)** Corresponding phase shift of the measured photocurrent vs chopper frequency..... 161

**Figure 4.13 (a)** Observed photocurrent for three on/off light cycles for BTB MJ with top and bottom illumination **(b)** Observed OCP for three on/off light cycles for BTB MJ with top and bottom illumination. 405 nm diode laser and Keithley 6517 is used to the measurement. ... 162

**Figure 4.14 (a)** Photocurrent spectrum of BTB MJ for the top and bottom illumination. **(b)** Phase shift of the same junction in panel (a) for the bottom and top illumination..... 163

**Figure 4.15** Correlation of the PC polarity and molecular orbitals. Frontier orbital energy diagram for the examined molecules relative to vacuum reference along with their Density Functional Theory (DFT) optimized molecular structure are shown. Orbital energies were calculated by DFT B3LYP 6-31G(d), in Gaussian 09. Fermi level of eC by UPS is -4.8 V vs vacuum.<sup>38</sup> Blue shading indicates molecules negative PC and OCP and red shading indicates molecules with positive PC and OCP..... 165

**Figure 4.16** Energy level alignment of the molecule in: **(a)** isolated molecule before contact with the electrode; **(b)** in contact with the surface of the electrode; **(c)** in contact and in electrostatic equilibrium for the molecular layer..... 167

**Figure 4.17** Schematics of the energy level alignment at the heterointerface molecular junction in case of **(a)** donor molecules; **(b)** acceptor molecules.  $V_B$  : potential shift in energy levels of molecules at bottom contact interface,  $V_T$  : potential shift at top contact interface,  $SCR_B$ : space charge region near bottom contact interface,  $SCR_T$ : space charge region near top contact interface..... 169

**Figure 4.18** Schematic of the proposed mechanism for photocurrent production in thick molecular junction. Energy level diagram at zero bias with eight pair of localized HOMO and LUMO states for: **a)** AN junction as an example of a molecule with smaller  $\phi_h$  **b)** NDI junction as an example with smaller  $\phi_e$ . Arrows indicate possible excitation and relaxation paths for the electron. Blue rectangles show the barrier between molecular subunits. Dashed line within the molecule layer is the electrostatic potential profile resulting from partial charge transfer between the electrodes and the oligomeric molecule. Top corner inset of each panel shows the direction of charge separation upon absorption of light by the molecular layer. .... 171

## List of Abbreviations

|                          |  |
|--------------------------|--|
| <b>AB</b>                | Azobenzene                                       |
| <b>ACN</b>               | Acetonitrile                                     |
| <b>AN</b>                | Anthracene                                       |
| <b>AQ</b>                | Anthraquinone                                    |
| <b>A.U.</b>              | Arbitrary Unit                                   |
| <b>BTB</b>               | Bisthienyl benzene                               |
| <b>AFM</b>               | Atomic Force Microscopy                          |
| <b>eC</b>                | electron-Beam Evaporated Carbon                  |
| <b>ELA</b>               | Energy level alignment                           |
| <b>FL</b>                | Fluorene   |
| <b>HOMO</b>              | Highest Occupied Molecular Orbital               |
| <b>IPE</b>               | Internal Photoemission                           |
| <b>LUMO</b>              | Lowest Unoccupied Molecular Orbital              |
| <b>LUSO</b>              | Lowest Unoccupied System Orbital                 |
| <b>ME</b>                | Molecular Electronics                            |
| <b>MJ</b>                | Molecular Junction                               |
| <b>NAB</b>               | Nitroazobenzene                                  |
| <b>NB</b>                | Nitro benzene                                    |
| <b>NDI</b>               | Naphthalene di-imide                             |
| <b>NP</b>                | Nitrophenyl                                      |
| <b>NAB</b>               | Nitroazobenzene                                  |
| <b>FL</b>                | Fluorene   |
| <b>OTPPF</b>             | Optically transparent Pyrolyzed Photoresist Film |
| <b>PPF</b>               | Pyrolyzed Photoresist Film                       |
| <b>PC</b>                | Photocurrent                                     |
| <b>PVD</b>               | Physical Vapor Deposition                        |
| <b>QCM</b>               | Quartz Crystal Microbalance                      |
| <b>TBABF<sub>4</sub></b> | Tetrabutylammonium Tetrafluoroborate             |
| <b>TB</b>                | Thienyl Benzene                                  |
| <b>UPS</b>               | Ultraviolet Photoelectron Spectroscopy           |



**WF** Work Function

**IPA** Isopropyl Alcohol

**GC** Glassy Carbon

**XPS** X-ray Photoelectron Spectroscopy

**AQ** Anthraquinone

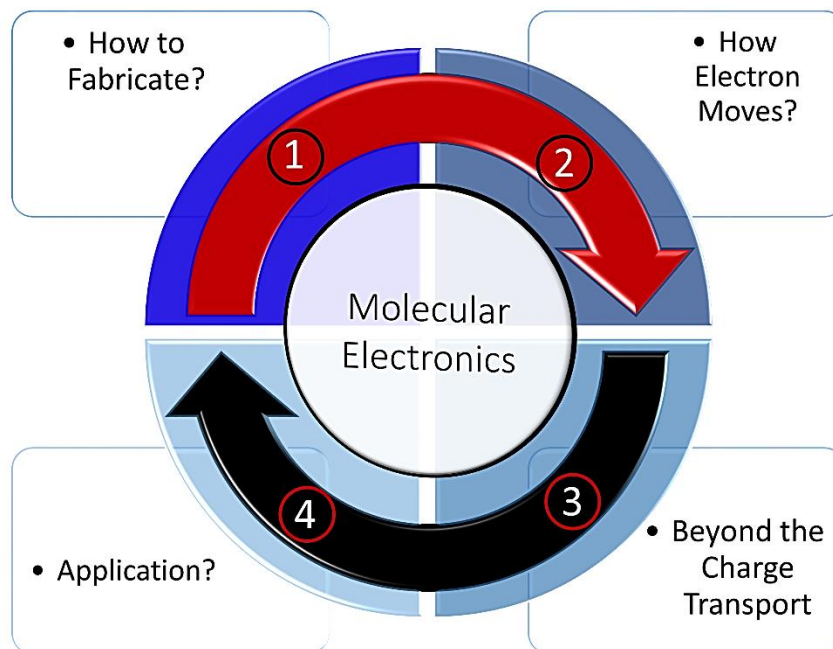
**NDI** Naphthalene Di-imide

# CHAPTER 1

## INTRODUCTION

## 1.1 Overview of molecular electronics

Molecular electronics (ME) usually refers to a branch of nanotechnology with molecular nanosized building blocks as active circuit components.<sup>1-13</sup> The history of ME dates back to 1974 when Aviram and Ratner theoretically provided the basics for the rational design of a molecule to resemble a function (rectification) of silicon-based devices.<sup>14</sup> ME is partly motivated by the Moore's law and extending the technical demands of miniaturization of traditional silicon-based electronics. However, fabrication techniques developed for conventional silicon-based electronics have nearly reached their miniaturization limitation, implying that an intrinsic change in fundamental and function is needed to progress further in computing technology.<sup>3, 7</sup> Due to the wealth of organic structures available, molecules may enable a variety of electronic functions that inorganic semiconductors cannot offer. If we consider molecular electronics as a wheel like the one shown in Figure 1.1, we can identify four main driving parts: i) How to fabricate molecular junction? ii) What is the charge transport mechanism? iii) Is it possible to promote electronic charge transport by other physical stimuli? iv) What are the real-world applications of ME?



**Figure 1.1** Four important issues in Molecular electronics

This chapter summarizes some notable advances, theoretically and experimentally, in each of the four areas of Figure 1.1. Special attention is devoted to the studies that are directly or indirectly related to the next three chapters.

## 1.2 How to fabricate molecular junction?

After 30 years since ME was proposed, still one of the main challenges in the major is fabrication of reliable “molecular junctions”. Many experimental paradigms have been developed to provide contact between conventional conductors (electrodes) and a single or ensemble of molecular units.

In terms of fabrication of molecular junctions, one may consider two different types: single molecule and ensemble. Table 1.1 from a recent review summarizes some paradigms

of the molecular layer fabrication (approaches and techniques used for fabrication of molecular junction).<sup>13</sup> Although single-molecule junctions have received considerable attention and contributed significantly to the fundamental understanding of the physical phenomena at the molecular scale, the focus of this thesis is on the ensemble architecture of molecular junctions.

**Table 1.1** Comparison of different approaches for molecular junction fabrication. Table adapted with permission from ref [13]

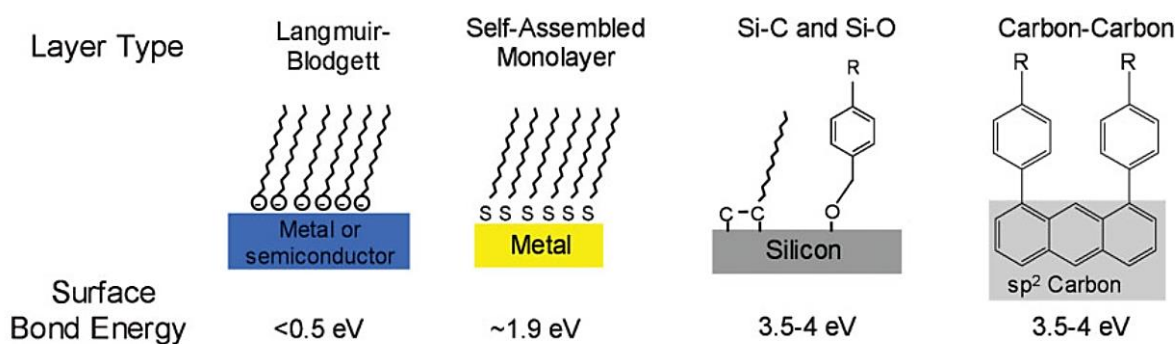
| methods for molecular junctions          | number of molecules | gating control  | addressability | fabrication     | yield <sup>a</sup> | ref |
|--|---------------------|-----------------|----------------|-----------------|--------------------|-----|
| scanning probe microscopy                | single              | electrochemical | difficult      | sophisticated   | H                  | 15  |
| mechanically controllable break junction | single              | electrostatic   | no             | sophisticated   | H                  | 16  |
| electromigration nanogap                 | single              | electrostatic   | yes            | sophisticated   | L                  | 17  |
| electrochemical deposition               | single              | electrostatic   | yes            | sophisticated   | H                  | 18  |
| surface-diffusion-mediated deposition    | single              | no              | no             | sophisticated   | H                  | 19  |
| lift-and-float approach                  | ensemble            | no              | difficult      | straightforward | H                  | 20  |
| liquid metal                             | ensemble            | electrochemical | difficult      | straightforward | H                  | 21  |
| nanopore or nanowell                     | ensemble            | no              | yes            | straightforward | M                  | 22  |
| nanoimprint lithography                  | ensemble            | no              | yes            | sophisticated   | H                  | 23  |
| self-aligned lithography                 | ensemble            | electrostatic   | difficult      | straightforward | M                  | 24  |
| on-wire lithography                      | ensemble            | no              | difficult      | sophisticated   | M                  | 25  |
| buffer interlayer-based junction         | ensemble            | no              | possible       | straightforward | H                  | 26  |
| crosswire or crossbar                    | ensemble            | no              | possible       | sophisticated   | M                  | 27  |
| on-edge molecular junction               | ensemble            | no              | difficult      | straightforward | H                  | 10  |
| CNT-based junction                       | single              | electrostatic   | yes            | sophisticated   | M                  | 28  |
| graphene-based junction                  | single              | electrostatic   | yes            | sophisticated   | H                  | 29  |
| silicon-based junction                   | ensemble            | no              | difficult      | sophisticated   | M                  | 30  |
| polymer-based junction                   | ensemble            | no              | difficult      | sophisticated   | M                  | 31  |

a) L: low; M: middle; H: high

### 1.2.1 Ensemble type of the molecular junction fabrication

Despite extensive focus of worldwide research, making soft, stable and reliable electrical contact to nano-active layer in such a reproducible way is the limiting factor for scaling and transferring the prototypes to real world applications. The first step in the fabrication of the molecular junction is determining the method of attachment of molecules to the electrodes. The nature of this attachment will affect the selection of appropriate bottom and top contacts for the molecular junction. Molecular layer attachments to the electrode are

usually classified based on the strength of the bond between the molecule and the electrode surface: i) Physisorption, ii) Chemisorption. There is no clear distinction between these two classes. Figure 1.2 shows schematics of four typical modes of the molecular surface attachment along with their surface bonding energy. Interested readers are referred to the provided citations for a detailed overview of the surface modification with the molecular layer.<sup>7, 12</sup>



**Figure 1.2** Typical surface modification with approximate surface bond energy. Figure reproduced with permission from ref [7]

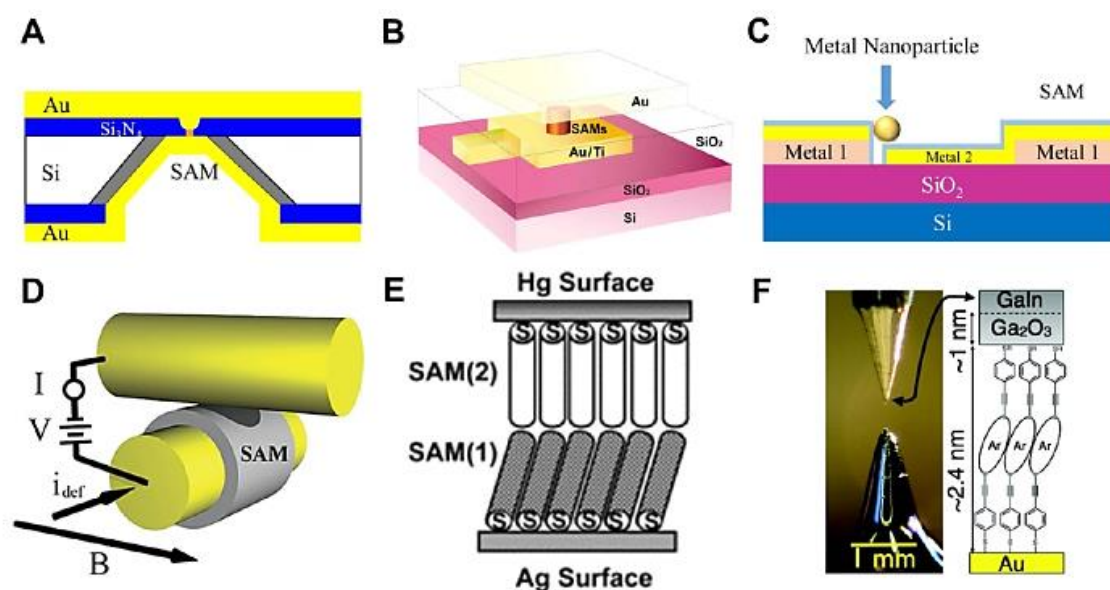
A molecule or ensemble of molecules does not stand alone as a device. As in any electrical device, at least two metal contacts are needed. The gap between the contacts is as small as a few nanometres.<sup>5</sup>

Table 1.2 lists common methods for fabricating ensemble molecular junctions along with difficulty of fabrication, yield, and possibility of massive production for each class, and Figure 1.3 shows a schematic of several listed platforms.<sup>5</sup>

**Table 1.2** Comparison of fabrication techniques for ensemble fabrication of molecular junction. Table adapted with permission from ref [5]

| techniques                            | difficulty of fabrication | yield <sup>a</sup> | possibility of a massive production | ref    |
|---------------------------------------|---------------------------|--------------------|-------------------------------------|--------|
| nanopore                              | straightforward           | low                | applicable                          | 32     |
| microscale <i>via</i> hole            | straightforward           | low                | applicable                          | 33     |
| nanoparticles bridged                 | sophisticated             | medium             | applicable                          | 34     |
| crosswire                             | sophisticated             | medium             | inappropriate                       | 27     |
| liquid metal                          | straightforward           | medium to high     | inappropriate                       | 21     |
| eutectic gallium–indium               | straightforward           | high               | inappropriate                       | 35     |
| conducting polymer interlayer         | straightforward           | high               | applicable                          | 26, 36 |
| carbon-based materials interlayer     | straightforward           | high               | applicable                          | 37-39  |
| nanotransfer imprint                  | straightforward           | medium             | applicable                          | 27     |
| direct metal transfer                 | straightforward           | medium to high     | applicable                          | 21     |
| microfluidic channel                  | straightforward           | high               | applicable                          | 38     |
| surface diffusion-mediated deposition | sophisticated             | high               | applicable                          | 37     |

a) <20%: low; 20-70%: medium; >70%: high



**Figure 1.3** Examples of ensemble molecular junction platforms. (a) Nanopore, (b) Microscale via hole, (c) Nanoparticles bridged, (d) Crosswire, (e) Hg liquid metal, (f) Eutectic gallium-indium based. Figure reproduced with permission from ref [5]

### 1.2.2 Diazonium chemistry for grafting ensembles of molecular layer

Molecular layer grafting and functionalization of the surface is important in many fields and applications, including molecular electronics. One of the most versatile methods for covalent attachment of the molecules to the variety of surfaces and further growing the layer through

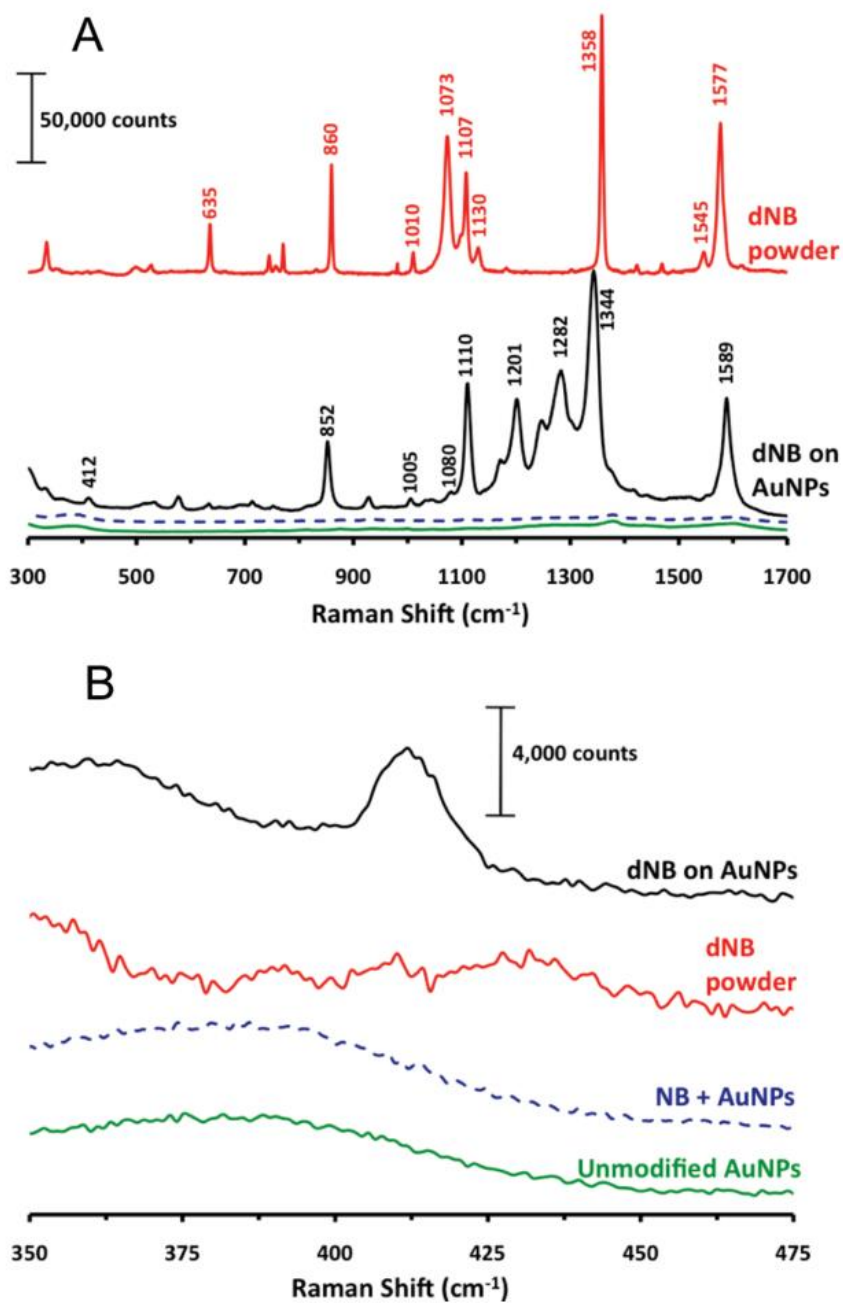
the covalent bond involves the electroreduction of aryl diazonium salt. This technique has attract attention since its introduction (20 years ago) and investigated extensively evident from the increasing number of papers and reviews on its mechanism and applications.<sup>40</sup> It is well established that the aryl diazonium with accepting electron from the substrate can release the  $N_2$  as gas and the resultant aryl radical can attack the surface and form a covalent bond.

Efforts have therefore been made to validate the existence of covalent bond in the case of diazonium modification. Arguments start with indirect evidence of strength of covalent bond in comparison to physisorbed species or self-assembled layers.<sup>40</sup> The layers fabricated by Diazonium reduction are stable for a very long time, at least six month. The resistance of the layers to ultrasonication is also considered as a strong proof for presence of covalent bond. Since the very first publications, it has been demonstrated that the ultrasonication for long time in wide range of solvents cannot remove the grafted layers. Thermal stability of the layer as another indicative of existence of strong bond is also investigated by several groups including thermal gravimetric analysis (TGA). Electrochemistry on the surface of grafted layer (after deposition) has been investigated to further test the stability of layers. In one study, the surface was polarized to very negative (2 V/SCE) or very positive (1.8 V/SCE) potentials to remove the grafted layers and even after scanning at these high potentials, XPS showed the layers are not completely removed. In addition, the stability of grafted layers has also been investigated by irradiation with soft X-rays and also AFM scratching and these studies also prove the strength of the bonding expected for covalent modification.<sup>40</sup>

As direct spectroscopic evidence for covalent bond formation, the XPS, Raman and IR signatures of the surface-aryl bond have been reported in several papers for a variety of molecular structures and surfaces. For example Figure 1.4 shows Raman spectra of Au



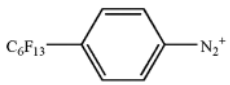
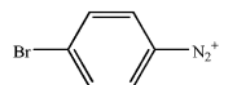

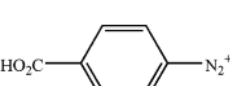
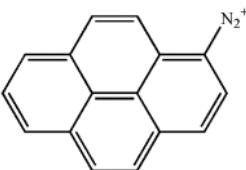
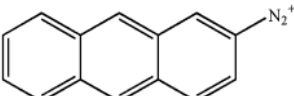
nanoparticle modified with nitrobenzene through diazonium chemistry.<sup>41</sup> Peak at 400  $\text{cm}^{-1}$  is the signature of Au-C covalent bond. In the same study, the formation of Au-C bond is also further proved by high-resolution electron energy loss spectroscopy (HREELS). DFT simulation demonstrated the degree of multilayer formation on Au nanoparticle.



**Figure 1.4** (A) Raman spectrum of solid Diazonium Nitrobenzene (NB) (Red) and SERS spectra of diazonium NB-modified 40 nm AuNPs (Black line), 40 nm Au nanoparticles (NP) reacted with NB (Blue), and unmodified 40 nm AuNPs (Green). (B) Expanded Raman and SERS spectra of the samples in section (A). Figure reproduced with permission from ref [41]

In an interesting study, the mechanism of diazonium grafting of aryl layers on the surface of glassy carbon electrodes was investigated by time-of-flight secondary ion mass spectroscopy (TOF-SIMS).<sup>42</sup> Table 1.3 shows the structure of the molecules studied and grafted on the surface in this study.

**Table 1.3** Structure of the molecule grafted on the surface of GC and further analyzed by TOF-SIMS. Table adapted with permission from ref [42].

| Diazonium<br>$\text{ArN}_2^+$  | Experimental conditions       |                         |
|--|-------------------------------|-------------------------|
|  | Potential =<br>-0.5 V/Ag/AgCl | no potential<br>applied |
|  <b>1</b> | G <sub>1</sub>                | S <sub>1</sub>          |
|  <b>2</b> | G <sub>2</sub>                | S <sub>2</sub>          |
|  <b>3</b> | G <sub>3</sub>                |                         |
|  <b>4</b> | G <sub>4</sub>                |                         |
|  <b>5</b> | G <sub>5</sub>                |                         |
|  <b>6</b> | G <sub>6</sub>                |                         |

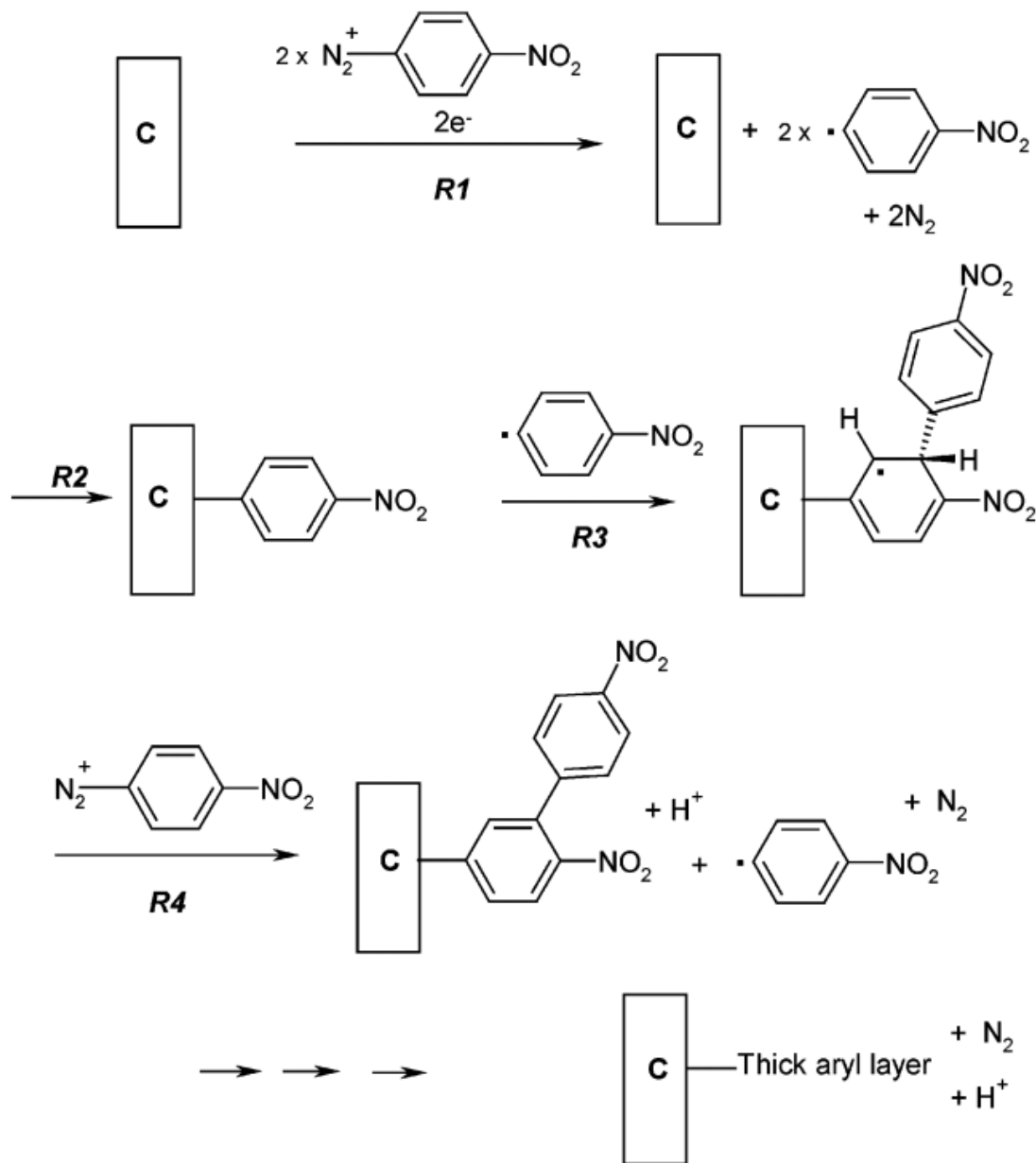
The results of the mass measurement on the surface of glassy carbon for the samples indicated in Table 1.3 are summarized in Table 1.4. The results demonstrate the existence of fragments containing aryl dimers, trimers, and tetramers, thus providing strong and direct evidence for multilayer formation through covalent bonding.

**Table 1.4** Mass ( $m/z$ ) and counts of the mass fragments from the surface of modified GC. Table adapted with permission from ref [42].

| sample         | ion formula   | mass ( $m/z$ ) | counts     |
|----------------|---|----------------|------------|
| G <sub>1</sub> | [C <sub>6</sub> H <sub>4</sub> C <sub>6</sub> F <sub>13</sub> ] <sup>+</sup>  | 395            | 6025       |
|                | [CH <sub>2</sub> -C <sub>6</sub> H <sub>4</sub> C <sub>6</sub> F <sub>13</sub> ] <sup>+</sup>   | 409            | 1500       |
|                | [CH <sub>2</sub> CH <sub>2</sub> -C <sub>6</sub> H <sub>4</sub> C <sub>6</sub> F <sub>13</sub> ] <sup>+</sup> and [COC <sub>6</sub> H <sub>4</sub> C <sub>6</sub> F <sub>13</sub> ] <sup>+</sup>          | 423            | 18075      |
|                | [CHCF-C <sub>6</sub> H <sub>4</sub> C <sub>6</sub> F <sub>13</sub> ] <sup>+</sup> and [C <sub>3</sub> H <sub>8</sub> -C <sub>6</sub> H <sub>4</sub> C <sub>6</sub> F <sub>13</sub> ] <sup>+</sup>         | 439            | 1275       |
|                | [CH <sub>2</sub> CH <sub>2</sub> -C <sub>6</sub> H <sub>3</sub> C <sub>6</sub> F <sub>13</sub> -C <sub>6</sub> H <sub>4</sub> C <sub>6</sub> F <sub>13</sub> ] <sup>+</sup>                               | 817            | 1725       |
|                | [O-C <sub>6</sub> H <sub>4</sub> C <sub>6</sub> F <sub>13</sub> ] <sup>-</sup>  | 411            | 1525       |
|                | [C≡CC <sub>6</sub> H <sub>4</sub> C <sub>6</sub> F <sub>13</sub> ] <sup>-</sup>   | 419            | 125        |
|                | [O-C <sub>6</sub> H <sub>3</sub> C <sub>6</sub> F <sub>13</sub> -C <sub>6</sub> H <sub>4</sub> C <sub>6</sub> F <sub>13</sub> ] <sup>-</sup>  | 805            | 625        |
|                | [C <sub>6</sub> H <sub>4</sub> Br] <sup>+</sup>   | 155, 157       | 5450, 6675 |
|                | [CH <sub>2</sub> C <sub>6</sub> H <sub>4</sub> Br] <sup>+</sup>   | 169, 171       | 1225, 1500 |
| G <sub>2</sub> | [CH <sub>2</sub> CH <sub>2</sub> C <sub>6</sub> H <sub>4</sub> Br] <sup>+</sup> and [COC <sub>6</sub> H <sub>4</sub> Br] <sup>+</sup>   | 183, 185       | 5800, 6625 |
|                | [C <sub>6</sub> H <sub>3</sub> C <sub>6</sub> H <sub>4</sub> Br] <sup>+</sup>   | 230, 232       | 1075, 1075 |
|                | [C <sub>6</sub> H <sub>4</sub> NO <sub>2</sub> ] <sup>-</sup>   | 122            | 1750       |
| G <sub>3</sub> | [OC <sub>6</sub> H <sub>4</sub> NO <sub>2</sub> ] <sup>-</sup>  | 138            | 3950       |
|                | [CCC <sub>6</sub> H <sub>4</sub> NO <sub>2</sub> ] <sup>-</sup>   | 146            | 2125       |
|                | [O <sub>2</sub> C <sub>6</sub> H <sub>4</sub> NO <sub>2</sub> ] <sup>-</sup>  | 154            | 400        |
|                | [C <sub>3</sub> H <sub>2</sub> C <sub>6</sub> H <sub>4</sub> NO <sub>2</sub> ] <sup>-</sup>   | 160            | 450        |
|                | [C <sub>3</sub> H <sub>3</sub> C <sub>6</sub> H <sub>4</sub> NO <sub>2</sub> ] <sup>-</sup>   | 161            | 1825       |
|                | [CCOC <sub>6</sub> H <sub>4</sub> NO <sub>2</sub> ] <sup>-</sup>  | 162            | 2875       |
|                | [CHC <sub>6</sub> H <sub>5</sub> NO <sub>2</sub> C <sub>6</sub> H <sub>4</sub> NO <sub>2</sub> ] <sup>-</sup>   | 258            | 850        |
|                | [OC <sub>6</sub> H <sub>3</sub> NO <sub>2</sub> C <sub>6</sub> H <sub>4</sub> NO <sub>2</sub> ] <sup>-</sup>  | 259            | 650        |
|                | [CCC <sub>6</sub> H <sub>3</sub> NO <sub>2</sub> C <sub>6</sub> H <sub>4</sub> NO <sub>2</sub> ] <sup>-</sup>   | 267            | 175        |
|                | [CHC <sub>6</sub> H <sub>3</sub> NO <sub>2</sub> C <sub>6</sub> H <sub>5</sub> NO <sub>2</sub> C <sub>6</sub> H <sub>4</sub> NO <sub>2</sub> ] <sup>-</sup>   | 379            | 350        |
|                | [CHC <sub>6</sub> H <sub>3</sub> NO <sub>2</sub> C <sub>6</sub> H <sub>5</sub> NO <sub>2</sub> C <sub>6</sub> H <sub>3</sub> NO <sub>2</sub> C <sub>6</sub> H <sub>4</sub> NO <sub>2</sub> ] <sup>-</sup> | 500            | 50         |
|                | [OC <sub>6</sub> H <sub>3</sub> NO <sub>2</sub> C <sub>6</sub> H <sub>3</sub> NO <sub>2</sub> C <sub>6</sub> H <sub>3</sub> NO <sub>2</sub> C <sub>6</sub> H <sub>4</sub> NO <sub>2</sub> ] <sup>-</sup>  | 501            | 75         |
| G <sub>4</sub> | [C <sub>6</sub> H <sub>5</sub> CO <sub>2</sub> ] <sup>-</sup>   | 121            | 375        |
|                | [OC <sub>6</sub> H <sub>3</sub> CO <sub>2</sub> ] <sup>-</sup>  | 135            | 1725       |
|                | [OCC <sub>6</sub> H <sub>3</sub> CO <sub>2</sub> ] <sup>-</sup>   | 147            | 1500       |
|                | [O <sub>2</sub> CC <sub>6</sub> H <sub>3</sub> CO <sub>2</sub> ] <sup>-</sup>   | 163            | 225        |
|                | [OCCH <sub>2</sub> CH <sub>2</sub> C <sub>6</sub> H <sub>4</sub> COOH] <sup>-</sup>   | 177            | 10875      |
|                | [C <sub>20</sub> H <sub>13</sub> O <sub>5</sub> ] <sup>-</sup>  | 333            | 300        |
|                | [C <sub>2</sub> C <sub>16</sub> H <sub>9</sub> ] <sup>-</sup>   | 225            | 225        |
| G <sub>5</sub> | [O <sub>2</sub> C <sub>16</sub> H <sub>9</sub> ] <sup>-</sup>   | 233            | 1250       |
|                | [C <sub>16</sub> H <sub>8</sub> C <sub>16</sub> H <sub>8</sub> ] <sup>-</sup>   | 400            | 300        |
|                | [CC <sub>16</sub> H <sub>8</sub> C <sub>16</sub> H <sub>9</sub> ] <sup>-</sup>  | 413            | 375        |
|                | [C <sub>16</sub> H <sub>9</sub> ] <sup>+</sup>  | 201            | 700        |
|                | [C <sub>17</sub> H <sub>9</sub> ] <sup>+</sup>  | 213            | 450        |
|                | [C <sub>2</sub> HC <sub>16</sub> H <sub>9</sub> ] <sup>+</sup>  | 226            | 475        |

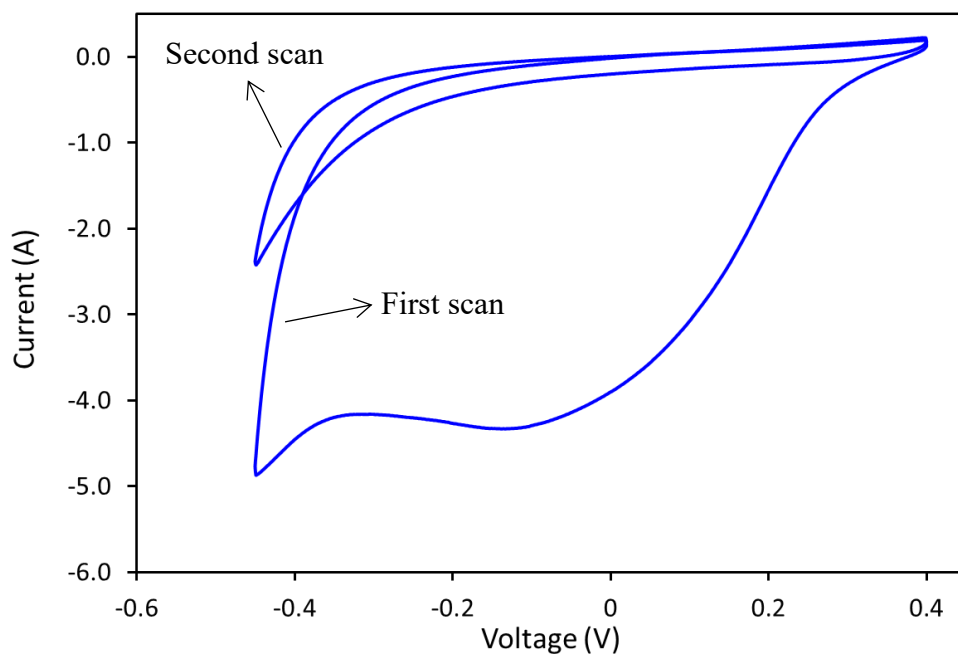
The mechanism shown in Figure 1.5 was proposed based the given results. First, diazonium ion accepts the electron from the surface, releases N<sub>2</sub> gas and forms the phenyl radical. The radical ion can attack the surface and form a covalent bond. Remaining radical can attack the first layer and make the covalent bond with the grafted molecules (R<sub>3</sub>). R<sub>4</sub> shows the possible

pathway for further radical formation and after radical formation, the same procedure could be repeated to yield multilayer formation.



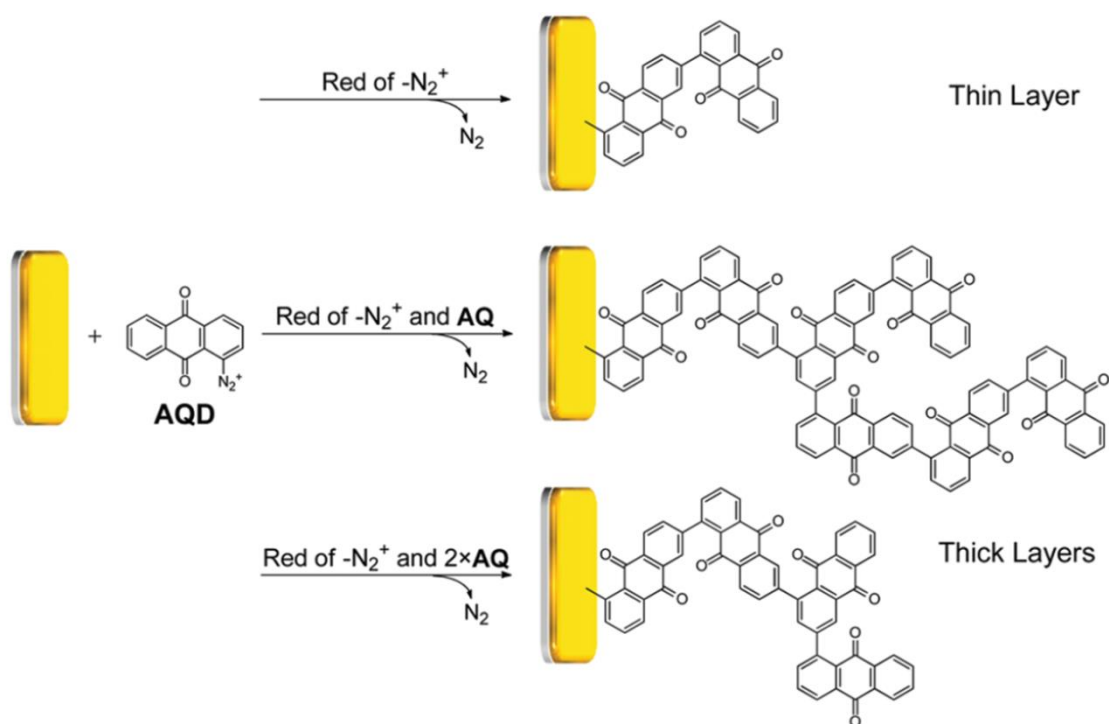
**Figure 1.5** Proposed mechanism for multilayer formation through diazonium grafting. Figure reproduced with permission from ref [42].

To further understand the simple electrografting experiment with a diazonium salt, Figure 1.6 shows the cyclic voltammogram (CV) of 2-anthraquinone diazonium ion (AQ-N<sub>2</sub><sup>+</sup>) in acetonitrile. CV grafting shows a broad irreversible wave on the first scan that disappears on the second scan. This behavior is typical of diazonium salts and the disappearance of the wave corresponds to the formation of organic layer on the surface that blocks the electron transfer from the electrode to diazonium species. Deposited layer can be discerned by the naked eye if it reaches a thickness of at least 10 nm. Note that the most of the events (multilayer formation) happen in the first cycle and repeating cycles (depend on the molecule and voltage) does not change the thickness of deposited layers significantly, but it helps to fill the possible pinholes and increase uniformity in the organic film.

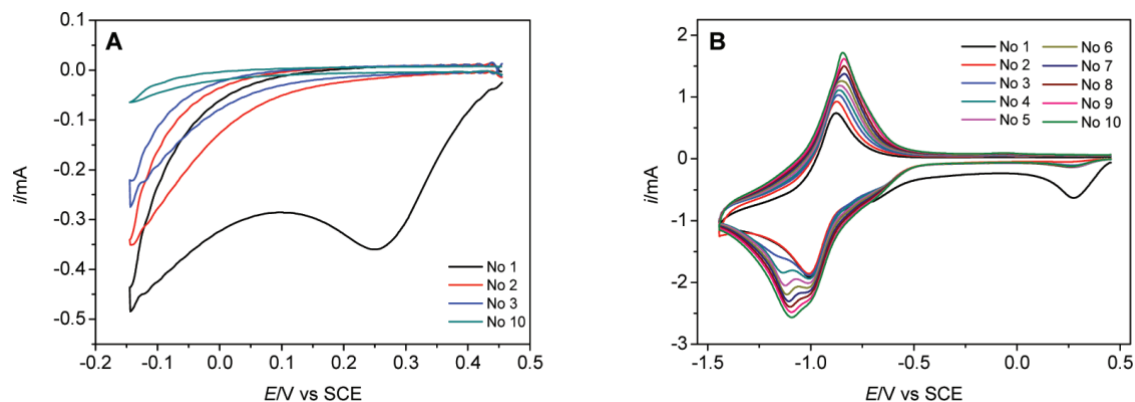


**Figure 1.6** Representative Cyclic Voltammogram (CV) for grafting of AQ on the surface of carbon electrode.

It has been shown that in case of anthraquinone, which is a redox active molecule, the deposited molecular layer could be as thick as  $> 500$  nm.<sup>40, 43</sup> Figure 1.7 shows the possible pathway for growing thin and thick layer and the corresponding cyclic voltammogram for thick and thin molecular layers shown in Figure 1.8.

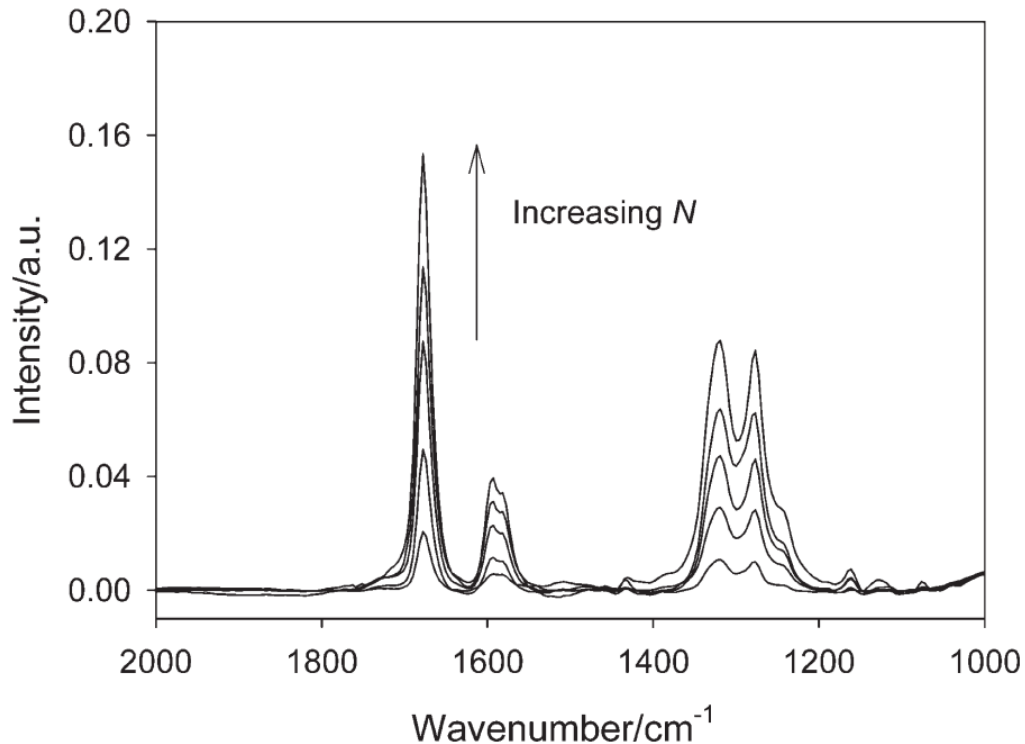


**Figure 1.7** Suggested schematics of formation of AQ-based films obtained from electroreduction of  $AQ-N_2^+$  at three different potentials. Figure reproduced with permission from ref [43].



**Figure 1.8** Representative cyclic voltammograms recorded at a gold-covered QCM crystal on 2 mM AQD, and  $E$  (sweeping) = (A)  $-0.145$  or (B)  $-1.445$  V vs SCE in MeCN. Figure reproduced with permission from ref [43].

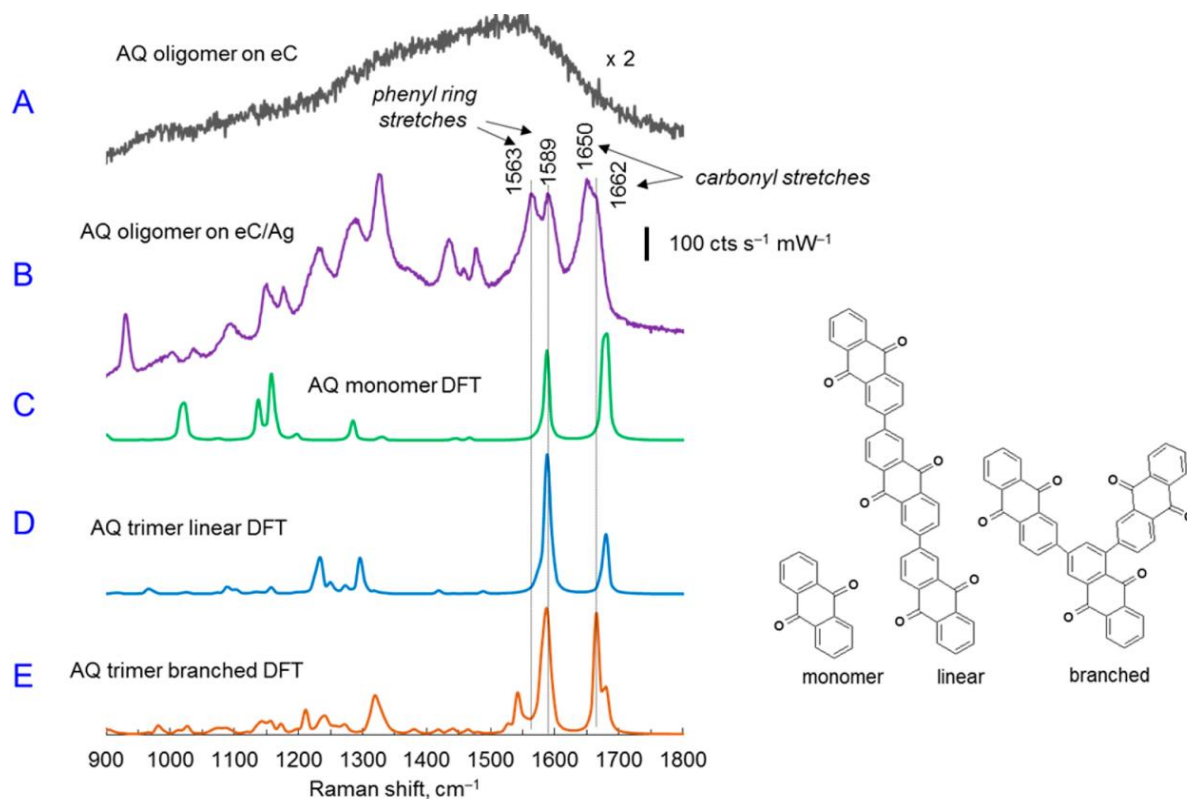
Infrared reflection absorption spectroscopy (IRRAS) was employed to investigate the chemical structure of the growing film during cyclic voltammetric sweeping. Figure 1.9 shows the IRRAS spectra of five Au-AQ plates with the  $1680\text{ cm}^{-1}$  band corresponding to the stretching of C=O (aryl ketone), the  $1595$  and  $1585\text{ cm}^{-1}$  bands to the C=C aromatic stretching, and the  $1320$  and  $1275\text{ cm}^{-1}$  bands to the ring stretching and C-H bending, respectively. These signals are consistent with the presence of an organic layer consisting of AQ units solely with no indication of the corresponding alcohols as evidenced by the lack of OH signals. Also, the ratio of C=O/C=C intensities ( $\sim 2.4$ ) is independent of  $N$ , indicating that the layer has the same chemical composition and average orientation throughout the growth process.



**Figure 1.9** IRRAS spectra of Au-Anthraquinone plates prepared from 2 mM AQD with increasing thickness. Figure reproduced with permission from ref [44].

In another study, Raman was used to characterize layer growth for a range of molecular structures including anthraquinone. Spectrum of grafted anthraquinone on eC/Ag is shown in Figure 1.10.<sup>45</sup> Both the on-ring stretch ( $1589\text{ cm}^{-1}$ ) and carbonyl stretch ( $1668\text{ cm}^{-1}$ ) are split in the multilayer, but not in the DFT spectra of either the AQ monomer or the linear oligomer. DFT predicts splitting of both bands in at least one of the possible branched isomers (panel E), indicating that AQ growth occurs both with and without branching.



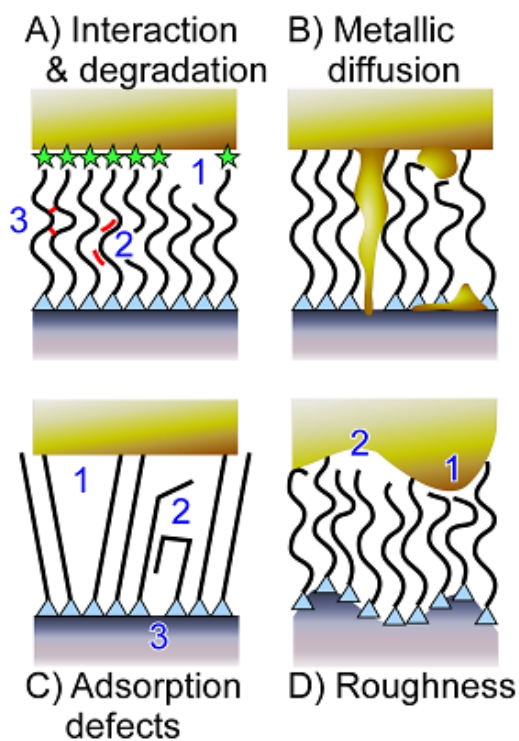


**Figure 1.10** Raman spectra of Anthraquinone (AQ) multilayers on eC (A) and on eC/Ag (B), and simulated Raman spectra of the monomer (C), linear trimer (D), and branched trimer (E) of anthraquinone. Dihedral angles between AQ units are assumed to be  $\sim 38^\circ$  in optimized oligomers. Figure reproduced with permission from ref [45].

Although electroreduction of diazonium salts provides a robust and reliable approach for covalently grafting of molecular layers on a carbon surface, the resultant film on the surface is a somewhat disordered structure. This disorder is expected for highly reactive aryl radical mediated reactions and it is difficult to determine individual subunit orientations, dihedral angles, and minority species in the molecular film. However, the grafted layers have highly reproducible and unique characteristics that enable us to fabricate highly stable and robust molecular junctions. These special characteristics are discussed in following chapters.

### 1.2.3 Possible factors affecting the performance of MJJs

As the feature size of the component decreases, factors like electro-migration, surface roughness, uniformity and stability of electrodes become important for determining device performance. Figure 1.11 illustrates four possible damage and deformation sources in molecular layer: i) Interaction and degradation in molecular layer like molecular fracturing, formation of double bonds and cross-linking, ii) Metallic filament formation that can be caused by simultaneous diffusion or electromigration of contacts, iii) Defects in molecular layer like missing sites and loop formation, iv) Roughness of contacts which makes high and low current regions in junctions.<sup>11</sup>

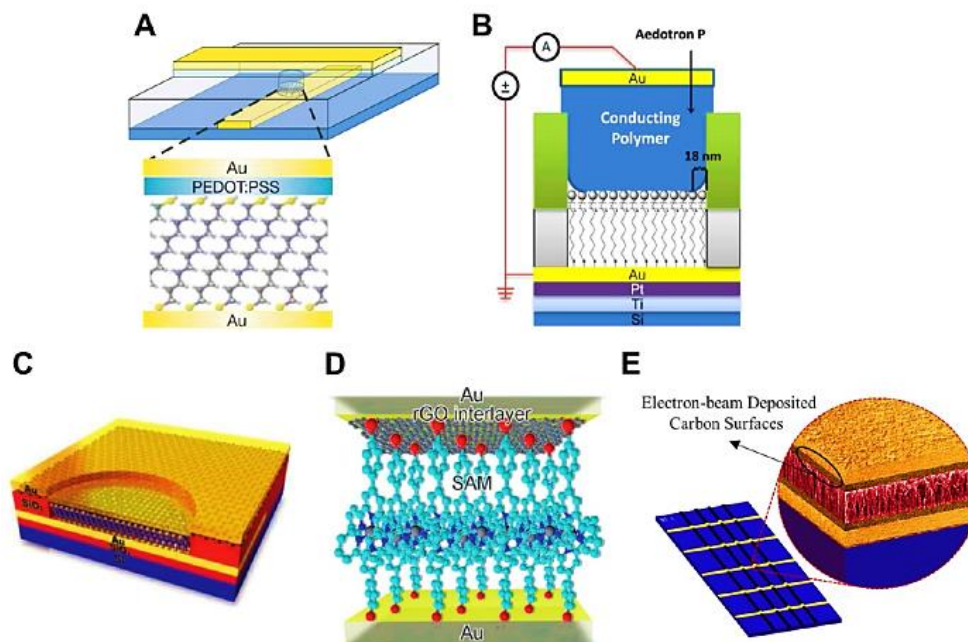


**Figure 1.11** Schematic illustration of the possible damage and defects in molecular layers. **(A)** Stars represent the interaction of molecular end group with deposited metal (formation of a top chemi-contact). Labels: 1) molecular fracture, 2) formation of double-bonds, and 3) cross-linking. **(C)** Labels: 1) grain boundary in a crystalline SAM, 2) gauche kinks and looping, and 3) missing sites.

(D) Digits: 1) a hot spot of shorter gap and 2) a cold spot of extra voids. Figure reproduced with permission from ref [11]

#### **1.2.4 Interlayer buffer in fabrication of cross-bar molecular junction**

Among different approaches for the fabrication of ensemble molecular junctions, cross-bar fabrication with a buffer interlayer has attracted considerable attention in recent years. As mentioned in Table 1.2, these techniques have a straightforward procedure with high fabricated device yield (>70%) and suitability to massively parallel production. The problem of low device yield of the metal evaporated contacts in sandwich configuration (cross-bar) can be effectively solved by adding a buffer interlayer between metal and molecular components.<sup>5</sup> Different interlayer materials have been proposed and successfully tested for fabrication of high yield solid-state-based ensemble molecular junctions. Figure 1.12 shows schematics of five approaches in conducting interlayered-based junctions. Conducting polymer, graphene, graphene oxide and carbon are recent examples for solid-state interlayer.<sup>5</sup>



**Figure 1.12** Several examples of high-yield ensemble molecular junctions; based on the conducting buffer interlayer: **(A)** Conducting polymer PEDOT:PSS, **(B)** Conducting polymer Aedotron P, **(C)** Graphene, **(D)** Reduced graphene oxide, **(E)** Electron-beam deposited carbon. Figure reproduced with permission from ref [5]

The fabrication of large area all-carbon molecular junction with e-beam carbon as an interlayer is investigated in Chapter 2. Stability, device yield, transparency, and flexibility of the fabricated junctions are assessed and discussed. Section 1.5 describes further how reliable and robust fabrication of molecular junctions is the limiting factor for transitioning of ME to real-world applications.

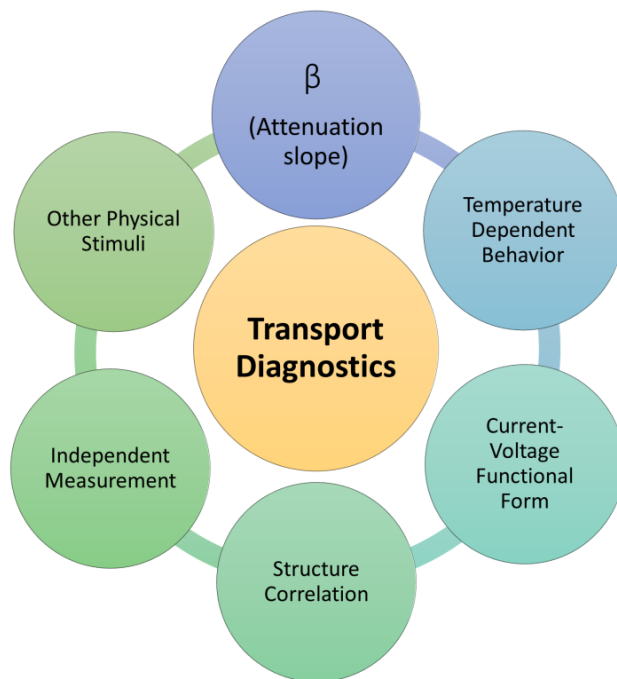
### 1.3 How do the electrons move through molecules?

The central question from the beginning of molecular electronics, regardless of the fabrication techniques or the molecules involved, has been the nature of the charge transport mechanism in molecular junctions, where the transport distance is just a few nanometers.

Some important principles related to the basics of underlying transport mechanism are reviewed next.

### 1.3.1 Transport diagnostics

Whenever we talk about the transport mechanism especially in nanometric scale, there are criteria that help narrow the list of possible governing mechanisms, which include but are not limited to thickness dependent conductivity ( $\beta$ ), functional form of current–voltage response, temperature-dependence, structure correlations, and finally the effect of other physical stimuli (Figure 1.13).



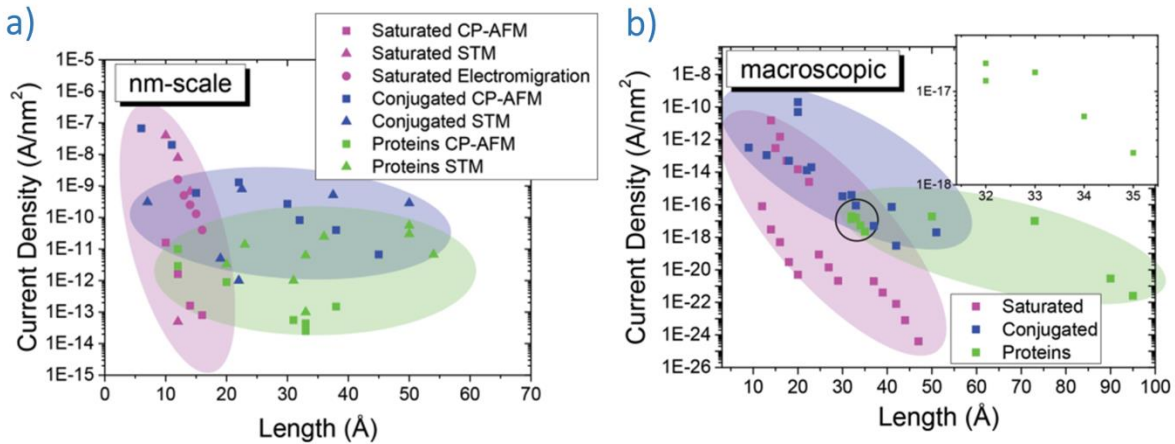
**Figure 1.13** Six main steps in understanding of the transport mechanism in a molecular junction.

#### 1.3.1.1 Attenuation slope, beta ( $\beta$ )

An important parameter in diagnostics of the charge transport mechanism in ME is beta ( $\beta$ ) as a measure of thickness dependent conductivity.  $\beta$  describes the attenuation of current through the junction as a function of the distance between contacts:

$$J = \alpha e^{-\beta d} \quad (1.1)$$

Where  $J$  is the current density,  $\alpha$  is constant prefactor and  $d$  is the thickness of molecular layer.  $\beta$  is the slope of the plot of  $\ln J$  vs  $d$ , and has units of  $\text{nm}^{-1}$  or  $\text{\AA}^{-1}$ . Not only the absolute value of the beta can differentiate between various mechanisms, but also changes in  $\beta$  for particular molecule can imply a change or transition in dominant transport mechanism.<sup>46, 47</sup> As shown in Figure 1.14, there is statistically valid difference between the  $\beta$  value in transport through the alkane and  $\pi$ -conjugated molecules.



**Figure 1.14 a)** Collection of data from several studies of nanometer-scale contact area molecular junctions. Current densities ( $\text{A}/\text{nm}^2$ ) at 0.1 V is plotted as a function of molecular layer thickness.

**b)** Collection of data from several studies for macroscopic contact molecular junctions. The inset plot is a magnification of the circled points for protein group. The shaded areas provide visual guides only.

Figure reproduced with permission from ref [46]

Table 1.5 lists the experimentally measured  $\beta$  values for a variety of platforms and methods. The junctions with alkane layer show a beta of  $4.3$  to  $8 \text{ nm}^{-1}$  and junctions with  $\pi$ -conjugated molecules show a beta of  $1$  to  $3.3 \text{ nm}^{-1}$ .<sup>7</sup>

**Table 1.5** Comparison of  $\beta$  for variety of molecular layers in different fabrication paradigm. Table adapted with permission from ref [7]

| Molecule type              | Method                   | System                     | $\beta$ [ $\text{\AA}^{-1}$ ] | Reference |
|----------------------------|--------------------------|----------------------------|-------------------------------|-----------|
| Alkane                     | Electrochemistry         | Au/alkanethiolate          | 0.8                           | 42        |
| Alkane                     | Single-molecule junction | Au/alkanedithiol/Au        | 0.84                          | 43        |
| Alkane                     | Ensemble junction        | Au/alkanedithiol/PEDOT:PSS | 0.57–0.66                     | 26        |
| Alkane                     | Ensemble junction        | Ag/alkanethiolate/eGaN     | 0.43                          | 44        |
| Aromatic                   | Electrochemistry         | Carbon/phenylene           | 0.22                          | 45        |
| Phenylene ethynylene       | Electrochemistry         | Au/thiolate                | 0.33                          | 46        |
| Oligothiophene (OTP)       | STM Break                | Au/OTP/Au                  | 0.1                           | 47        |
| Carotenoid polyenes (CP)   | STM Break                | Au/CP/Au                   | 0.22                          | 48        |
| Phenylene ethynylene (PE)  | cpAFM                    | Au/PE/Au                   | 0.21                          | 49        |
| Oligophenyleneimines (OPI) | cpAFM                    | Au/OPI/Au                  | 0.3                           | 50        |

### 1.3.1.2 Functional form of the Current-Voltage curve

Another important criterion for device performance is the mathematical relationship between the current and applied voltage, which is usually called a functional form of  $IV$  behavior. It is not always easy to find the functional form for the entire range of the applied bias. Actually, fitting  $IV$  curves to defined functional forms is tricky for several reasons. First, sometimes well-fitted functional form raises the risk of jumping to a conclusion about the mechanism, without further considering the underlying concepts and consequences. For example, linearity of  $\ln J$  with  $V^{1/2}$  is taken as an indication of Schottky or Poole-Frenkel mechanism.<sup>8</sup> However, many other mechanisms like variable range hopping or even thermally assisted tunneling can follow the same functional form.<sup>57</sup> Second, there is a common tendency to divide the single  $IV$  curves into multiple parts and then fit each part separately to different functions. In this way, it is possible to fit any taken forms to any curves ( $IV$  curves). Four approaches that can help reduce the risk of bias in fitting and drawing conclusions from the functional form include the following:

- Systematically find the best functional form with fitting and mathematical simulation programs, rather than the test of the presupposed functional forms
- Avoid dividing the curves into different regions and fit each part separately.

- Consider the underlying assumptions of the mechanism, no matter how it is mathematically fitted.
- If one functional form is well-fitted to the experimental data, calculate and check the other derived parameters from the fitting. The value of the parameters should physically make sense and be validated by independent measurements.

### **1.3.1.3 Independent measurement**

Apart from the electronic measurements, additional complementary techniques or characterization are usually necessary to test the validity of underlying assumptions and proposed hypothesis. Optical characterization of the molecular layer including UV-Vis, XPS, UPS, Raman, and IR can give insights into the important parameters in charge transport. For example, UV-Vis measurement is a powerful tool to estimate effective conjugation length (ECL) in the molecular layer. Independent measurements should be designed for the specific purpose in order to test a hypothesis about transport. For example, if the experimentally measured electronic behavior of a molecular junction can be fitted with the Schottky equation, measurement of the dielectric constant as a function of thickness can be used as a tool to check the dielectric constants derived from fitting. Dielectric constants can be measured by independent techniques like impedance spectroscopy. As another relevant example, if there is a hypothesis that the transport is controlled by the hole barrier; UPS measurement can provide a good estimate of the offset of HOMO relative to the Fermi-level<sup>58</sup>. Subsequently, comparison of the beta and conductivity of MJ with the barriers estimated by UPS measurement for different structure of molecules is a useful assessment of the mentioned hypothesis.



#### 1.3.1.4 Temperature dependence

Temperature dependence can differentiate between activated and non-activated transport mechanisms. Activation energy ( $E_a$ ) can be calculated by the Arrhenius equation:

$$k = Ae^{(-E_a/KT)} \quad (1.2)$$

where  $k$  is the rate coefficient (current density in a transport study),  $A$  is a constant,  $K$  is the Boltzmann constant and  $T$  is the temperature in Kelvin. Plot of  $\ln J$  vs  $1/T$  is usually called Arrhenius plot and the slope of the line permits calculation of the activation energy. The value of the activation energy enables the scientist to compare the degree of temperature dependence of the current to that for various transport mechanisms. Specifically, the value of  $E_a$  may be used to differentiate between redox exchange hopping and a non-activated tunneling mechanism. Also, the relation between activation energies and applied bias for different regions of the temperature range can provide further information about the mechanism.

#### 1.3.1.5 Structure correlations

Correlation between the structure of molecules and the transport characteristics is one of the main goals in molecular electronics and is a required step toward rational design of ME devices. Moreover, finding the correlation between the structure of the molecule and transport characteristics can provide strong evidence for the nature of the transport mechanism. For example, the correlation between HOMO or LUMO energy level offsets

with respect to the Fermi level with conductivity and  $\beta$  value is expected for direct, single step tunneling.

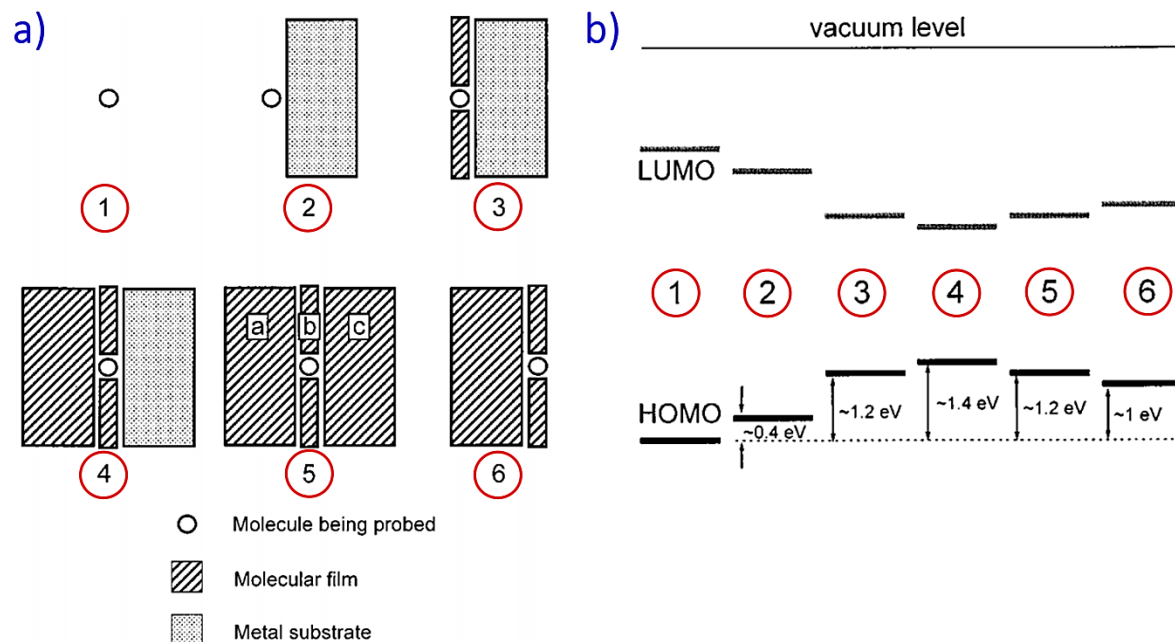
#### **1.3.1.6 Physical stimuli**

Valuable information about the details of the transport mechanism and energy level alignments in the studied system can be provided by external physical stimuli such as interactions with light <sup>1</sup>. The effects of various physical stimuli beyond the charge transport are discussed in section 1.4.

#### **1.3.2 Energy level alignment**

Whenever the molecule is brought in contact with the surface, several physical effects modify the MO energy levels of both the molecule and the contact. The energy level alignment (ELA) discusses how the energy levels of the different materials are aligned relative to one another. Fundamentally, ELA has a significant impact on the charge transport properties by modification of energy levels and controlling the effective barriers at the interface. It is apparent that a detailed understanding of the ELA is crucial to analyzing the transport characteristics.<sup>12, 59-63</sup>

Figure 1.15 shows different scenario for the environments of molecules brought into contact with a conducting surface. Hill et al. have estimated the HOMO level shift of a single molecule in each environment using UPS, optical gap measurements, and theoretical calculations.<sup>64</sup> They attributed the changes to the differences in vacuum level shift, dipolar layer formation, and potential screening.

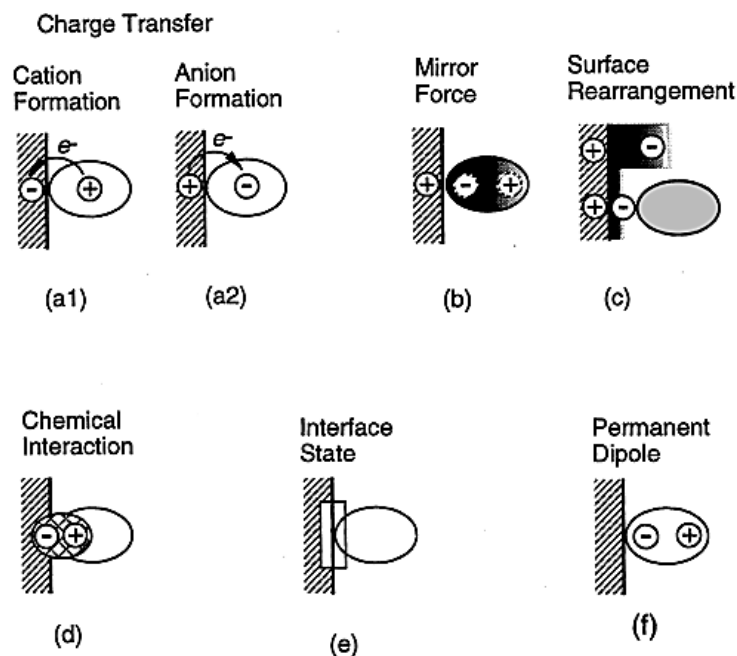


**Figure 1.15** a) Several scenarios for environments of a single molecule: **1)** molecule in gas phase, **2)** isolated molecule on a metal surface, **3)** one complete molecular layer on a metal surface, **4)** first molecular layer on metal surface, beneath a molecular film, **5)** bulk molecular film, away from both the metal interface and the film surface, and **6)** surface of a molecular film. **b)** Changes in HOMO and LUMO levels depending on the molecular environments shown in panel a. Figure reproduced with permission from ref [64]

### 1.3.2.1 Vacuum level shift

When an organic molecules contacts a metal surface, a dipole layer may be formed right at the interface, with several contributions such as charge transfer across the interface, redistribution of the electron cloud, interfacial chemical reactions, and other types of rearrangement of electronic charge.<sup>60, 63, 65</sup> It is important to understand the origin of the interfacial interactions that lead to the dipolar layer, which is responsible for the vacuum level shift. The value of this shift is determined by the magnitude of the imposed dipole. Figure 1.16 shows the possible factors that affect forming the interfacial dipole layer<sup>63</sup>. Note

that the interfacial dipole is not related to the polarity of the molecule and it takes place even for nonpolar molecules. Details of each effect are beyond the scope of this chapter, but it is discussed in the cited review.

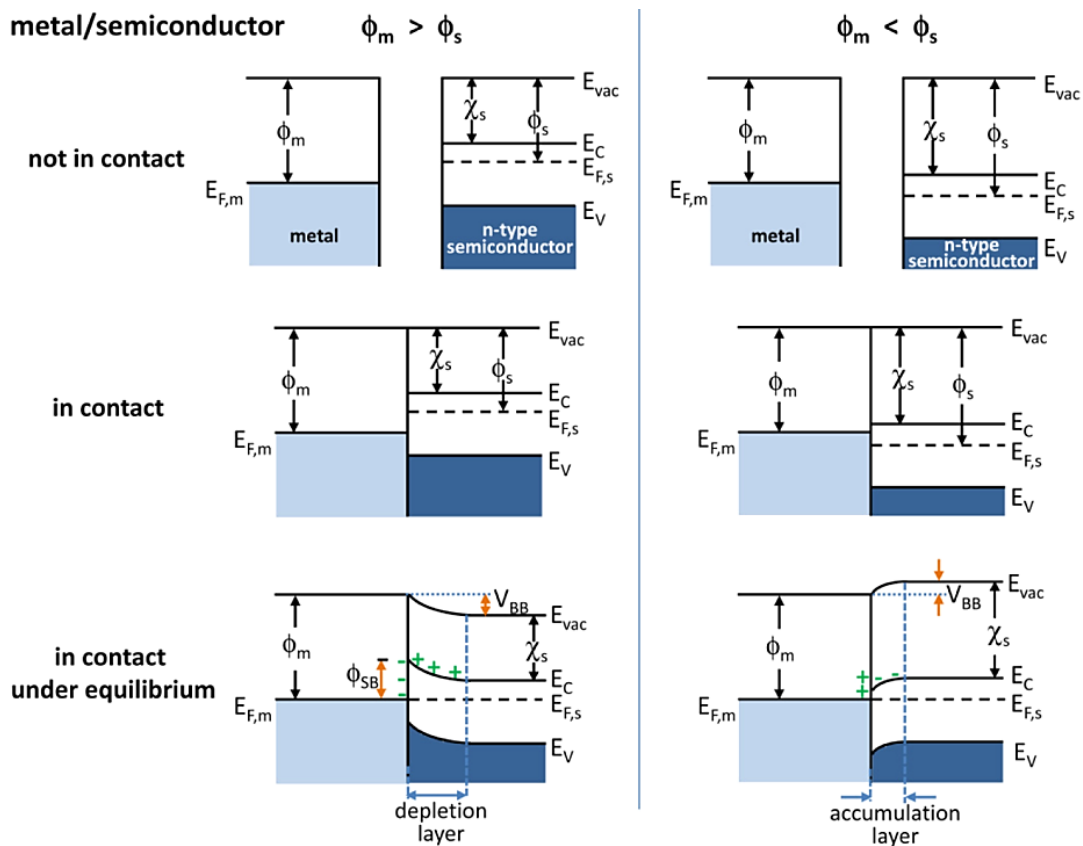


**Figure 1.16** Several possible factors that affect formation of an interfacial dipole layer at an organic/metal interface: **a)** Charge transfer across the interface, **b)** Concentration of electrons in the adsorbate leading to positive charging of the vacuum side, **c)** Rearrangement of electron cloud at the metal surface, with the reduction of tailing into vacuum, **d)** Strong chemical interaction between the surface and the adsorbate leading to the rearrangement of the electronic cloud and also the molecular and surface geometries (both directions of dipoles possible), **e)** Existence of interface state serving as a buffer of charge carriers, and **f)** Orientation of polar molecules or functional groups. Figure reproduced with permission from ref [63]

### 1.3.2.2 Band bending

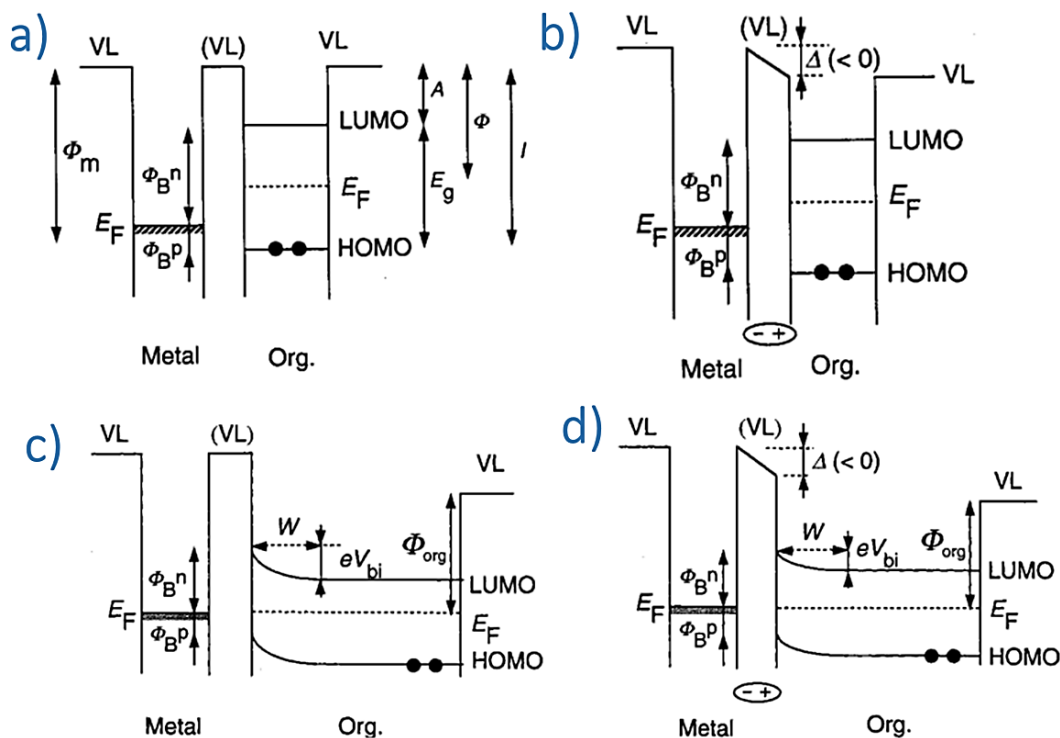
Another important effect in ELA is the band bending concept, which originally comes from the study of traditional inorganic semiconductors. Band bending is a purely electrostatic

effect where an electrostatic potential energy of a given state (valence and conduction band in semiconductors) become a function of the position within the material with respect to the surface. When the metal and semiconductor are in contact, free electrons will transfer between metal and semiconductor due to the work function difference.<sup>66</sup> Figure 1.17 shows the two scenarios of upward and downward band bending in semiconductors, depending on the position of semiconductor Fermi-level relative to the Fermi-level of the metal.



**Figure 1.17** Two common scenarios for energy band diagrams (upward and downward shift) of metal and n-type semiconductor contacts in different stages.  $E_{vac}$ : vacuum energy;  $E_C$ : the energy of conduction band minimum;  $E_V$ , the energy of valence band maximum;  $\phi_m$ : metal work function;  $\phi_s$ : semiconductor work function;  $\chi_s$ , electron affinity of the semiconductor. Figure reproduced with permission from ref [66]

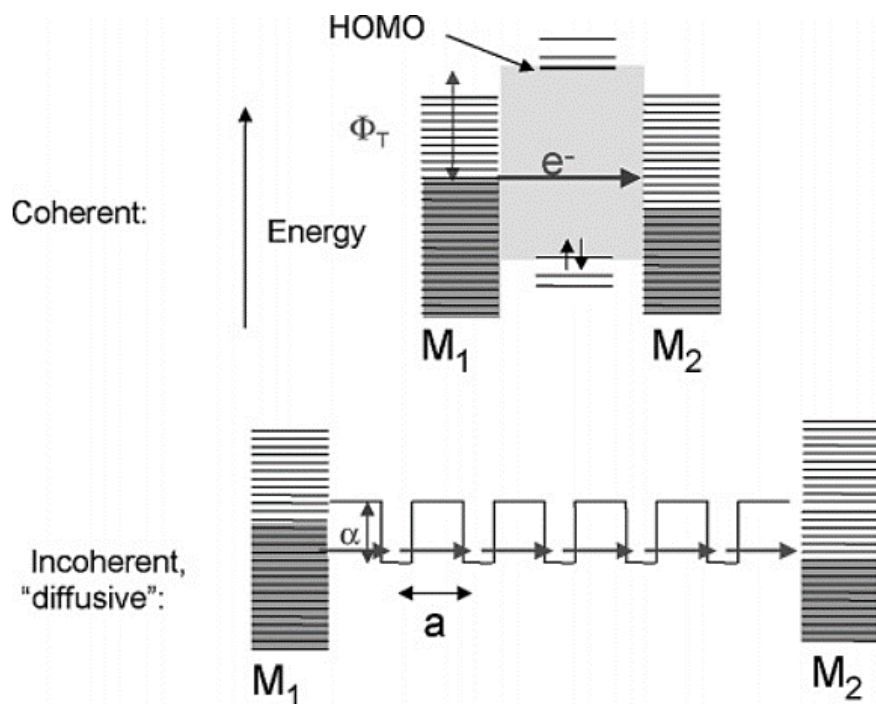
The applicability of the band bending concept in organic/metal interfaces has been investigated, discussed and reviewed.<sup>63, 67, 68</sup> Actually, band bending is reasonably successful in answering question arising from light interactions, charge separation and photocurrent in organic/metal junctions. If the charge redistribution takes place between the metal and molecules, charge separation modifies the electrostatic potential profile of the system. The resulting depletion or accumulation layer thickness ( $W$ ) is dependent on various parameters including the magnitude of  $V_{bi}$  (description in Figure 1.11), dielectric constant, concentration and delocalization length of free charge carriers. Diffusion layer thickness ( $W$ ) for typical Si is of the order of 10  $\mu\text{m}$ , but it is not clear and established for organic materials and it can be in a range of few nm.<sup>63, 68</sup> Figure 1.18 shows the scenario of upward band bending in an organic device with (panel c) and without (panel d) considering the vacuum level shift at the interface. The concept of vacuum level shift and bend bending are the basis of discussions in chapter 4.



**Figure 1.18** **a)** Electronic structure of a metal and an organic solid at an infinite distance.  $\Phi_B^n$  and  $\Phi_B^p$  denote the injection barriers for electron and hole. **b)** Contact of a metal and a thin organic solid layer. Interfacial energy diagram with a shift of VL at the interface due to dipole layer formation. In this figure, the organic side is charged positive, making this side more stable (low energy) for an electron, and making the sign of shift negative. **(c)** Interfacial energy diagram with band bending. The energy levels are bent by the charge redistribution in the organic layer to achieve electrical equilibrium with the alignment of the Fermi levels of the two sides.  $V_{bi}$  : built-in potential,  $W$ : diffusion layer of thickness. **(d)** Same bending scenario as the panel c with considering the vacuum level shift. Figure reproduced with permission from ref [63]

### 1.3.3 Coherent vs incoherent transport

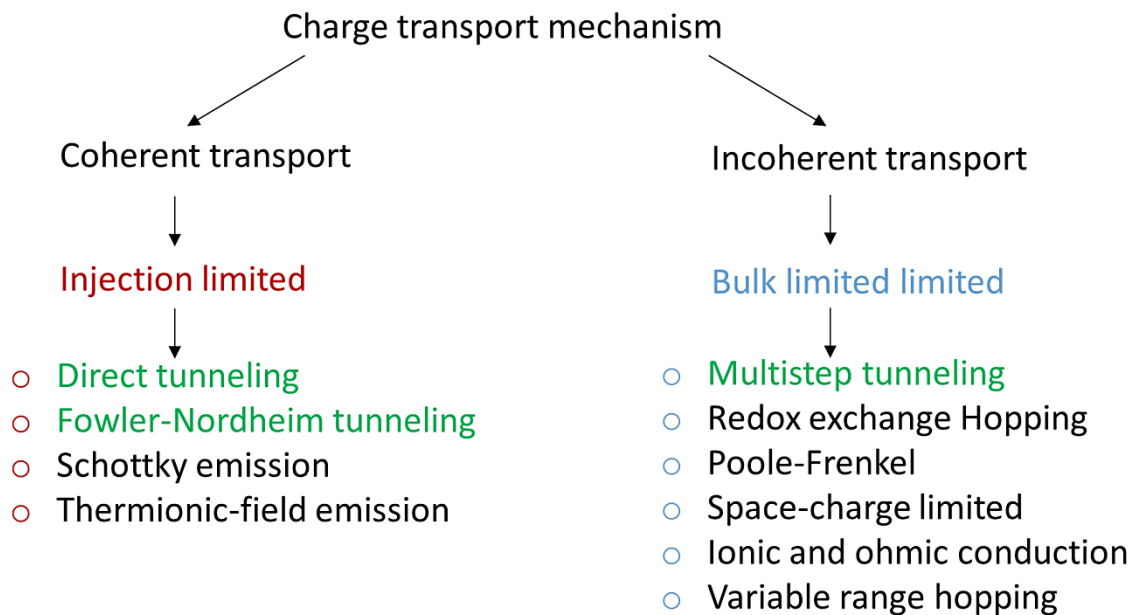
Electronic conduction in organic materials has been a subject of considerable interest in the quest to understand charge transport characteristics in molecular junctions. In one simple view, transport can be categorized as coherent and incoherent transport.<sup>69</sup> Figure 1.19 schematically shows the difference between these two classes. In the coherent limit, thickness of the molecular layer is not much greater than the delocalization length in the molecular layer. Correspondingly, localized sites within the molecular layer do not contribute effectively in the transport and charges do not reside and relax in the molecular layer. In contrast, incoherent transport may be viewed as a series of discrete steps during charge transfer across the molecular layer<sup>70</sup>.



**Figure 1.19** Simple schematics of the difference between coherent and incoherent transport. Figure reproduced with permission from ref [70]

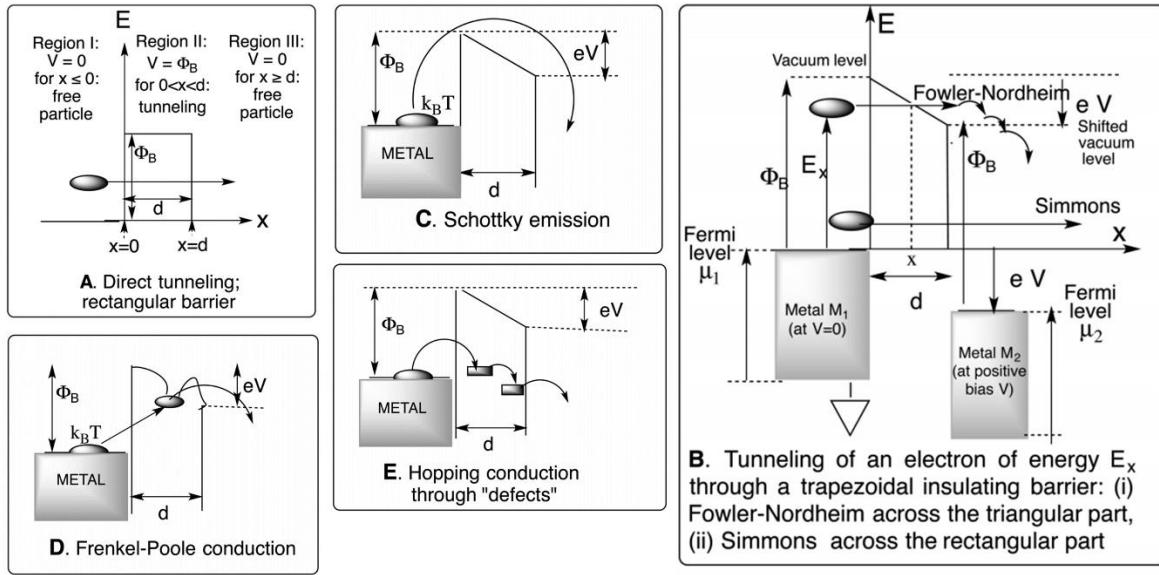
For the case of a high density of localized states and high thickness of the molecular layer, the incoherent mechanism becomes dominant. Transition of the dominant transport mechanism from coherent to incoherent (inelastic) is usually observed as the layer thickness exceeds 4-5 nm in the case of aromatic molecular layers,<sup>46, 47 71</sup> Figure 1.20 shows a classification of the two charge transport mechanisms.





**Figure 1.20** Coherent vs incoherent transport diagram. Green color indicates weakly temperature dependent transport mechanism.

These mechanisms have been reviewed and compared in many studies. Figure 1.21 provides a graphical outline of several of the commonly studied mechanisms. The details of each mechanism are beyond the scope of this chapter and interested readers are referred to the cited reviews.<sup>11, 13, 72, 73</sup> However, several features of mechanisms closely related to this thesis are summarized in continue.



**Figure 1.21** Schematics of indicated transport mechanisms with their effective barriers and charge movement pathway. **(A)** Direct tunneling across a rectangular barrier. **(B)** Fowler-Nordheim tunneling across the triangular top part of a trapezoidal insulating barrier between two metallic electrodes, and Simmons tunneling through the lower rectangular part. **(C)** Schottky emission. **(D)** Poole-Frenkel conduction. **(E)** Hopping conduction through defects (slow) or virtual states (superexchange, fast). Figure reproduced with permission from ref [72]

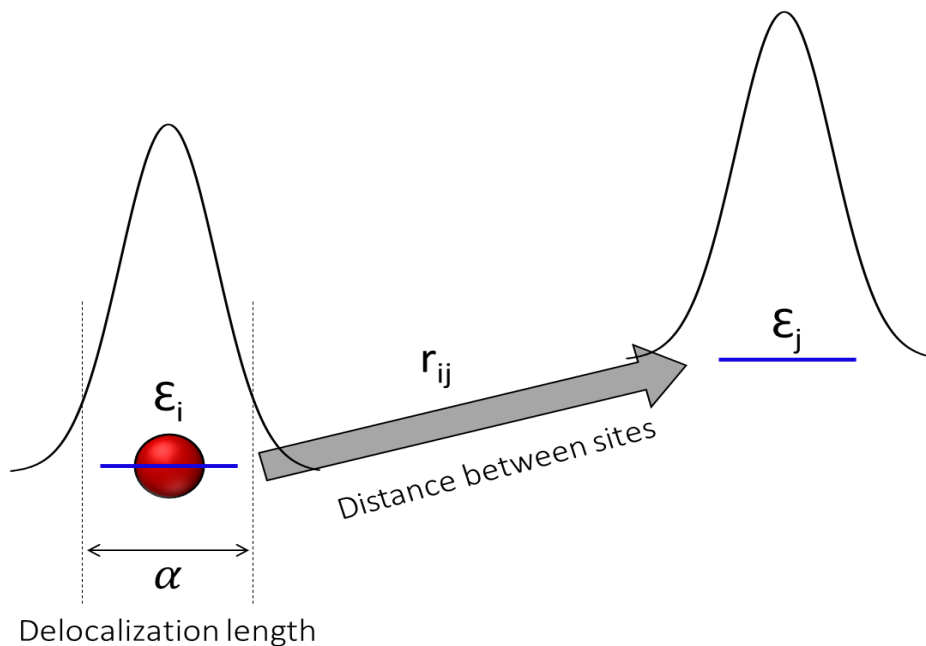
### 1.3.4 General remarks on conduction properties in disordered materials

This section focuses on the basic foundation involved in charge transport in disordered materials with localized states. Many mechanisms described in the large literature on transport in disordered materials provide possibilities to consider in molecular electronic devices.

For the case of sequential transport between localized states, the Miller-Abraham master expression (eq 1.3) is often used to state the probability of transport between states ( $v_{ij}$ ) across a distance  $r_{ij}$  as depending on two exponential factors,<sup>57, 74, 75</sup> where  $\alpha$  is the localization length and  $K$  the Boltzman constant:

$$v_{ij} \sim \exp\left(\frac{-2r_{ij}}{\alpha}\right) \exp\left(\frac{-\Delta E}{KT}\right) \quad (1.3)$$

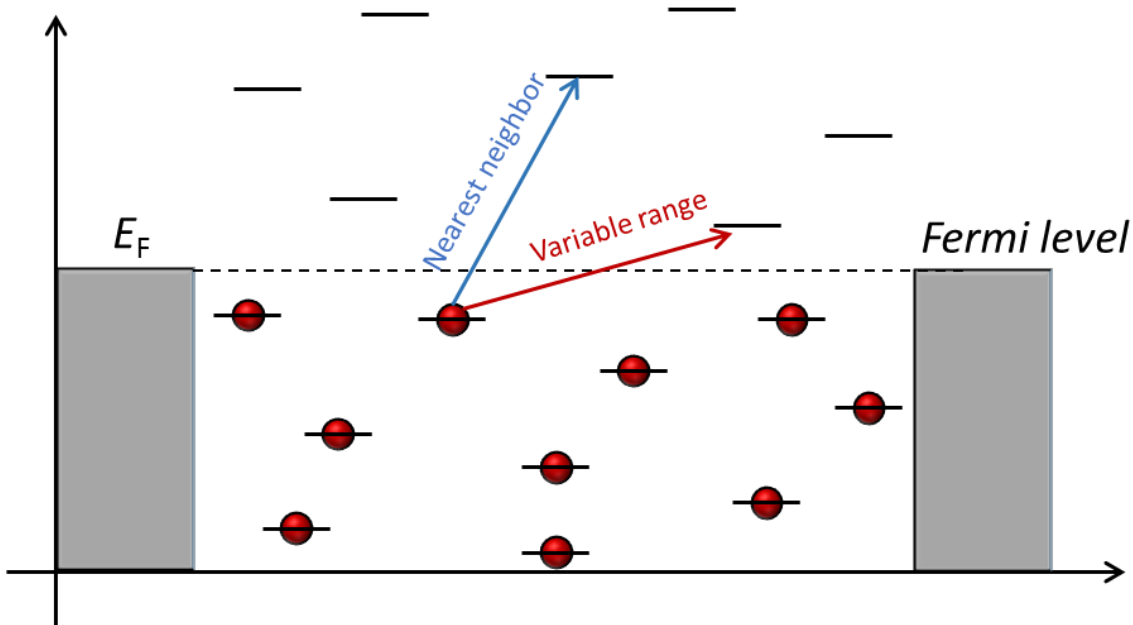
Figure 1.22 schematically shows the parameters used in equation 1.3, with  $\Delta E = \epsilon_j - \epsilon_i$



**Figure 1.22** Schematics of the hopping transition between two localized  $i$  and  $j$  state along the contributing factors. Gaussian-like lines depicts carriers wave function at each site.<sup>76</sup>

The first exponential factor is the tunneling probability between two states and the second part considers activated transport between two states.  $\Delta E$  in the  $T$ -dependent term is the energy associated with any molecular motion which precedes charge transport, including changes in torsion angle, intramolecular vibrations, etc.

Nearest neighbor hopping (NNH) and variable range hopping (VRH) transport mechanisms in disordered materials are two common solutions to equation 1.3 with certain assumptions,<sup>77-79</sup> and the corresponding pathways are shown in Figure 1.23.



**Figure 1.23** Two possible hopping transition between filled and unoccupied states: 1) nearest neighbor hopping, 2) Variable range hopping. Dashed line depicts the position of Fermi-level.<sup>76</sup>

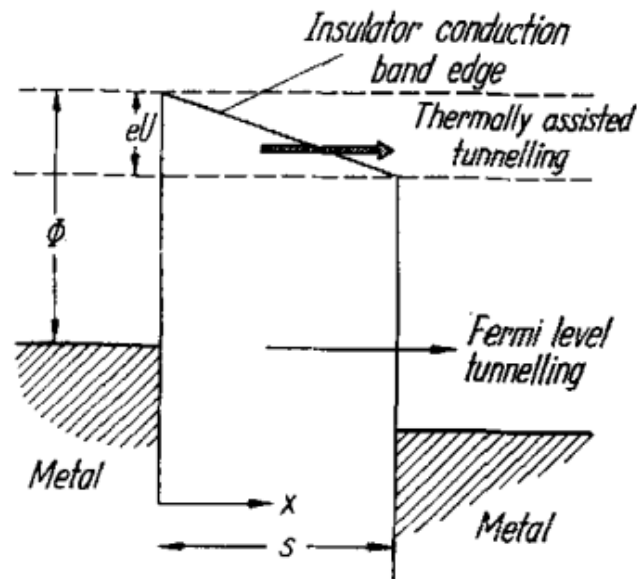
It is always important to look at the assumptions associated with each mechanism, regardless of its utility in explaining experimental observations or trends. For example, Stallinga has discussed how variable range hopping and Mott's assumptions (described below) are not conceptually and necessarily expandable to molecular electronics.<sup>57</sup> The detailed discussion behind the inconsistencies in assumptions is beyond the scope of this chapter and thesis; however, an important and interesting part of the paper reads as follows:

*“Note that the original theory (variable range hopping) was not intended to be used for conductive materials. Mott had a dilute system in mind, or based it on such a system. It is questionable whether the theory can be transposed to any low-mobility material — materials that superficially seem to behave the same, but intrinsically are very different — as is conventionally done by the organic materials community. The localized states — conjugated segments in organics — are in fact adjacent in amorphous materials and conduction takes*

*place between states of the host, not via dilute impurity levels. It is questionable whether the application of Mott's idea to amorphous materials, as done by Ambegaokar et al. and picked up by many others, is justified, even if it is mathematically correct and is consistent with the experimental data."*

### 1.3.5 Thermally assisted tunneling

A thermally assisted tunneling mechanism considers the scenario that the major contribution to the tunneling integral comes not energies close to the Fermi level, but higher energies above the Fermi level (as illustrated in Figure 1.24). Under appropriate assumption about parameters thermally assisted tunneling can yield the same current-voltage functional form as Schottky emission or Poole-Frenkel conduction, but may be distinguished by the weak temperature and field dependence of its pre-exponential factor. Three main conclusions from thermally assisted tunneling include: i) linearity of  $\ln J$  with  $V^{1/2}$ , ii) weakly temperature dependent, iii) linearity of  $\ln J$  with  $T$  instead of  $1/T$ .<sup>80</sup>



**Figure 1.24** Schematic representation of the energy bands of a metal-insulator-metal for thermally assisted tunneling compared to the Fermi-level tunneling. Figure reproduced with permission from ref [80]

### 1.3.6 Multistep tunneling

In order to have a conceptually sensible outcome from the master expression (eq 1.3) for hopping in a molecular wire, we have to re-examine basic concepts and use realistic assumptions based on an understanding of molecular layer properties. Although equation 1.3 appears to predict Arrhenius  $T$  dependence at first inspection, the localization length  $\alpha$  and the energy levels in the molecular layer vary significantly with molecular conformation, e.g. with the dihedral angle between molecules in an oligomer. Consequently, transport barriers and transport distances can vary with temperature and cause inhomogeneous broadening. Various treatments based on equation 1.3 lead to predictions of  $\ln J$  linearity with  $T$ ,  $T^2$ , and  $T^{-1/4}$  in addition to Arrhenius behavior.

For very low  $T$ , where vibrations or conformational changes are limited, transport becomes dominated by the first exponential, resulting in a series of presumably incoherent tunneling steps, with possibly variable length. In following chapters, temperature dependence and the first exponential in equation 1.3 are discussed in the context of the dominant transport mechanism.

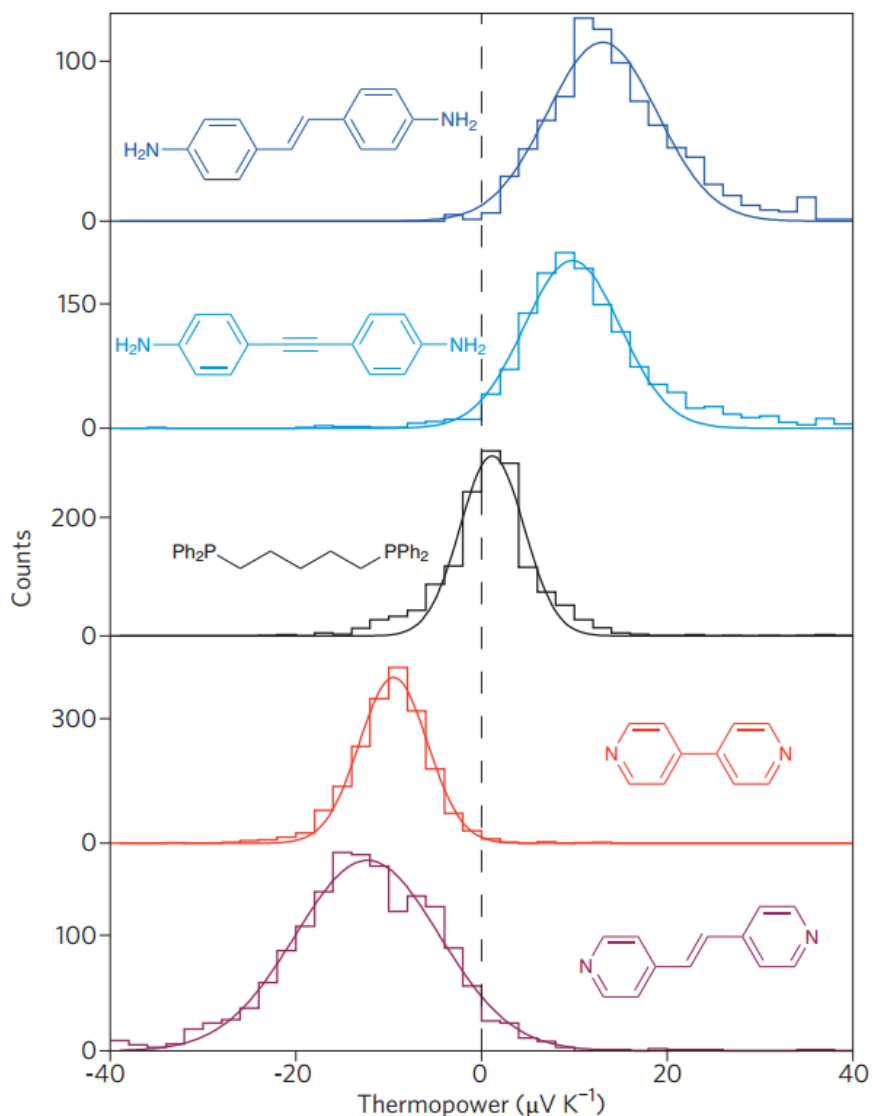
## 1.4 Beyond electronic charge transport

In recent years, scientists have started to probe the properties of molecular junctions beyond simple  $JV$  measurement. Various physical stimuli have been used to realize new physics involved in transport which are characteristic of the molecular junction. Pushing the

frontiers of measurement capabilities and exploring optical effects and thermoelectric, plasmonics, and spintronics phenomena have had a significant impact on our fundamental understanding of molecular junction characteristics and structure-function relationships.<sup>1</sup> These interdisciplinary research efforts at the molecular scale have also contributed to demonstrated possible functions of a molecular junction.

#### 1.4.1 Thermoelectric studies

Studying the electronic response to heating in a molecular junction provides insights into charge transport, and is called the thermoelectric effect.<sup>81-83</sup> The thermoelectricity, which measures either induced voltage drop or the induced current across the junctions with a gradient of temperature between electrodes, is important to understand the basic scientific mechanism of the thermoelectronic effect at the molecular level and possibly improves the technology for converting wasted heat into useful electrical energy. Furthermore, measured Seebeck coefficient ( $S = \Delta V/\Delta T$ ) of the molecular junctions can determine the relative position of frontier molecular orbitals (HOMO and LUMO) relative to the Fermi-level of the electrodes<sup>84</sup>. For example, Figure 1.25 shows the measured Seebeck coefficient for five molecules. Amine-terminated molecules (Number 1 and 2) have a positive Seebeck coefficient in agreement with calculations that show that the HOMO is closest molecular orbital to  $E_F$ . In contrast, pyridine-terminated molecular junctions have a negative Seebeck coefficient and conduct through the LUMO.<sup>84</sup>



**Figure 1.25** Histograms of Seebeck coefficient and fitting with Gaussian distribution for five indicated molecules. 1 and 2 exhibit positive S while 4 and 5 exhibit negative S. The Seebeck coefficient for 3 is close to zero. Figure reproduced with permission from ref [84]

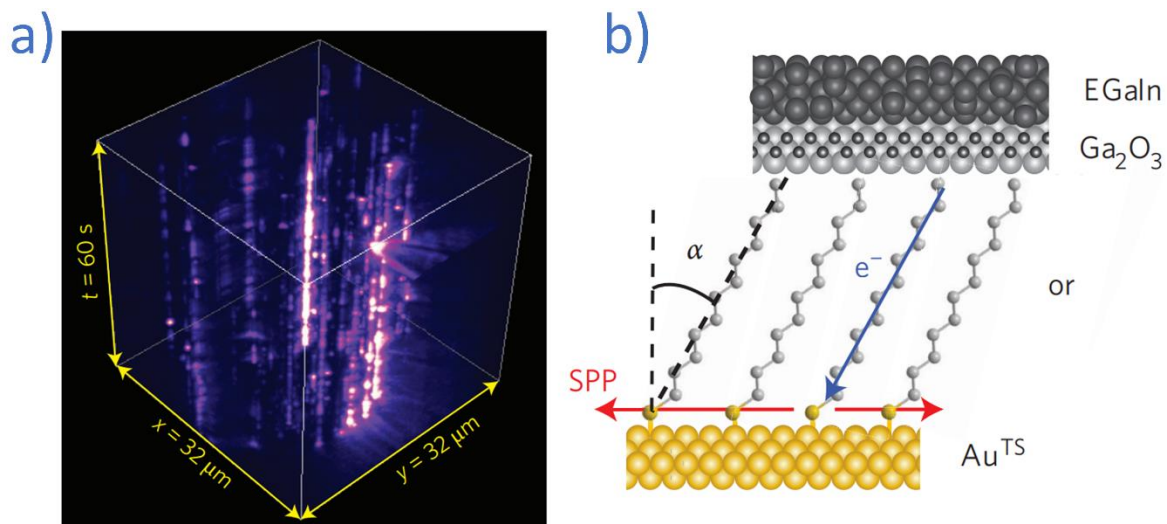
### 1.4.2 Molecular plasmonics

An emerging branch of photonics, called plasmonics, aims to use nanostructured materials that support “surface plasmons” for various purposes. The propagating electromagnetic modes are properly termed surface plasmon polaritons (SPPs), but are often



referred to simply as surface plasmons. SPPs deals with the electromagnetic wave that involves both charge motion in the metal (surface plasmon) and electromagnetic waves in the air or dielectric (polariton). SPPs are electromagnetic excitations propagating at the interface between a dielectric and a conductor, confined in the perpendicular direction relative to the surface. Plasmonics can potentially achieve highly complex miniaturized devices, thereby opening up new perspectives for integrated optoelectronic circuits at the nanoscale by controlling and manipulating light on the nanometer scale.<sup>85-87</sup>

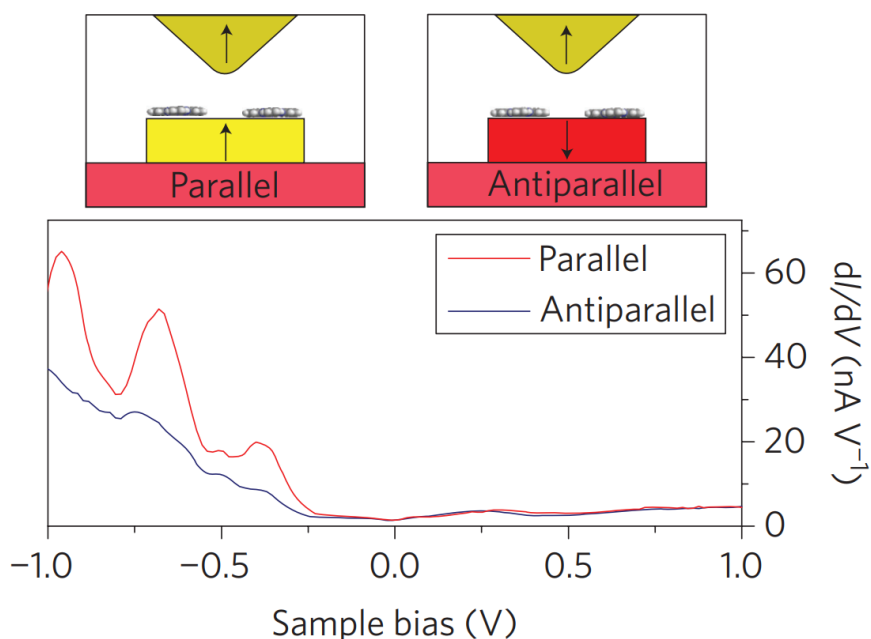
SPPs is investigated in molecular tunneling junctions, in which the structure of molecular layer and applied bias influence the polarization. During transport, some of the inelastically transferred electrons can couple to a plasmon mode. Direct excitation of plasmons by tunneling electrons have no background light and is very fast, comparable to the time scale of electron tunneling. Figure 1.26a demonstrates the blinking phenomena in plasmon emission for molecular tunnel junction shown in Figure 1.26b under bias (1.8 V).<sup>88</sup>



**Figure 1.26** **a)** Real plane images ( $x$ - $y$  plane) plotted as a function of time  $t$  ( $z$ -axis). Images were recorded at intervals of 0.5 second and obtained from a junction with self-assembled monolayer film at a bias of  $-1.8$  V. **b)** Schematics of the tested junctions in panel a. Figure reproduced with permission from ref [<sup>88</sup>]

### 1.4.3 Molecular spintronic

The early idea of the possibility of long-range ferromagnetic order in organic crystal led to the emergence of molecular spintronics as an alternative to practical inorganic magnetic devices. The promising field of molecular spintronics can be thought of as a tool to push the frontiers of molecular electronics toward simultaneous controlling of charge, spin states, and spin-spin coupling.<sup>89-93</sup> The central point is to use one or a few molecules, which respond to a magnetic field, to create molecular devices. Figure 1.27 shows magnetization orientation for phthalocyanine molecule on the surface of Co electrode probed at the Co-coated tungsten STM tip.<sup>94</sup> The measured differential conductance at the bottom demonstrates clear differences in the transport characteristics depending on the relative alignment of the orientation of tip and Co electrodes magnetization.



**Figure 1.27** Typical  $dI/dV$  spectra (differential conductance) taken on parallel and antiparallel oriented cobalt islands clearly reveal the spin-polarized density of states below the Fermi edge and effect of the magnetic field orientation on electronic behavior of junction. Figure reproduced with permission from ref [94]

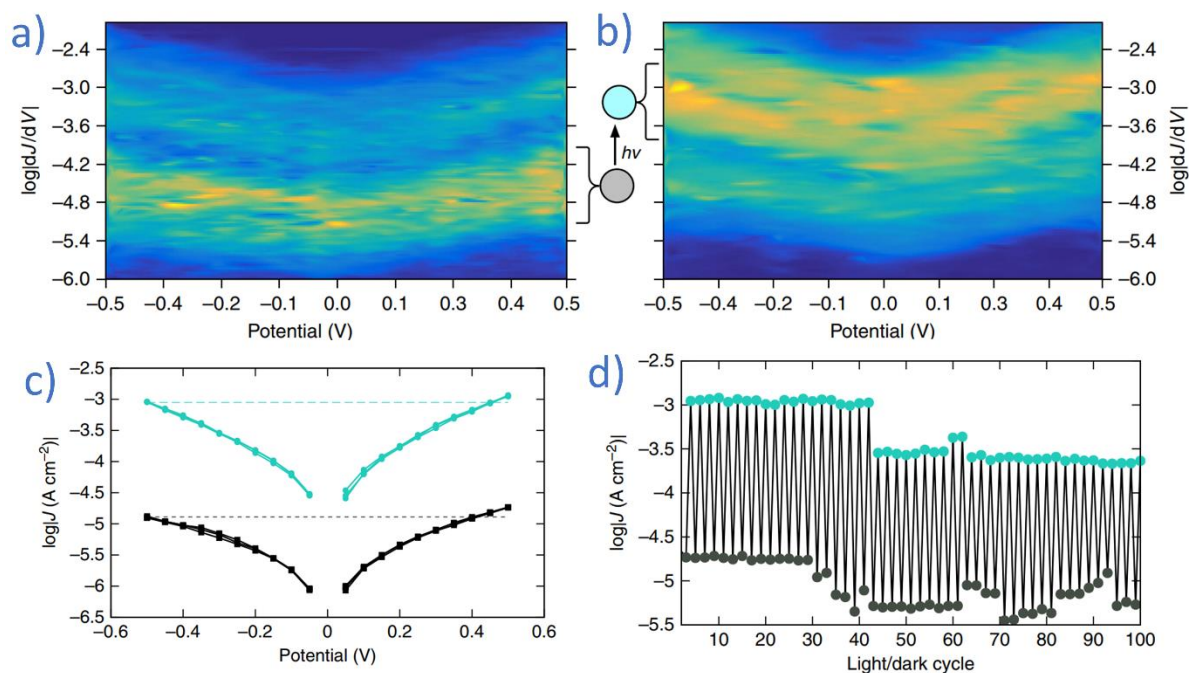
#### **1.4.4 Molecular Optoelectronics**

Studying the interaction of light as a physical stimulus of a molecular junction is referred to as molecular optoelectronics.<sup>95-98</sup> Optoelectronics can be a potentially powerful tool for diagnostics of transport and energy level alignments in molecular junctions on one hand, and have potentially high-level applications as optic devices like switches and sensors on the other hand.

##### **1.4.4.1 Photo-gating in conductance for molecular junction**

One of the interesting topics in molecular optoelectronics is photo-induced conductance switching, in which the tunneling probability of a metal/molecule/metal junction is affected by light illumination. One approach to realizing light-driven conductance switching is to find a system that does not photo-isomerize, but in which the electron transfer rate in the dark and light states differs.

Poorhossein et al. have described the reversible, light-induced gating of tunneling currents through nano-gaps between two parallel Au nanowires separated by a self-assembled molecular monolayer comprising hemicyanine dyes<sup>99</sup>. Hemicyanine dyes contain donor and acceptor sub-units through a molecular wire, causing a strong optical absorption and significant charge-transfer character. Figure 1.28 demonstrates how the tunneling current is affected by light illumination in the studied system.

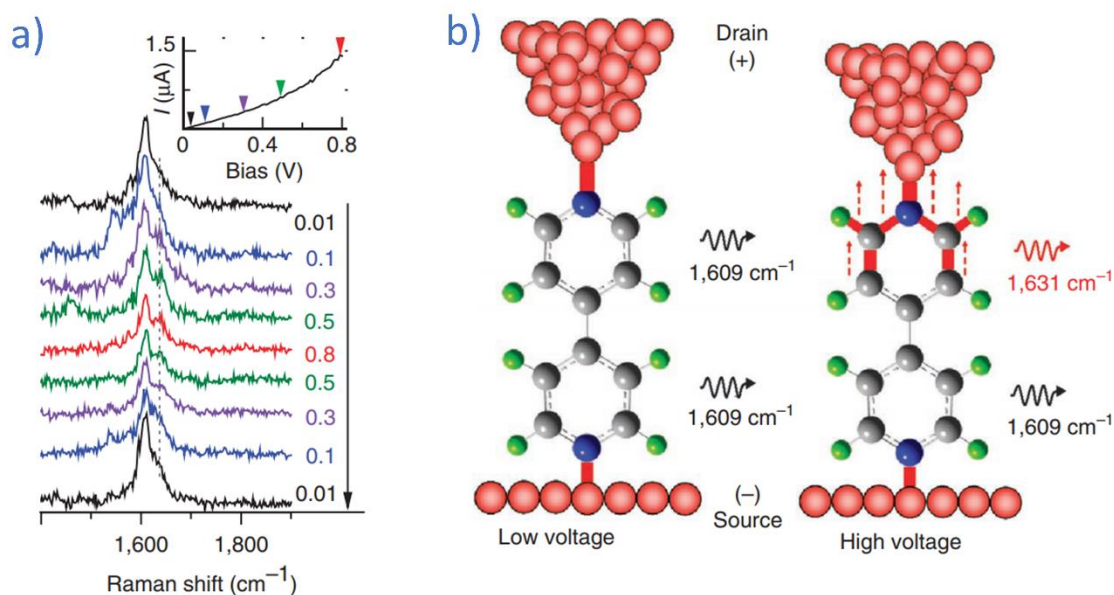


**Figure 1.28** (a) Conductance heat-map plot for AminoPyr without illumination (dark condition). The colors correspond to the frequencies of the histograms; lighter colors indicate higher frequencies. (b) conductance heat-map plot under illumination for the same junction shown in panel a. The colored circles correspond to data in the dark (grey) and under illumination (cyan). (c) Plots of  $\log J$  vs  $V$  for AminoPyr from a single device showing three traces each from dark–light cycle. The dashed lines show the slight asymmetry of the device in both the dark (black squares) and light (cyan circles) states. (d) The plot of conductance cycling of AminoPyr. The values of  $\log J$  at 0.5 V as a function of light/dark cycles for a range of 100 consecutive cycles. The time between each cycle is on the order of 60 s. These data show a clear, statistical difference between AminoPyr-dark and AminoPyr-light. Figure reproduced with permission from ref [99]

#### 1.4.4.2 Live Raman measurement during transport

Raman measurements on molecular junctions during charge transport can provide information about local structural and vibrational changes in molecules in operation, thus opening up new avenues of research, both experimentally and theoretically. In addition, monitoring the ratio of Stokes to anti-Stokes Raman peaks may be used to examine heating

of the molecule during charge transport. Figure 1.29 shows the Raman spectra for the Au/bipyridine/Au junction under elevated bias across the molecular junction.<sup>100</sup> The results clearly show the splitting in the vibration modes of bipyridine which resulted from the deformation of the pyridine ring in contact with the drain electrode at high bias.



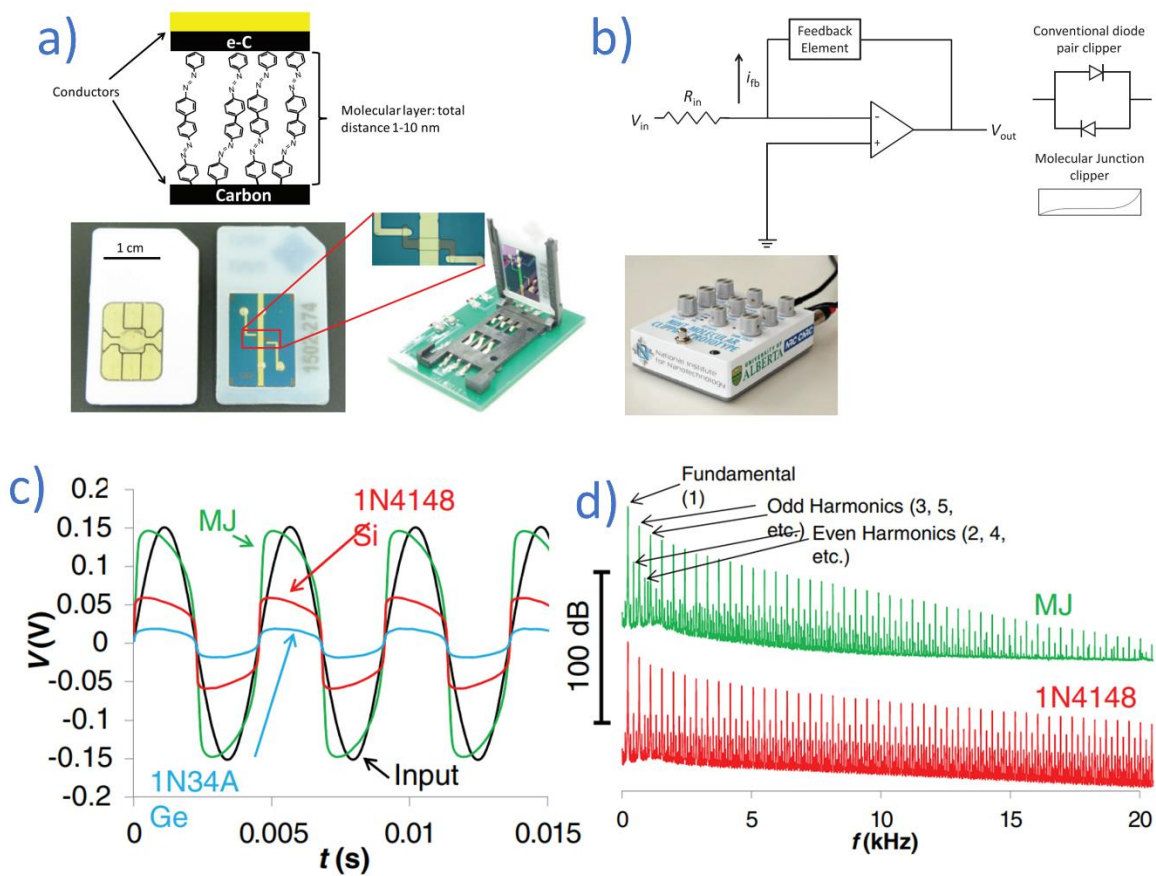
**Figure 1.29 (a)** The Raman band of bipyridine at  $1609\text{ cm}^{-1}$  at the elevated applied voltage across the junction. Inset: current-voltage curve for the examined junction. Tip enhanced Raman spectroscop setup is used to make a connection with single molecule of bipyridine and Raman measurement **(b)** The schematic for a possible explanation of band splitting at  $1609\text{ cm}^{-1}$  due to the applied voltage. Figure reproduced with permission from ref [100]

## 1.5 Real world applications of molecular electronics

ME has resulted in reported devices capable of handling a variety of electronic functions, including but not limited to nonlinear resistance,<sup>101, 102</sup> rectification,<sup>21, 103-105</sup> memory,<sup>106-108</sup> and conductance switching.<sup>109, 110</sup> However, after 30 years of intense research in ME, the success of ME is questionable in terms of commercialized applications. At least

one reason for commercialization difficult is the procedure for MJ fabrication. Most of the MJ fabrications reported to date were developed for research purposes. A small change in fabrication steps can lead to a large deviation in the functions, and affect the characteristic of the molecular junctions. As a result, demonstrating the functions using a particular paradigm of MJ fabrication cannot be easily extended to scale up fabrication. Furthermore, yield, stability, reproducibility, and cost of the fabrication are among other limitations in the commercialization of a ME device. I believe that we should review the fabrication paradigms carefully and take the applicability of scale-up fabrication into account from the first point. This is the main reason behind the loop in molecular electronics which constantly return back to the fabrication step and consequently affect the next phases of the loop.

To the best of my knowledge, the analogue clipping circuit used in electronic music is the first commercialized application of molecular electronics. The applicability of non-linear resistance in large area MJs for distortion of audio input signal waveform was enabled by carbon-based molecular junctions.<sup>5</sup> Advances in the fabrication process to realize stable, reproducible and inexpensive MJs are the main requirements for success in commercialization. Figure 1.30 shows the fabricated chips integrated into SIM (subscriber identification module) card holder for the functional prototype amplifier (Figure 1.30b). MJ yield similar distortion response to the diode clippers, but different harmonics in the sound and consequently unique output sound.<sup>111</sup>



**Figure 1.30** (a) Cross-sectional schematic of an idealized molecular junction structure and a photograph of the molecular junctions with a SIM-card format to simplify testing and integration into analog circuits. (b) Simplified schematic of the clipping amplifier section of the circuit employed in the prototype for the op-amp clipping gain stage. (c) Output waveforms for sine-wave input. (d) The power spectra for the Si and MJ waveforms with odd and even harmonics labeled. Figure reproduced with permission from ref [111]

## 1.6 Scope of Thesis

The overall objective of the research work described in this thesis is to provide insight into the transport mechanism in large area all-carbon molecular junction. Chapter 2 describes the applicability of eC electrodes for reliable fabrication of high yield and stable cross-bar

molecular junctions. In addition, flexibility and semitransparency of the completed junctions with eC electrodes are demonstrated.

In Chapter 3, multistep tunneling as a dominant and most consistent charge transport mechanism in thick all-carbon molecular junctions is described. Four molecules are tested and compared in the thickness range of 2 to 11 nm to investigate structure-function relation in the transport.

Chapter 4 addresses the possibility of studying the charge separation and transport mechanism upon illumination by UV-Vis light. Using AC and DC measurement setup, light interaction with junctions at zero applied bias for eight distinct molecular structure in one device structure. This chapter demonstrates hetero-interface nature of all-carbon molecular junctions and provides clear molecular signature relating structure to electronic behavior.

Finally, this thesis is ended with final thoughts and conclusion of all the work presented herein. Also, outlook on future work and directions of molecular electronics is presented.



# CHAPTER 2

Robust all-Carbon Molecular Junctions on Flexible or  
Semi-Transparent Substrates Using Process-  
Friendly Fabrication

## 2.1 INTRODUCTION

Development of the field of Molecular Electronics was stimulated by intense scientific interest in the behavior of single molecules or molecular monolayers as elements in electronic circuits. The small size and wide range of electronic configuration of molecules were investigated to enable new electronic functions and possibly further extend the exponential increase in device density in microelectronic devices. Recent reviews of the progress of molecular electronics document the many experimental paradigms used to provide contact between conventional conductors and molecular components,<sup>8, 13, 46</sup> notably the quest for a molecular rectifier first proposed in 1974.<sup>14</sup> This chapter deals with “ensemble” molecular junctions (MJs), in which a large number of molecules are bonded to a conductive substrate, then a “top contact” is applied by one of several methods. Many distinct electronic effects of ensemble molecular devices have been demonstrated, such as nonlinearity,<sup>47, 58, 112, 113</sup> rectification,<sup>114-118</sup> bistability,<sup>119, 120</sup> photocurrents,<sup>97, 118, 121-123</sup> light emission,<sup>124-126</sup> and redox events.<sup>120, 127-129</sup> A key issue of molecular electronics is integration of molecular devices into microelectronic circuits, with sufficient lifetime and temperature tolerance to be widely practical in real applications. The impediments to developing robust, practical MJs often lie in the requirement for substrates which are flat on a molecular scale, possible electromigration or oxidation of metallic contacts, and the difficulties in adapting laboratory fabrication methods to real-world processing and operating conditions.

Our group has developed carbon-based molecular junctions based on covalent bonding of molecular layers to flat (< 0.4 nm rms) sp<sup>2</sup> hybridized carbon surfaces made by pyrolysis of novolac photoresist, *i.e.* pyrolyzed photoresist films (PPF). PPF is patternable by photolithography, thermally stable, not subject to electromigration, and electrochemical

reduction of diazonium reagents on PPF provides a variety of molecular layer structures and thicknesses. A top contact of electron beam deposited carbon (eC) or Cu yields molecular junctions with high yield (>90%), good reproducibility, long cycle life (>10<sup>9</sup> scans)<sup>130</sup> and wide temperature tolerance (6 – 600 K).<sup>130, 131</sup> PPF/azobenzene/eC/Au MJs were produced for implementation in audio processing, and consumer devices containing 390 MJs were sold publically in late 2015.<sup>111</sup>

PPF is structurally similar to glassy carbon, but is a relatively poor conductor (~200 S/cm), and the requirement for slow pyrolysis at >1000 °C in forming gas is not readily amenable to large scale manufacturing. PPF can be made thin enough to provide partial optical transparency,<sup>132, 133</sup> but its low conductivity as a thin film restricts possible applications. This project was undertaken to combine the high conductivity and partial transparency of thin metal films with the flatness and surface modification chemistry of PPF, while also avoiding high temperature processing. Electron-beam deposited carbon has been described previously for deposition of 7-300 nm thick films of conducting carbon on quartz<sup>134, 135</sup> or silicon,<sup>136</sup> in some cases resulting in a partially transparent electrode. This Chapter focuses on “all-carbon” molecular junction consisting of a covalently bonded molecular layer between Au/carbon electrodes made by successive electron-beam deposition of Au and carbon at room temperature. Complete molecular junctions may be fabricated on rigid or flexible materials, and retain the strong C-C bond which underlies the stability of diazonium-derived molecular layers. The resulting carbon/molecule/carbon MJs can be made with conventional vacuum deposition with high yield and excellent stability, and avoid the high temperatures and material transfer steps often required for previous MJ designs.

## 2.2 EXPERIMENTAL SECTION

### 2.2.1 Fabrication of molecular junction

Cross-bar molecular junction fabrication has three main steps: bottom contact deposition, molecular layer grafting, and top contact deposition.

#### 2.2.1.1 Bottom contact deposition

The initial substrate was Si with 300 nm of SiO<sub>x</sub> (prepared with wet oxidation) or polyethylene-terephthalate (PET). Electron-beam deposited carbon will be denoted as eC, and layer thicknesses by subscripts in nm, e.g. Au<sub>15</sub>/eC<sub>10</sub>. Substrate layers of Cr, Au, and eC were deposited without breaking vacuum, as were the top contacts of eC/Au. The Cr/Au/eC bottom electrode was fabricated by electron beam deposition of 3 nm Cr (at 0.3 nm/s), 15 nm Au (at 0.3 nm/s) and 10 nm of eC (at < 0.1 nm/s). Beam current was adjusted during deposition of eC to maintain the rate <0.1 nm/s (determined with quartz microbalance). The substrate Au layer was 15 nm in the crossbar geometry in order to maximize transparency, but 20-30 nm layers yield similar results. Electron beam deposition was carried out in commercially available systems, either a Kurt Lesker PVD 75 or a Johnsen Ultravac 3000-GE vacuum system. A high energy (7 kV) electron beam is directed onto a target of Au or high purity graphite (source) by a magnetic field in a vacuum of 10<sup>-5</sup> torr or less. Au purity was 99.99% and carbon source was 3 mm diameter spectroscopically pure graphite rods (SPI Supplies, PA) in a graphite crucible. Atoms and clusters from the target then travel in a straight line to the sample, positioned normal to the atom beam and 20-30 cm from the e-beam target. Deposition was carried out using a physical shadow mask with four parallel 0.25 mm wide lines. E-beam chamber pressure was kept lower than 4 × 10<sup>-5</sup> Torr throughout the deposition. The work function of eC was determined with ultraviolet photoelectron

spectroscopy on four different samples with minimal air exposure to be  $4.83 \pm 0.06$  eV, comparable to  $4.7 \pm 0.1$  eV determined similarly for PPF. The same deposition conditions were used to prepare Cr/Au/eC devices on PET transparency film.

PPF electrode fabrication is described in detail elsewhere.<sup>137</sup> Briefly, positive photoresist (AZ 4330) was spun onto each sample, followed by a soft bake at 80 °C and then photolithography was carried out with a UV exposure. Development was done in a 1:3 dilution of AZ developer: water. Substrates with photoresist features were pyrolyzed in a 1-inch tube furnace by heating under a flow of forming gas (5% H<sub>2</sub>, balance N<sub>2</sub>) to 1050 °C for 1 hour. After cooling in flowing forming gas, the PPF surface consists of sp<sup>2</sup> carbon similar to glassy carbon with RMS roughness lower than 0.5 nm.

#### **2.2.1.2 Molecular layer grafting**

Molecular layer deposition by diazonium ion reduction for molecular junction fabrication is reported previously.<sup>58, 137, 138</sup> A conventional three-electrode electrochemical cell with Ag/Ag<sup>+</sup> electrode as reference and Pt wire as a counter electrode was used for electrochemical grafting of a molecular layer on the surface of the Au/eC and PPF substrates. The solution was 1 mM anthraquinone diazonium fluoroborate dissolved in acetonitrile (ACN) containing 0.1 M tetrabutylammonium hexafluorophosphate (TBAPF<sub>6</sub>) as supporting electrolyte. ACN and supporting electrolyte were used without further purification. The thickness of grafted molecular layer was controlled by sweeping the potential from 0.4V to -0.6V (vs Ag/Ag<sup>+</sup>) at 50 mV/s for repeated cycles. After modification, the sample was rinsed with acetonitrile and dried using a stream of nitrogen. Measurement of molecular layer thickness was done using AFM, using the same procedure described in the supplementary

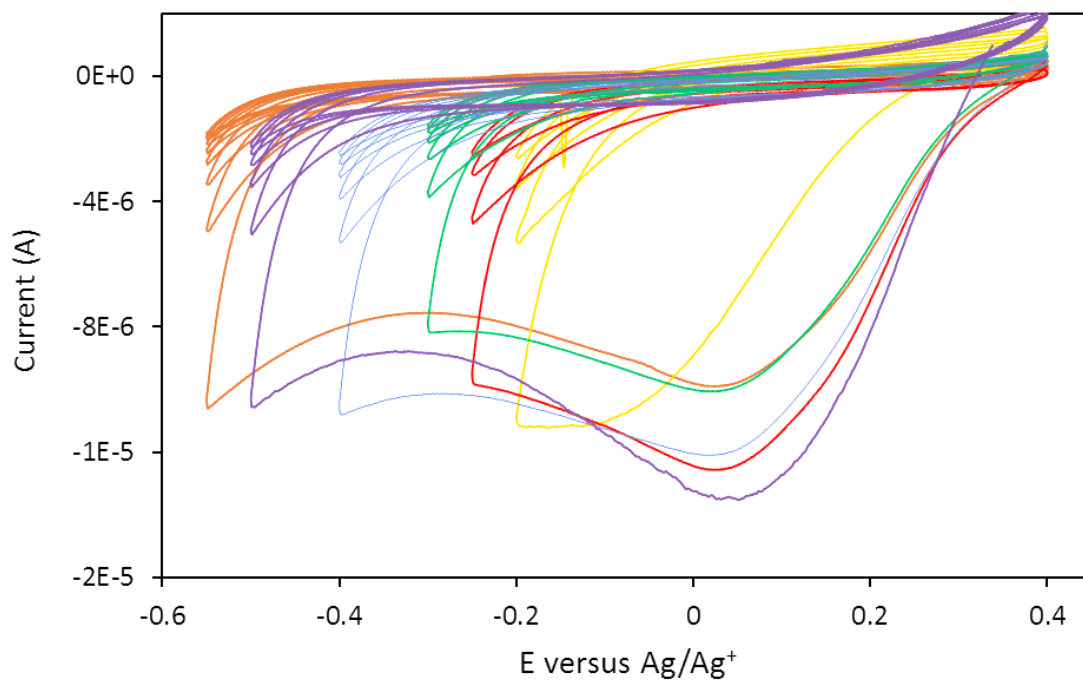
data of a previous report <sup>58</sup>. Electrochemical parameters used for deposition of molecular layers on the surface of each electrode are mentioned in continue.

#### 2.2.1.2.1 PPF modification with anthraquinone

The parameters used for grafting of molecular layer on the surface of PPF are listed in Table 2.1 and corresponding cyclic voltammograms are shown in Figure 2.1.

**Table 2.1** Electrochemical parameters for grafting Anthraquinone molecular layer on the surface of PPF

| Anthraquinone Grafting | Sweep range (E vs. Ag/Ag <sup>+</sup> ) | No. of cycles | Scan rate (mV/s) | Thickness (nm) |
|------------------------|---|---------------|------------------|----------------|
| Sample 1               | 0.4 – (-0.20)                           | 6             | 50               | 2.2            |
| Sample 2               | 0.4 – (-0.25)                           | 6             | 50               | 2.9            |
| Sample 3               | 0.4 – (-0.30)                           | 6             | 50               | 3.4            |
| Sample 4               | 0.4 – (-0.40)                           | 8             | 50               | 3.9            |
| Sample 5               | 0.4 – (-0.50)                           | 8             | 50               | 4.3            |
| Sample 6               | 0.4 – (-0.55)                           | 8             | 50               | 5.5            |



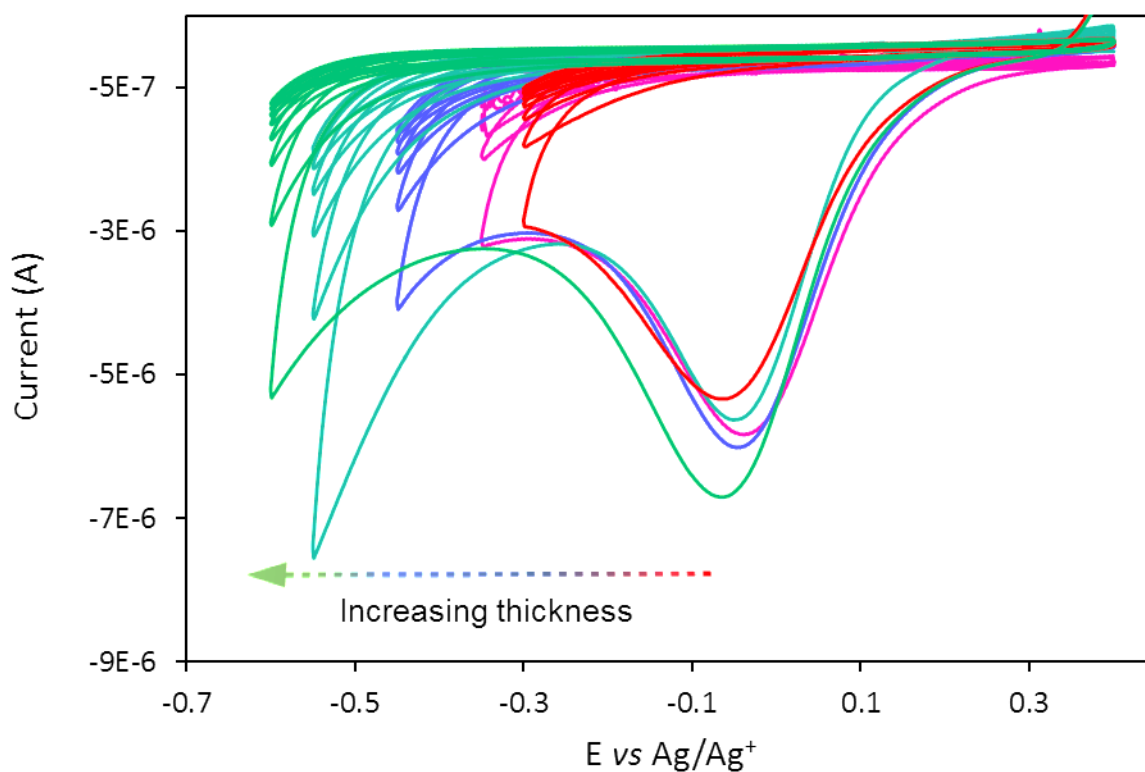
**Figure 2.1** Cyclic voltammogram of reduction of AQ diazonium ion on PPF. Cyclic voltammogram of reduction of AQ diazonium ion on PPF.

#### 2.2.1.2.2 Cr/Au/eC modification

The parameters used for grafting of molecular layer on a Cr/Au/eC electrode are listed in Table 2.2 and corresponding cyclic voltammograms are shown in Figure 2.2.

**Table 2.2** Anthraquinone grafting parameters for  $\text{Cr}_3/\text{Au}_{15}/\text{eC}_{10}$

| Anthraquinone Grafting | Sweep range (E vs. $\text{Ag}/\text{Ag}^+$ ) | No. of cycles | Scan rate (mV/s) | Thickness (nm) |
|------------------------|--|---------------|------------------|----------------|
| Sample 1               | 0.4 – (-0.30)                                | 6             | 50               | $2.3 \pm 0.25$ |
| Sample 2               | 0.4 – (-0.35)                                | 6             | 50               | $2.9 \pm 0.35$ |
| Sample 3               | 0.4 – (0.45)                                 | 6             | 50               | $3.8 \pm 0.27$ |
| Sample 4               | 0.4 – (-0.55)                                | 6             | 50               | $4.5 \pm 0.38$ |
| Sample 5               | 0.4 – (-0.60)                                | 8             | 50               | $5.1 \pm 0.32$ |



**Figure 2.2** Cyclic voltammogram grafting of anthraquinone on the surface of  $\text{Cr}_3/\text{Au}_{15}/\text{eC}_{10}$ .

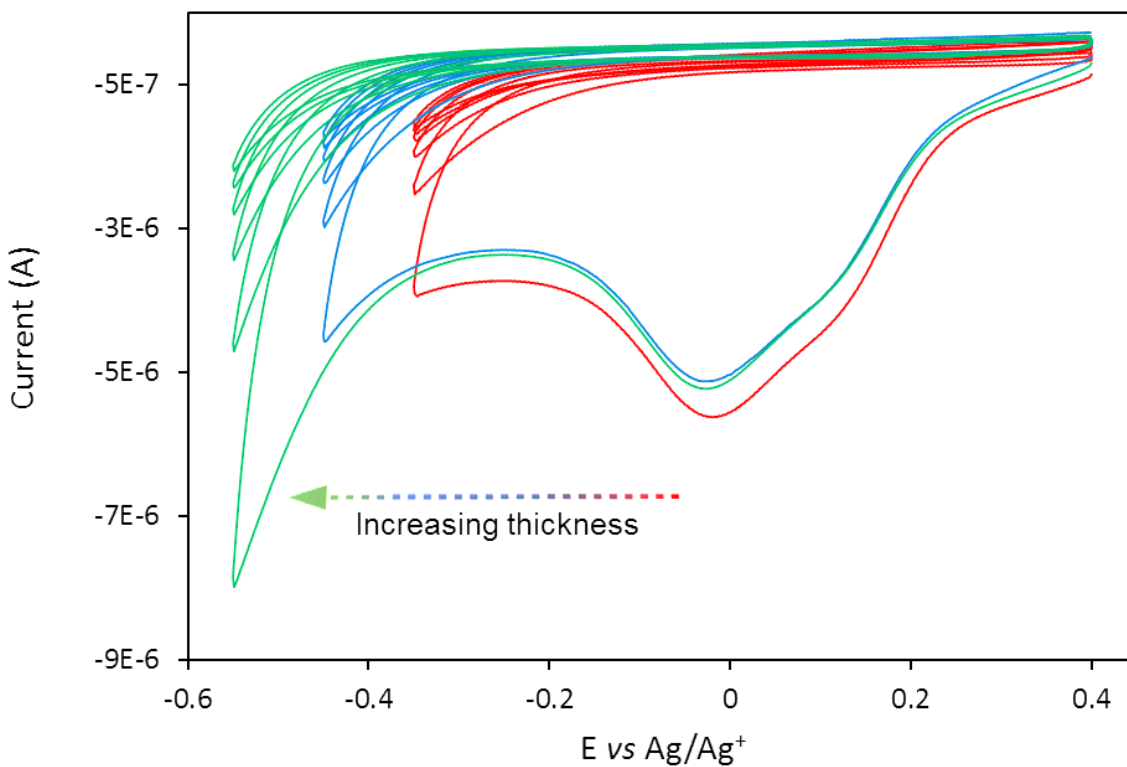


### 2.2.1.2.3 Cr/Au modification

The parameters used for grafting of molecular layer on the surface of Cr/Au electrode are listed in Table 2.3 and corresponding cyclic voltammograms are shown in Figure 2.3.

**Table 2.3** Anthraquinone grafting parameters on Cr<sub>3</sub>/Au<sub>15</sub> surfaces

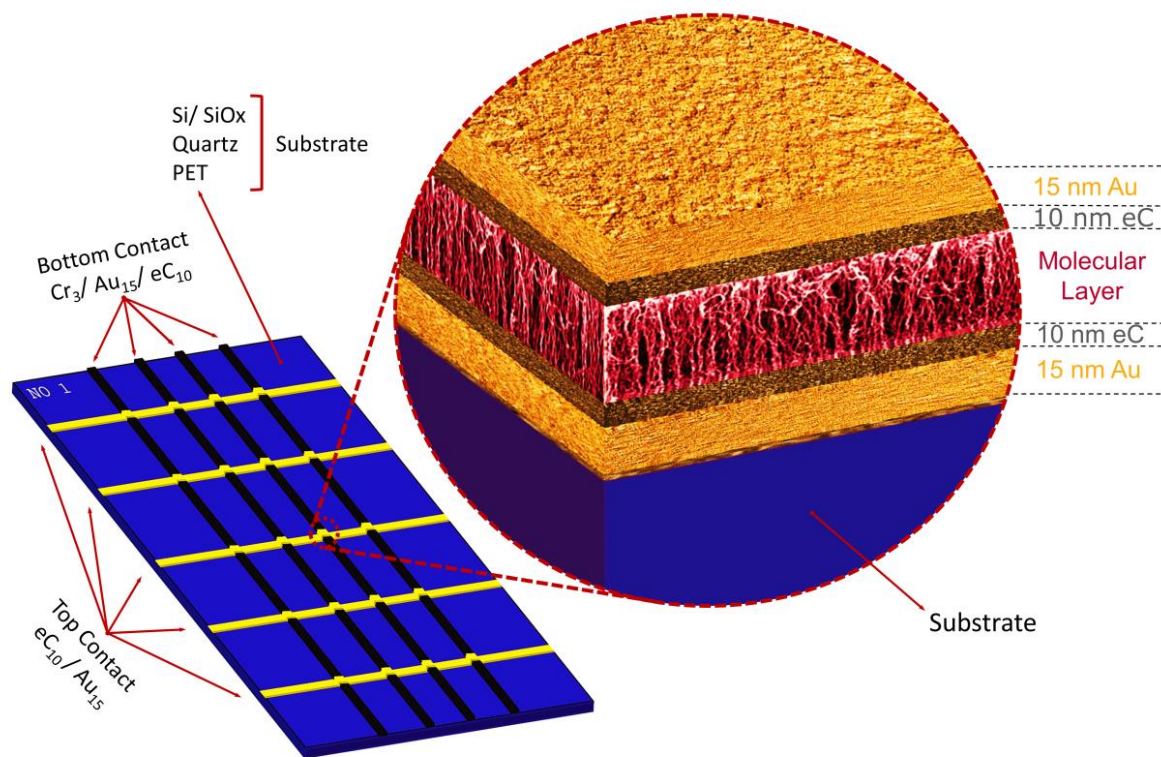
| Anthraquinone Grafting | Sweep range (E vs. Ag/Ag <sup>+</sup> ) | No. of cycles | Scan rate (mV/s) | Thickness (nm) |
|------------------------|---|---------------|------------------|----------------|
| Sample 1               | 0.4 – (-0.35)                           | 6             | 50               | 3.1 ± 0.42     |
| Sample 2               | 0.4 – (-0.45)                           | 6             | 50               | 4.2 ± 0.50     |
| Sample 3               | 0.4 – (-0.55)                           | 6             | 50               | 5.2 ± 0.53     |



**Figure 2.3** Cyclic voltammogram grafting of anthraquinone on the surface of Cr<sub>3</sub>/Au<sub>15</sub>.

### 2.2.1.3 Top contact deposition

The top contact electrode was comprised of electron beam deposition of 10 nm eC and 15 nm Au through a physical shadow mask with 0.25 mm openings oriented perpendicular to the bottom contact, which results in a crossbar junction of 250 in 250  $\mu\text{m}$ . Complete fabricated chip is shown schematically in Figure 2.4



**Figure 2.4** Schematic illustrations Au/eC/molecule/eC/Au molecular junctions using electron-beam deposited carbon adjacent to molecular layer. Each chip is 1.8 x 1.2 cm. Final dimension of each junction is 250 x 250  $\mu\text{m}$ .

### 2.2.2. Wafer scale lithography for eC junction

In addition to the crossbar geometry, an “integrated” format was fabricated with a lithographic lift-off process rather than shadow mask, in part to reduce contact resistance and

also provide a wider range of junction dimensions. It also provides electrical isolation of the junctions, a single, common contact for electrochemical surface modification, and probe contact pads of Au rather than eC. This procedure results in a “chip” of 25 molecular junctions, with the entire substrate protected by photoresist. Details of the fabrication are as follows:

**I.** 4” silicon (100) wafer substrates with 300 nm of thermally grown silicon oxide were used as the base substrates. Substrates were cleaned using a hot piranha solution (concentrated H<sub>2</sub>SO<sub>4</sub>:30% H<sub>2</sub>O<sub>2</sub>, 3:1 v/v) for 15 min and rinsed with deionized water before drying. A bilayer photoresist stack was spin-coated onto the wafers. First, LOR 0.7A resist (MicroChem) was spun on at 200 rpm for 10 seconds followed by 2000 rpm for 45 seconds. The wafer was then baked for 2 minutes on a hot plate for 170 °C. The top layer resist, HPR 504 (MicroChem), was spun on at 500rpm for 10 seconds followed by 400 rpm for 45 seconds and soft baked for 90 seconds at 115 °C on a hot plate. Wafers were allowed to rehydrate for 15 minutes before being patterned using a photomask and UV exposure. Exposed wafers were developed in MF-26A developer (Microposit) for approximately 40 seconds under gentle agitation until fully developed. Fully developed wafers were rinsed with deionized water and dried with nitrogen.

**II.** Patterned wafers are loaded into a Johnson Ultravac (JUV) e-beam deposition system for metal deposition of Cr<sub>4</sub>/Au<sub>30</sub>. The system is pumped down to a base pressure of 4x10<sup>-7</sup> torr prior to deposition. After the metal deposition, the chamber is vented and a shadow mask is aligned and attached to each individual wafer for the eC<sub>10</sub>. The JUV has pumped down again and the 10nm of e-beam carbon is evaporated. An addition coating of HPR 504, same parameters, is spun onto the wafers as a barrier layer to protect the samples

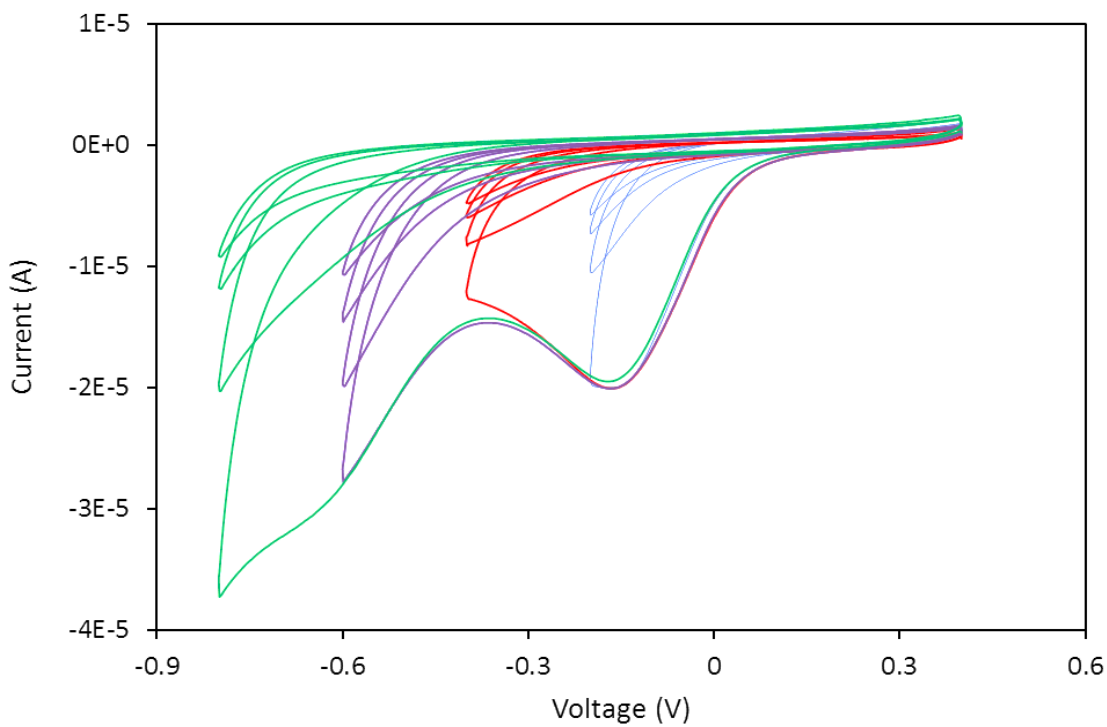
from the atmosphere and dicing saw residue. The wafers are diced using a Disco DAD 321 dicing saw into individual die chips of 13mm x 18.5mm which can be stored until use.

**III.** In order to prepare the chips for electrochemistry, diced chips are immersed in dimethyl sulfoxide (Fisher certified ACS) for 1 hour to lift-off the photoresist layers. The chips are held in either an upright position or device layer down depending on the holder to ensure that any metal or dicing particles coming off the sample during lift-off do not fall back onto the surface of the chips. Chips are then sonicated in fresh DMSO, DI water, and IPA for 10 minutes each as a final clean prior to electrochemistry.

**IV.** Electrochemical procedure for grafting of molecular layer was the same as described in section 2.2.1.2. Nitro-azobenzene (NAB) diazonium fluoroborate salt (1 mM) was used for grafting of the molecular layer. Grafting parameters are listed in Table 2.4 and corresponding cycling voltammetry is shown in Figure 2.5.

**Table 2.4** Electrochemical grafting parameters for NAB on integrated chips

| NAB Grafting | Sweep range<br>(E vs. Ag/Ag <sup>+</sup> ) | No. of cycles | Scan rate<br>(mV/s) | Thickness<br>(nm) |
|--------------|--|---------------|---------------------|-------------------|
| Sample 1     | 0.4 – (-0.20)                              | 4             | 100                 | 3.6 ± 0.24        |
| Sample 2     | 0.4 – (-0.40)                              | 4             | 100                 | 4.1 ± 0.29        |
| Sample 3     | 0.4 – (-0.60)                              | 4             | 100                 | 4.8 ± 0.31        |
| Sample 4     | 0.4 – (-0.80)                              | 4             | 100                 | 6.2 ± 0.43        |



**Figure 2.5** Cyclic voltammograms for grafting different thicknesses of Nitro-azobenzene (NAB) on the surface of integrated  $\text{Cr}_4/\text{Au}_{30}/\text{eC}_{10}$  chips in acetonitrile solution of 1 mM NAB and 0.1 M TBAPF<sub>6</sub>.

V. The procedure for top contact deposition was the same as described in Section 2.2.1.3, except the Au thickness was increased to 20 nm since transparency was not required.

Yields and relative standard deviations for the four examples are listed in Table 2.5.

**Table 2.5** Statistics of integrated Cr<sub>4</sub>/Au<sub>30</sub>/eC<sub>10</sub>/NAB/eC<sub>10</sub>/Au<sub>20</sub> junctions

| NAB Thickness (nm) | Yield | Voltage (V) | Mean J @ V (A/cm <sup>2</sup> ) | Standard deviation of J | RSD (%) |
|--------------------|-------|-------------|---------------------------------|-------------------------|---------|
| 3.6±0.24           | 6/6   | 0.4         | 2.1                             | 0.19                    | 9       |
| 4.1±0.29           | 6/6   | 0.9         | 2.3                             | 0.3                     | 14      |
| 4.8±0.31           | 8/8   | 1.3         | 2.7                             | 0.6                     | 22      |
| 6.2±0.43           | 8/8   | 2           | 2.3                             | 0.15                    | 6       |

a. yield indicates the number of the junction with no evidence of direct eC/eC contact (a “short”)

### 2.2.3 Electrical and optical apparatus

Current–voltage (*IV*) curves were obtained using a Keithley 2602A source-measurement unit or a custom-built LabVIEW measurement system that has been described previously<sup>137</sup>. *IV* curves were obtained in 4-wire mode unless indicated otherwise. UV-Vis absorption spectra were obtained with a Perkin Elmer Lambda 1050 dual beam spectrometer. XPS analyses were acquired with an AXIS 165 spectrometer equipped with a monochromatic Al K $\alpha$  source (1486.6 eV), a custom-built spectrometer consisting of an Ar<sup>+</sup> ion laser (514.5 nm), a 50 mm f/1.8 collection lens, a holographic reflection grating (2000 grove/mm), and an Andor back-thinned CCD detector cooled to -80° C was used to acquire the spectra<sup>139</sup>. Raman shift was calibrated with naphthalene and polystyrene.

## 2.3 RESULTS AND DISCUSSION

### 2.3.1 Characterization of eC electrode

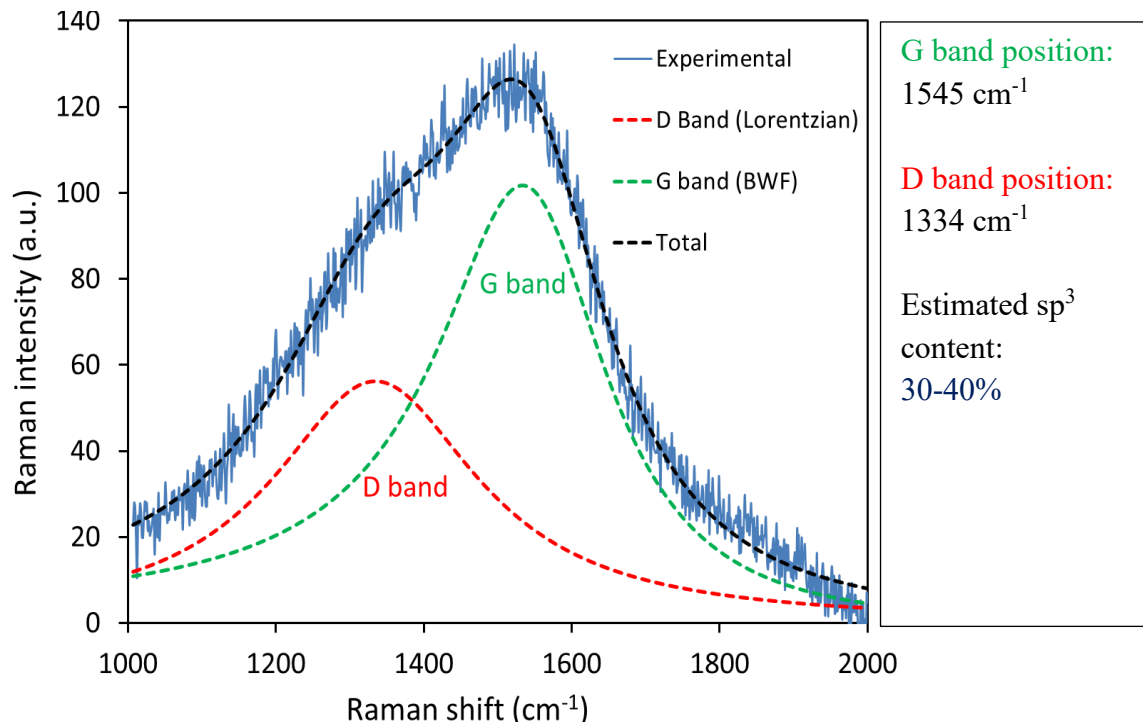
#### 2.3.1.1 Spectroscopic characterization of eC electrode

eC is presumably formed by carbon atoms and clusters striking a solid surface and rapidly forming a variety of bonds to adjacent particles, thus forming an amorphous mixture of  $sp^1$ ,  $sp^2$  and  $sp^3$  hybridization. Although the detailed structure of eC is both complex and disordered, Raman spectroscopy and X-ray photoelectron spectroscopy (XPS) provide estimates of  $sp^3$  content and Ultraviolet Photoelectron Spectrum (UPS) provides estimate for work function and Fermi-level ( $E_F$ ).

##### 2.3.1.1.1 Estimation of $sp^3$ content with Raman spectroscopy

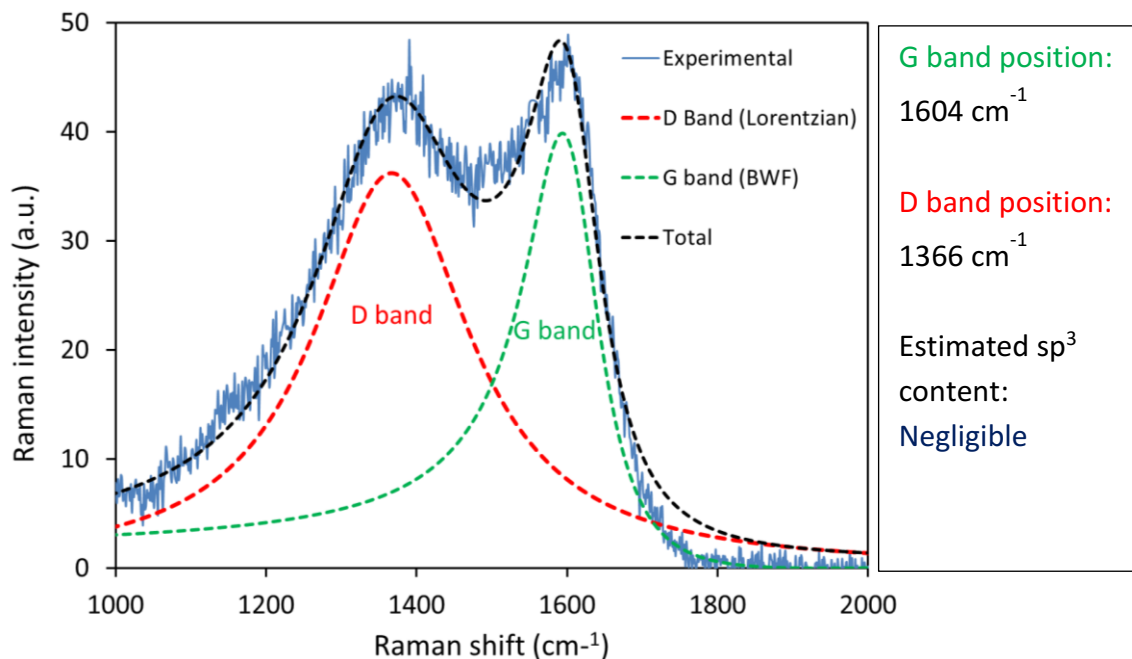
Interpretation of Raman spectra of amorphous carbon to determine hybridization and bonding geometry has been described<sup>140, 141</sup>. Raman spectra of e-beam carbon on silicon have been presented previously,<sup>136</sup> and show a broad peak from  $\sim 1000$  to  $\sim 1600$   $cm^{-1}$ , in the region of the  $sp^2$  carbon bands, indicating a very disordered structure. Pyrolysis at 1000 °C led to observable “D” and “G” bands at  $\sim 1360$   $cm^{-1}$  and  $\sim 1600$   $cm^{-1}$ , similar in position to the bands observed for PPF. In the current experiments, As suggested in the literature, Breit-Wigner-Fano (BWF) fitting for the G peak and a Lorentzian for the D peak results in the excellent deconvolution for all carbon Raman with low residuals<sup>141</sup>. The relative positions of the D and G bands following deconvolution were used to estimate the % $sp^3$  content according to the procedure of Ferrari and Robertson<sup>141</sup>. Raman spectra and deconvolutions of spectra to D and G peaks of different type of carbon are shown in Figure 2.6-2.9, including the estimated  $sp^3$  content indicated for each case. Several reports have described the deconvolution of the

broad carbon bands into D and G components, and the relationship of their positions and intensities to the  $sp^3/sp^2$  ratio of the carbon film<sup>140, 141</sup>. The as-deposited eC is estimated to be 30-40%  $sp^3$  hybridized carbon, with the remainder  $sp^2$ , but the  $sp^3$  content becomes negligible after annealing at 1000 °C (Figure 2.7). The same analysis applied to PPF and glassy carbon yield negligible  $sp^3$  content (Figure 2.8 and 2.9).

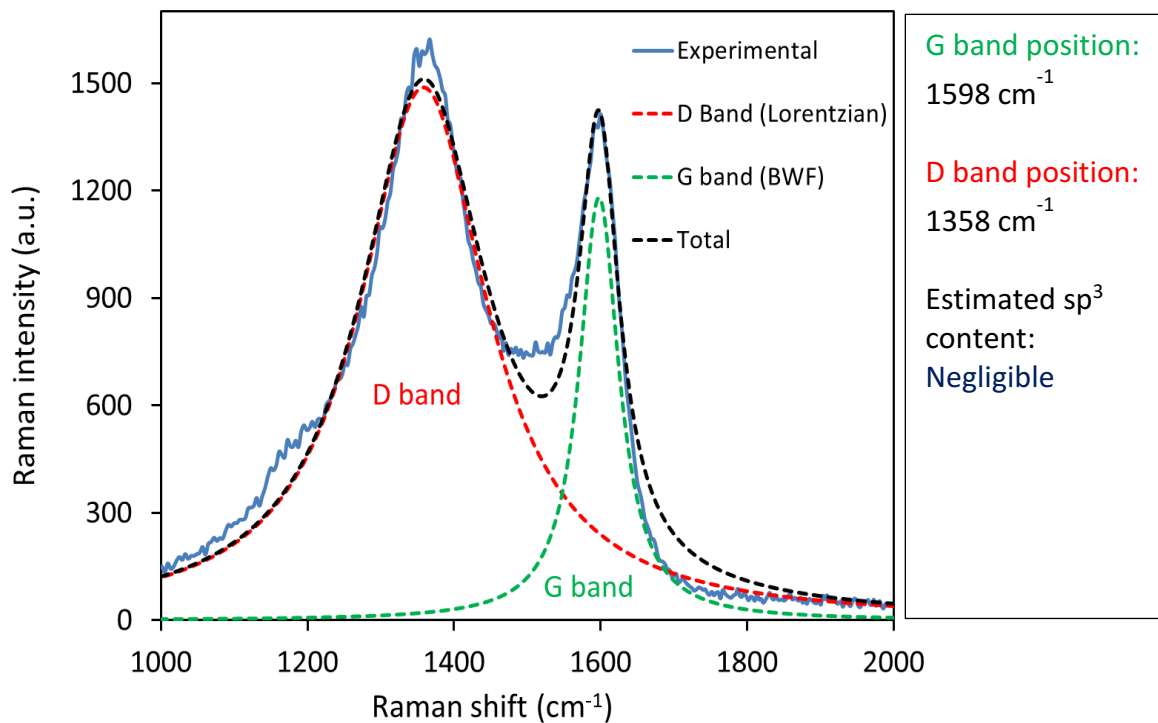


**Figure 2.6** Raman spectrum of electron-beam deposited carbon (eC).

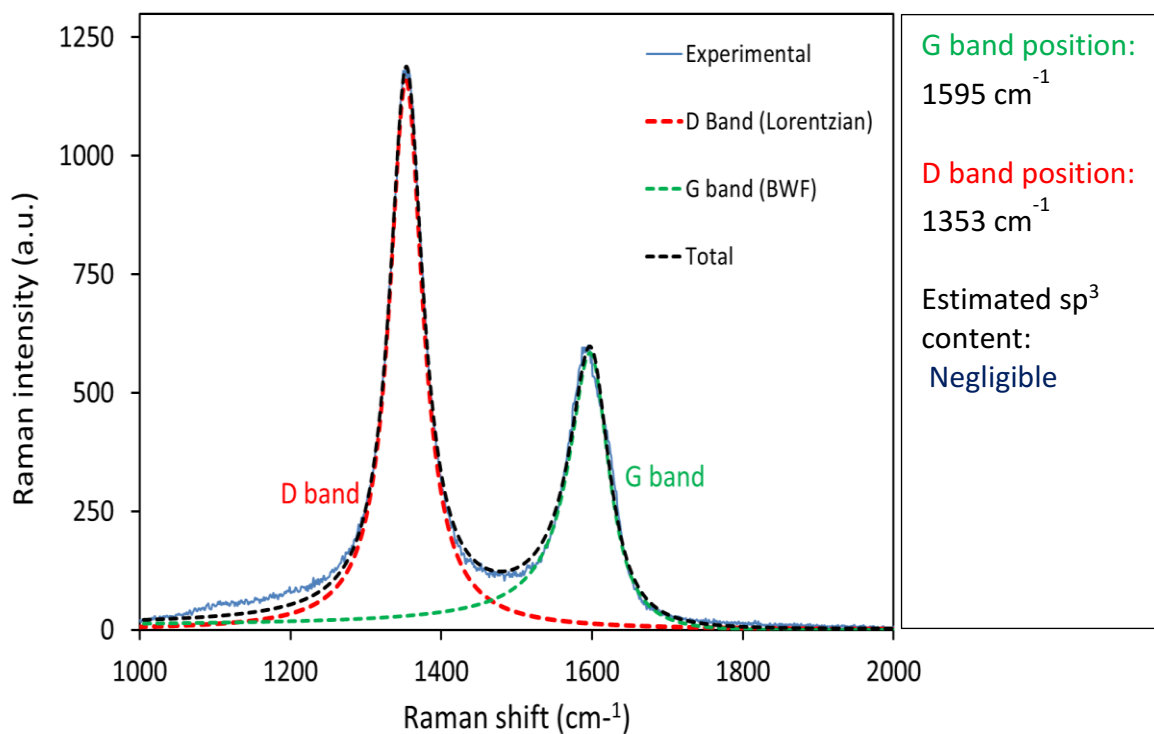




**Figure 2.7** Raman spectra of eC after 3 Hours annealing at 1000 °C in forming gas



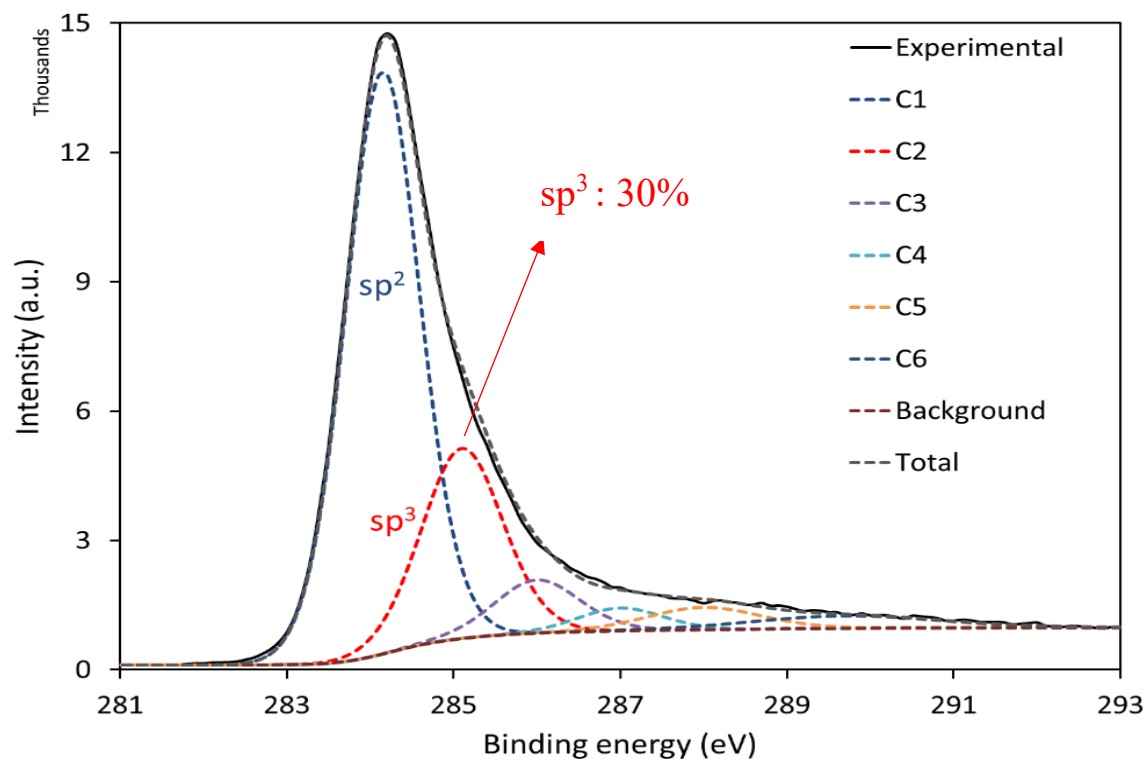
**Figure 2.8** Raman spectra of pyrolyzed photoresist (PPF).



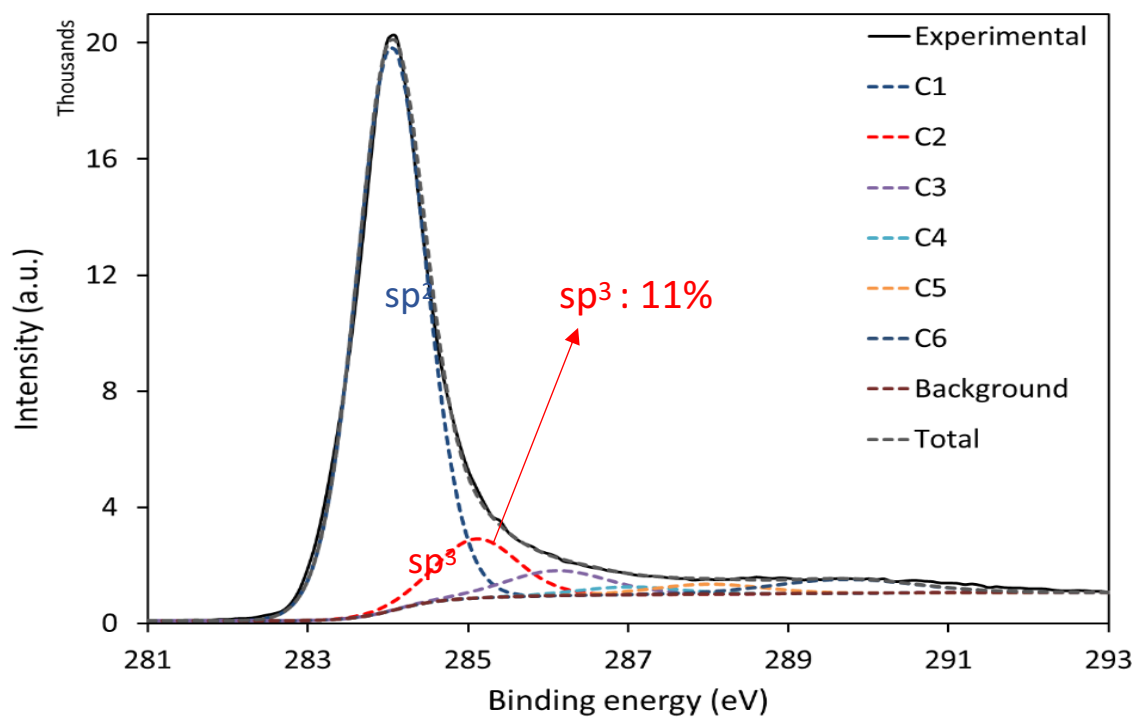
**Figure 2.9** Raman spectra of glassy carbon (GC).

### 2.3.1.1.2 Estimation of sp<sup>3</sup> content with XPS spectroscopy

X-ray photoelectron spectroscopy (XPS) has also been used to estimate the sp<sup>3</sup>/sp<sup>2</sup> content of disordered carbon materials, based on relative intensities of components of the C<sub>1s</sub> band<sup>142, 143</sup>. XPS spectra of the C<sub>1s</sub> region for eC is shown in Figure 2.10, and the sp<sup>3</sup> content indicated by the XPS is 30% for as-deposited eC, which decreases to 11% upon annealing (Figure 2.11). Although the sp<sup>3</sup> percentages from XPS and Raman should be considered approximate, they clearly indicate significant sp<sup>3</sup> content in as-deposited eC, which is distinct from that of PPF or annealed eC.



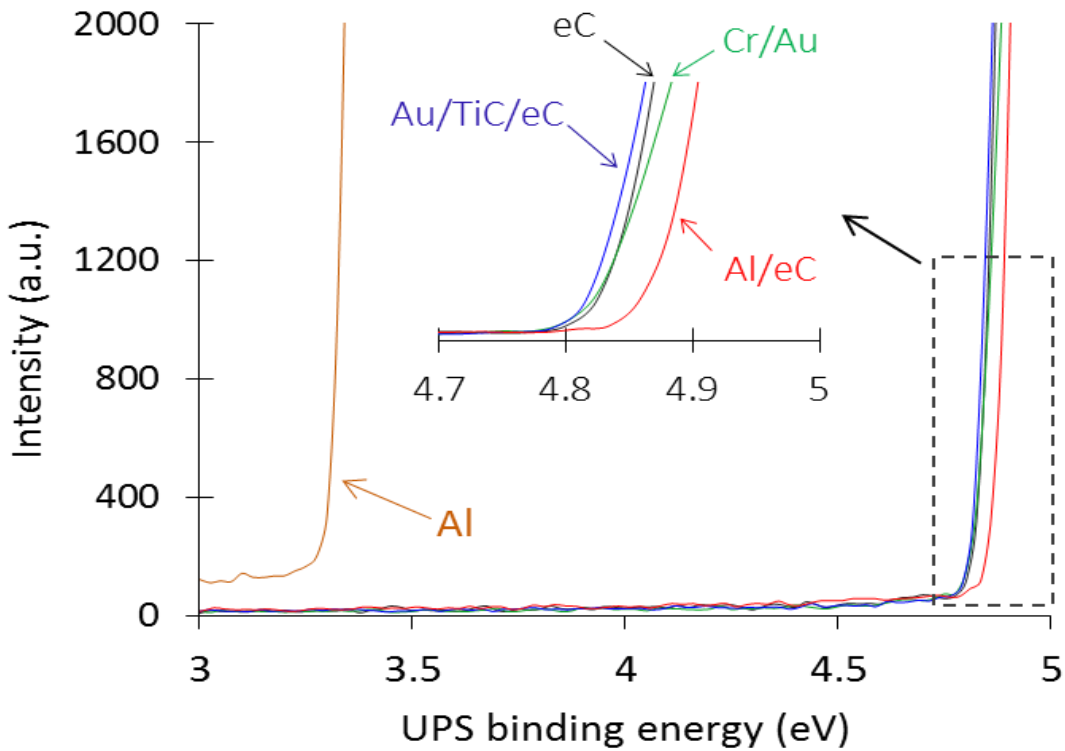
**Figure 2.10** XPS C 1s region of electron beam deposited carbon (eC).



**Figure 2.11** XPS C 1s region of eC after 3 hours annealing at 1000 °C.

### 2.3.1.1.3 Work function estimation by Ultraviolet Photoelectron Spectrum (UPS)

Figure 2.12 shows UPS spectra of eC<sub>10</sub> alone, Cr<sub>3</sub>/Au<sub>30</sub> and Cr<sub>3</sub>/Au<sub>30</sub>/TiC<sub>3</sub>/eC<sub>10</sub> (all on Si/SiOx), from which the onset of photoemission at ~4.8 eV indicates the work function (WF) of the surface. TiC is used as an adhesion layer between eC and Au, which eliminate occasional delamination of eC in long time of ultra-sonication and electrochemistry. The onset binding energies are within experimental error ( $\pm 0.1$  eV) for these three surfaces, indicating that the WF of the top eC<sub>10</sub> layer is not significantly altered by the underlying metal or TiC layer. In addition, aluminum was examined due to its much lower WF compared to Au or eC. Bare Al exhibits a WF of 3.3 eV by UPS, while the Al<sub>40</sub>/eC<sub>10</sub> surface is very similar to the other eC terminated surfaces, at ~4.8 eV. The absence of observable photoemission at 3.3 eV for Al/eC is also an indication that negligible bare Al remains on the Al/eC surface, and therefore that eC coverage of the underlying surface is complete by this measure.



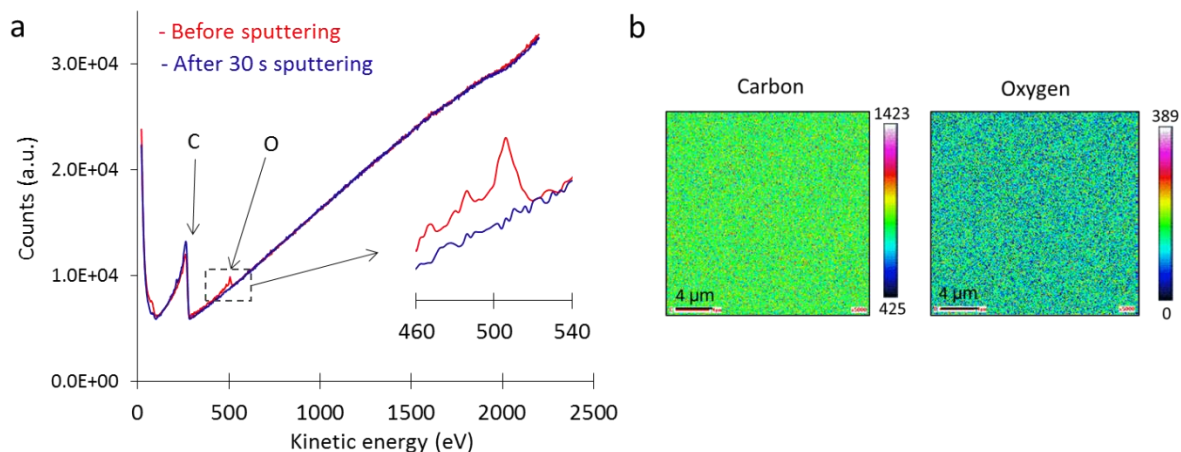
**Figure 2.12** UPS spectra of eC, Al, Al/eC, Cr/Au and Au/TiC/eC surfaces. The substrate for all cases was Si/SiO<sub>x</sub>.

### 2.3.1.2 Surface coverage of eC layer

#### 2.3.1.2.1 Auger survey and elemental mapping

An Auger electron spectrum for the Cr<sub>3</sub>/Au<sub>30</sub>/TiC<sub>3</sub>/eC<sub>10</sub> surface is shown in Figure 2.13a, with the peak at 250 – 300 eV feature corresponding to carbon and the ~500 eV peak to surface oxygen. The removal of the ~500 eV band by Ar<sup>+</sup> sputtering indicates that the oxygen content is superficial, and not detectable below the eC surface. Figure 2.13b shows Auger emission maps for the initial Cr<sub>3</sub>/Au<sub>30</sub>/TiC<sub>3</sub>/eC<sub>10</sub> surface, showing an even distribution of both carbon and oxygen across the electrode surface. Neither Au nor Ti was detectable in

the Auger survey scans (Figure 2.13a) or with elemental mapping (Figure 2.13b), consistent with the absence of pinholes in the eC film detectable by Auger spectroscopy.

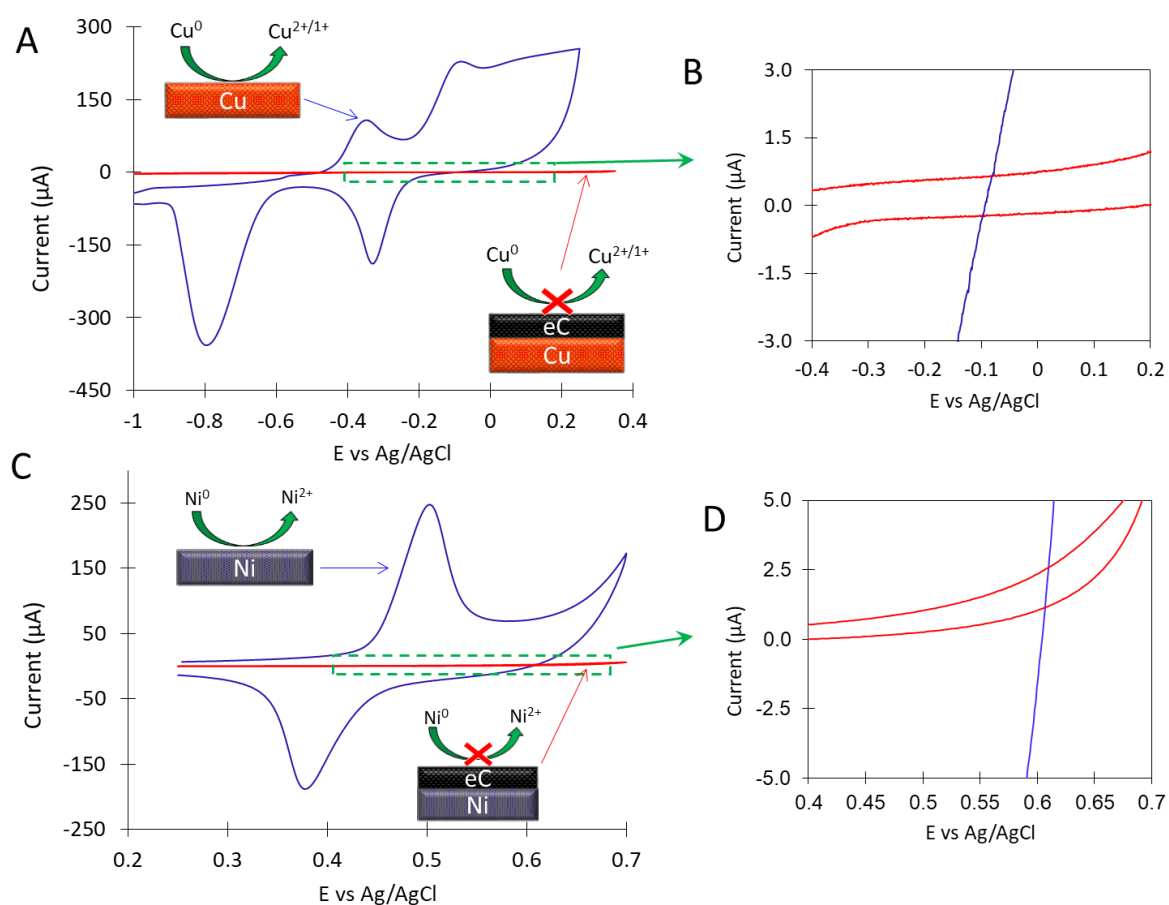


**Figure 2.13 (a)** Auger electron spectra of Si/SiO<sub>x</sub>/Cr<sub>3</sub>/Au<sub>30</sub>/TiC<sub>3</sub>/eC<sub>10</sub> before and after 30 second sputtering. The inset is the magnification of the oxygen peak at 505 eV. **(b)** Auger surface mapping of selected peak of oxygen at 505 eV and carbon at 260 eV for the surface of Au<sub>30</sub>/TiC<sub>3</sub>/eC<sub>10</sub> without sputtering. Ti and Au are undetectable by either a survey scan or elemental maps.

### 2.3.1.2.2 Surface coverage evaluation by electrochemistry

Although the absence of Au or Ti responses in the Auger spectra implies good surface coverage with low pinhole density, the possibility of exposure of the metal underlying eC was examined further. Coverage of graphene on metal electrodes has been assessed by attempting to oxidize Cu or Ni electrodes underneath single or multilayer graphene.<sup>144-147</sup> Figure 2.14A (blue curve) shows voltammetry of an unmodified Cu electrode in 0.1 M NaOH electrolyte, exhibiting prominent features characteristic of Cu corrosion and redeposition. A Cu electrode with 10 nm of eC (*i.e.* Si/SiO<sub>x</sub>/Cr<sub>4</sub>/Cu<sub>40</sub>/eC<sub>10</sub>) in the same electrolyte yielded the red voltammogram in Figure 2.14a, with the dotted region expanded in Figure 2.14b. No features for Cu redox activity are evident with the eC modified electrode,

and the current for the first oxidation peak at  $E = -0.33\text{ V}$  is a factor of  $>2000$  smaller than that on the bare Cu electrode. The blockage of metal oxidation by  $eC_{10}$  is similar for a Ni electrode, shown in Figure 2.14c and d, with no observable redox features apparent for the Ni/ $eC_{10}$  electrode in 0.1 M NaOH.

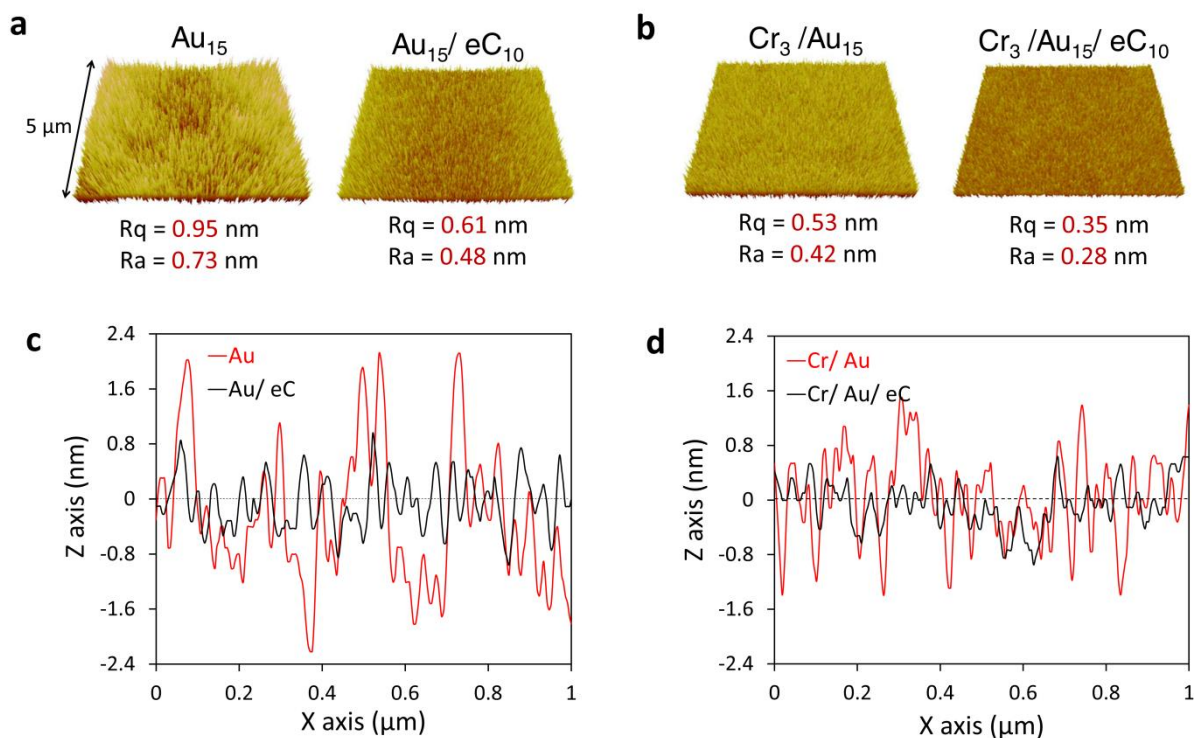


**Figure 2.14** (a) CV for the Si/SiOx/Cr<sub>3</sub>/Cu<sub>40</sub> and Si/SiOx/Cr<sub>3</sub>/Cu<sub>40</sub>/TiC<sub>3</sub>/eC<sub>10</sub> surface in alkaline solution (NaOH 0.1M) at 0.1 V/s. (b) Magnification of voltammograms shown in panel A for the region of Cu oxidation. (c) CV obtained for Si/SiOx/Cr<sub>3</sub>/Ni<sub>30</sub> and Si/SiOx/Cr<sub>3</sub>/Ni<sub>30</sub>/TiC<sub>3</sub>/eC<sub>10</sub> in alkaline solution (NaOH 0.1M) at 0.1 V/sec. (d) Magnification of voltammograms shown in panel C for the region of Ni oxidation. The area of the exposed electrode was 0.28 cm<sup>2</sup> for all cases.

### 2.3.1.3 Surface roughness of eC electrode

As the feature size of the active component decreases, factors such as electromigration, surface roughness, film uniformity and stability of electrodes begin to limit device performance.<sup>148-150</sup> Experience with numerous MJs having molecular layers of 1-5 nm thickness indicates that substrate roughness should be less than 0.5 nm rms (by AFM); e.g. the PPF used in previous reports<sup>58, 112, 130, 138, 151</sup> and in commercial devices<sup>111</sup> ranged from 0.4 to 0.5 nm rms. Figure 2.15 shows AFM images and line scans of various films deposited on Si/SiOx (300 nm) with an initial roughness of 0.15 nm rms. E-beam deposition of Au directly onto Si/SiOx forms the well-known island film with high rms roughness ( $R_q$ ) of 0.95 nm, and peak-to-peak variation ( $R_{pp}$ ) often exceeding  $\pm 4$  nm. Deposition of 10 nm of eC on top of this rough Au surface results in the smoother surface of Figure 2.15a, with  $R_q = 0.61$  nm and  $R_{pp}$  of approximately  $\pm 1.5$  nm. The decrease in roughness was unexpected, since the low likelihood of carbon diffusion and island formation should track the underlying surface. The commonly used technique of applying a chromium adhesion layer to reduce roughness is shown in Figure 2.15b, with the resulting Cr<sub>3</sub>/Au<sub>15</sub> film having  $R_q = 0.53$  nm. eC deposition on this surface also reduces roughness (Figure 2.15d) to  $R_q = 0.35$  nm [note that subscripts on layer identities indicate layer thickness in nm, e.g. Au<sub>15</sub>.] The roughness decrease is very consistent, and valuable for subsequent fabrication of MJs, with one possible origin of the effect being rapid formation of covalent bonds between incoming carbon atoms and clusters forming a “superlayer” which bridges defects or grain boundaries in the underlying metal.





**Figure 2.15** (a) AFM images of e-beam deposited Au and Au/eC surfaces on Si/SiO<sub>x</sub> substrate. Subscripts indicate thicknesses of each deposited layer in nm. Ra and Rq are average and root mean square roughness, respectively. (b) AFM images of the surface of e-beam deposited Cr/Au and Cr/Au/eC surfaces on Si/SiO<sub>x</sub> substrate. (c) AFM line scan profiles of surfaces shown in panel (a). (d) AFM line scan profiles of surfaces shown in panel (b).

### 2.3.1.4 Sheet resistance of eC electrode

The resistivity of PPF is in the range of 0.003 to 0.006 Ω-cm for pyrolysis at 1100 °C, although this value varies significantly with film thickness and thermal history.<sup>151-154</sup> It is similar to the 0.005 Ω-cm reported for glassy carbon, consistent with a glassy, sp<sup>2</sup> carbon material. An early report on eC deposited on quartz reported a sheet resistance of 2000 – 5000 Ω/square for a 300 nm film, corresponding to a resistivity of 0.06 to 0.15 Ω-cm.<sup>134</sup> Four-point probe measurements were carried out on eC films deposited directly on quartz

yield the results shown in Table 2.6, which are averages of five measurements across a “blanket” eC film for each thickness. Ten to thirty nm thick eC films have sheet resistances of  $10^4 - 10^5 \Omega/\square$ , yielding resistivities of 0.03 to 0.16  $\Omega\text{-cm}$ , similar to that reported for the 300 nm thick film.<sup>134</sup> The low conductivity of eC can result in significant ohmic losses in thin films, with a 10 nm film of a 0.05 x 1 cm strip having a predicted resistance of  $\sim 3 \text{ M}\Omega$ . However, we showed previously that since the current in a MJ passes through the short dimension of the eC film (*i.e.* 10 nm), its contribution to resistance is negligible, and the  $JV$  responses of PPF/NAB/eC/Au MJs were indistinguishable for eC thicknesses of 2 to 30 nm (NAB=nitroazobenzene).<sup>138</sup> In order to use eC as a substrate, it was deposited onto a  $\text{Cr}_3/\text{Au}_{15}$  film, without breaking vacuum. The sheet resistances of various Au/eC bilayers listed in Table 2.6 are 1-3  $\Omega/\square$ , compared to  $>10^4 \Omega/\square$  for eC alone, reducing the resistance predicted for a 0.05 x 1 cm strip from 3  $\text{M}\Omega$  for  $\text{eC}_{10}$  alone to 60  $\Omega$  for a  $\text{Au}_{15}/\text{eC}_{10}$  bilayer. The Au carries most of the current in the lateral directions of the Au/eC film, and the  $\text{eC}_{10}$  resistance in series with the molecular layer is less than 0.3  $\text{m}\Omega$  for a 250 x 250  $\mu\text{m}$  molecular junction. The higher conductivity of Au/eC films compared to PPF eliminates most of the ohmic potential error when acquiring  $JV$  curves in 2-wire mode, as shown Figure 2.19. In addition, we will show below that the  $\text{Cr}_3/\text{Au}_{15}/\text{eC}_{10}$  films are excellent substrates for molecular junction fabrication, are partially optically transparent and can be patterned lithographically.

**Table 2.6** 4-Point probe resistances of eC and Au films on Quartz (Q) and SiOx

|   | Sheet resistance<br>(ohm/□) | Resistivity<br>(ohm-cm) |
|---|-----------------------------|-------------------------|
| Q/eC <sub>3</sub> <sup>(a)</sup>                            | 1.04E+09                    | 312                     |
| Q/eC <sub>10</sub>  | 167400                      | 0.167                   |
| Q/eC <sub>20</sub>  | 19940                       | 0.040                   |
| Q/eC <sub>30</sub>  | 11310                       | 0.034                   |
| mean(10-30 nm)  | -                           | 0.080                   |
| Q/Cr <sub>4</sub> /Au <sub>15</sub> /eC <sub>10</sub>       | 2.98                        | -                       |
| Q/Cr <sub>4</sub> /Au <sub>30</sub> /eC <sub>10</sub>       | 1.03                        | -                       |
| Si/SiOx/Cr <sub>4</sub> /Au <sub>30</sub> /eC <sub>10</sub> | 1.05                        | -                       |
| PPF (1000 nm) <sup>39</sup>                                 | 51                          | 0.005                   |
| eC (310 nm) <sup>31</sup>                                   | 44000                       | 0.136                   |
| OTPPF <sup>b</sup> (40 nm) <sup>29</sup>                    | 500                         | 0.002                   |

a. subscripts denote layer thicknesses in nm

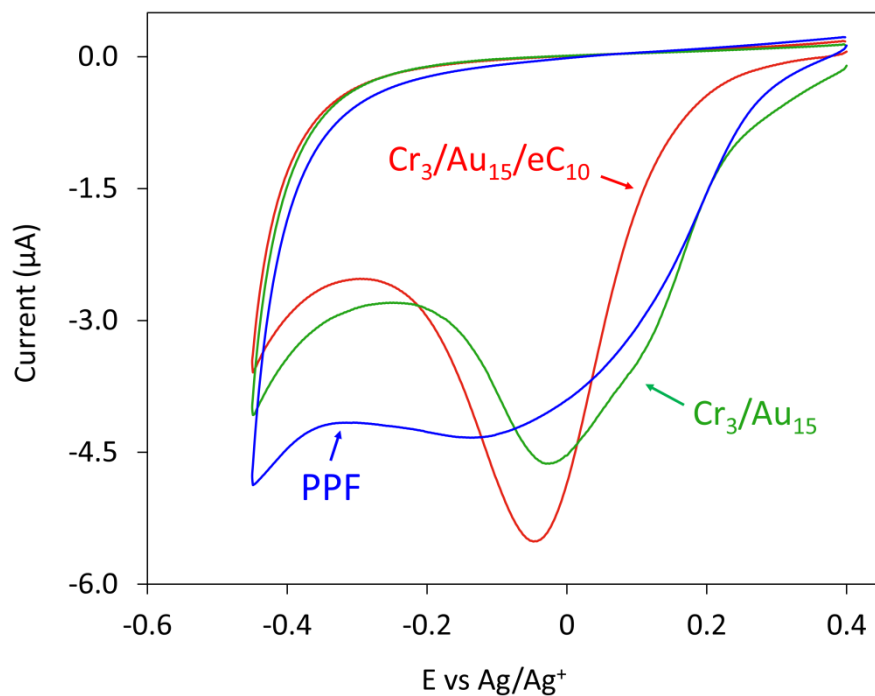
b. optically transparent PPF

### 2.3.2 Molecular layer grafting on eC electrode

The eC resembles various “diamond like carbon” materials<sup>155-159</sup> and sputtered carbon films<sup>160, 161</sup> in this respect, although the microstructure and specific bonding geometries may be different. Note that eC is near the disordered extreme for carbon materials compared to fullerenes, diamond, and graphite, and is likely isotropic in its structure and properties. The important properties of eC for MJ fabrication are flatness, sufficient conductivity, stability,

substrate adhesion, ability to modify the eC surface with covalent C-C bonds to molecular layers, and suitability for lithographic patterning, as described below.

Voltammetric curves for reduction of 2-anthraquinone (AQ) diazonium reagent are compared in Figure 2.16 for PPF, Au, and eC, in acetonitrile in all cases. The reduction peak corresponds to formation of a phenyl radical which binds to the surface as a mono- or multilayer. The shape and peak potential of the reduction wave on PPF vary for different diazonium precursors, but in all cases studied to date, the reduction peaks are better defined on Au/eC than on PPF. The lower resistance of the Au/eC contact avoids ohmic potential error, and the greater structural disorder of eC likely has more nucleation sites for phenyl radical attachment. As will be described next, well defined electrochemical layer formation also contributes to high junction reliability.

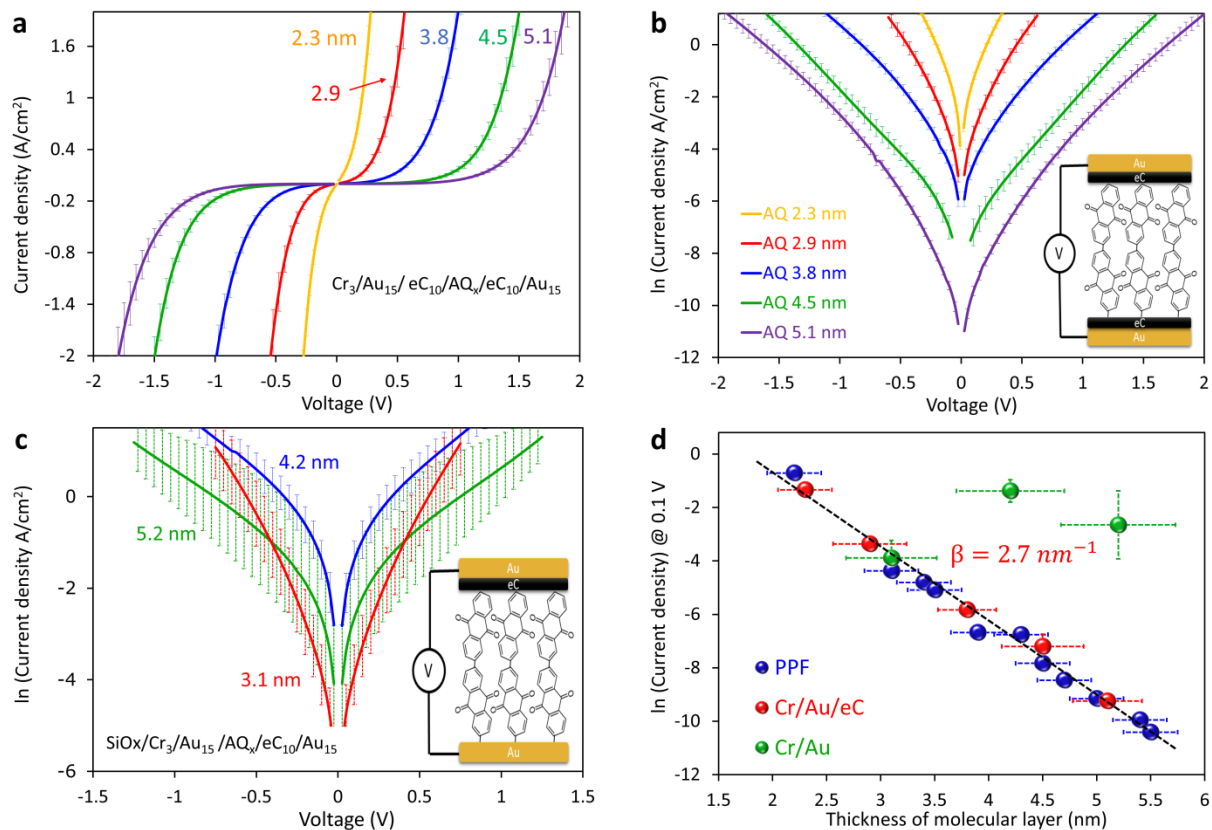


**Figure 2.16** Cyclic voltammograms of Anthraquinone diazonium solution on PPF, Cr/Au, and Cr/Au/eC surfaces. The solution was contained 1 mM AQ diazonium fluoroborate in acetonitrile with 0.1 M tetrabutylammonium hexafluorophosphate (TBAPF<sub>6</sub>) as supporting electrolyte, and scan rate was 50 mV/s for all cases. Detailed grafting conditions and cyclic voltammograms are shown in section 2.2.1.2.

### 2.3.3 Electronic behavior of eC/molecule/eC junctions

Current-density vs bias voltage ( $JV$ ) curves for five thicknesses of AQ in Si/SiO<sub>x</sub>/Cr<sub>3</sub>/Au<sub>15</sub>/eC<sub>10</sub>/AQ<sub>x</sub>/eC<sub>10</sub>/Au<sub>15</sub> molecular junctions are shown in Figure 2.17, on both linear (panel a) and semi-logarithmic scales (panel b). The yield (# of MJs not shorted) for all junctions fabricated with eC is 100% and the standard deviations of current density are shown in Figure 2.17 as error bars. Vapor deposited Au has been used successfully for ensemble MJ fabrication,<sup>116, 117, 162</sup> but in most cases requires template stripping to provide a sufficiently flat substrate surface.<sup>44, 47, 114, 163-167</sup> Figure 2.17c shows results from junctions

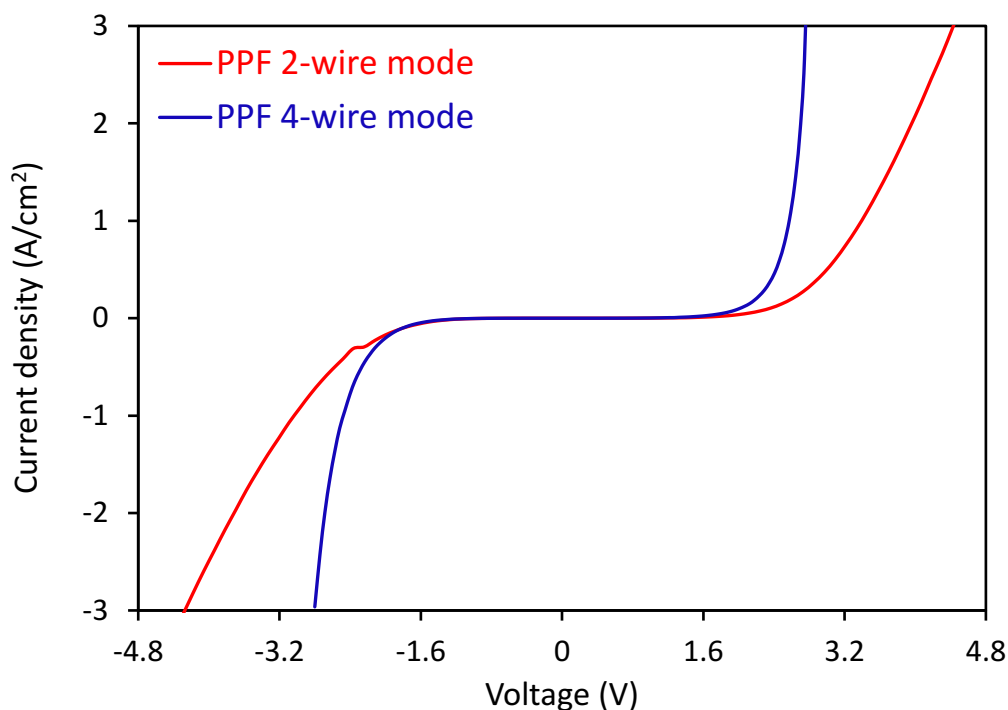
fabricated with an identical procedure to that for Figure 2.17a, but omitting the substrate eC layer to yield Cr<sub>3</sub>/Au<sub>15</sub>/AQ<sub>x</sub>/eC<sub>10</sub>/Au<sub>15</sub>. For the e-beam deposited Au substrate without the additional eC layer, the yield was low (> 50% “shorts”) and reproducibility of non-shortcd devices was poor. The variability of current density was large enough to obscure the effect of AQ thickness, as evident from comparison of the 3 nm and 5.3 nm cases. A more complete test of the effect of thickness on  $JV$  behavior is shown in Figure 2.17d, which plots  $\ln(J)$  at  $V = 0.1$  V vs AQ layer thickness for three different substrates. The slope of such plots yields the attenuation coefficient  $\beta$ , which is widely used to compare the thickness dependences of molecular tunnel junctions.<sup>46, 168-170</sup> The slope and intercept of the  $\beta$  plot for PPF (Figure 2.17d) are  $-2.8 \pm 0.13$  and  $4.7 \pm 0.55$  respectively. The slope and intercept of the same plot for Au/eC are  $-2.7 \pm 0.12$  and  $4.7 \pm 0.47$ . These results from PPF and Au/eC electrode are statistically indistinguishable, and comparable to the  $-2.7 \pm 0.6$  nm<sup>-1</sup> slope observed for eight aromatic MJs in PPF/molecule/Cu devices.<sup>58</sup>  $J$  values for the Au substrate lacking the eC<sub>10</sub> layer deviated greatly from the line in Figure 2.17d, and exhibited the high standard deviations apparent in Figure 2.17c.



**Figure 2.17** (a) Current density vs bias voltage ( $JV$ ) curves for junctions fabricated by Cr/Au/eC electrode as bottom contact, determined with a Keithley 2602A sourcemeter. AFM thicknesses of anthraquinone molecular layer are indicated in nm. Yield for tested junctions was 100% (non-shorted junctions) and error bars represent  $\pm$  standard deviation for 8 junctions of each thickness. (b) Semi-logarithmic scale of  $JV$  curves shown in panel (a). Right side inset: schematics of tested junctions (Cr layer under the Au is not shown in schematics). (c) Semi-logarithmic scale of  $JV$  curves for junctions fabricated by Cr/Au electrode as a bottom contact. Yield for tested junction was lower than 50% (non-shorted) and error bars represent  $\pm$  standard deviation for non-shorted junctions. (d) Corresponding attenuation plot at 0.1 V for different bottom electrodes.  $\beta$  is the slope of observed for  $SiO_x/Au_{15}/eC_{10}/AQ_x/eC_{10}/Au_{15}$  devices.

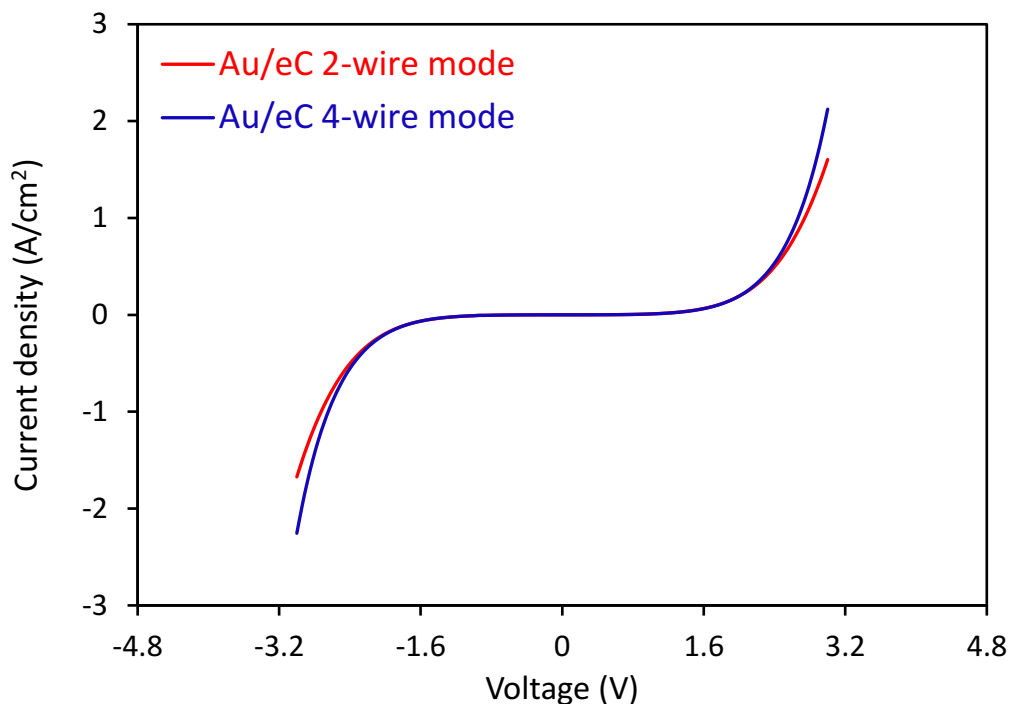
### 2.3.3.1 Comparison of two- and four-wire mode measurements

Four-wire mode measurement can be used to compensate contact resistance and internal ohmic losses in the PPF or eC films; however, many laboratory and practical applications use a two-wire geometry. Two- and four-wire mode measurements for molecular junctions made with PPF and Cr/Au/eC substrate electrodes are compared in Figure 2.18 and 2.19, respectively. In the case of PPF, the relatively high resistance of the PPF substrate distorts the 2-wire measurement due to ohmic potential losses (Figure 2.18). Since the sheet resistance of Au/eC is at least a factor of ten lower than that of PPF (Table 2.6), much less distortion is observed (Fig. 2.19). The small error apparent in Figure 2.19 is likely due to the contact resistance between the tungsten probes and the Au contact points or the residual resistance of the Au<sub>30</sub> film, and is completely compensated using 4-wire geometry.



**Figure 2.18** Comparison of two- and four-wire mode measurement for PPF/ NAB /eC<sub>10</sub>/Au<sub>20</sub>.





**Figure 2.19** Comparison of two- and four-wire mode measurement for  $\text{Cr}_3/\text{Au}_{30}/\text{eC}_{10}/\text{NAB}/\text{eC}_{10}/\text{Au}_{20}$ .

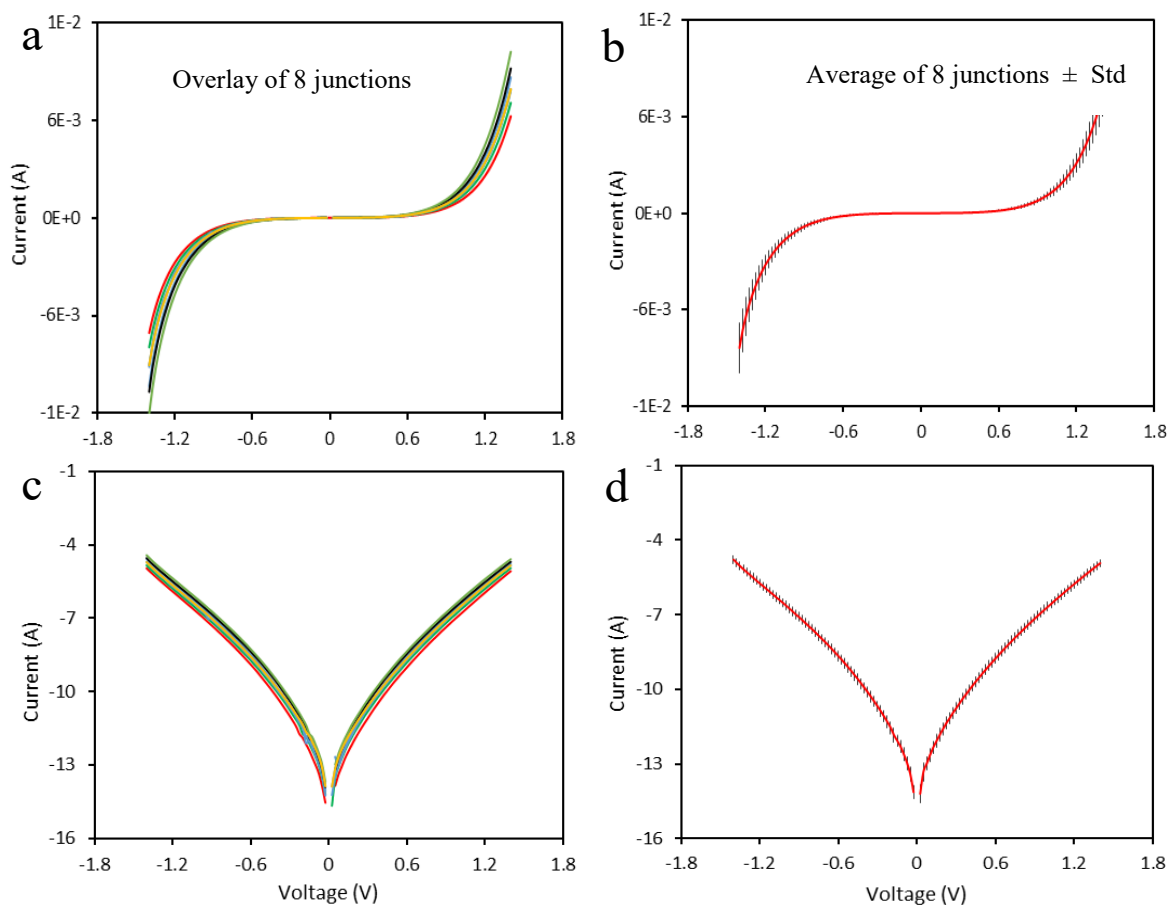
### 2.3.4 Statistics of the fabricated eC junction

Error bars in  $JV$  plots in Figure 2.17 are standard deviations of current density for all 8 junctions on a given chip, with yield for all five samples being 100% of non-shortened junctions. An example of the raw data set for  $\text{Cr}_3/\text{Au}_{15}/\text{eC}_{10}/\text{AQ}/\text{eC}_{10}/\text{Au}_{15}$  junctions is shown in Figure 2.20, which is an overlay of  $JV$  curves in linear and semi-logarithmic scale for eight different junctions with an AQ thickness of 3.8 nm. The RSD of current for the eight junctions shown varies from 18% at 1.4 V to 27% at 0.1 V. In the case of Cr/Au bottom electrode, the yield was lower than 50% (*i.e.* > 50% shorted) and standard deviations exceeded 50%, as indicated by the error bars in Figure 2.17c. Yields and relative standard deviations for the five examples shown in Figure 2.20 are listed in Table 2.7.

**Table 2.7** *JV* Statistics of SiO<sub>x</sub>/Cr/Au/eC/AQ/eC/Au junctions

| Thickness (nm) | Yield <sup>a</sup> | Bias (V) | Mean J @ V<br>(A/cm <sup>2</sup> ) | Standard<br>deviation of J | RSD (%) |
|----------------|--------------------|----------|------------------------------------|----------------------------|---------|
| 2.3 ± 0.25     | 8/8                | 0.3      | 2.6                                | 0.46                       | 17      |
| 2.9 ± 0.35     | 8/8                | 0.6      | 2.9                                | 0.85                       | 28      |
| 3.8 ± 0.27     | 8/8                | 1.0      | 2.1                                | 0.41                       | 20      |
| 4.5 ± 0.28     | 8/8                | 1.5      | 2.0                                | 0.45                       | 21      |
| 5.1 ± 0.32     | 8/8                | 1.9      | 2.2                                | 0.67                       | 28      |

a. yield indicates the number of the junction with no evidence of direct eC/eC contact (a “short”)

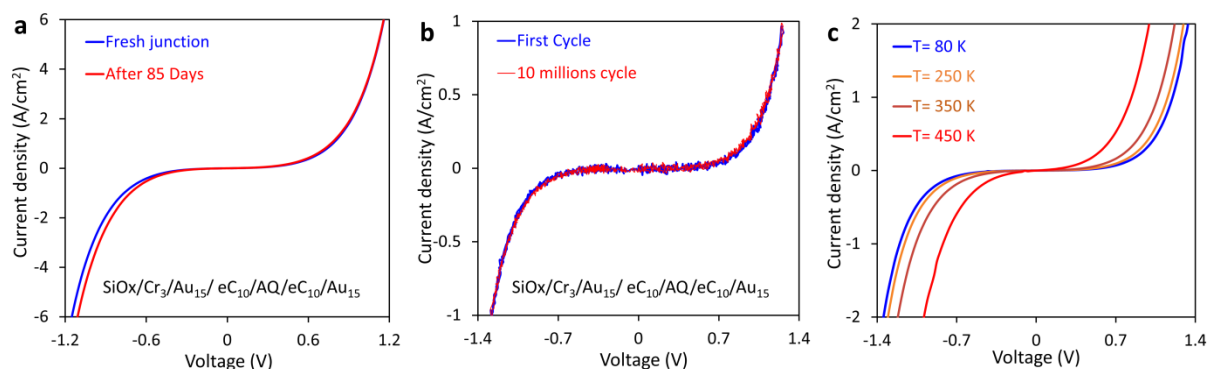


**Figure 2.20** Statistics for  $\text{Cr}_3/\text{Au}_{15}/\text{eC}_{10}/\text{AQ}_{3.8}/\text{eC}_{10}/\text{Au}_{15}$  junctions **a)** Overlay of eight measured  $IV$  curves **b)** Average of eight  $IV$  curves  $\pm$  standard deviation **c)** Overlay of eight  $\ln(I)$  versus voltage **d)** Average of eight  $\ln(I)$  versus voltage  $\pm$  standard deviation.

### 2.3.5 Stability of junctions fabricated by eC electrode

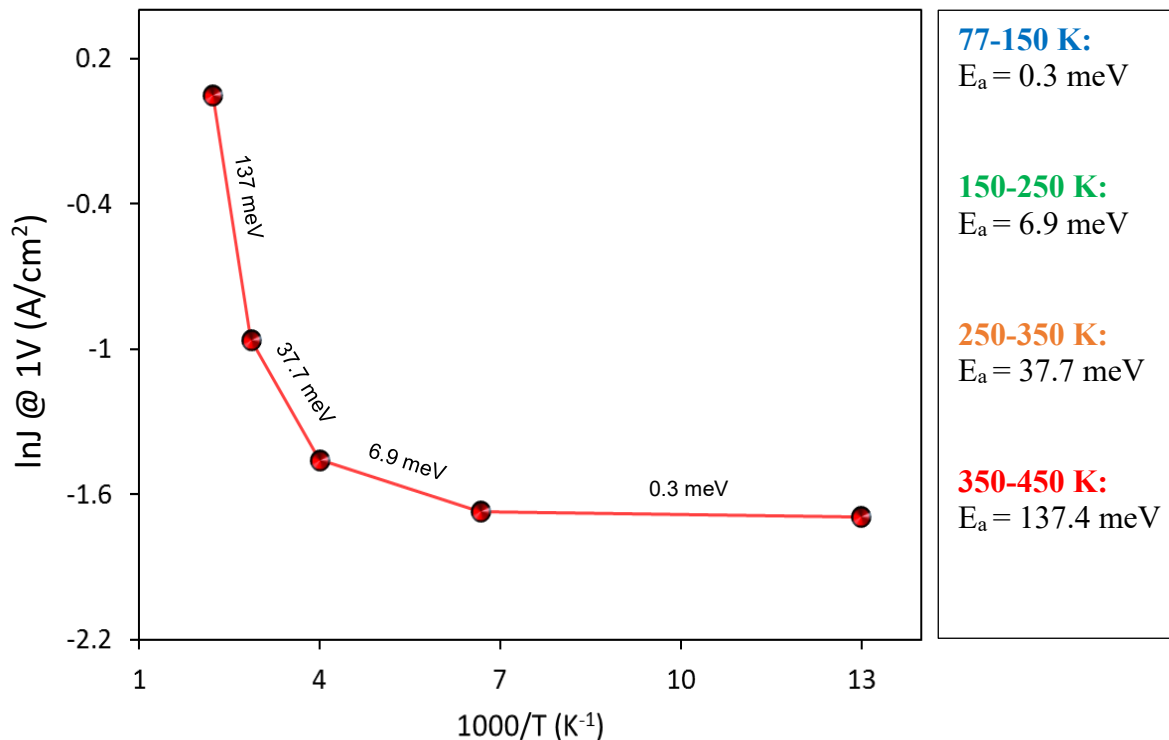
One advantage of “all carbon” MJs is stability, with the eC layers resistant to both oxidation and electromigration. We reported previously that PPF/nitroazobenzene/eC/Au were unchanged by current densities exceeding  $1000 \text{ A/cm}^2$  at  $\pm 3\text{V}$ , while the analogous PPF/nitroazobenzene/Cu/Au broke down when the Cu/Au was biased more positive than  $+2 \text{ V}$ .<sup>138</sup> The present Au/eC/AQ/eC/Au devices were subjected to several stability tests, with the results shown in Figure 2.21. Panel (a) shows a typical  $JV$  response for a MJ with a 3.4 nm

layer of AQ, both initially and after storage in air for 85 days. Figure 2.21b shows a different device before and after scanning  $10^7$  times to  $\pm 1.3$  V in air, and showed no changes in shape or current magnitude. This high operational stability significantly exceeds that using different self-assembly fabrication methods reported in the literature.<sup>26, 37, 171-173</sup> Figure 2.21c shows  $JV$  responses acquired between 80 and 450 K in vacuum, and the associated Arrhenius plot is provided in Figure 2.22.



**Figure 2.21** (a) Overlay of  $JV$  curves for fresh Au/eC/AQ/eC/Au junction before and after being stored in ambient air for 85 days. AQ thickness  $\approx 3.6$  nm. (b) Overlay of  $JV$  curve of a Au/eC/AQ/eC/Au junction before and after 10 million  $JV$  cycles to  $\pm 1.3$  V in air at 1000 V/sec. AQ thickness  $\approx 4.4$  nm. (c)  $JV$  curves for a single Au/eC/AQ/eC/Au junction at four temperatures from 77 to 450 K in vacuum. AQ thickness  $\approx 4.4$  nm. Corresponding Arrhenius plot is shown in Figure 2.22. Junctions were deposited on a Si/SiOx substrate with 3 nm Cr adhesion layer in all cases.

The Arrhenius plot for the temperature dependence of the  $JV$  curves in Figure 2.21c is shown in Figure 2.22. Also, The apparent activation energies are similar to those observed for PPF/molecule/Cu MJs<sup>130</sup>, with near zero slope between 77 and 150 K and  $\sim 38$  meV slope near 300 K. As noted above, the successful application of 390 PPF/azobenzene/eC/Au devices in consumer electronics over a period of six months with no known failures<sup>111</sup> provides clear evidence of the stability of “all-carbon” MJs.

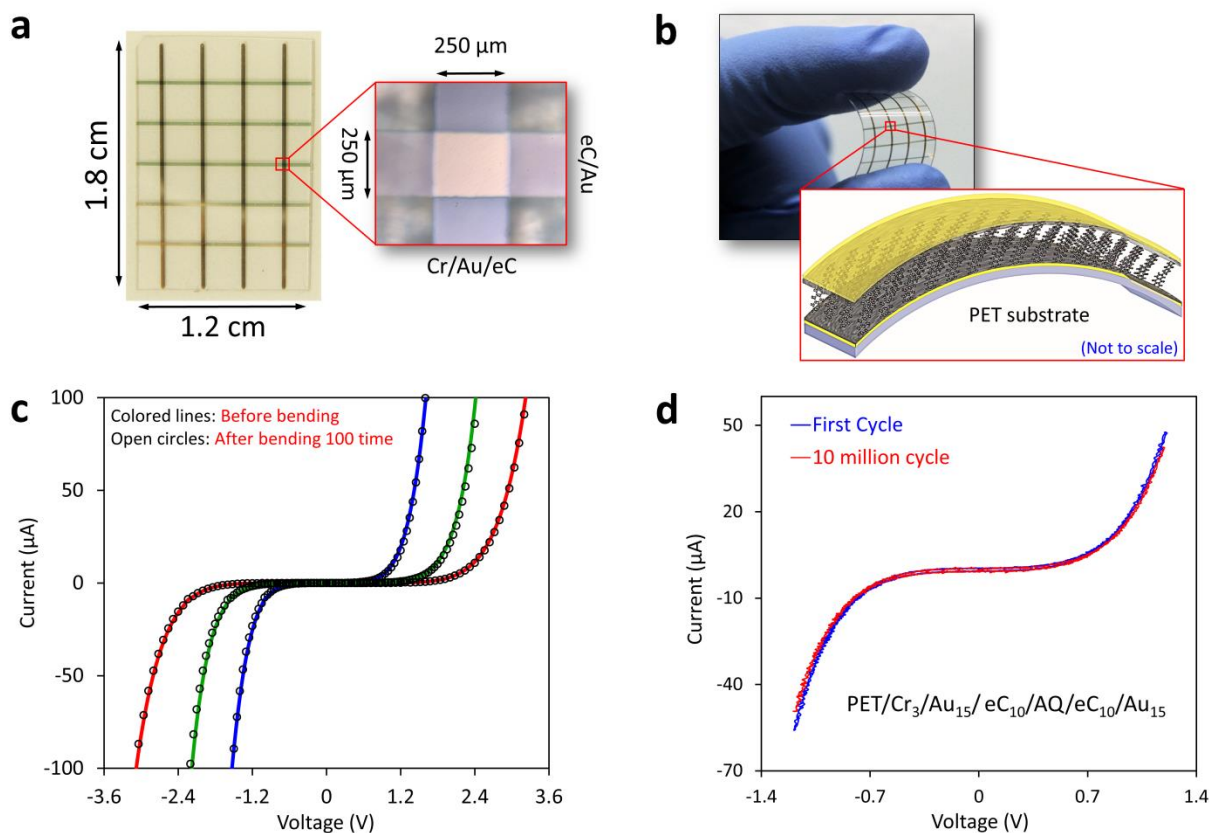


**Figure 2.22** Arrhenius plot for  $\text{Cr}_3/\text{Au}_{15}/\text{eC}_{10}/\text{AQ}_{4.5}/\text{eC}_{10}/\text{Au}_{15}$  molecular junction. Approximate activation energies in different ranges of temperature are indicated.

### 2.3.6 Flexibility of eC junctions

Fabrication of stable electronic devices on a flexible substrate is a significant objective toward realizing next generation nano-electronic technologies in consumer products.<sup>174, 175</sup> As noted above, one disadvantage of PPF is the requirement for high pyrolysis temperatures over an  $\sim 8$  hour period, which is impractical in commercial production, and especially for many flexible materials. The Au/eC substrate and eC/Au top contact can be applied at room temperature on a variety of substrates which would not

tolerate PPF formation. Figure 2.23a shows images of complete Cr<sub>3</sub>/Au<sub>15</sub>/eC<sub>10</sub>/AQ/eC<sub>10</sub>/Au<sub>15</sub> MJs deposited on polyethylene-terephthalate (PET) “transparency” film, and 6b shows the ability of the entire assembly to flex. Figure 2.23c (lines) is the *JV* response for three different AQ thicknesses. Eight junctions for each thickness showed the same characteristic *JV* shape as AQ devices on SiO<sub>x</sub> with no “shorts”, however the standard deviation of *J* was higher. The variability was likely due to molecular layer thickness variations, possibly due to static charges which affected the electrochemical deposition. The points superimposed on the same curves are the *JV* responses for each device after being flexed 100 times to the extent shown in Figure 2.23b. Since the total MJ thickness of ~60 nm is much less than the radius of curvature during bending, the strain on the MJ itself is small. Also, eC is a disordered, amorphous type of carbon without crystalline structure which in may make it more tolerant of mechanical stress in thin film structures.<sup>140</sup> Combined with strong bonding between eC and the molecular layer, the mechanical properties of eC provides stable junctions with identical *JV* response before and after bending (Figure 2.23c). Note also that the PET surface is not flat on a nanometer scale like Si/SiO<sub>x</sub> or quartz substrate, but has defects visible in an optical microscope. Apparently the MJ deposition process is sufficiently conformal, or the defects are sparse enough that yield is high, albeit with variations in current density. The PET substrate did not permit AFM “scratching”<sup>176</sup> to determine molecular layer thickness due to deformation and roughness, hence the thicknesses were estimated from the diazonium reduction conditions. Figure 2.23d shows the initial *JV* cycle for a PET/Cr/Au/eC/AQ/eC/Au device plus a second *JV* curve obtained after 10<sup>7</sup> bias cycles to ± 1.5 V, indicating excellent flexible device stability.



**Figure 2.23** (a) Optical image of PET/Cr<sub>3</sub>/Au<sub>15</sub>/ eC<sub>10</sub>/AQ/eC<sub>10</sub>/Au<sub>15</sub> devices deposited on transparency film (PET). Magnification shows an individual junction. (b) Optical image of the fabricated device on PET substrate while bent. (c)  $JV$  curves of junctions fabricated on flexible PET substrate before (lines) and after (points) being bent 100 times to the degree shown in panel (b), which reduced the 1.8 cm dimension in panel (a) to  $\sim 1.4$  cm. Three AQ thicknesses were deposited electrochemically but were not be verified by AFM. (d) Overlay of  $JV$  curve of freshly fabricated AQ junction on flexible PET substrate before (blue) and after (red) 10 million  $JV$  cycles to  $\pm 1.3$  V in air.

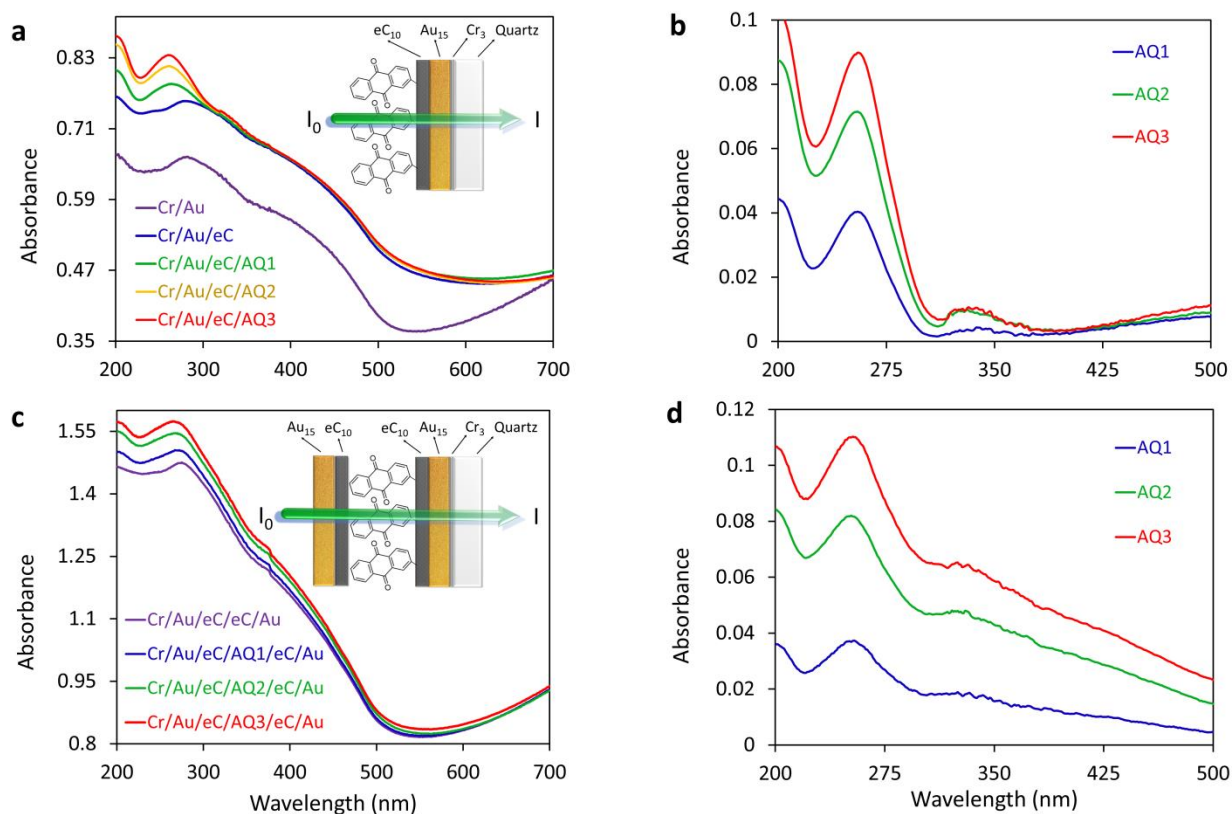
### 2.3.7 Transparency of eC junctions

Molecular optoelectronics refers to an area that investigates both measurement capabilities (e.g. optical spectroscopy) and our fundamental understanding of electronic transport mechanisms in molecular junctions.<sup>1</sup> Optoelectronics with molecular junctions requires one or both conducting contacts to be partially transparent in order to conduct

measurements in the local environment. Both eC<sup>134, 135</sup> and PPF<sup>132, 133</sup> were investigated previously with the objective of making optically transparent carbon electrodes, usually on quartz substrates. However, the high sheet resistance of partially transparent layers of eC and PPF creates ohmic potential errors which can be serious in either electrochemical or electronic applications. We have used metal/eC films previously for making sufficiently transparent top contacts on molecular junctions to monitor device structure while functioning with Raman<sup>127, 177</sup> and UV-Vis spectroscopy,<sup>178, 179</sup> and to observe light emission<sup>124</sup> by MJs. The combination of Au<sub>15</sub>/eC<sub>10</sub> was used in the current work partly to provide transparency, and the combination of low sheet resistance and optical transmission with the stability and surface chemistry of carbon makes Au/eC films attractive both as substrates and top contacts. Figure 2.24a shows absorbance spectra of several “blanket” e-beam coatings on a quartz slide, referenced to an uncoated slide in air. The Q/Cr<sub>3</sub>/Au<sub>15</sub>/eC<sub>10</sub> junction substrate, which is 30-40 % transparent in the visible range, and the addition of anthraquinone layers (4-11 nm thick) yields additional absorbance in the region expected for free anthraquinone (220-280 nm). Figure 2.24b shows the same spectra after subtraction of the spectrum of an unmodified Q/Cr<sub>3</sub>/Au<sub>15</sub>/eC<sub>10</sub> sample, clearly showing the absorbance of the AQ layer. The Au<sub>15</sub>/eC<sub>10</sub> electrode layer is clearly sufficiently transparent for optical spectroscopy and observation of photoeffects, including while the device is in operation, but to date such measurements have been constrained to reflection geometry through one partially transparent electrode. Figure 2.24c shows the absorbance of a complete molecular junction in *transmission* mode with the optical beam passing through both electrodes and the AQ layers. Subtraction of the spectrum of Q/Cr<sub>3</sub>/Au<sub>15</sub>/eC<sub>20</sub>/Au<sub>15</sub> “blank” containing no AQ layer yields the spectra of Figure 2.24d. The spectra of 7b and 7d are quite similar, with differences likely due to variation of internal



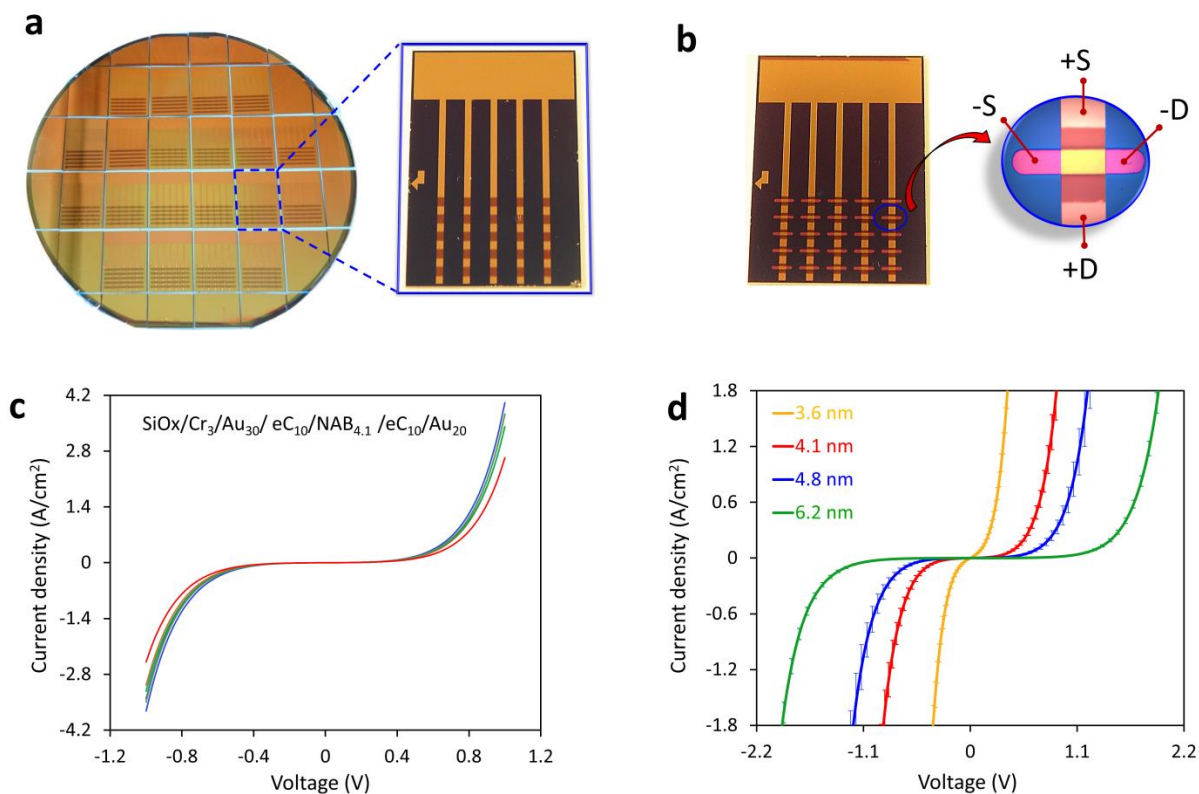
reflection efficiencies at the AQ/eC interfaces. Although one transparent contact is sufficient for Raman monitoring of the device under bias in reflection geometry, the transmission geometry enabled by two transparent contacts is generally easier to interpret than reflection mode for UV-Vis absorption spectroscopy.



**Figure 2.24** (a) Optical absorbance of Quartz/Cr<sub>3</sub>/Au<sub>15</sub>/eC<sub>10</sub>/AQ relative to an air reference. Three different thicknesses of AQ molecular layer are shown. (b) Absorbance spectra of panel (a) following subtraction of the unmodified Q/Cr<sub>3</sub>/Au<sub>15</sub>/eC<sub>10</sub> spectrum, to yield the absorbance due to the AQ molecular layers. (c) Absorbance spectrum of complete Quartz/Cr<sub>3</sub>/Au<sub>15</sub>/eC<sub>10</sub>/AQ/eC<sub>10</sub>/Au<sub>15</sub> junction relative to an air reference, for three different thicknesses of Anthraquinone. (d) Absorbance from panel (c) following subtraction of the spectrum of a "blank" Q/Cr<sub>3</sub>/Au<sub>15</sub>/eC<sub>20</sub>/Au<sub>15</sub> sample.

### 2.3.8 Wafer scale lithography for eC molecular junctions

The Cr/Au/eC substrates shown in Figure 2.4 were deposited through a shadow mask, which imposes constraints on the width and shapes of the “stripes” and the sharpness of their edges. Photolithography permits a wider range of patterns and dimensions, and a diced wafer consisting of twenty substrates made with conventional photolithography is shown in Figure 2.25a. When transparency is not required, the Au thickness was increased to 30 nm, so that the substrate pattern is initially Cr<sub>3</sub>/Au<sub>30</sub> across the entire chip. Contact with Au/eC with standard tungsten probes sometimes results in significant contact resistance in 2-wire mode, so eC is deposited only on the junction region through a shadow mask. In the final junction shown in Figure 2.25b, the molecular layer is in contact only with eC at both electrodes, and the probes contact only Au, as shown. The Cr/Au/eC substrate may be coated with photoresist for protection during long term storage or shipping, which is stripped off before modification with the molecular layer. The large Cr/Au pad at the top permits electrical contact to all five “stripes” during electrochemical reduction of the diazonium solution, and a razor cut after deposition across the five stripes isolates the electrode lines from each other for subsequent electronic testing. Finally, the eC/Au top contact is deposited on the modified Cr/Au/eC substrate through a shadow mask with a pattern of 25 rectangles, resulting in 25 MJs which can be contacted by 2, 3, or 4 probes on Au surfaces without stray currents or interference from nearby devices. We refer to the design of Figure 2.25b as “integrated”, in order to distinguish it from the “crossbar” format of Figure 2.4 made entirely with shadow masks.



**Figure 2.25** (a) Image and enlargement of 100 mm diameter wafer of integrated chip design after dicing but before molecular layer deposition. (b) Completed chip with 25 Si/SiOx/Cr<sub>3</sub>/Au<sub>30</sub>/eC<sub>10</sub>/NAB/eC<sub>10</sub>/Au<sub>20</sub> after molecular layer and top contact deposition. NAB= nitroazobenzene oligomers. Magnification shows individual junction with the position of four probes for electrical contact to Au surfaces. (c) Overlay of  $JV$  curves for 8 junctions selected randomly on a chip with a 4.1 nm thick layer of NAB. (d) Average  $JV$  curves for integrated junctions with four different NAB thicknesses. Yield for tested junction was 100% of non-shortcd junctions and error bars represent  $\pm$  standard deviation for 6-8 junctions of each thickness. Statistics were given in Table 2.6.

molecular junctions, with the final resist layer of a chip shown in Figure 2.25a removed preceding electrochemical deposition of Nitroazobenzene (NAB) molecular layer thicknesses of 3.6, 4.1, 4.8 and 6.2 nm. After deposition of the eC<sub>10</sub>/Au<sub>20</sub> top contacts, twenty-eight MJs on the four samples were selected randomly and tested, involving 6-8 MJs

on each chip. The yield was 100%, meaning that none of the devices exhibited an eC/eC short circuit. Figure 2.25c shows 8 overlaid  $JV$  curves for the chip with NAB thickness of 4.1 nm, which had a relative standard deviation of current density of 13% for  $|V| = 1 V$ . Figure 2.25d shows averaged  $JV$  curves with error bars of  $\pm$ standard deviation of  $J$  for the four thicknesses examined. Direct comparison of the  $JV$  responses for crossbar vs integrated MJs is difficult due to thickness differences, but the attenuation plots of  $\ln J$  vs  $d$  may be compared directly. For the NAB MJs of the type shown in Figure 2.4,  $\beta (0.3 V) = 2.2 \pm 0.31 \text{ nm}^{-1}$  and an intercept of  $6.3 \pm 1.2$ , while the microfabricated devices had  $\beta (0.3 V) = 2.0 \pm 0.22 \text{ nm}^{-1}$  and an intercept of  $5.7 \pm 1.8$ . Therefore, the  $JV$  behavior of the integrated and crossbar eC/NAB/eC devices are statistically indistinguishable. Although the junctions shown in figure 2.25b are relatively large ( $250 \times 500 \mu\text{m}$ ), eCarbon devices are completely compatible with previous lithographic methods<sup>137</sup> for fabricating a range of junction areas from  $3 \times 3 \mu\text{m}$  to  $400 \times 400 \mu\text{m}$ .

## 2.4 CONCLUSION

Successive e-beam deposition of carbon and Au provides the very flat surface, low sheet resistance, and chemical stability important to the fabrication and performance of molecular junctions. Au/eC as a substrate shows excellent behavior for surface modification by reduction of diazonium ions, and eC/molecule/eC have excellent lifetime and no apparent tendency to electromigration or oxidation. All-carbon MJs tolerate a 100-450 K temperature range and endure millions of  $JV$  cycles in ambient air without observable effects on electronic behavior. All-carbon MJs based on e-beam carbon may be deposited on flexible substrates and do not subject the substrate to high temperatures, thus significantly increasing the range of materials onto which molecular electronic devices can be incorporated. Partial

transparency of one or both contact surfaces in all-carbon MJs permits live monitoring of molecular junctions under bias with optical spectroscopy as well as photocurrent generation and emission of photons. All three of these approaches have proven valuable as diagnostics of MJ structure and operation, and may have applications combining molecular electronics and photonics.

# CHAPTER 3

## Structure Controlled Long-Range Sequential Tunneling in Carbon-Based Molecular Junctions

### 3.1 INTRODUCTION

The field of Molecular Electronics (ME) investigates charge transport in single molecules or ensembles of molecules oriented between conducting contacts acting as elements in electronic circuits. A core principle in ME is the control of charge transport by variations in molecular structure, and the possibly wide variety of electronic functions which may be available with molecular components but difficult with conventional semiconductors. Numerous experimental paradigms have been employed in extensive research on how structure controls transport, in alkane, aromatic and oligomeric molecular junctions (MJs).<sup>8, 9, 13, 170, 180</sup> A key parameter in charge transport is the length of the molecular component ( $d$ , in nm) between conducting contacts, and the dependence of MJ current on  $d$  is often a useful diagnostic for transport mechanism. For example, the exponential dependence of current density,  $J$  (A/cm<sup>2</sup>) at a given bias voltage on  $d$  is often cited as an indication of quantum mechanical tunneling, with the slope of  $\ln J$  vs  $d$  yielding  $\beta$ , the attenuation coefficient with units of  $\text{\AA}^{-1}$  or  $\text{nm}^{-1}$ .<sup>181</sup> From transport measurements in donor-acceptor complexes, modified electrodes, and MJs of both single molecules and ensembles,  $\beta$  is generally accepted to equal 6-9  $\text{nm}^{-1}$  for aliphatic molecules,<sup>26, 48, 50, 182, 183</sup> while  $\beta$  is in the range of 2-5  $\text{nm}^{-1}$  for conjugated or aromatic molecules<sup>52, 54, 58, 130</sup> and  $< 1 \text{ nm}^{-1}$  for certain metal complexes with strong electronic coupling between molecular subunits.<sup>184-186</sup> Carbon based MJs with carbon/molecule/Cu or carbon/molecule/carbon structures containing aromatic molecular layers exhibit  $\beta$  values of  $\sim 2.1$  to  $3.3 \text{ nm}^{-1}$  and a weak dependence on variations in structure for  $d < 5 \text{ nm}$  due to strong electronic coupling with between the molecules and contacts.<sup>58, 130, 138</sup>

Plots of  $\ln J$  vs  $d$  for conjugated and aromatic MJs are often reported to extend from  $d < 1$  nm to  $d = 5$  nm, depending on molecular structure and experimental paradigm. For example, oligomers of phenyleneimines exhibit  $\beta = 3.0$  nm<sup>-1</sup> for  $d < 4$  nm, then a change in slope to  $\beta = 0.9$  nm<sup>-1</sup> for  $d = 4$  to 7.5 nm.<sup>71, 187</sup> A similar change in slope was reported for oligophenylethynyl molecules, with  $\beta = 0.9$  nm<sup>-1</sup> for  $d = 1$  to 2.5 nm and  $\beta = 0.3$  nm<sup>-1</sup> for  $d = 2.5$  to 5.1 nm.<sup>188</sup> In several cases, the change in slope was attributed to a change in mechanism from direct or coherent tunneling to “hopping” involving a series of steps between sites in the molecular layer.<sup>46, 189</sup> For bis-thienyl benzene (BTB) oligomers in carbon based MJs, linearity of the attenuation plot with  $\beta = 2.9$  nm<sup>-1</sup> was observed for  $d = 2 - 8$  nm, then  $\beta = 1.0$  nm<sup>-1</sup> for  $d = 8-16$  nm and  $\beta \approx 0.02$  nm<sup>-1</sup> for 16-22 nm. For BTB, the 1.0 nm<sup>-1</sup> region extended from  $d = 8$  to 22 nm at low temperature, thus ruling out activated redox exchange.<sup>190</sup> The general consensus to date associates the linear  $\beta \sim 3$  nm<sup>-1</sup> region for conjugated molecules to direct tunneling, with a barrier determined by the offset between the electrode Fermi level and the molecular orbital closest in energy. Such transport may involve “electron tunneling” mediated by the molecular LUMO or “hole tunneling” mediated by the HOMO, and is often referred to as the “single level model”.<sup>113, 165</sup> For transport distances above 3-5 nm in conjugated molecules, several alternatives to coherent tunneling have been proposed, including redox exchange,<sup>71, 191</sup> polaron tunneling,<sup>169</sup> and field ionization,<sup>190</sup> although coherent tunneling remains a possibility.<sup>185</sup> The dependence of junction current on temperature, thickness, and bias are valuable for determining transport mechanism, and each mechanism may be affected by molecular structure quite differently.

Our laboratory has studied carbon-based MJs containing aromatic oligomers covalently bonded to conducting carbon surfaces, with Cu or carbon/Au top contacts. For molecular



layer thicknesses in the range of 2-5 nm, transport has the characteristics of coherent tunneling, with weak temperature dependence and linear attenuation plots with  $\beta = 2.7 \pm 0.6 \text{ nm}^{-1}$  for seven different aromatic structures and  $> 400 \text{ MJs}$ .<sup>58</sup> However, both  $\beta$  and current density were very similar for aromatic structures, despite a variation of  $>2.3 \text{ eV}$  in the HOMO and LUMO levels of the free molecules. We attributed this result to strong electronic coupling between the molecules and the contacts, which reduces the influence of electron donating or withdrawing groups on the observed transport barrier. Strong coupling between graphitic electrodes and aromatic molecules is also predicted theoretically, leading to significant shifts in HOMO and LUMO levels in graphene-molecule model structures relative to those of the free molecules.<sup>192-194</sup> The current investigation was undertaken to address two questions about transport through organic films with thicknesses greater than 5 nm. First, how far does the exponential dependence on layer thickness extend past 5 nm; and second, what transport mechanisms become operative once coherent tunneling becomes negligible? Three aromatic molecular layers that could be extended to thicknesses  $> 5 \text{ nm}$  were examined, and compared to past results for a thiophene derivative in the same thickness range. A detailed analysis of the current-voltage response of diazonium-derived fluorene oligomers between carbon contacts and  $d = 2.3$  to  $8.6 \text{ nm}$  revealed unexpected behavior which is inconsistent with either coherent tunneling or the “single level” model commonly applied to aromatic MJs. Comparison to anthraquinone (AQ) and nitroazobenzene (NAB) MJs permitted insights into the factors controlling charge transport, and a multistep tunneling mechanism explains the experimental results.

## 3.2 EXPERIMENTAL SECTION

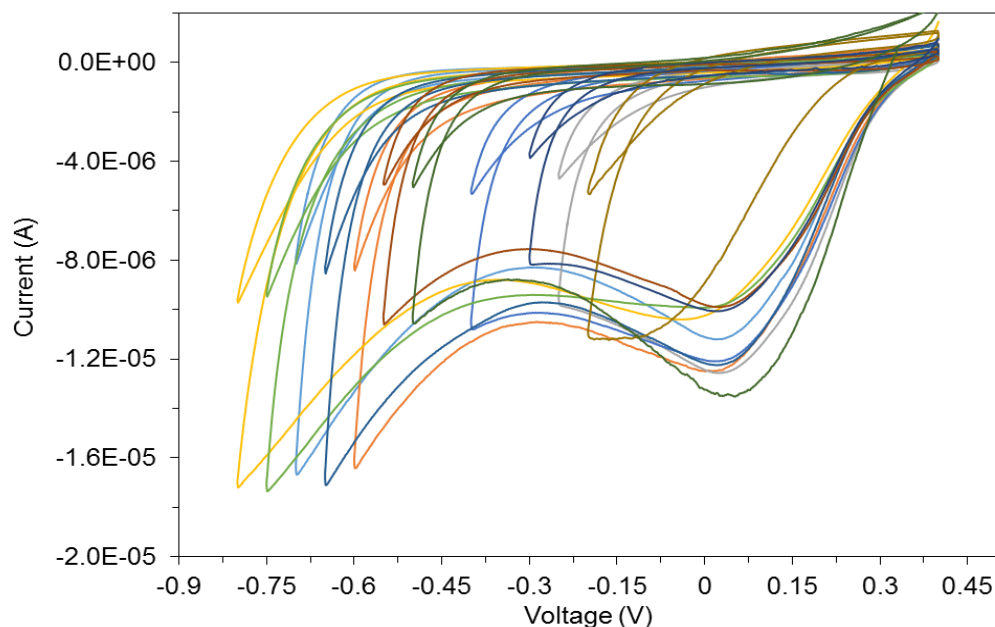
Historically the work related to this Chapter is done before the Chapter 2. The molecular junction fabrication steps are similar to those described in chapter 2 except the bottom contact. Fabrication of junctions on pyrolyzed photoresist film (PPF) was conducted as described previously, with electron-beam deposited carbon (eC) and Au top contacts.<sup>138, 190</sup> Junctions are designated with subscripts in nm on the “stack” of contacts and molecular layers, *viz.* PPF/FL<sub>5.0</sub>/eC<sub>10</sub>/Au<sub>20</sub> (FL<sub>5.0</sub> designates a Fluorene oligomer with  $d = 5.0$  nm). The same junction structure was used in all cases, with variation only of the identity and thickness of the molecular layer, and the junction area was 0.00125 cm<sup>2</sup> (250 x 500 μm). To address minor differences in fabrication steps in comparison to chapter 2, the detailed of each step is described below.

### 3.2.1 Fabrication of bottom contact (PPF)

Pyrolyzed photoresist film (PPF) electrode fabrication is described in detail elsewhere.<sup>137</sup> Briefly, positive photoresist (AZ 4330) was spin coated on each sample, followed by a soft bake at 80 °C and then photolithography was carried out with a UV exposure. Development was done in a 1:3 dilution of AZ developer: water. Resulting four lines with 500 μm width were pyrolyzed in a 1-inch tube furnace by heating under a flow of forming gas (5% H<sub>2</sub>, balance N<sub>2</sub>) to 1050 °C for 1 hour. After cooling in flowing forming gas, the PPF surface consists of sp<sup>2</sup> carbon similar to glassy carbon with RMS roughness lower than 0.5 nm.

### 3.2.2 Molecular layer grafting and thickness measurement

Electrochemical reduction of diazonium species on the surface is used for grafting molecular layer on the surface of bottom contact (PPF). A conventional three-electrode electrochemical cell with  $\text{Ag}/\text{Ag}^+$  electrode as reference and Pt wire as a counter electrode was used for grafting. The solution was 1 mM diazonium salt of the molecule (AQ, NAB, FL) dissolved in acetonitrile containing 0.1 M tetrabutylammonium hexafluorophosphate ( $\text{TBAPF}_6$ ) as supporting electrolyte. The thickness of grafted molecular layer was controlled by sweeping the potential from 0.4 to  $-1.3$  V (vs.  $\text{Ag}/\text{Ag}^+$ ) at 50 mV/s for repeated cycles. After modification, the sample was rinsed with acetonitrile and dried using a stream of nitrogen. First two cycles of corresponding CV for grafting of AQ molecular layer are shown in Figure 3.1 and electrochemical parameters used for grafting of AQ, NAB and FL are listed in Table 3.1. Parameters for BTB grafting are reported previously.<sup>4</sup>

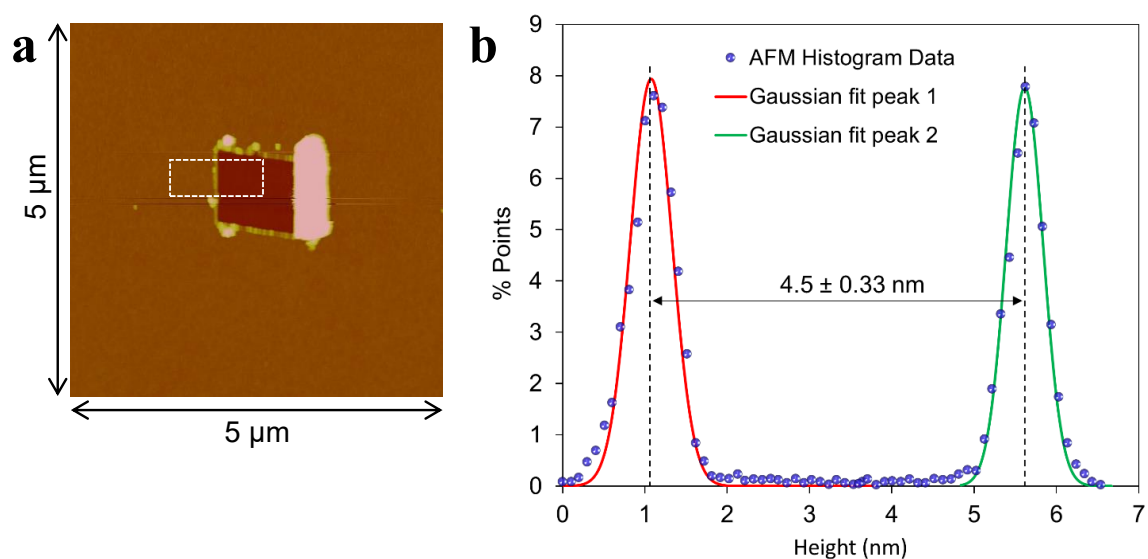


**Figure 3.1** Cyclic voltammograms during grafting of Anthraquinone on the surface of PPF, with a variation of negative potential limit causing AQ layers with different thicknesses.

**Table 3.1** Electrochemical parameters for grafting of molecule on the surface of PPF

| Molecule      | Sweep range<br>(V vs Ag/Ag <sup>+</sup> ) | No. of cycles | Scan rate<br>(mV/s) | Thickness<br>(nm) |
|---------------|---|---------------|---------------------|-------------------|
| Fluorene      | 0.4 – (-0.35)                             | 6             | 50                  | 2.3 ± 0.3         |
|               | 0.4 – (-0.40)                             | 6             | 50                  | 2.9 ± 0.3         |
|               | 0.4 – (-0.45)                             | 7             | 50                  | 3.4 ± 0.2         |
|               | 0.4 – (-0.50)                             | 7             | 50                  | 3.9 ± 0.4         |
|               | 0.4 – (-0.60)                             | 8             | 50                  | 4.1 ± 0.3         |
|               | 0.4 – (-0.70)                             | 8             | 50                  | 4.5 ± 0.3         |
|               | 0.4 – (-0.75)                             | 8             | 50                  | 5.0 ± 0.4         |
|               | 0.4 – (-0.80)                             | 8             | 50                  | 5.5 ± 0.4         |
|               | 0.4 – (-0.90)                             | 8             | 50                  | 6.1 ± 0.4         |
|               | 0.4 – (-1.00)                             | 8             | 50                  | 7.1 ± 0.5         |
|               | 0.4 – (-1.10)                             | 10            | 50                  | 7.6 ± 0.5         |
|               | 0.4 – (-1.20)                             | 10            | 50                  | 8.0 ± 0.7         |
|               | 0.4 – (-1.30)                             | 10            | 50                  | 8.6 ± 0.6         |
| Anthraquinone | 0.4 – (-0.20)                             | 6             | 50                  | 2.2 ± 0.3         |
|               | 0.4 – (-0.25)                             | 6             | 50                  | 2.9 ± 0.3         |
|               | 0.4 – (-0.30)                             | 6             | 50                  | 3.4 ± 0.4         |
|               | 0.4 – (-0.35)                             | 8             | 50                  | 3.9 ± 0.4         |
|               | 0.4 – (-0.40)                             | 8             | 50                  | 4.3 ± 0.4         |
|               | 0.4 – (-0.50)                             | 8             | 50                  | 5.5 ± 0.5         |
|               | 0.4 – (-0.55)                             | 8             | 50                  | 6.2 ± 0.5         |
|               | 0.4 – (-0.60)                             | 8             | 50                  | 7.1 ± 0.6         |
|               | 0.4 – (-0.65)                             | 8             | 50                  | 8.0 ± 0.5         |
|               | 0.4 – (-0.70)                             | 8             | 50                  | 8.9 ± 0.6         |
|               | 0.4 – (-0.75)                             | 8             | 50                  | 9.5 ± 0.6         |
|               | 0.4 – (-0.80)                             | 8             | 50                  | 10.6 ± 0.5        |
| NAB           | 0.4 – (-0.30)                             | 6             | 40                  | 3.2 ± 0.3         |
|               | 0.4 – (-0.35)                             | 6             | 40                  | 4.1 ± 0.3         |
|               | 0.4 – (-0.40)                             | 6             | 40                  | 4.5 ± 0.4         |
|               | 0.4 – (-0.45)                             | 8             | 40                  | 5.1 ± 0.4         |
|               | 0.4 – (-0.50)                             | 8             | 40                  | 5.9 ± 0.5         |
|               | 0.4 – (-0.65)                             | 8             | 40                  | 7.4 ± 0.6         |
|               | 0.4 – (-0.80)                             | 10            | 40                  | 10.1 ± 0.6        |

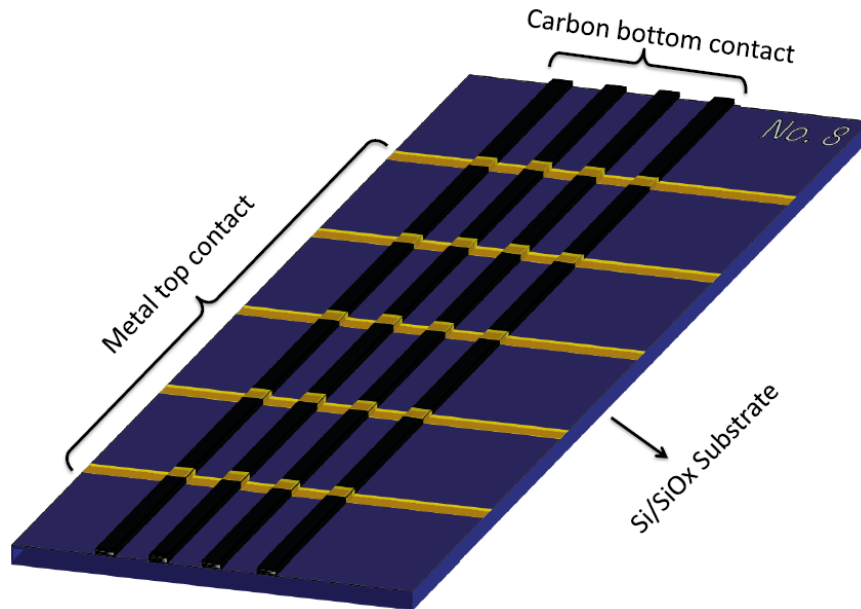
Measurement of molecular layer thickness was done using AFM “scratching” technique, using the same procedure described previously<sup>58, 176</sup>. The example of the AFM measurement is shown in Figure 3.2. Thickness measurements were done adjacent to one of the junctions of each sample. First, contact mode was applied to scratch a trench (1 x 1  $\mu\text{m}$ ) in the molecular layer, then a 5 x 5  $\mu\text{m}$  tapping mode image was then obtained in the area surrounding and including the trench (Figure 3.2a). A histogram generated from the height data was fitted by two separate Gaussian functions (for the two different height distributions), with the height determined as the difference between the centers of the two functions and the uncertainty given as the quadrature addition of the two best-fit  $\sigma$  values. Thicknesses mentioned in Table 3.1 are determined in the same way.



**Figure 3.2 (a)** AFM Tapping mode 5 x 5  $\mu\text{m}$  tapping mode image of a 1 x 1  $\mu\text{m}$  “trench” made in a PPF/FL layer using contact mode AFM. **(b)** Histogram of heights determined within the white rectangle of the AFM image. Uncertainty in thickness is the quadrature addition of the two Gaussian  $\sigma$  values.

### 3.2.3 Top contact deposition to complete junction

The top contact electrode was comprised of electron beam deposited 10 nm eC and 15 nm Au through a physical shadow mask with 0.25 mm openings oriented perpendicular to the bottom contact, which results in a crossbar junction with area of  $0.125 \text{ mm}^2$ . Deposition was done in an electron beam evaporator (Kurt J. Lesker PVD75) with typical pressure below  $7 \times 10^{-6}$  Torr in starting point of deposition. Deposition rate was 0.01 nm/sec for eC and 0.03 nm/sec for Au. Characteristics of eC are investigated previously<sup>38</sup>. The schematics of the final fabricated chip is shown in Figure 3.3. Bottom four or six junctions are measured for all cases.

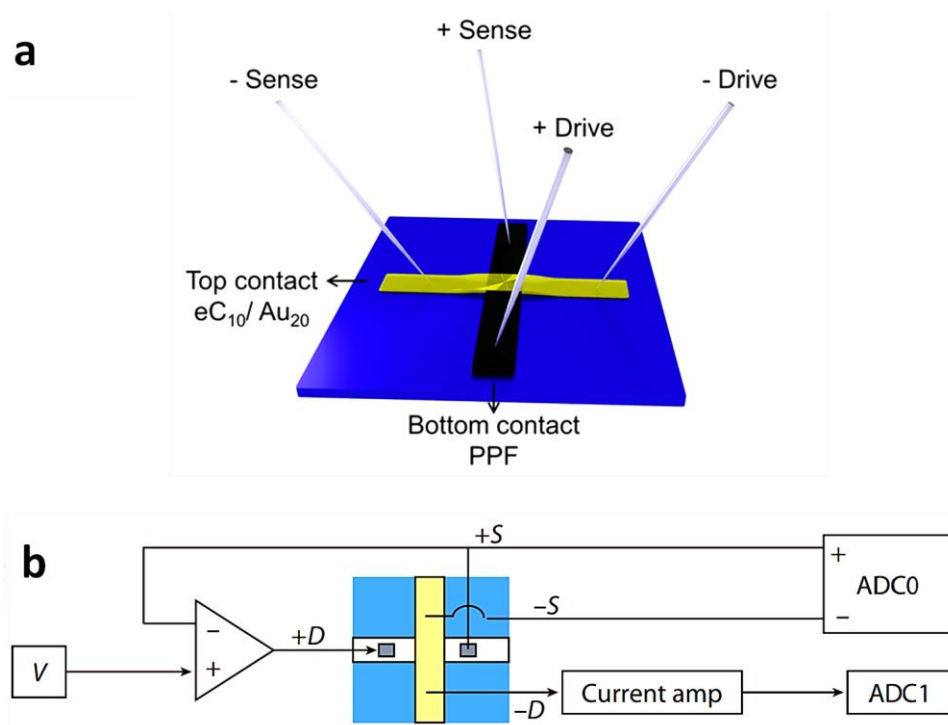


**Figure 3.3** Schematics of fabricated complete chips. Bottom contact consists of four patterned parallel PPF lines. Top contact consists of eC (10 nm) and Au (20 nm).

### 3.2.4 Electrical measurement

All current–voltage curves were obtained using a Keithley 2602A source-meter in 4-wire mode. Measurements are all done in the air except temperature dependence measurement. Low temperature experiments are done in a vacuum chamber with pressure

below  $10^{-5}$  Torr. The home-made program is used to acquire the data in order to have dynamic NPLC from 25 to 0.001 during the measurement based on the sensitivity required. Figure 3.4 shows the connections used for 4-wire mode measurement. The +Drive and +Sense are connected to PPF electrode (bottom contact) and -Drive and -Sense is connected to eC/Au electrode (top contact).

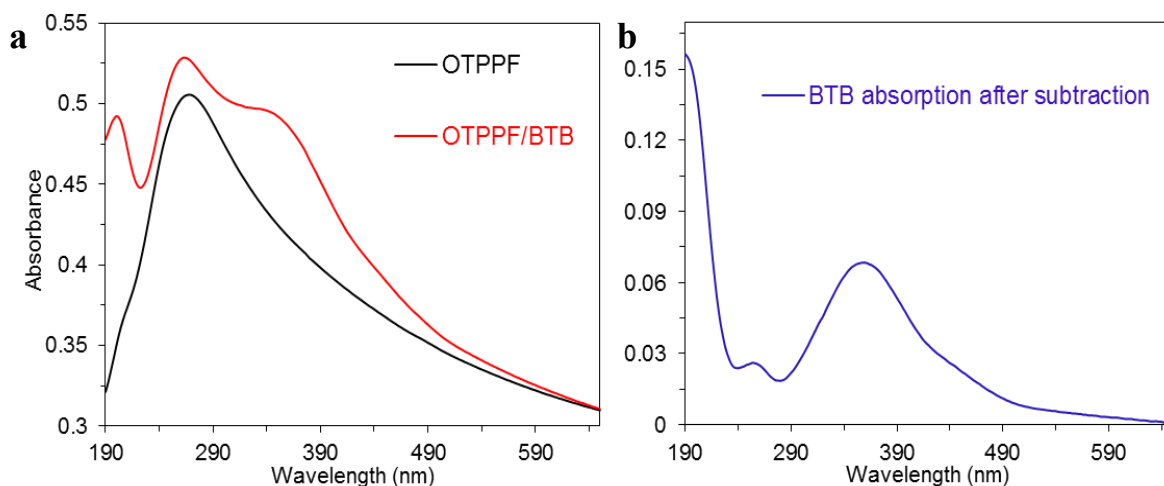


**Figure 3.4** (a) Schematics of 4-wire mode electrical connection. (b) Schematics of 4-wire mode electrical measurement setup. ADC1 stands for the analog-to-digital channel for current and ADC0 monitors voltage that has a differential input.

### 3.2.5 UV-Vis measurement on grafted molecular layer

Polished quartz wafers (Technical Glass Products, Inc.) were diced into 1.8 x 1.2 cm chips to serve as substrates. The details for fabrication of optically transparent PPF (OTPPF) is described elsewhere<sup>133</sup>. Briefly, a commercially available photoresist (AZ-P4330-RS) was

diluted (12 % by volume) using propylene glycol methyl ether acetate, then this solution was spin coated onto quartz slides at 6000 rpm for 60 sec. The slides were pyrolyzed in a 1-inch tube furnace by heating under a flow of forming gas (5% H<sub>2</sub>, balance N<sub>2</sub>) to 1050 °C for 1 hour. All UV-Vis absorption spectra were obtained with a Perkin-Elmer Lambda 1050 dual beam spectrometer. The absorption spectra of the optically transparent PPF (OTPPF) films were then obtained, with a typical result shown in Figure 3.5-a, black curve. The same OTPPF substrate was then modified with molecular layers with different thickness. Procedure for grafting molecular layer is the same as described in section 1.2. An example of the absorbance spectrum obtained for a layer of BTB on OTPPF is shown in Figure 3.5-a, red curve. Figure 3.5-b shows the subtraction of the unmodified OTPPF spectrum from the red curve of 6a, to clearly show the absorbance of the BTB molecular layer. The same procedure was used for all UV-Vis measurement on the molecular layer in this chapter.

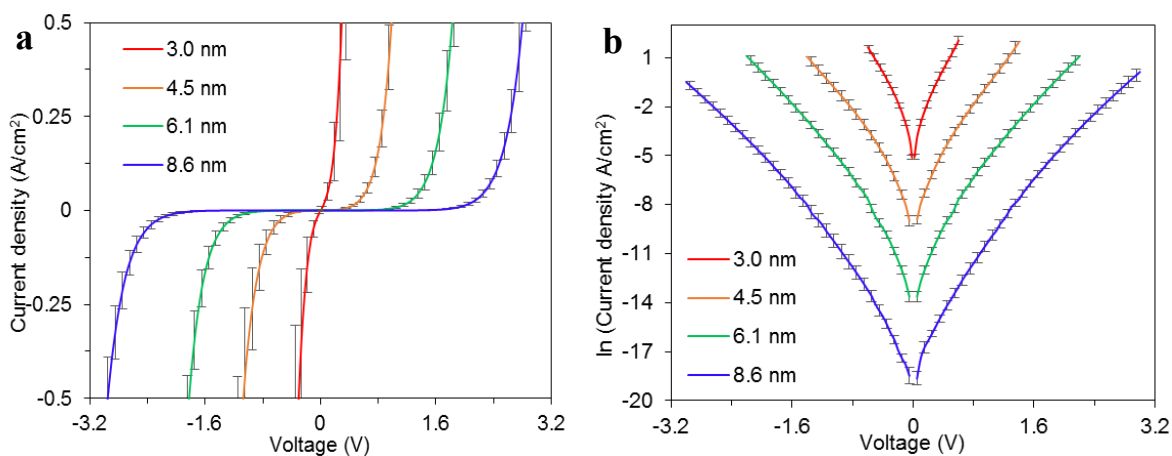


**Figure 3.5 (a)** UV-Vis absorption spectra for optically transparent PPF (black) and OTPPF modified with a BTB layer (red). **(b)** OTPPF/BTB spectrum after subtraction of unmodified OTPPF spectrum.



### 3.2.6 Statistics of fabricated junctions

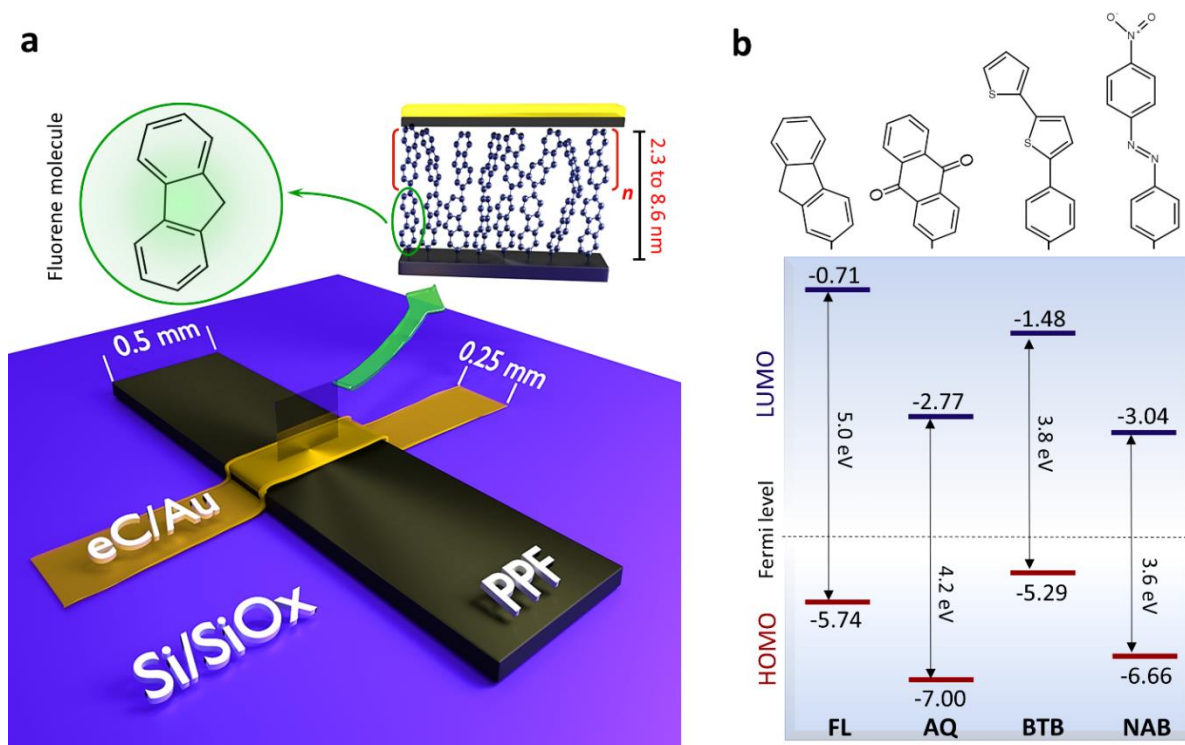
As reported previously, relative standard deviations (RSD) for the current density measured for a series of independent molecular junctions made with the procedures outlined above are in the range of 10-30%<sup>38, 58, 138</sup>.  $JV$  curves for MJs with four different thicknesses of Fluorene in linear and semilogarithmic scale are shown in Figure 3.6 panel a and panel b, respectively. Error bars are standard deviations of current density for four measured junctions on a given chip shown in Figure 3.3.



**Figure 3.6 (a)**  $JV$  curves for different FL thicknesses, with each curve representing the average of four junctions on a single sample. Yield for tested junctions was 100% of non-shorted junctions and error bars represent  $\pm$  standard deviation for four junctions of each thickness. **(b)** Semilogarithmic plot of  $JV$  curves shown in panel a.

### 3.3 RESULTS

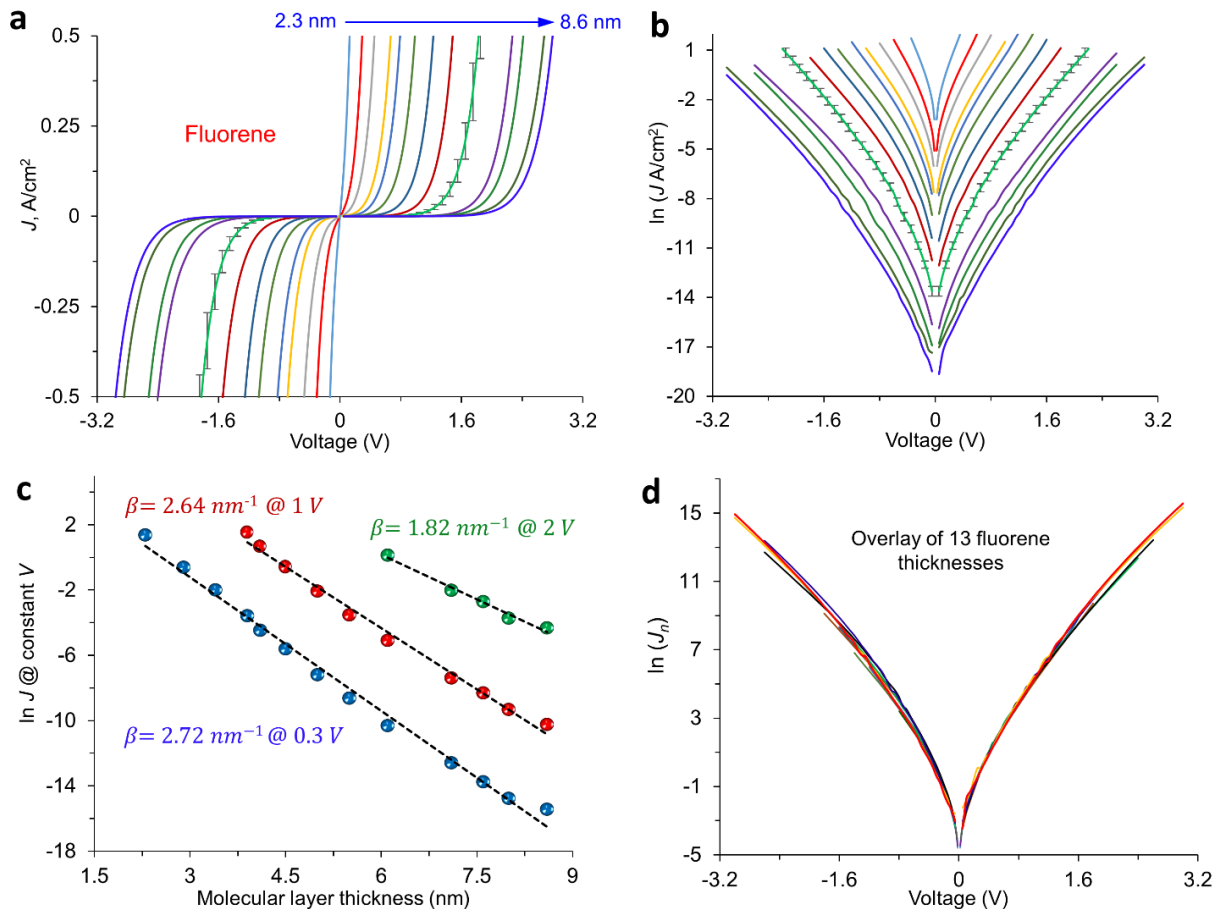
In each subheadings of the results section, Fluorene (FL) molecular junctions with thicknesses ( $d$ ) of 2.3 to 8.6 nm were examined in detail initially in order to characterize transport for molecular layers with  $d > 5$  nm. However, additional MJs containing nitroazobenzene (NAB), anthraquinone (AQ), and bis-thienyl benzene (BTB) were examined for comparison, before proposing a transport mechanism. Figure 3.7a shows a junction schematic and cross section of a completed device, as well as the structure of fluorene and its oligomer. Figure 3.7b shows the four aromatic molecules examined in the current work, with the DFT-predicted energy levels of the free molecules relative to the vacuum level.



**Figure 3.7** (a) Schematic illustration of PPF/fluorene/eC<sub>10</sub>/Au<sub>20</sub> molecular junction.  $n$  is a number of repeating units of oligomer which determine final thickness of molecular layer. (b) Structures and frontier orbital energy diagram for FL, AQ, NAB and BTB, relative to a vacuum reference. Orbital energies were calculated by Density Functional Theory (DFT) B3LYP 6-31G(d), in Gaussian 09. Fermi level of PPF and eC is -4.8 V vs vacuum.

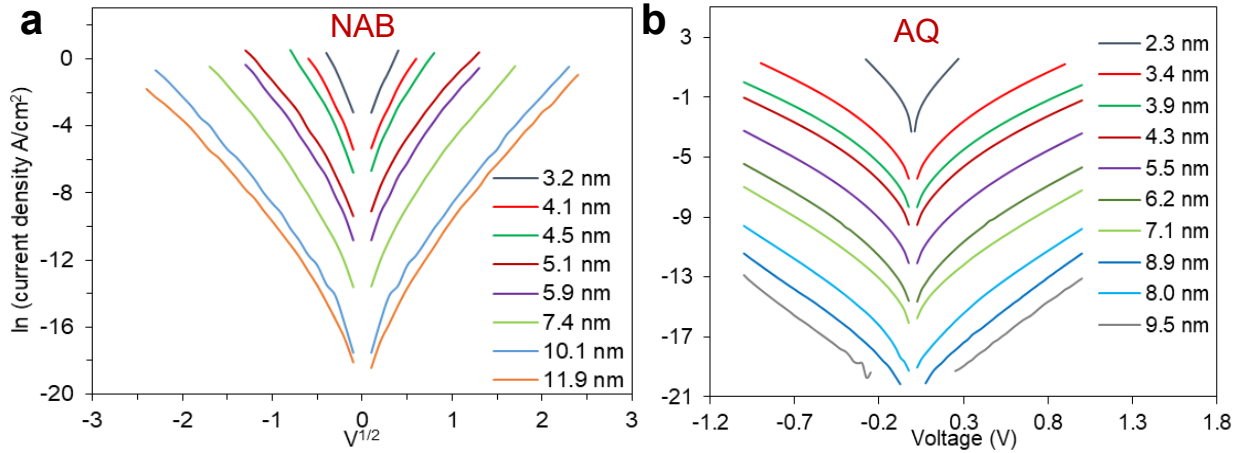
### 3.3.1 Electrical behavior of molecular junctions

Current-density vs bias voltage ( $JV$ ) curves for fluorene MJs with thirteen thicknesses in the range of 2.3 to 8.6 nm are shown in Figure 3.8a. Error bars on the response for 6.1 nm thickness indicate typical standard deviations of  $J$ , and all curves are averages of four separate MJs. Additional statistics and sample  $JV$  curves were shown in Figure 3.6. The same results are shown in semilog format in Figure 3.8b, with error bars shown for the 6.1 nm case. Comparison of the  $JV$  curves clearly illustrates that: (i) junction conductance depends nonlinearly on bias, (ii)  $JV$  curves are nearly symmetric with respect to bias polarity for all thicknesses; (iii) there is a strong thickness dependence of conductivity, with conductance decreasing monotonically with thickness at all bias values. Note also that the  $\ln J$  vs  $V$  curves do not exhibit the linearity expected for direct tunneling, and this point will be discussed in more detail below. Attenuation plots of  $\ln J$  vs junction thickness ( $d$ ) are shown in Figure 3.8c, for three bias values. For  $V=0.3$  V,  $\beta = 2.72$  nm<sup>-1</sup>, in good agreement with that reported previously for seven other diazonium-derived aromatic junctions ( $\beta = 2.7 \pm 0.6$  nm<sup>-1</sup>)<sup>58</sup> and  $\beta = 2.9$  nm<sup>-1</sup> for BTB devices with  $d < 8$  nm<sup>190</sup>. Note particularly that the exponential decrease in current density for FL devices extends well beyond the usual limit for direct tunneling of 3-5 nm, with minor changes in slope over the entire 2.3-8.6 nm range. A further test of the similarity of the  $JV$  response for different thicknesses is an overlay of the  $JV$  curves after normalization of the currents for all curves at  $V = 0.3$  V to  $J = 1$  A/cm<sup>2</sup>, as shown in Figure 3.8d. The thirteen curve shapes are very similar over the entire voltage range, implying that the  $J$  vs  $V$  behavior for all thicknesses has similar shape and dependence on bias.



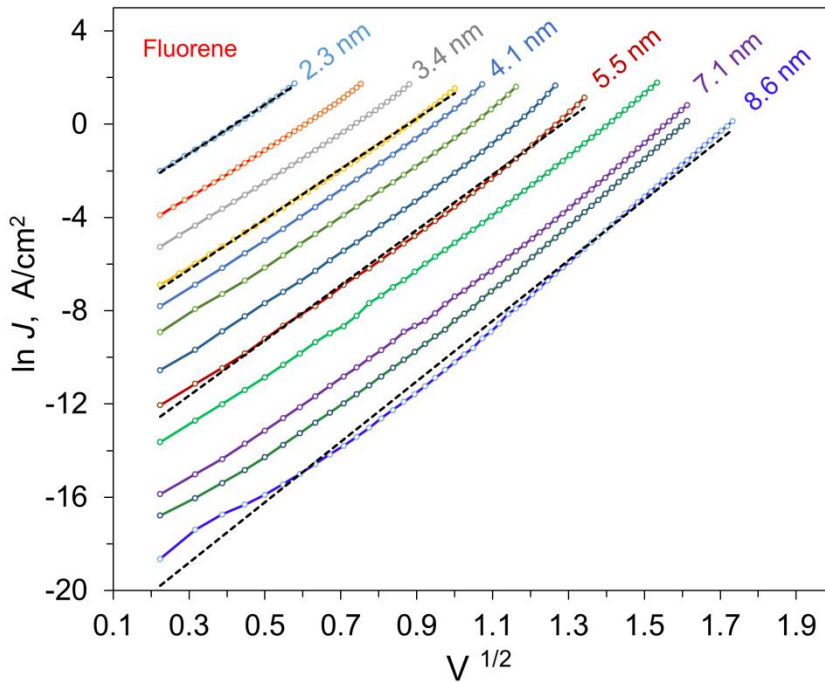
**Figure 3.8** (a) Current density vs bias voltage ( $JV$ ) curves for PPF/FL $_d$ /eC $_{10}$ /Au $_{20}$ .  $d$  is a thickness of fluorene molecular layer:  $d = 2.3, 3.0, 3.4, 3.8, 4.1, 4.5, 5.0, 5.5, 6.1, 7.1, 7.6, 8.0, 8.6$  nm in the order indicated. Each curve is an average of four independent junctions, with a typical deviation shown for  $d = 6.1$  nm junction. (b) Semilogarithmic plot of  $JV$  curves shown in panel a. (c) Corresponding attenuation plot for  $V = 0.3, 1.0$  and  $2.0$  V, with the slopes ( $\beta$ ) indicated. (d) Overlay of normalized semilogarithmic  $JV$  curves shown in panel b. Current density of each thickness was normalized to  $J = 1$  A/cm $^2$  at  $0.3$  V.

AQ and NAB junctions in a range of  $\sim 2$  to  $11$  nm are fabricated to be compared with FL junctions. Figure 3.9-a and -b shows  $JV$  curves in semilogarithmic scale for NAB and AQ, respectively. The  $JV$  curves of BTB junctions were reported previously<sup>190</sup>.



**Figure 3.9**  $JV$  curves in semilogarithmic scale for different thicknesses of (a) NAB, (b) AQ

As noted above, the nonlinearity of the  $\ln J$  vs  $V$  plots in Figure 3.8b is not expected for direct tunneling, and other transport mechanisms can result in such curvature. Poole-Frenkel transport between coulombic traps and Schottky emission at interfaces can both predict linearity of  $\ln J$  with  $V^{1/2}$ , due to changes in the respective barriers with increases in electric field.<sup>195</sup> We considered these mechanisms previously for BTB devices in the thickness range of 8-12 nm, but rejected them due to inconsistency with the temperature dependence of the  $JV$  curves.<sup>190</sup> Figure 3.10 shows  $\ln J$  vs  $V^{1/2}$  plots for comparison to  $\ln J$  vs  $V$  in Figure 3.8b, and statistics for linear fits of  $\ln J$  to  $V$ ,  $\ln J$  to  $V^{1/2}$ ,  $\ln J/V$  to  $V^{1/2}$  and other possible functional forms are listed in Table 3.2.



**Figure 3.10** Natural log of current density vs square root of bias voltage for the same series of fluorene junctions shown in Figure 3.8, for positive bias. Order of thickness is the same as in Figure 3.8a.

**Table 3.2**  $R^2$  for Fluorene data shown in Figure 3.8b of the main text, following least square fit to the abscissa indicated.

| Thickness (nm) | $\ln J$ vs $V$ | $\ln(J/V)$ vs $V^{1/2}$ | $\ln J$ vs $V^{1/2}$ |
|----------------|----------------|-------------------------|----------------------|
| 2.3            | 0.9734         | 0.9296                  | 0.9988               |
| 2.9            | 0.9736         | 0.9552                  | 0.9988               |
| 3.4            | 0.9767         | 0.9685                  | 0.9991               |
| 3.9            | 0.9753         | 0.9747                  | 0.9992               |
| 4.1            | 0.9832         | 0.9781                  | 0.9977               |
| 4.5            | 0.9837         | 0.9780                  | 0.9972               |
| 5.0            | 0.9836         | 0.9811                  | 0.9969               |
| 5.5            | 0.9832         | 0.9818                  | 0.9972               |
| 6.1            | 0.9799         | 0.9868                  | 0.9981               |
| 7.1            | 0.9832         | 0.9841                  | 0.9967               |
| 7.6            | 0.9859         | 0.9812                  | 0.9954               |
| 8.0            | 0.9843         | 0.9811                  | 0.9946               |
| 8.6            | 0.9849         | 0.9813                  | 0.9947               |

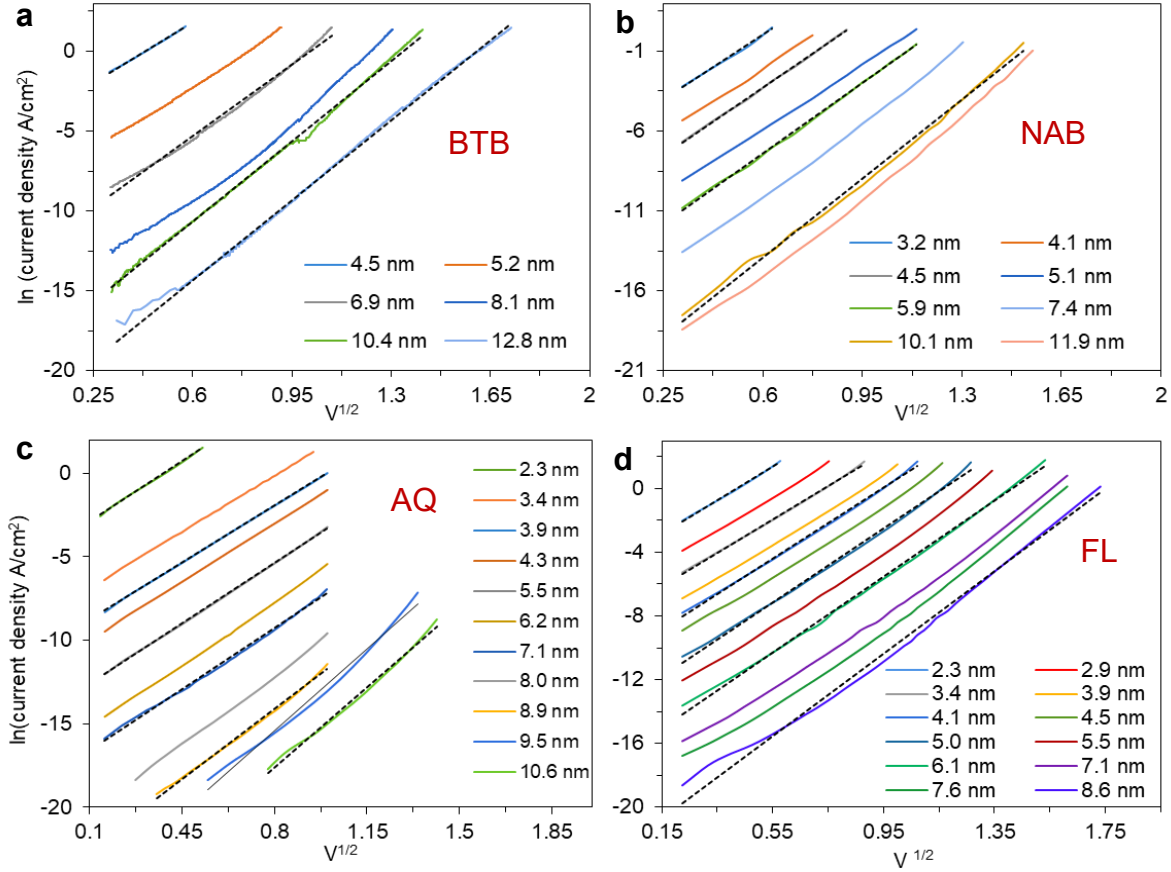
For  $d = 2.3$  to  $6.1$  nm, the  $\ln J$  vs  $V^{1/2}$  plots are very linear, with  $R^2$  above 0.997 in all cases, while  $R^2$  for the  $\ln J$  vs  $V$  plots ranges from 0.973 to 0.985. Slight upward curvature of the  $\ln J$  vs  $V^{1/2}$  plots is observed for  $d = 7.1$  to  $8.6$  nm, but still results in a better linear fit ( $R^2 > 0.994$  for  $d = 8.6$  nm) than either  $\ln J$  vs  $V$  ( $R^2 > 0.985$ ) or  $\ln J/V$  vs  $V^{1/2}$  ( $R^2 = 0.981$ ). The slopes, intercepts and  $R^2$  values for linear fits of  $\ln J$  vs  $V^{1/2}$  plots of all thirteen FL thicknesses are listed in Table 3.3.

**Table 3.3** Slopes and intercepts for plots of  $\ln J$  vs  $V^{1/2}$  for Fluorene MJs

| <i>Thickness (nm)</i> | <i>Intercept (b)</i> | <i>Slope (a)</i> | $R^2$  |
|-----------------------|----------------------|------------------|--------|
| 2.3                   | -4.45                | 10.623           | 0.9985 |
| 3.0                   | -6.40                | 10.668           | 0.9984 |
| 3.4                   | -7.74                | 10.584           | 0.9989 |
| 3.8                   | -9.46                | 10.788           | 0.9991 |
| 4.1                   | -10.58               | 11.233           | 0.9977 |
| 4.5                   | -11.74               | 11.234           | 0.9972 |
| 5.0                   | -13.55               | 11.633           | 0.9969 |
| 5.5                   | -15.19               | 11.838           | 0.9972 |
| 6.1                   | -16.91               | 11.995           | 0.9981 |
| 7.1                   | -19.43               | 12.267           | 0.9967 |
| 7.6                   | -20.79               | 12.699           | 0.9954 |
| 8.0                   | -21.62               | 12.614           | 0.9946 |
| 8.6                   | -22.70               | 12.970           | 0.9947 |

In order to show the effect of the molecular structure on the functional form,  $\ln J$  vs  $V^{1/2}$  for a range of thickness of other examined molecular junctions is shown in Figure 3.11. As it is apparent from Figure 3.11, linearity of  $\ln J$  with square root of applied voltage is a general

functional form for the examined MJs it is not dependent on the structure of the molecular layer.



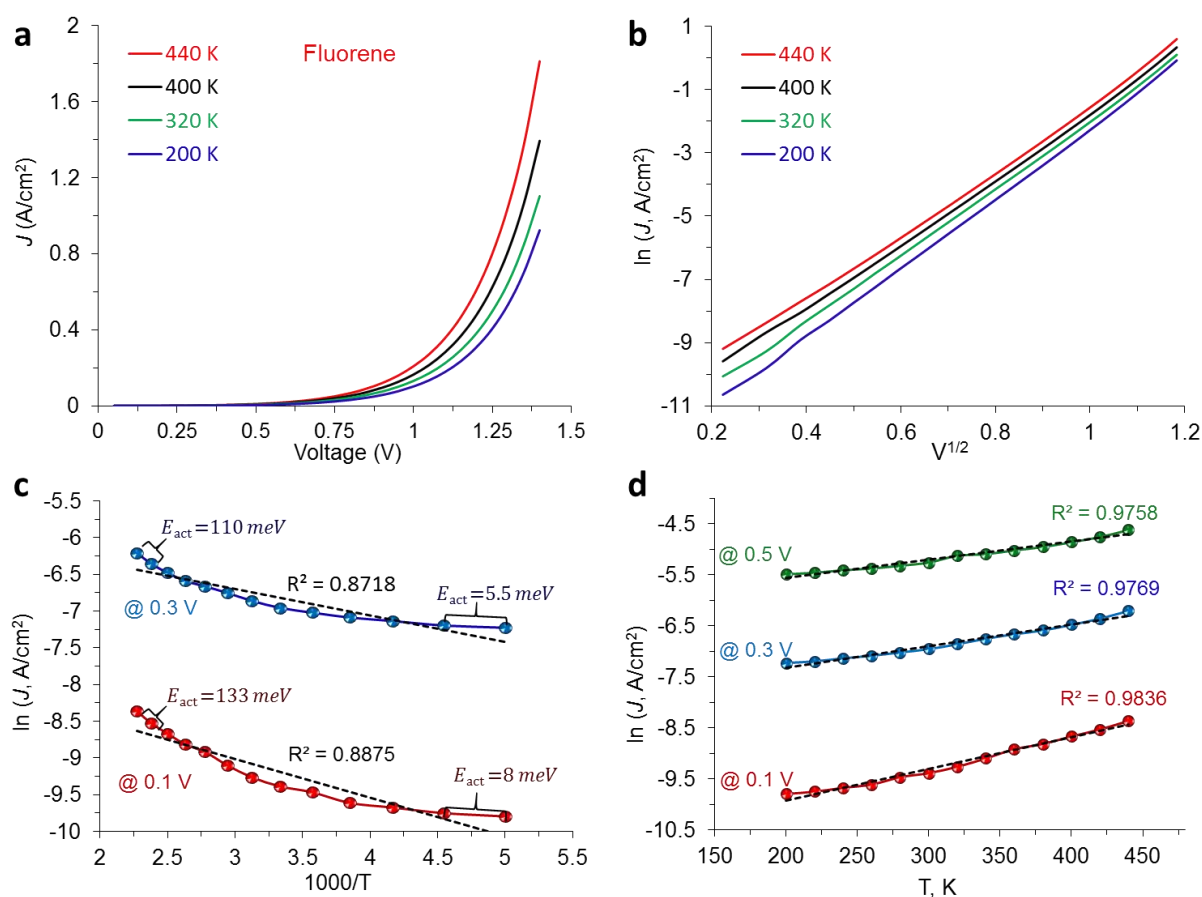
**Figure 3.11**  $\ln J$  vs  $V^{1/2}$  for indicated thicknesses of (a) BTB, (b) NAB, (c) AQ, (d) FL.

### 3.3.2 Temperature dependent conductivity

We reported previously that BTB molecular junctions with  $d > 16$  nm exhibited Arrhenius temperature dependence with  $E_{act} > 100$  meV above 200K, but thinner molecular layers and  $T < 200$  K had apparent Arrhenius slopes in the range of 0-50 meV.<sup>190</sup> We also reported that aromatic MJs with  $d < 5$  nm had weakly temperature dependent  $JV$  response, consistent with coherent tunneling with the addition of Fermi function broadening for  $T >$

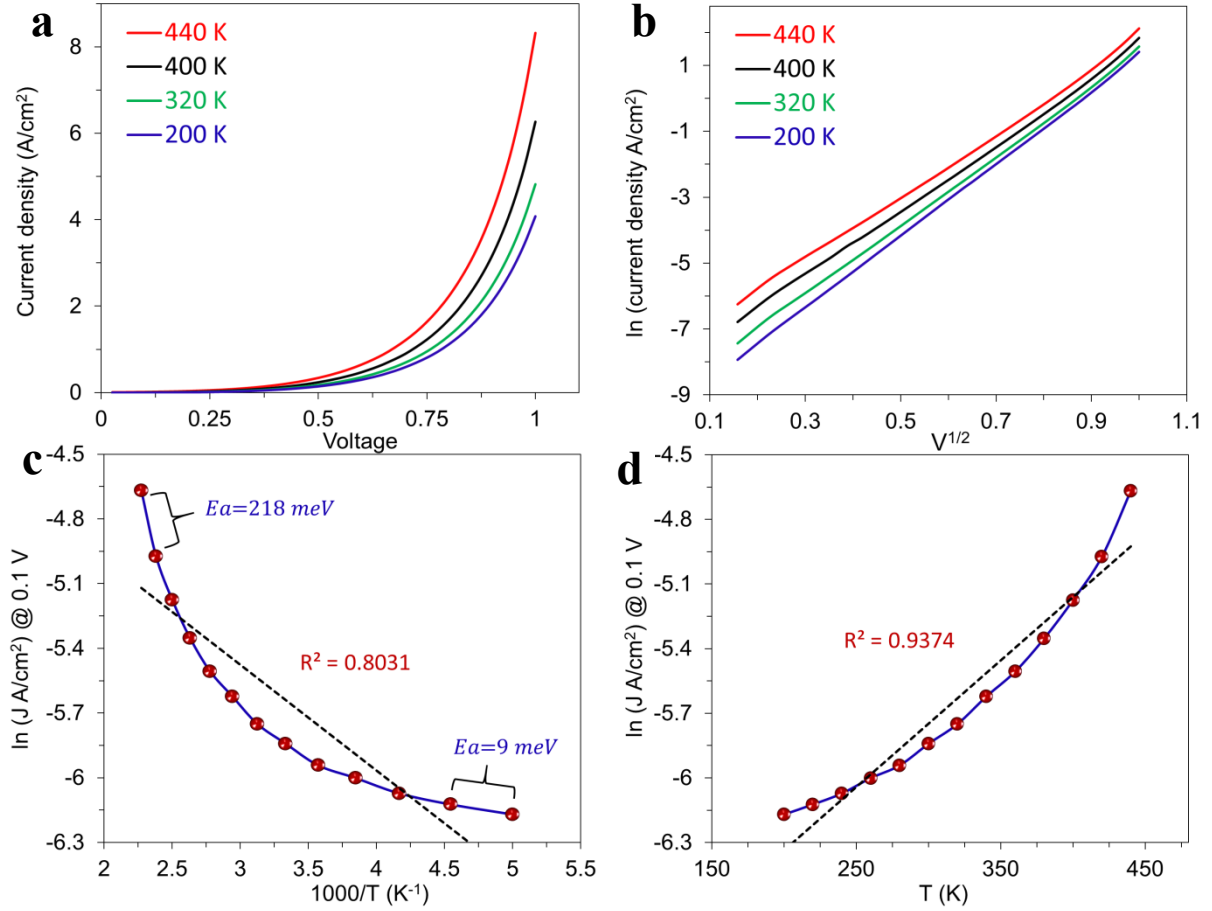


200 K.<sup>130</sup> Tunneling in single porphyrin oligomers over a distance to 5-10 nm exhibited Arrhenius slopes of 80 – 220 meV, but were concluded to be inconsistent with a hopping model.<sup>185</sup> The  $JV$  curves for FL devices with  $d = 5.5$  nm shown in Figure 3.12a exhibit a weak dependence on temperature with  $J$  at 440 K less than twice that of  $J$  at 200K. Plots of  $\ln J$  vs  $V^{1/2}$  remain linear from 200 K to 440 K (Figure 3.12b). The Arrhenius plots of Figure 3.12c for two bias values show no linear regions, with a significant change in slope over the observed  $T$  range.

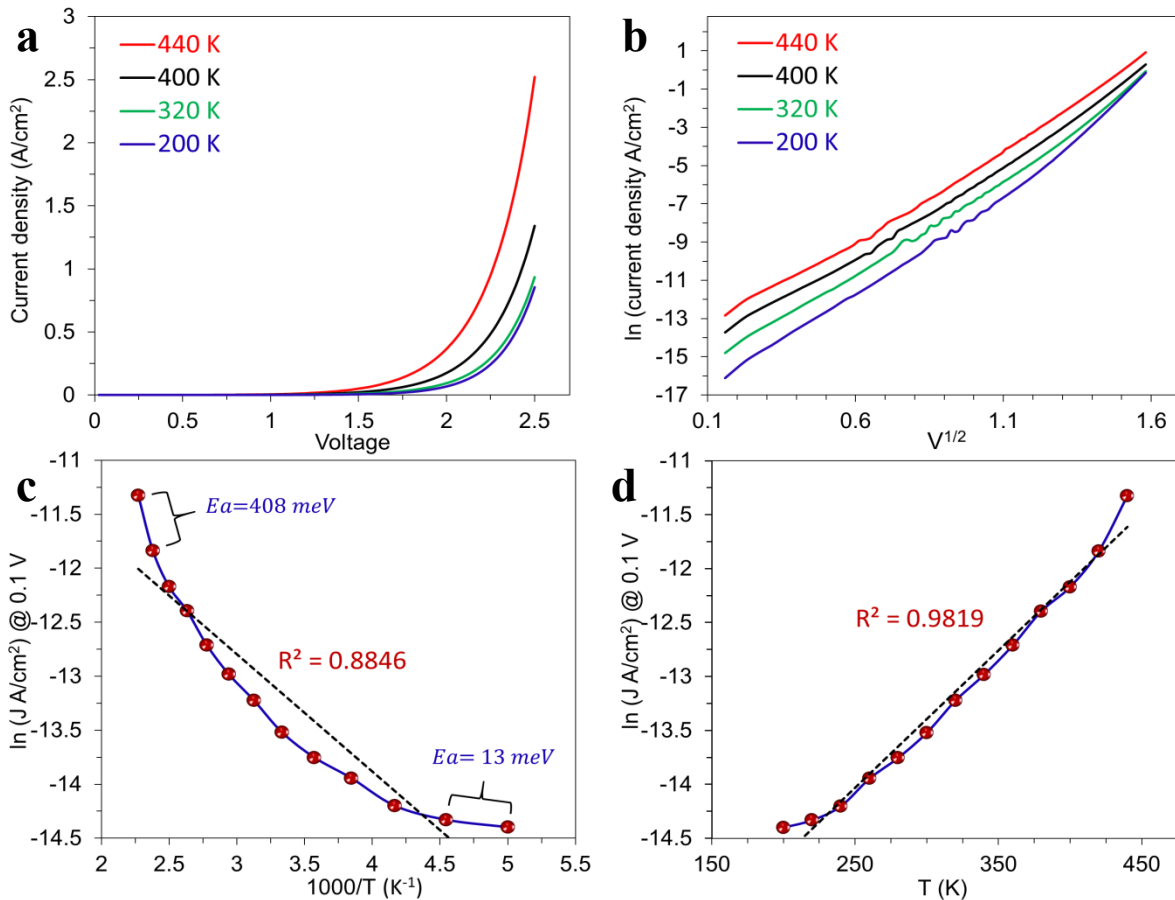


**Figure 3.12** (a)  $JV$  curves for PPF/FL<sub>5.5</sub>/eC<sub>10</sub>/Au<sub>20</sub> junction at four temperatures from 200 to 440 K in vacuum. (b)  $\ln J$  vs  $V^{1/2}$  plots for curves in panel a. (c) Arrhenius plots at 0.1 and 0.3 V, with apparent activation energies for high and low  $T$  segments. (d)  $\ln J$  vs  $T$  at 0.1, 0.3 and 0.5 V.  $R^2$  for linear fits of the lines are indicated.

To see the effect of thickness, similar results and analysis for the FL junctions with  $d = 3.8$  and  $7.6$  nm are shown in Figure 3.13 and Figure 3.14, respectively.

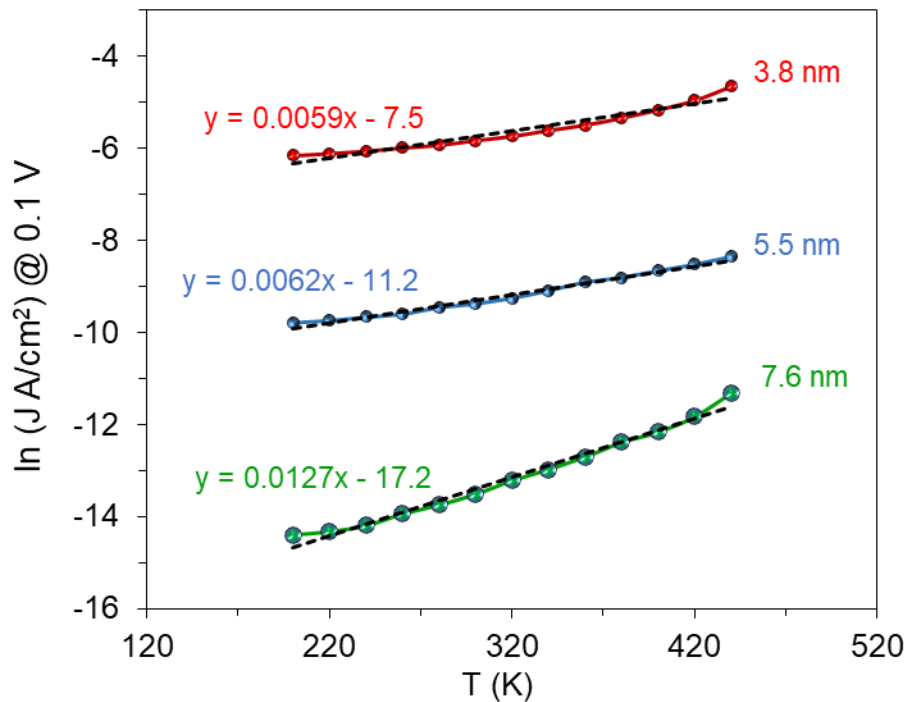


**Figure 3.13** (a)  $JV$  curves for PPF/FL<sub>3.8</sub>/eC<sub>10</sub>/Au<sub>20</sub> junction at four temperatures from 200 to 440 K in vacuum. (b)  $\ln J$  vs  $V^{1/2}$  plots for curves in panel a. (c) Arrhenius plots at 0.1, with apparent activation energies for high and low  $T$  segments. (d)  $\ln J$  vs  $T$  at 0.1 V.  $R^2$  for linear fits of the lines are indicated.



**Figure 3.14** (a)  $JV$  curves for PPF/FL<sub>7.6</sub>/eC<sub>10</sub>/Au<sub>20</sub> junction at four temperatures from 200 to 440 K in vacuum. (b)  $\ln J$  vs  $V^{1/2}$  plots for curves in panel a. (c) Arrhenius plots at 0.1, with apparent activation energies for high and low  $T$  segments. (d)  $\ln J$  vs  $T$  at 0.1 V.  $R^2$  for linear fits of the lines are indicated.

In order to have a direct comparison in temperature dependence between different thicknesses of Fluorene junction, Figure S13 shows the overlay of  $\ln J$  vs Temperature for 3.8, 5.5 and 7.6 nm of Fluorene molecular layer at  $V = 0.1$  V.



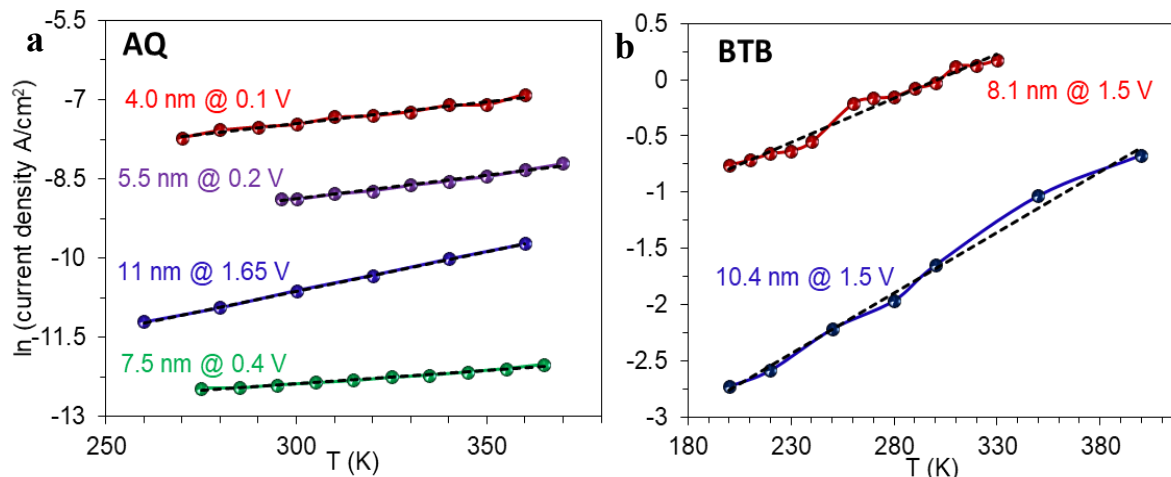
**Figure 3. 15**  $\ln J$  vs  $T$  at 0.1 V for fluorene junction at different thickness. Slopes and intercepts for linear fits of the lines are indicated.

Although these results are inconsistent with Arrhenius behavior, apparent activation energies ( $E_{act}$ ) are provided over limited temperature ranges listed in Table 3.4. For  $d = 5.5$  nm at  $V = 0.1$  V, the apparent Arrhenius slopes are 8 meV in the 200-220 K range, 51 meV for 300-320K, and 133 meV for 420-440K. We found that the plots of  $\ln J$  vs  $T$  shown in Figure 3.12- Figure **3.14d** are more linear than the Arrhenius format, with  $R^2 > 0.97$  compared to  $< 0.89$  for Figure 3.12- Figure **3.14c**. This fact remains valid for other measured thicknesses. The linearity of  $\ln J$  vs  $T$  from 240 to 440 K still indicates a temperature dependent mechanism in this range, but clearly not classical Arrhenius behavior.

**Table 3.4** Calculated apparent activation energies for Fluorene junctions

| Thickness | Voltage | $E_a$ meV<br>(200 – 220 T) | $E_a$ meV<br>(280 – 300 T) | $E_a$ meV<br>(360 – 380 T) | $E_a$ meV<br>(420 – 440 T) |
|-----------|---------|----------------------------|----------------------------|----------------------------|----------------------------|
| 3.8 nm    | 0.1 V   | 8.8                        | 33.1                       | 83.2                       | 218.1                      |
|           | 0.5 V   | 3.5                        | 17.2                       | 64.3                       | 161.0                      |
|           | 1.0 V   | 2.8                        | 15.3                       | 39.1                       | 142.4                      |
| 5.5 nm    | 0.1 V   | 8.5                        | 28.9                       | 61.0                       | 133.1                      |
|           | 0.5 V   | 5.7                        | 22.7                       | 37.9                       | 110.7                      |
|           | 1.0 V   | 3.7                        | 14.7                       | 36.6                       | 110.5                      |
|           | 1.5 V   | 0.54                       | 14.8                       | 40.1                       | 140.3                      |
| 7.6 nm    | 0.1 V   | 13.0                       | 83.9                       | 186.5                      | 408.1                      |
|           | 0.5 V   | 42.9                       | 43.4                       | 67.8                       | 423.5                      |
|           | 1.0 V   | 21.2                       | 68.9                       | 166.3                      | 352.5                      |
|           | 1.5 V   | 14.7                       | 54.7                       | 139.0                      | 398.7                      |
|           | 2.0 V   | 10.7                       | 57.5                       | 104.1                      | 420.3                      |
|           | 2.5 V   | 0                          | 26.1                       | 60.4                       | 323.6                      |

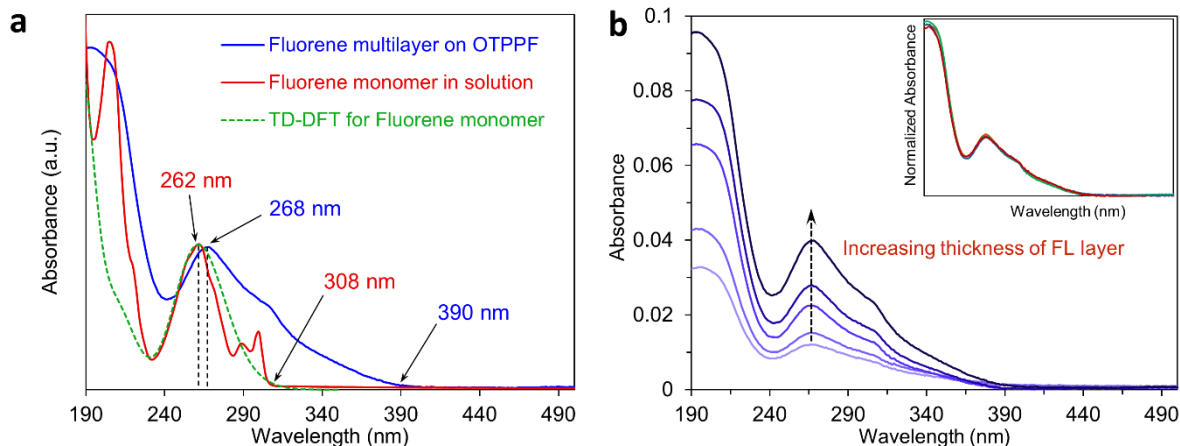
The temperature dependence of BTB was reported for a range of thicknesses previously,<sup>190</sup> and is qualitatively similar to that of FL, with low apparent activation energies and curved Arrhenius plots. If the same BTB data is replotted as  $\ln J$  vs  $T$ , linearity is observed for 8.1 and 10.4 nm, shown in Figure 3.16. AQ exhibits linearity of  $\ln J$  vs  $T$  for four thicknesses (Figure 3.16), and NAB shows apparent Arrhenius slopes of  $< 50$  meV for  $d = 3.5, 8.0$  and  $35$  nm.<sup>124</sup>



**Figure 3.16** (a)  $\ln J$  vs  $T$  for AQ junctions at indicated thickness and voltage (b)  $\ln J$  vs  $T$  for BTB at indicated thickness and voltage.

### 3.3.3 Optical Absorption by Molecular Layers

A direct indication of molecular orbital energies in the molecular layer is provided by the UV-Vis absorption spectrum of fluorene bonded to optically transparent PPF (OTPPF).<sup>121, 132, 133</sup> Here, we use UV-Vis absorption to gain insight into electronic coupling within the molecular layer and between the molecules and the contacts. Figure 3.17a shows a UV-Vis spectrum of fluorene monomer in acetonitrile, compared to that of a diazonium derived FL molecular multilayer grafted on the surface of OTPPF. In the latter case, a spectrum of unmodified PPF was subtracted to reveal the molecular layer spectrum (as described in Experimental section).



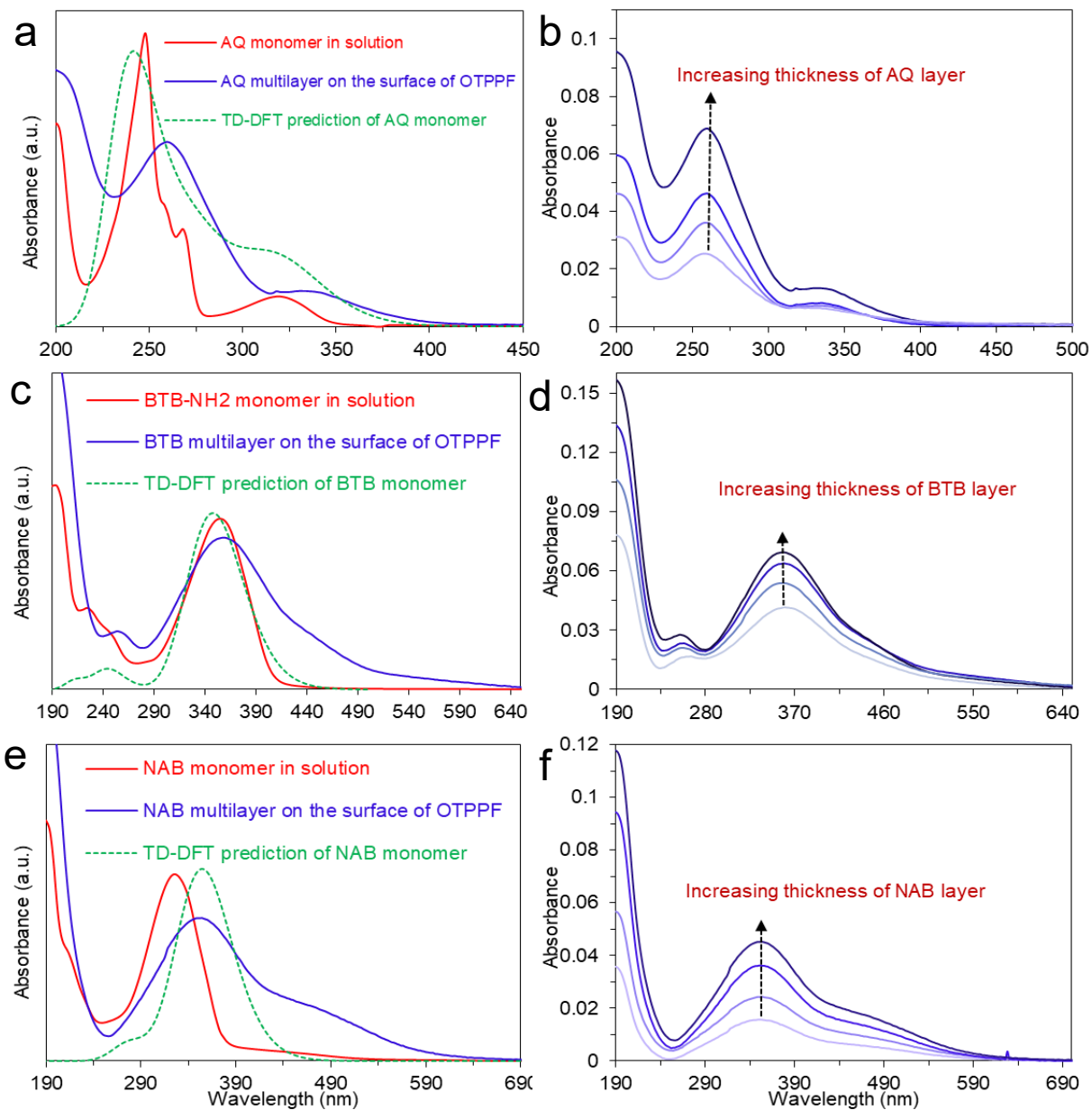
**Figure 3.17** (a) Optical absorbance spectrum of fluorene monomer in acetonitrile (red) and fluorene multilayer bonded to the surface of OTPPF (Blue), after subtraction of unmodified OTPPF spectrum. TD-DFT prediction of fluorene monomer spectrum is dashed green line. (b) Optical absorbance of four thicknesses of fluorene on OTPPF in the range of  $\sim 2$  to 9 nm. Inset: normalized spectra for different fluorene thicknesses.

There is a small (6 nm) red shift in the peak absorption wavelength upon fluorene bonding to PPF, but also a  $\sim 80$  nm red shift in the onset of the absorbance at 390 nm. At least some of this shift is due to electronic coupling<sup>192-194</sup> between the fluorene and the OTPPF, and was reported previously for OTPPF/nitroazobenzene bonded to OTPPF.<sup>133</sup> Figure 3.17b shows the absorption spectra of four films of FL on OTPPF with thicknesses increasing from  $\sim 2$  to 9 nm, as indicated. The onset of absorbance at 390 nm does *not* change with increasing thickness, and the normalized spectra in the inset show that the entire spectrum shape is unchanged with thickness. Several authors have discussed a “localization length”<sup>69</sup> or “effective conjugation length”<sup>196</sup> as the oligomer length where additional subunits no longer change the absorption spectrum.<sup>47, 169, 184, 185</sup> Tsuda, *et al.*<sup>196</sup> reported that the localization length can extend to more than 12 fused coplanar porphyrin units with 175 nm red shift per subunit. However, the localization length in non-fused aromatic oligomers can be decreased

by the nonzero dihedral angles of neighboring units and disordering in the molecular layer. For example, Choi *et al.* have shown that electronic coupling for conjugated oligophenyleneimine (OPI) wire extends over 3 repeating units with  $\sim 100$  nm red shift in the UV-Vis absorption peak and then remains constant at 400 nm for longer OPI wires.<sup>71</sup>

In the present case of Fluorene, however, increasing layer thickness does not change the absorption spectrum, and is a direct indication of weak electronic coupling between FL subunits. The large red-shift of the absorbance onset which occurs for all thicknesses of FL multilayer grafted on the surface compared to FL monomer in solution may have at least three origins: (i) electronic coupling between FL and the graphitic  $\pi$  system of the carbon electrode, (ii) intermolecular  $\pi$ - $\pi$  interactions in the FL layer, and (iii) structural variations in FL-FL coupling within the molecular layer. At least over the thickness range examined, these effects do not produce an observable change in the UV-Vis absorption spectrum with layer thickness. We conclude that a covalent bond between aromatic molecules is not enough to extend delocalization significantly beyond fluorene subunits in an oligomeric fluorene multilayer. The invariance of the UV-Vis spectrum with thickness past a few nm clearly indicates weak electronic interactions between subunits, and implies a localization length approximately equal to one or at most two fluorene molecules. Similar optical measurements and analysis is done for other molecular structure and results are compared in Figure 3.18.



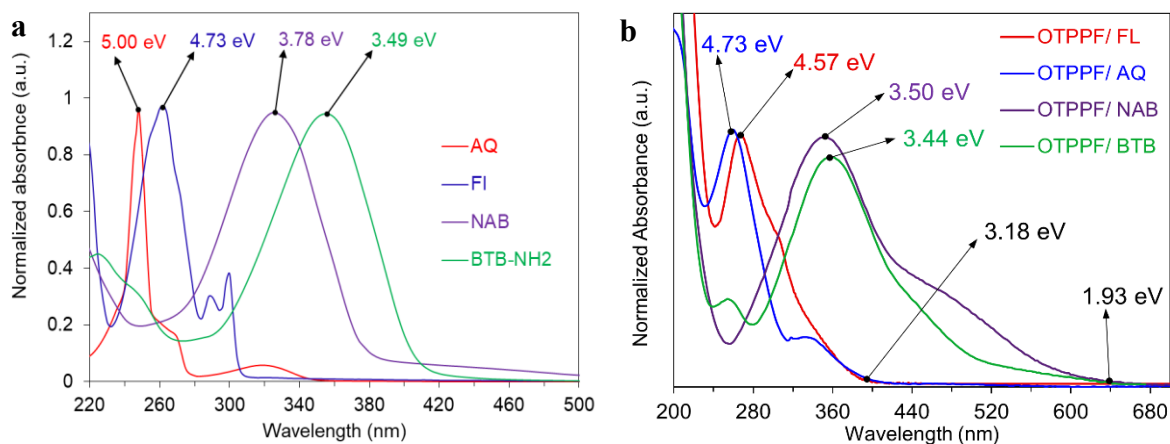


**Figure 3.18** Overlays of UV-Vis spectra of molecule's monomer in solution (ACN), multilayer on OTPPF, and TD-DFT (B3LYP 6-31G) spectra for **(a)** AQ, **(c)** BTB, and **(e)** NAB. The optical absorbance of the grafted molecules on the surface of OTPPF with increasing molecular layer thickness for **(b)** AQ, **(d)** BTB, and **(f)** NAB.

Consideration of the molecular layer as a series of weakly interacting molecular orbitals is an important factor in controlling transport, and is discussed in more detail below.

### 3.3.4 Structural Effects on Junction Behavior

To investigate effects of molecular structure on the electronic behavior observed for fluorene MJs, anthraquinone (AQ) and nitroazobenzene (NAB) films and devices were investigated, and compared to BTB reported previously.<sup>190</sup> The UV-Vis spectra of the FL, AQ, NAB, and BTB bonded to OTPPF are compared in Figure 3.19b after subtraction of the unmodified PPF spectrum, and Table 3.5 lists the optical gap and absorption onsets as well as DFT predictions. Also, UV-Vis absorption spectra for monomer of molecules in acetonitrile solution is shown in Figure 3.19a to be compared with the multilayers grafted on the surface (Figure 3.19b). Notice that both the peak absorption and onset of absorption occur at significantly lower energy for BTB and NAB compared to AQ and FL. It is apparent that the absorption onset for molecules bonded to OTPPF shows a significant red shift compared to monomers in solution, but the peak and onset wavelengths do not vary further with increasing thickness. Salient absorbance spectra for the four molecules are summarized in Table 3.5.



**Figure 3.19 (a)** UV-Vis absorption spectra for the indicated monomeric molecules in acetonitrile solution, with concentrations near  $1 \times 10^{-4}$  M. Spectra were normalized to their absorbance maxima to

permit comparison. **(b)** Absorbance spectra for FL, AQ, NAB and BTB multilayers bonded to OTPPF, all following subtraction of unmodified OTPPF spectrum.

**Table 3.5** Orbital Energies, UV-Vis absorption and Current Densities

|   | FL                     | AQ                     | NAB                    | BTB                    |
|---|------------------------|------------------------|------------------------|------------------------|
| DFT LUMO <sup>a</sup> (eV)                          | -0.71                  | -2.76                  | -3.03                  | -1.48                  |
| DFT HOMO <sup>a</sup> (eV)                          | -5.75                  | -7.00                  | -6.66                  | -5.29                  |
| DFT H-L gap (eV)                                    | 5.04                   | 4.24                   | 3.63                   | 3.81                   |
| TD-DFT peak <sup>b</sup> (eV)                       | 4.71                   | 5.12                   | 3.49                   | 3.52                   |
| UV-Vis peak <sup>b,c</sup> (eV)                     | 4.57                   | 4.73                   | 3.50                   | 3.44                   |
| UV-Vis onset <sup>c</sup> (eV)                      | 3.18                   | 3.12                   | 1.93                   | 1.93                   |
| J (8 nm) <sup>d</sup> , A/cm <sup>2</sup> , @ 0.5 V | 2.2 x 10 <sup>-6</sup> | 1.7 x 10 <sup>-6</sup> | 6.1 x 10 <sup>-5</sup> | 2.9 x 10 <sup>-4</sup> |
| J (10 nm) <sup>d</sup> , A/cm <sup>2</sup> @ 0.5 V  | -                      | 2.1 x 10 <sup>-8</sup> | 5.2 x 10 <sup>-6</sup> | 1.2 x 10 <sup>-4</sup> |

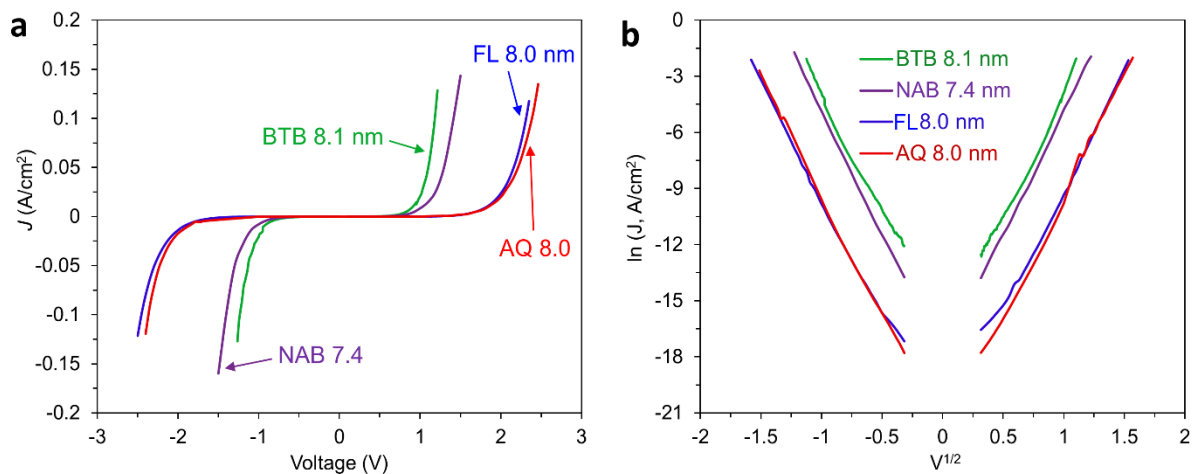
a. for free molecule monomers vs vacuum reference, B3LYP 6-31G(d)

b. major peak predicted for the free molecule in region of 200-700 nm

c. peak or onset for molecular multilayer bonded to OTPPF, after OTPPF spectrum subtracted.

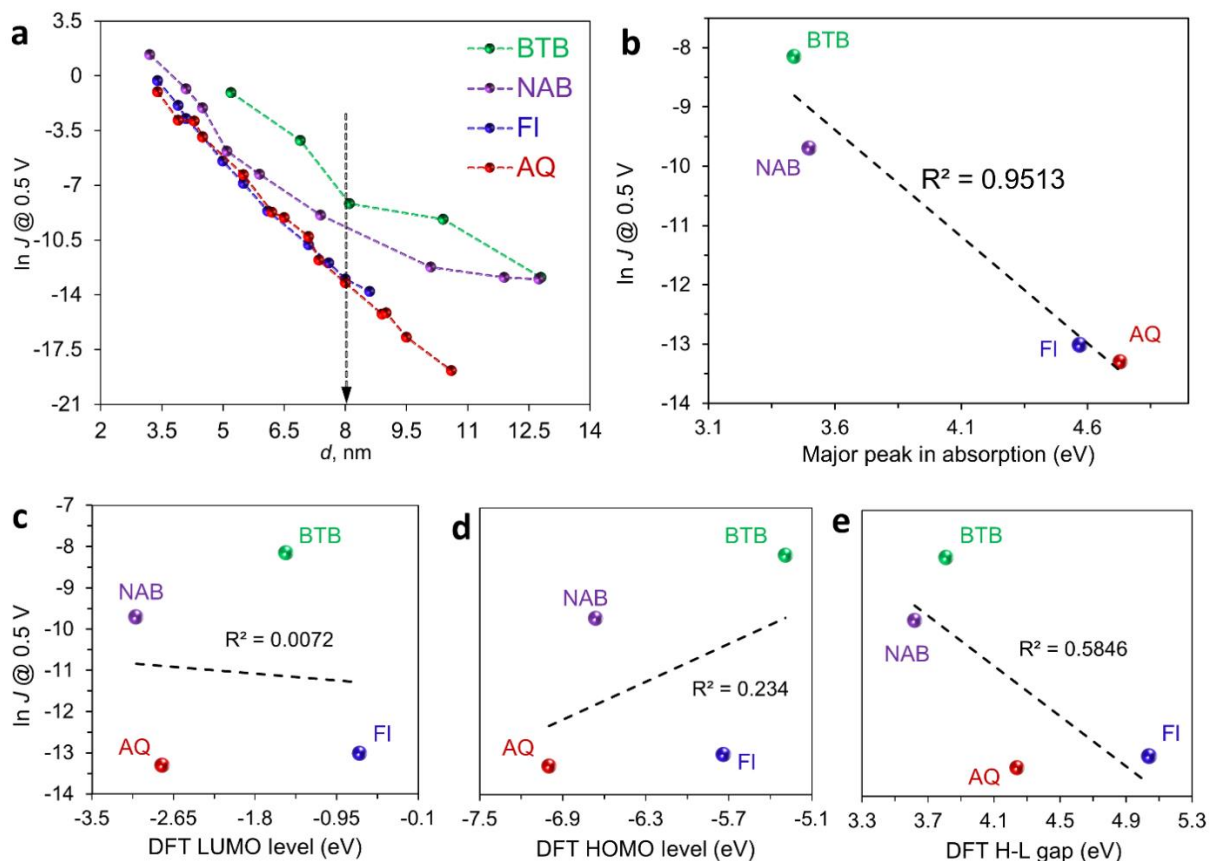
d. interpolated from attenuation plot of Figure 3.21.

Molecular junctions were fabricated with the same PPF/molecule/eC/Au junction structure in all cases and  $d$  ranging from 3-13 nm.  $JV$  curves for the four molecules similar thicknesses in the range of  $d = 7.4$  to 8.1 nm are shown in Figure 3.20a, all exhibiting symmetry with bias and similar shape. However,  $J$  for BTB and NAB is much higher than that of FL and AQ, by a factor of  $\sim 100$  for  $V = \pm 1$  V. Plots of  $\ln |J|$  vs  $V^{1/2}$  for the same examples shown in Figure 3.20b, showing linearity similar to Fluorene ( $R^2 = 0.9902$  to 0.9992 for all four cases) and large difference in  $J$  over the entire bias range.



**Figure 3.20** (a)  $JV$  curves of BTB, NAB, FL and AQ with thicknesses close to 8 nm. (b)  $\ln |J|$  vs  $V^{1/2}$  plots for curves in panel a.

A statistically more valid comparison of the four molecules over a wide thickness range is the attenuation plot of Figure 3.21a, which incorporates data from  $\sim 120$  MJIs with the PPF/molecule/eC/Au structure. Note that all four molecules have  $\beta$  values near  $2.7 \text{ nm}^{-1}$  for  $d < 5 \text{ nm}$ , and that FL and AQ are indistinguishable, with both equal  $\beta$  and equal  $J$  over the range of  $d = 3.4 - 8.6 \text{ nm}$ . However, BTB and NAB depart significantly from the  $\beta \sim 2.7 \text{ nm}^{-1}$  line when  $d$  exceeds  $5 \text{ nm}$ , resulting in very different attenuation slopes (e.g.  $\sim 1.0 \text{ nm}^{-1}$  for BTB above  $8 \text{ nm}$ <sup>190</sup>). Note that for  $d \sim 10 \text{ nm}$ ,  $J$  for NAB at  $0.5 \text{ V}$  is  $> 250$  times greater than that for AQ, while  $J$  for BTB is  $> 5000$  times larger than that for AQ.



**Figure 3.21** (a) Attenuation plots for BTB, NAB, FL, AQ, all obtained at 0.5 V. (b)  $\ln J$  for  $V=0.5 \text{ V}$  and  $d=8 \text{ nm}$  for the four molecules plotted vs the energy of the main UV-Vis absorption peak of the molecular layer.  $R^2$  is the correlation coefficient for the linear fit shown. (c) The same  $\ln J$  plotted vs the DFT determined LUMO energy of the free molecules (d)  $\ln J$  vs free molecule HOMO energy from DFT. (e)  $\ln J$  vs the DFT determined HOMO-LUMO gap.

### 3.4 DISCUSSION

The experimental results demonstrate several unusual and in some cases unexpected aspects of transport in conjugated carbon-based molecular junctions. First, the exponential dependence of current on molecular layer thickness persists well beyond 5 nm, up to  $d = 8.6 \text{ nm}$  for FL and  $d = 10.6 \text{ nm}$  for AQ (Figure 3.21a). Second, linear  $\ln J$  vs  $V^{1/2}$  behavior was observed for all four molecules over a range of thicknesses, instead of the  $\ln J$  vs  $V$  linearity

expected for coherent tunneling (Figure 3.11). Third, the optical gap of all four molecules is red shifted upon bonding to PPF, particularly the onset of absorbance at long wavelengths. However, the UV-Vis absorption spectrum is not further red shifted with increasing thickness of molecular layers for all four molecules (Figure 3.17-Figure 3.19). Fourth, the temperature dependence does not exhibit linear Arrhenius behavior anywhere between 200 and 440 K for the tested molecules, and the apparent activation energy decreases to less than 20 meV below ~250 K. For AQ, FL and BTB,  $\ln J$  vs  $T$  is more linear ( $R^2$  typically  $> 0.94$ ) than  $\ln J$  vs  $1/T$  ( $R^2$  typically 0.80-0.89).

The results also show clear inconsistencies with transport mechanisms reported for other types of junction fabrication and molecular structures. The linearity of the attenuation plots for FL and AQ, and the similarity of  $JV$  curve shapes over the 2-11 nm thickness range is not expected if the transport mechanism changes above 3-5 nm, as proposed for several other conjugated systems<sup>46, 71, 187-189</sup>. Furthermore, fitting the FL results to a Simmons tunneling model with both image charge and effective mass corrections ( $m^*/m_o = 0.3$ ,  $\epsilon = 6$ )<sup>130</sup> requires a reduction of the barrier height from 2.2 eV for  $d = 3.4$  nm to 0.75 eV for  $d = 8.6$  nm to yield the observed currents. Such a reduction is physically unreasonable and is contradicted by the UV-Vis absorption results, which show little change in absorption spectrum for both FL and AQ with layer thickness. Inspection of Figure 3.21c-d and Table 3.5 leads to serious inconsistencies with a “single level” model based on a tunneling barrier between the electrode Fermi level and either the molecular HOMO or LUMO. The PPF and e-Carbon Fermi levels determined from Kelvin probe and ultraviolet photoelectron spectroscopy (UPS) are both -4.8 V vs vacuum<sup>38, 197</sup>. From free molecule DFT energies, the HOMO or LUMO offsets for FL and AQ should differ by  $>2$  eV (for LUMOs) or  $>1.2$  eV

(for HOMOs) which should result in a large difference in tunneling current due to the resulting changes in barrier height. However, Figure 3.21a shows that the current densities for FL and AQ are very similar over a 2-9 nm thickness range and Figure 3.21c-d show no correlation between the DFT HOMO and LUMO levels and the observed current density at  $V = 0.5$  V when  $d \sim 8$  nm.

These observations contradict a model assuming a tunneling barrier determined by the offsets of either the HOMO or LUMO relative to the electrode Fermi level. The similarity of transport for AQ and FL when  $d < 5$  nm may be caused by strong coupling to the electrodes,<sup>58, 192, 194</sup> but only if such coupling extends up to and beyond 8 nm. Not only is this contradicted by the UV-Vis results, but NAB and BTB do show significant departures from  $\beta$ -linearity for  $d > 5$  nm. Although there is poor correlation of individual orbital energies with junction current, the HOMO-LUMO (H-L) gap correlates much better, determined either from the DFT energies (Figure 3.21e,  $R^2 = 0.585$ ) or from the UV-Vis absorption maxima of the molecular layer (Figure 3.21b,  $R^2 = 0.951$ ). The junction current also correlates well ( $R^2 = 0.905$ ) with the optical H-L gap predicted from TD-DFT for each of the four molecules, provided in Table 3.5. The consequences of this correlation are significant, in that the results imply that the H-L gap determines transport when  $d > 5$  nm, rather than the relationship of either the HOMO or LUMO energies to the contact Fermi level.

A transport mechanism controlled by the H-L gap instead of the offset of either the HOMO or LUMO levels from the contact Fermi level is possible in carbon based systems with some significant modifications to common models for transport in molecular junctions. First, suppose transport is “bulk” controlled rather than “interface” controlled. The strong electronic coupling between PPF and aromatic molecules and the linearity of the  $\beta$  plot over

>8 nm imply that interfacial transport is *not* rate limiting. Provided interfacial “injection” of carriers is faster than transport in the film interior, the offsets between orbitals and the electrode Fermi levels should not affect the current density. Second, coherent tunneling may dominate transport only in a situation where the tunneling distance is not much greater than the localization length.<sup>69</sup> The absence of changes in the UV-Vis spectra with thickness indicates limited delocalization within the molecular layer, since strong electronic coupling between molecules should decrease the optical gap for higher  $d$ . In the case of weak intermolecular interactions, transport might occur along a series of localized states, perhaps as small as a HOMO or LUMO orbital of individual molecules. Transport by a series of tunneling steps between localized states has been considered for several decades, and is related to common mechanisms in disordered organic films, such as nearest neighbor hopping (NNH) and variable range hopping (VRH).<sup>57, 74, 75, 79, 198</sup> Linearity of  $\ln J$  with  $T$  instead of  $1/T$  is predicted in the case of thermally assisted or multistep tunneling,<sup>79, 80, 199, 200</sup> and is consistent with the nearly linear  $\ln J$  vs  $T$  behavior for Fluorene MJs shown in Figure 3.12d and for BTB and AQ MJs shown Figure 3.16.

#### 3.4.1 Discussion about relevance of Pool-Frankel and Schottky mechanism

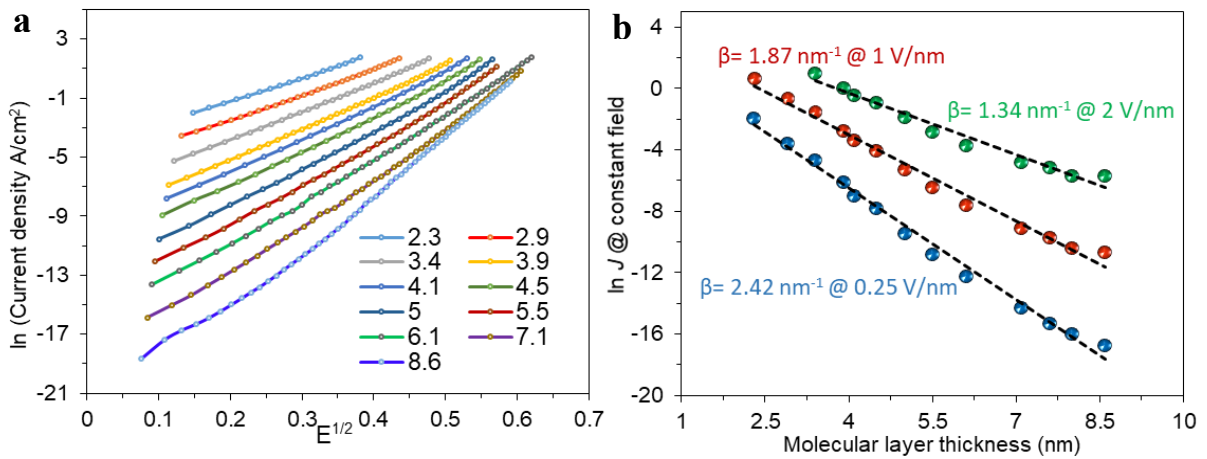
The linearity of  $\ln J$  with  $V^{1/2}$  apparent in Figure 3.11 is expected for Poole-Frankel transport between “traps” or Schottky emission at interfaces, as noted above. A recent report on transport in molecular junctions containing iron-porphyrin multilayers with  $d > 10$  nm concluded that the linear  $\ln J$  vs  $V^{1/2}$  behavior observed was due to Schottky emission at the electrode interfaces.<sup>201</sup> Both PF and Schottky include a field dependent barrier height ( $\phi$ ), given by equation (1), where  $\phi_0$  is the barrier height at zero field,  $q$  is the elementary charge,



$\epsilon$  the relative dielectric constant of the molecular layer,  $\epsilon_0$  the permittivity of free space, and  $V$  and  $d$  were defined previously:

$$\phi = \phi_0 - \left( \frac{q}{4d\pi\epsilon\epsilon_0} \right)^{1/2} V^{1/2} \quad (\text{eq 3.1})$$

Schottky and Pool-Frankel are field dependent charge transport mechanisms, in a sense that at constant field for different thicknesses of the molecular layer, there should be constant conductivity. Figure 3.22-a shows  $\ln J$  of Fluorene junctions versus  $E^{1/2}$  for a range of thicknesses. The lines are not parallel anymore like Figure 3.11 but still, they don't converge to the single line. In order to make it clear, Figure 3.22-b shows the corresponding attenuation plot at constant applied field.



**Figure 3.22 (a)**  $\ln J$  vs  $E^{1/2}$  plots for curves for Fluorene junctions with thickness indicated in nm. **(b)** Attenuation plot at the constant field for the line shown in panel a at  $E = 0.25, 1$  and  $2$  V/nm, with the slopes ( $\beta$ ) indicated.

It is apparent from the Figure 3.22-b that there is an exponential dependence between current density and thickness at the constant field, and the attenuation slope ( $\beta$ ) is field dependent.

With attention to the equation 3.2 and 3.3 for Schottky emission and P-F mechanism, it means that the barrier height ( $\phi_0$ ) and dielectric constant ( $\epsilon$ ) are changing with thickness:

$$\text{Schottky equation: } \ln J = \ln AT^2 - \left( \frac{\phi_0 - \left( \frac{q}{4\pi\epsilon\epsilon_0} \right)^{1/2}}{kT} \right) E^{1/2} \quad (\text{eq 3.2})$$

$$\text{Pool-Frankel equation: } \ln \left( \frac{J}{E} \right) = \ln N_0 q \mu - \left( \frac{\phi_0 - \left( \frac{q}{\pi\epsilon\epsilon_0} \right)^{1/2}}{kT} \right) E^{1/2} \quad (\text{eq 3.3})$$

Where,  $A$  is the Richardson constant,  $\phi_0$  barrier height,  $\epsilon_0$  the permittivity of vacuum,  $k$  the Boltzmann constant, and  $q$  the electron charge.  $\mu$  and  $N_0$  are the mobility of carrier and the number of traps at zero field, and they are assumed constant at  $1 \times 10^{-6}$  cm/V.s and  $1 \times 10^{17}$  e/cm<sup>3</sup>, respectively. The fitting was done with two variable, barrier height ( $\phi_0$ ) and dielectric constant ( $\epsilon$ ). The obtained values from the fitting of Schottky and Pool-Frankel are listed in Table 3.6 and Table 3.7, respectively.

**Table 3.6** Parameters obtained by fitting of Pool-Frankel mechanism to experimental data.

| Thickness<br>(nm) | Barrier height<br>$\phi_0$ (eV) | Dielectric<br>constant ( $\epsilon$ ) | $R^2$  | Activation energy ( $E_a$ meV) <sup>b</sup> |                   |                   |
|-------------------|---------------------------------|---------------------------------------|--------|---|-------------------|-------------------|
|                   |                                 |                                       |        | @ 0.1 V                                     | @ 0.5 V           | @ 1.0 V           |
| 2.3               | -0.04                           | 78.86                                 | 0.9296 | -104 <sup>a</sup>                           | -152 <sup>a</sup> | -189 <sup>a</sup> |
| 2.9               | 0.01                            | 47.30                                 | 0.9552 | -61 <sup>a</sup>                            | -117 <sup>a</sup> | -158 <sup>a</sup> |
| 3.4               | 0.03                            | 59.48                                 | 0.9685 | -26 <sup>a</sup>                            | -92 <sup>a</sup>  | -141 <sup>a</sup> |
| 3.9               | 0.07                            | 45.03                                 | 0.9753 | 16  | -56 <sup>a</sup>  | -110 <sup>a</sup> |
| 4.1               | 0.12                            | 28.94                                 | 0.9781 | 50  | -36 <sup>a</sup>  | -100 <sup>a</sup> |
| 4.5               | 0.14                            | 28.43                                 | 0.9781 | 72  | -11 <sup>a</sup>  | -73 <sup>a</sup>  |
| 5.0               | 0.23                            | 15.10                                 | 0.9801 | 143   | 35                | -46 <sup>a</sup>  |
| 5.5               | 0.23                            | 18.83                                 | 0.9818 | 154   | 62                | -7 <sup>a</sup>   |
| 6.1               | 0.28                            | 15.33                                 | 0.9868 | 198   | 101               | 28                |
| 7.1               | 0.34                            | 12.24                                 | 0.9841 | 258   | 157               | 82                |

|     |      |       |        |     |     |     |
|-----|------|-------|--------|-----|-----|-----|
| 7.6 | 0.38 | 10.51 | 0.9810 | 288 | 183 | 104 |
| 8.0 | 0.40 | 9.53  | 0.9800 | 316 | 208 | 128 |
| 8.6 | 0.42 | 8.59  | 0.9813 | 334 | 225 | 143 |

*a* When the barrier height is small, even low applied bias can make the sign of effective barrier height negative in Pool-Frankel equation, which obviously doesn't have physical meaning.

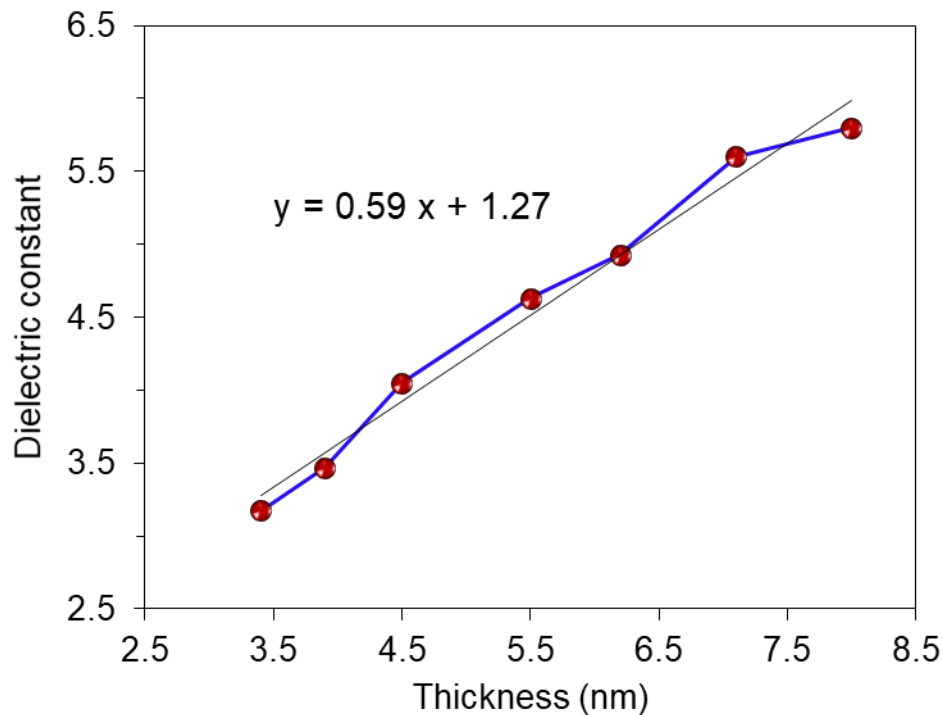
*b* Activation energies are calculated based on the fitted barrier height and dielectric constant.

**Table 3.7** Parameters obtained by fitting of Schottky mechanism to experimental data

| Thickness (nm) | Barrier height $\phi_0$ (eV) | Dielectric constant ( $\epsilon$ ) | $R^2$  | Activation energy ( $E_a$ meV) <sup>a</sup> |         |         |
|----------------|------------------------------|------------------------------------|--------|---|---------|---------|
|                |                              |                                    |        | @ 0.1 V                                     | @ 0.5 V | @ 1.0 V |
| 2.3            | 0.54                         | 8.21                               | 0.9988 | 447   | 339     | 258     |
| 2.9            | 0.59                         | 6.79                               | 0.9988 | 497   | 389     | 308     |
| 3.4            | 0.62                         | 5.68                               | 0.9991 | 532   | 425     | 345     |
| 3.9            | 0.66                         | 4.90                               | 0.9992 | 574   | 466     | 384     |
| 4.1            | 0.69                         | 4.16                               | 0.9977 | 600   | 487     | 402     |
| 4.5            | 0.72                         | 3.80                               | 0.9972 | 630   | 517     | 432     |
| 5.0            | 0.77                         | 3.19                               | 0.9801 | 674   | 556     | 468     |
| 5.5            | 0.81                         | 2.79                               | 0.9969 | 714   | 595     | 505     |
| 6.1            | 0.86                         | 2.45                               | 0.9972 | 758   | 636     | 546     |
| 7.1            | 0.92                         | 2.03                               | 0.9967 | 820   | 696     | 604     |
| 7.6            | 0.96                         | 1.76                               | 0.9954 | 852   | 724     | 628     |
| 8.0            | 0.98                         | 1.69                               | 0.9946 | 874   | 747     | 651     |
| 8.6            | 1.00                         | 1.49                               | 0.9947 | 899   | 768     | 670     |

*a* Activation energies are calculated based on the fitted barrier height and dielectric constant

Apart from the physically unreasonable values of fitted barrier height and dielectric constant, the trend of changing parameters with thickness could be more important. The fitting analysis shows the significant decrease in dielectric constant with increasing thickness for both P-F and Schottky mechanism. Dielectric constant for the Fluorene junctions were measured experimentally by means of impedance spectroscopy. The result shown in Figure 3.23, indicate opposite trend for changing dielectric constant with thickness.



**Figure 3.23** Dielectric constant measured by impedance spectroscopy for Fluorene junctions versus thickness of Fluorene molecular layer.

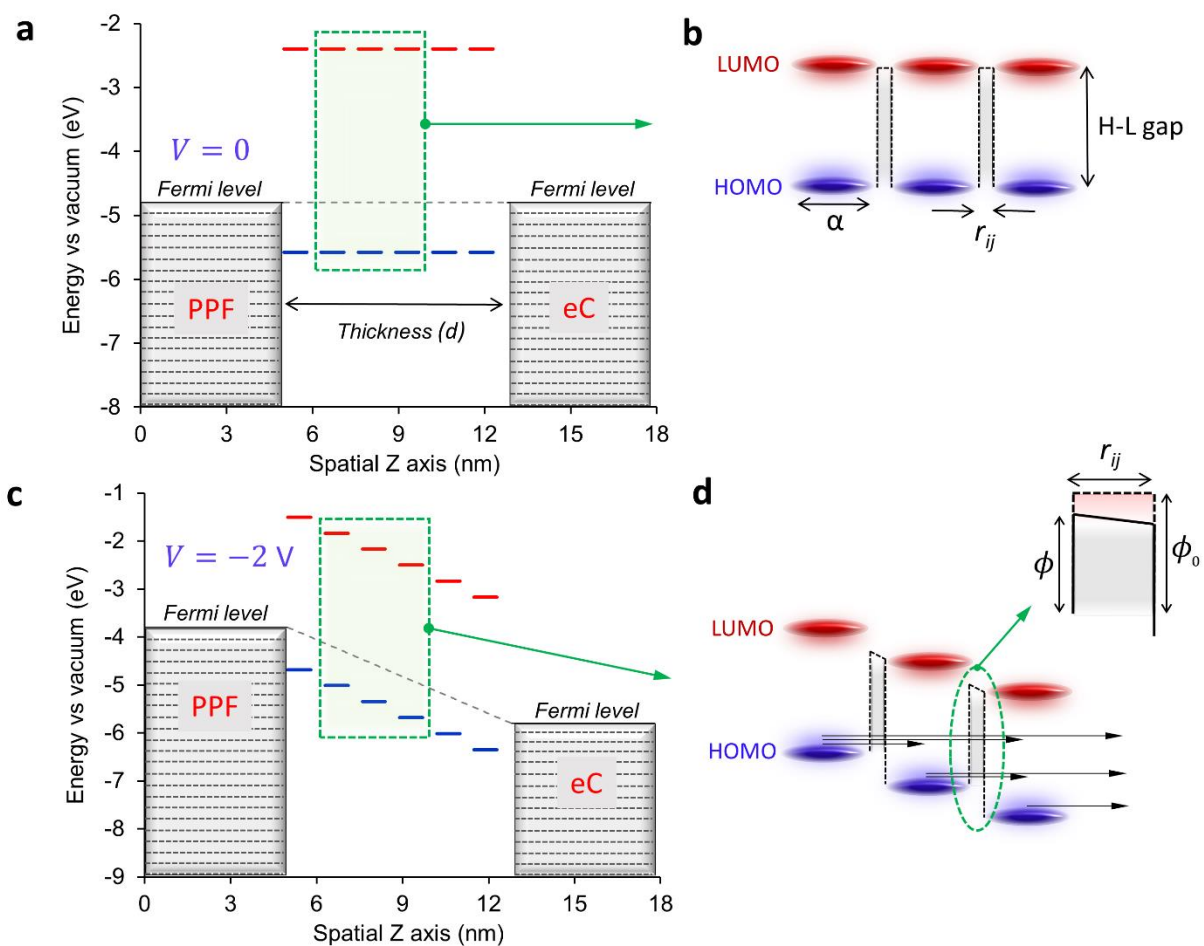
Attempts to fit the Poole-Frankel or Schottky mechanisms to the observed  $JV$  curves for FL with varying thickness yielded physically unreasonable parameters, with barrier heights and dielectric constants that vary significantly with  $d$  (Table 3.6 and Table 3.7). PF and Schottky emission should show Arrhenius temperature behavior with much stronger  $T$

dependence than any of the MJs reported here. However, the barrier height for sequential tunneling can also exhibit a dependence on electric field *via* equation (1), and thus yield  $\ln J$  vs  $V^{1/2}$  linearity, distinguished from Schottky or P-F mechanisms by weak temperature dependence (linearity of  $\ln J$  with  $T$ ) and high thickness dependence.<sup>80, 199, 200</sup> Unlike the conclusion for Fe-porphyrin MJs,<sup>201</sup> transport in the carbon-based MJs studied here is controlled by “bulk” properties of the organic layer rather than “injection” at the interfaces. *In effect, transport barriers associated with the electrode/molecule interface become irrelevant to transport, provided electronic coupling at the interfaces is strong compared to that between localized states within the molecular layer interior.*

### 3.4.2 Proposed multistep tunneling mechanism

The schematic of Figure 3.24a depicts several elements of the proposed mechanism for multi-step tunneling transport. Six pairs of HOMO and LUMO states represent the molecular layer, where each orbital may be localized on one or at most two FL molecules, with a localization length of  $\alpha$  shown in Figure 3.24b. These orbitals are broadened by disorder, electronic coupling and vibrational states, and are separated by a distance  $r_{ij}$ , resulting in a tunneling barrier with a height equal to the H-L gap and width equal to  $r_{ij}$ . Note that the orbital energies near the electrode interfaces are perturbed by electronic coupling with the contacts, and may shift and broaden relative to the electrode Fermi level by partial charge transfer to the electrodes, often called a “vacuum level shift”.<sup>58, 68, 202, 203</sup> Provided “injection” of carriers is fast relative to bulk transport, the observed current is limited by tunneling through the H-L barrier and tunneling may occur across more than one H-L gap (as shown in Figure 3.24d). In an applied electric field (Figure 3.24c and d), the barrier height is

reduced, as shown in the inset of Figure 3.24d. Under this model the important factors controlling the current density are the H-L gap in the “bulk” molecular layer,  $r_{ij}$ ,  $\alpha$ , and the number of steps required to transit across layer thickness  $d$ . The relative energies of the orbitals and the electrode Fermi level are not relevant to transport, since the rate limiting step is tunneling across the H-L barrier within the molecular layer interior. A transport mechanism controlled by the molecular layer properties rather than the contacts, as we propose here, may be an advantage of aromatic carbon contacts such as  $sp^2$  hybridized carbon or graphene. Several recent reports using carbon based molecular junctions have identified attractive electronic properties and/or high stability when molecules are covalently bonded to carbon contacts.<sup>38, 110, 173, 204</sup>



**Figure 3.24** (a) Energy level diagram at zero bias for a fluorene junction with six pair of localized HOMO and LUMO states, using free molecule DFT energies and a PPF Fermi level of  $-4.8$  eV. (b) Magnification of three paired H-L states.  $\alpha$  and  $r_{ij}$  are the localization length and tunneling distance between two neighboring states. (c) The same diagram as panel a for  $V = -2$  V bias (PPF negative), assuming a linear potential profile through the molecular layer. (d) Magnification of panel c, with inset showing the tunneling barrier with height  $\phi_0$  at zero bias and  $\phi$  with bias applied. Arrows indicate possible tunneling paths for electrons.

Finally, the current multistep tunneling model depends on “sites” separated by a barrier determined by the H-L gap in the film interior, and assumes relatively rapid carrier transport at the carbon electrode interfaces due to strong electronic coupling between the graphitic  $\pi$  system and the aromatic molecules. At the simplest limit, an electron moves from the HOMO of the molecule at an electrode interface into the electrode, thus creating a hole which is filled by tunneling from a nearby HOMO through the H-L barrier. Depending on the time scale, the hole could result in reorganization, leading to polaron formation and a mechanism similar to “polaron tunneling” proposed recently by Taherinia, *et al.*<sup>169</sup> The small activation energies observed in the current devices, particularly at low  $T$ , are evidence against reorganization to a polaron being a prerequisite for transport, and are more consistent with a multi-step tunneling model such as that presented in Figure 3.24. In addition, a Marcus transport mechanism is not likely governing transport in the cases studied here for several reasons: (i) Temperature dependent experiment does not show the Arrhenius relation and  $\ln J$  of conductivity is linear with  $T$  rather than  $1/T$ , (ii) If the Marcus would be dominant transport mechanism, the beta should not be extended to 11 nm of molecular layer and expected beta for Marcus theory should be below  $0.5 \text{ nm}^{-1}$ , (iii) Outstanding linearity of  $\ln J$  with  $V^{1/2}$  in wide range of applied voltage and thickness of molecular layer is not predicted for Marcus transport, iv) The data shows clear correlation between the conductivity and H-L

gap of the examined molecules; however, the effective barrier in Marcus theory is associated with reorganization and not necessarily the H-L gap. Current research is focused on confirming the importance of the H-L gap to determining conductance in carbon-based molecular junctions, and investigating the generality of observation that carrier injections is not rate limiting.

### 3.5 CONCLUSION

Charge transport in aromatic carbon/molecule/carbon molecular junctions is strongly affected both by electronic coupling between the electrodes and the molecules, and by relatively weak coupling between oligomer subunits. As a result, efficient transport does not correlate with the energies of molecular orbitals relative to the electrode Fermi levels, but is directly controlled by the HOMO-LUMO energy gap in the molecular layer interior. The factors of >1000 differences in conductance with variations in molecular structure observed for  $d=10$  nm result from changes in the H-L gap indicated directly by UV-Vis absorption of molecular layers bonded to graphitic carbon. The unusual linearity of  $\ln J$  with  $V^{1/2}$  observed for all four molecules is consistent with lowering of the H-L tunneling barrier in the applied electric field, and the weak temperature dependence is expected for a multistep, sequential tunneling mechanism. The important parameters controlling electron transport are the H-L energy gap within the molecular layer, the tunneling distance between molecular orbitals ( $r_{ji}$ ), the localization length ( $\alpha$ ), and the number of steps required to traverse the molecular layer. At least for the case of strong electronic coupling between carbon electrodes and aromatic molecular layers, the findings provide useful guidance for rational design of molecular electronic devices with desired electronic behaviors.



# CHAPTER 4

## Orbital Control of Photocurrents in Large Area All-Carbon Molecular Junctions

## 4.1 INTRODUCTION

Molecular electronics (ME) refers to a research area pursuing the idea of using single molecules or layers of molecules as nanoscale functional building blocks in electronic devices<sup>1, 5, 9, 11, 13</sup>. ME has resulted in reported devices capable of handling a variety of electronic functions, including nonlinear resistance,<sup>101, 102</sup> rectification,<sup>21, 103-105</sup> memory,<sup>106-108</sup> and conductance switching.<sup>109, 110</sup> Recent advances in measurement capabilities and fabrication techniques have enabled researchers to push the frontiers of ME beyond the investigation of charge transport to broader aspects of spintronics,<sup>205, 206</sup> plasmonics,<sup>87, 123, 125</sup> optoelectronics,<sup>99, 207</sup> and thermoelectric effects.<sup>84, 208</sup> Molecular optoelectronics is an interdisciplinary research area that studies the interaction of light with the functioning molecular junction (MJ).<sup>97</sup> Apart from novel and potentially important applications, optoelectronic measurements can provide a direct and valuable diagnostic of electron transfer mechanism and energy level alignment of molecular layers in contact with electrodes in “molecular junctions (MJ)”.<sup>1, 97</sup> Detailed understanding of how molecular structure affects the energy landscape and charge transport in molecular devices is a core aspiration of molecular electronics, which should enable rational design of the molecular devices for the functions and characteristics which are difficult or impossible with conventional semiconductors.

Photocurrents generated by internal photoemission (IPE) have been used to probe energy barriers in classical inorganic tunnel junctions, and more recently in molecular electronic devices.<sup>121, 209-211</sup> The minimum photon energy required to generate a photocurrent (PC) is directly related to internal energy barriers, often the offsets between the contact Fermi levels and the highest occupied molecular orbital (HOMO) or lowest unoccupied molecular

orbital (LUMO), depending on the molecule involved. The PCs observed in thin molecular junctions (thickness,  $d < 4$  nm), with copper as a partially transparent top contact are consistent with the IPE mechanism, provided the photon energy is in a region where light absorption by direct HOMO-LUMO (H-L) transitions in the molecule is insignificant.<sup>121, 209</sup> The energy barriers observed with IPE on carbon/molecule/Cu MJs are similar to those measured by Ultraviolet Photoelectron Spectroscopy, and are consistent with transport measurements of similar MJs.<sup>58, 121, 209</sup> However, charge transport in carbon/molecule/Cu MJs with  $d < 5$  nm is weakly dependent on variations in molecular structure for aromatic molecules due to the strong electronic coupling between the molecular layer and the contacts.<sup>58, 212, 213</sup> Such coupling results in realignments of energy levels in the molecules from those of the isolated molecules, thus reducing the influence of orbital energies on transport barrier height.

Several reports have appeared on changes in transport behaviour when the molecular layer thickness exceeds 4-5 nm, some of which are attributed to a change in mechanism from coherent tunneling to an alternative “hopping” mechanism.<sup>46, 71, 101</sup> Recently, we showed that transport beyond 5 nm in carbon-based aromatic molecular junctions is controlled by the structure and orbital energies of the molecular layer.<sup>101</sup> We proposed multistep tunneling as a dominant transport mechanism, with a barrier determined by the H-L gap, and not by the charge injection barrier at the molecule/electrode interface. While coherent transport (single step tunneling) is not expected for across distances longer than 4-5 nm, PCs provide a potentially informative probe of internal energy levels in completed MJs, in order to elucidate how molecular structure affects transport.

We report herein an investigation of origins of the PC response in the large area carbon based MJs with  $d > 5$  nm and a variety of molecular structures. The “all carbon” MJ structure consisting of covalently bonded oligomers between electron-beam deposited carbon electrodes provided contacts with equal work functions and sufficient optical transparency to permit light transmission through the entire, functioning molecular junction. We demonstrate that both the H-L gap in the molecular layer and the energy offset of the frontier molecular orbitals relative to the electrode Fermi energy ( $E_F$ ) affect the PC, such that unequivocal assignment of the carrier sign becomes possible. The results are consistent with multistep tunneling through the H-L gap as the barrier for charge transfer within molecular layers thicker than 5 nm. Not only do PCs provide a diagnostic of device properties and transport mechanisms, but the results are also relevant to rational design of molecular electronic devices with unusual electronic behaviours.

## 4.2 EXPERIMENTAL SECTION

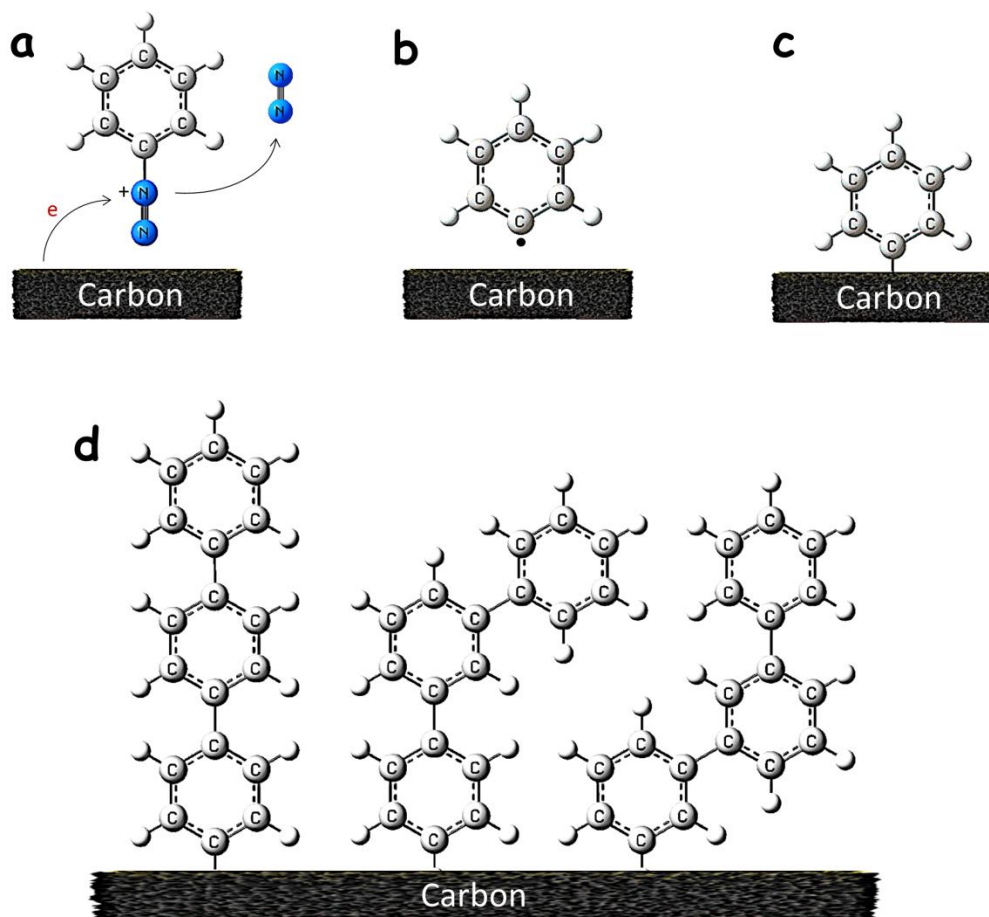
### 4.2.1 Junction fabrication

Large area molecular junctions were fabricated by established procedures<sup>38</sup> on as described in chapter 2 with covalently bonded molecular layer thicker than 4 nm. eC is a form of amorphous conducting carbon with 30-40 %  $sp^3$  hybridized carbon and the remainder  $sp^2$  carbon.<sup>38</sup> The bottom contact consists of the successive electron-beam deposition of Cr, Au, and eC. Combining adhesion ability of the deposited Cr layer and high conductivity of Au thin film with flatness and surface chemistry of eC makes an ideal electrode with demonstrated high stability and yields for MJ fabrication<sup>38</sup>. In brief, polished fused quartz wafer (from Technical Glass products, Inc.) were diced into 1.8 in 1.2 cm chips. For cleaning, the chips ultra-sonicated in acetone, isopropanol alcohol and water for 20 minutes. 3

nm Cr (at 0.3 nm/s), 15 nm Au (at 0.3 nm/s) and 10 nm of eCarbon (at < 0.1 nm/s) was deposited by electron-beam evaporator (Kurt Lesker PVD 75). The pressure of the chamber was kept below  $2 \times 10^{-5}$  Torr during the deposition. Au purity was 99.99% and carbon source was 3 mm diameter spectroscopically pure graphite rods (SPI Supplies, PA) in a graphite crucible. Deposition was carried out using a physical shadow mask with four parallel 0.3 mm wide opening lines, and the thickness was monitored by quartz microbalance inside the chamber.

#### **4.2.1 Molecular layer grafting and thickness measurement**

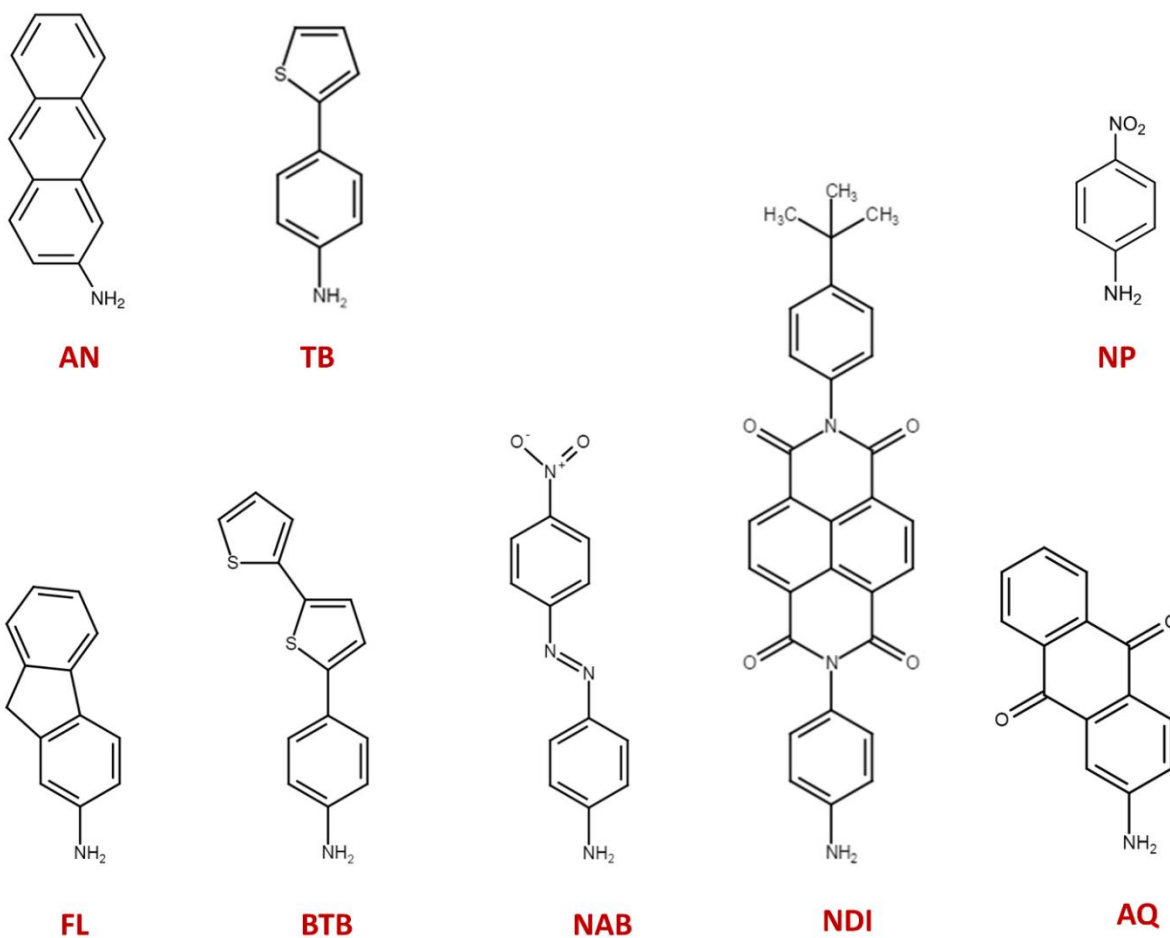
Molecular layers were covalently grafted on the surface of eC by electrochemical reduction of diazonium reagents in acetonitrile. The mechanism of covalent bonding of the molecule to the surface and further growing layer is investigated previously and schematically shown in Figure 4.1. This type of grafting is frequently used for fabrication of molecular junctions.<sup>38, 58, 101, 214</sup>



**Figure 4.1** Scheme of the electro-reduction and grafting of diazonium species on the surface: **(a)** diazonium species in the solution near to the surface of the electrode accept the electron and release  $N_2$  as a gas **(b)** Resulted radical medium approaches the surface **(c)** The radical react with the surface and make the covalent bond **(d)** With applying more negative potential to the electrode, electron from the electrode reaches the diazonium species and makes more radicals. These radicals react with the underlayer molecules to make multilayer.

A conventional three-electrode electrochemical cell consisting  $Ag/Ag^+$  (0.01M  $AgNO_3$  in ACN) reference electrode and Pt wire counter electrode was used for electrochemical grafting. The  $Ag/Ag^+$  reference electrode was calibrated against the redox potential of ferrocene. The redox potential of ferrocene is centered at  $\sim 87mV$  versus this

Ag/Ag<sup>+</sup> reference electrode. Diazonium species were made through either synthesis of isolated diazonium salts or in-situ procedure. The amine precursors of the diazonium ions employed are shown in Figure 4.2.

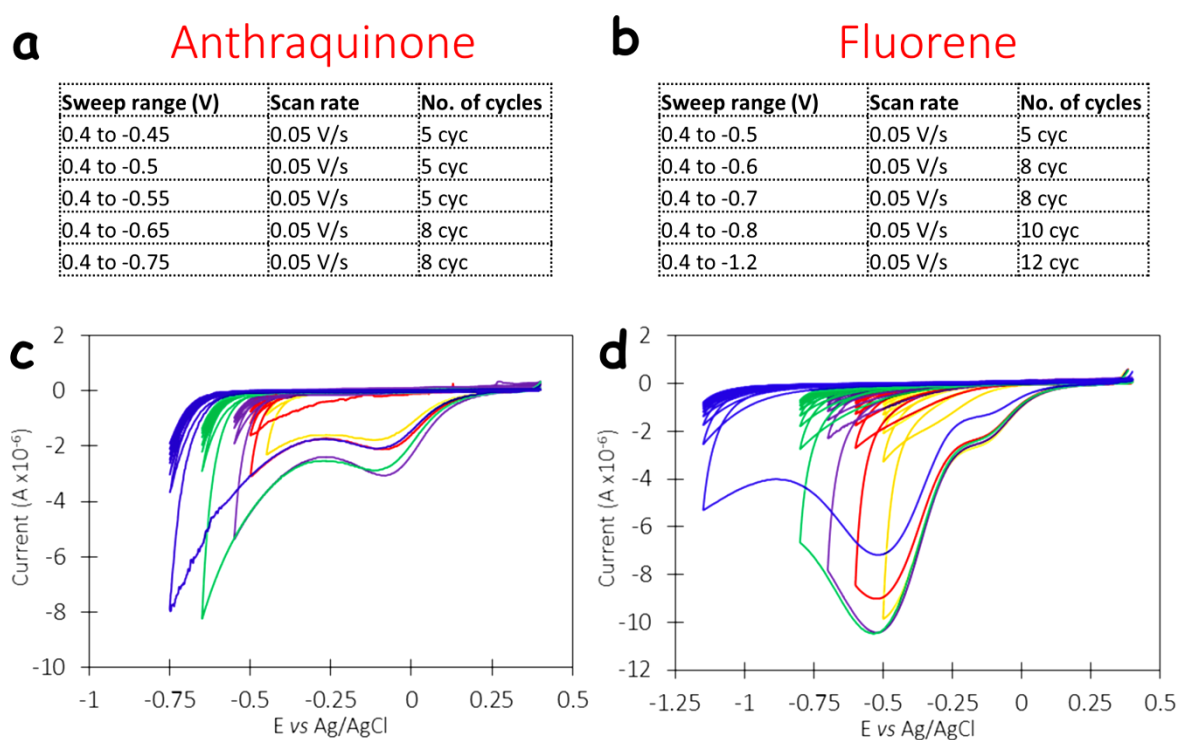


**Figure 4.2** Structure of amine precursor of eight examined molecules.

Anthracene (AN) and Bis-thienyl benzene (BTB) layers were grown by electro-reduction of diazonium ions formed *via in-situ* diazotization of the corresponding amines using tert-butyl nitrite. BTB layers were deposited from 20 mL of 0.5 mM solution of BTAB (amino BTB) in 0.1 M TBABF<sub>4</sub> in ACN by adding 30  $\mu$ L of t-butyl nitrite to the solution and sweeping the voltage from 0.4  $\rightarrow$  -0.5 to -1.2 V at 0.05 V/s for 2-10 cycles. Similarly, AN

layer was deposited from 20 mL of 0.5 mM solution of amino AN in 0.1 M TBABF<sub>4</sub> in ACN after addition of 30  $\mu$ L of t-butyl nitrite. Cyclic voltammetry scans was performed from 0  $\rightarrow$  -1.2 V at 0.05 V/s for 10 cycles to deposit the AN layer.

Nitrophenyl (NP), Naphthalene diimide (NDI), Thienyl benzene (TB), Fluorene (FL), Anthraquinone (AQ), and Nitro-azobenzene (NAB) layers were made from 0.5 - 0.1 mM solutions of the corresponding isolated diazonium salts in 0.1 M TBABF<sub>4</sub> in ACN. Grafting parameters and cyclic voltammetry of FL and AQ are shown in Figure 4.3 as examples.

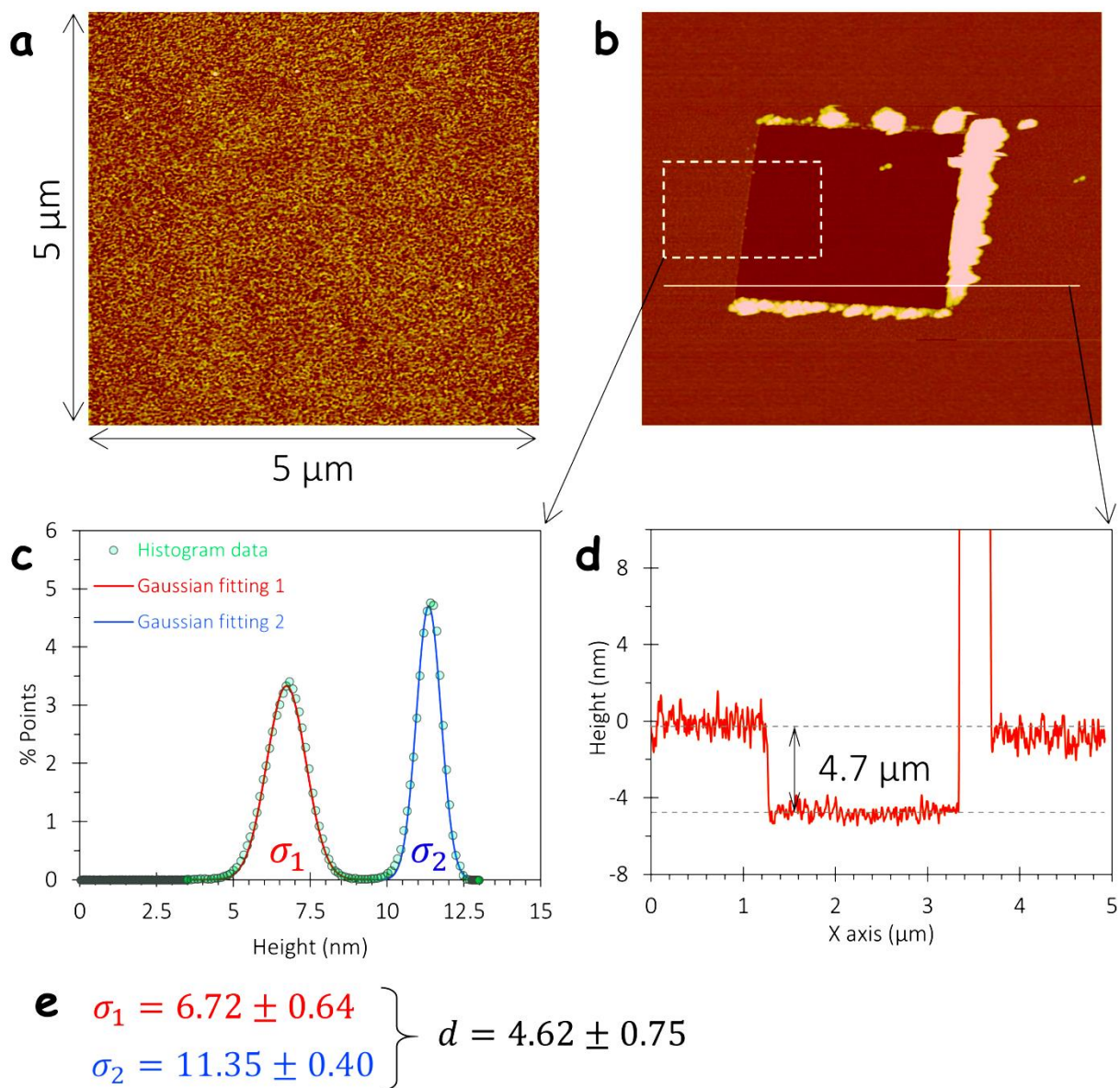


**Figure 4.3** (a) Electrochemical parameters used for grafting Anthraquinone molecular layer (b) Electrochemical parameters used for grafting Fluorene molecular layer (c) Corresponding cyclic voltammetry for AQ grafting (d) Corresponding cyclic voltammetry for FL grafting.

Measurement of molecular layer thickness was done by AFM “scratching” technique, using the same procedure described previously<sup>38, 214, 215</sup>. Thickness measurements were done adjacent to one of the junctions of each sample. The example of the AFM measurement on



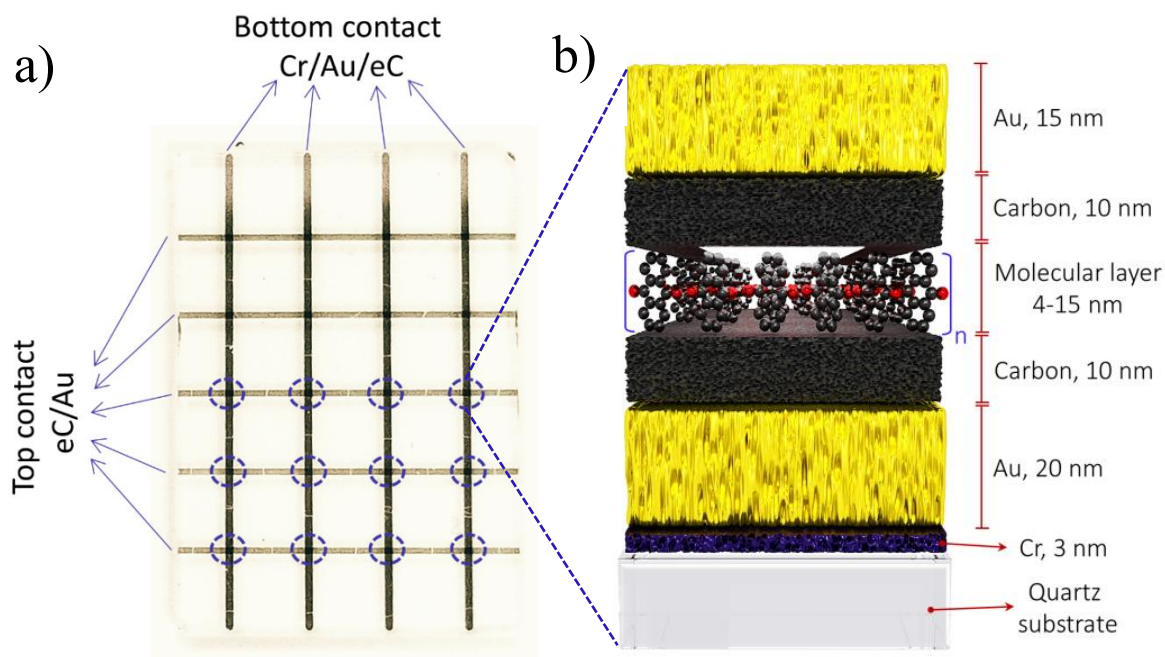
Si/SiO<sub>x</sub>/Cr/Au/eC/FL is shown in Figure 4.4. Panel (a) shows the tapping mode AFM image on top of the grafted molecular layer (5 x 5 μm). Contact mode approach was applied to scratch a trench (2 x 2 μm) in the molecular layer, then a 5 x 5 μm tapping mode image was obtained in the area surrounding and including the trench (Panel b). A histogram generated from the height data was fitted by two separate Gaussian functions (panel c). The thickness determined as the difference between the centers of the two functions and the uncertainty given as the quadrature addition of the two best-fit  $\sigma$  values (panel e). Line scan profile at indicated position is also shown in panel d.



**Figure 4.4** (a) Tapping mode AFM image on the surface of FL multilayer grafted on Cr/Au/eC electrode (b) Tapping mode AFM image on the same position as panel a after scratching the molecular layer (c) histogram of the from the height data in the shown area and fitted Gaussian distribution (d) line profile scan for the indicated position (e) Thickness of the molecular layer with associated uncertainty.

## 4.2.2 Completing the junction and electrical measurements

Deposition of top contact completes the molecular junction, designated: Cr<sub>3</sub> /Au<sub>20</sub> /eC<sub>10</sub> /NAB<sub>6.0</sub> /eC<sub>10</sub> /Au<sub>15</sub> (subscripts indicate layer thicknesses, and NAB= nitro-azobenzene oligomer in this example). The top contact electrode was comprised of electron beam deposition of 10 nm eC and 15 nm Au through a physical shadow mask with 0.3 mm openings oriented perpendicular to the bottom contact, which results in a crossbar junction of 0.09 mm<sup>2</sup> area. Deposition was done in the same evaporator as bottom contact deposited (Kurt J. Lesker PVD75) with typical pressure below  $5 \times 10^{-5}$  Torr during deposition. Deposition rate was 0.01 nm/sec for eC and 0.03 nm/sec for Au. The image of the final fabricated chip is shown in Figure 4.5a. Figure 4.5 panel b shows a cross section of a completed junction on a quartz substrate. Current vs bias voltage (*IV*) curves were obtained in four-wire mode as described previously<sup>38</sup>.



**Figure 4.5** (a) Optical picture of the completed chips. Each dotted circle shows individual cross-bar junction. (b) Schematic illustration of Quartz/Cr<sub>3</sub>/Au<sub>20</sub>/eC<sub>10</sub>/Anthraquinone/eC<sub>10</sub>/Au<sub>20</sub> molecular

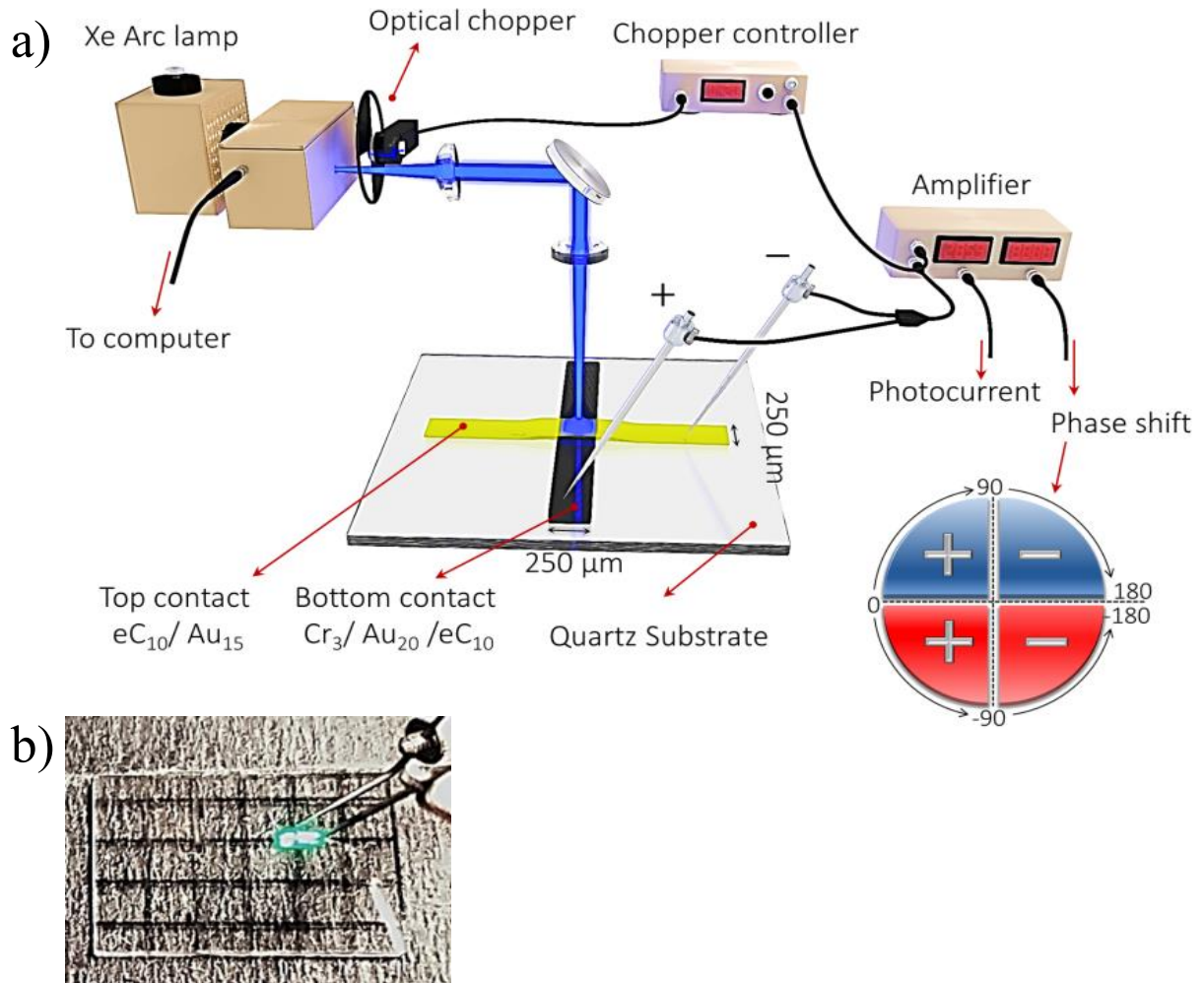
junction.  $n$  is a number of repeating units of oligomer which determine final thickness of molecular layer.

### 4.2.3 AC Photocurrent measurements

The schematic representation of the optical apparatus and PC measurement is shown in Figure 4.6a. A Xe arc source (Newport model 6256) as a broad band light source passed through a motorized monochromator model 74004 Cornerstone 130 1/8 m ( $\Delta\lambda = 13 \text{ nm}$ ) and then an optical chopper before being focused on the sample. The output light was chopped at frequency of  $\sim 405 \text{ Hz}$  and then focused on the junction by a series of lenses. The  $250 \times 250 \text{ }\mu\text{m}$  molecular junction was centered in the focal spot, which had a diameter of  $\sim 2 \text{ mm}$ . Illuminated molecular junction was connected via tungsten probe and BNC cables to the A/C input of a dual phase lock-in amplifier (LIA, Stanford-830). The AC PC phase and amplitude were monitored by a lock-in amplifier referenced to the chopping frequency while the wavelength was scanned by the monochromator. A home-mode LabView data acquisition program was controlling the output wavelength of the monochromator and recording the output current and phase shift from lock-in amplifier. Light intensity of selected wavelength was measured by Newport power meter (Model 1936-R) at the sample. Photocurrent (PC) polarity was determined by calibrating the phase shift output of the lock-in amplifier with a silicon photodiode as the sample.

The pie chart at the bottom of Figure 4.6a illustrates the correlation of phase shift and PC polarity, in which the negative sign of photo-generated current indicates movement of electrons from bottom to top contact in the external circuit. Laser illumination with dc current measurement was used for further validation of the PC sign for each of the eight molecular junction structures examined. Note that the area of the light illuminated on the sample is

much larger than the area of the junction. Actual optical image of the chip under illumination is shown in Figure 4.6b.



**Figure 4.6 (a)** Apparatus used for the PC measurement with continuum source, modulation by on optical chopper and detection with lock-in amplifier. Pie chart indicates the relationship between the measured phase shift from the lock-in amplifier and the PC polarity. **(b)** Optical image of the junction under illumination.

#### 4.2.4 External quantum efficiency calculation

In order to determine the external quantum efficiency (EQE), the incident optical power on the junction at each wavelength was measured by a Newport power meter (Model

1936-R). The light power density varied with wavelength as shown in Figure 4.7a, equaling 0.34 to 21.8 mW/cm<sup>2</sup> over the wavelength range of 250 to 650 nm. PCs were measured over the same range of wavelengths to determine junction EQE at each photon energy. As an example, the observed PC of a phenyl naphthalene di-imide (NDI) molecular junction is shown in Figure 4.7a. By combining the source output spectrum with the PC response as functions of wavelength, the yield or EQE as photoelectrons/incident photon was determined, and plotted in Figure 4.7b. The yield of the photocurrent at each wavelength is calculated by using the equations 4.1 to 4.3.

First, the photon flux (photon per second incident onto the junction) is given by:

$$P_f = \frac{P_i \times A_j}{h\nu \times A_b} \quad (\text{photon/s}) \quad (\text{eq 4.1})$$

Where  $h$  is Plank's constant ( $6.62607 \times 10^{-34} \text{ J.s}$ ),  $\nu$  the frequency of the incident light

( $c/\lambda$ ),  $P_i$  measured power at the sample,  $A_j$  area of junction,  $A_b$  area of the focused beam on the sample.

Second, electron flux (electron per second of) is given by:

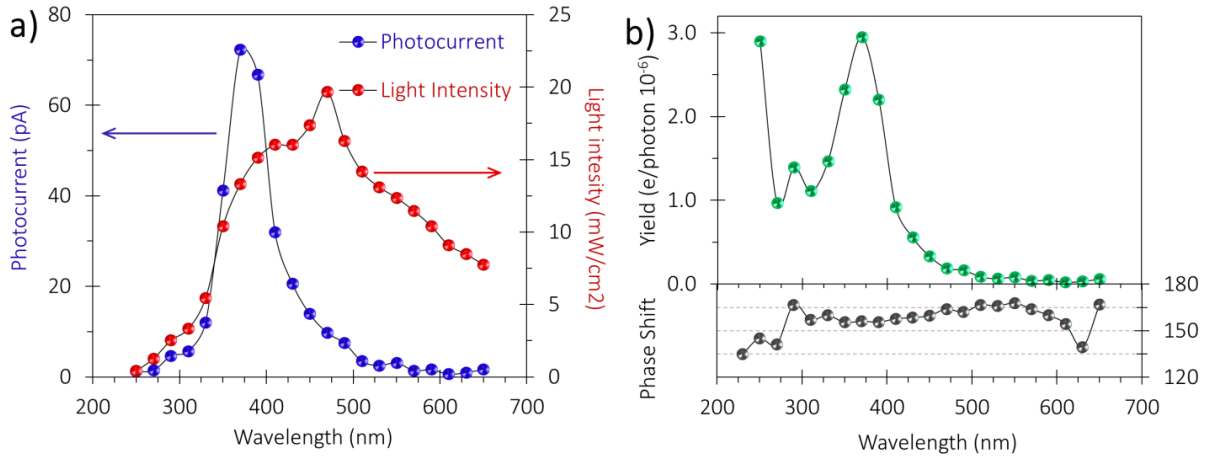
$$e_f = \frac{I_p}{q} \quad (\text{electron/s}) \quad (\text{eq 4.2})$$

Where  $I_p$  is the current measured by lock-in amplifier and  $q$  is the elementary charge of electron ( $1.60218 \times 10^{-19} \text{ C/e}$ ).

Finally, yield of the photocurrent is given by:

$$Y = \frac{e_f}{P_f} \quad (\text{electron/photon}) \quad (\text{eq 4.3})$$

The corresponding phase shift is also shown in Figure 4.7b, the  $\sim 150$  degree phase across the entire wavelength range indicates a negative PC, with electrons traveling from the bottom to the top contact in the external circuit.



**Figure 4.7 . a)** Overlay of Photocurrent spectrum for NDI MJ and illuminated light intensity of Xe arc lamp measured at the sample. **b)** Corresponding PC yield and phase shift spectra for NDI MJ shown in panel a.

#### 4.2.5 OCP and photocurrent under the bias measurements

405 nm laser diode mounted using Thorlabs LDC 210C controller kit and TED 200C thermoelectric temperature controller, was used as a source of illumination. The light intensity of the laser beam at the sample was determined using a Newport power-meter directly above the sample. The junction's bottom and top contact were connected to the input of the source-meter Keithley 6517 using tungsten probes and BNC cables. Exposure time was controlled with Thorlabs  $\emptyset 1$  optical beam shutter. The controller of the shutter was connected to the voltage output of the Keithley. A visual basic program was collecting the current or voltage data output from the Keithley and also opening and closing the shutter with applying the voltage to the shutter controller. In case of PC measurement under the bias,

another source-meter (Keithley 2602B) was used in series for applying the external field across the junction.

#### **4.2.6 UV-Vis absorbance spectroscopy**

Polished fused quartz wafer were diced into 1.8 in 1.2 cm chips to serve as substrate. 3 nm of Cr, 20 nm of Au and 10 nm of eC was deposited as a blank bottom contact (no lines). Optical absorbance of the chip was recorded using PerkinElmer Lambda 1050 dual beam spectrometer. Absorbance was reference to the air and the samples was held perpendicular to the direction of light beam using a holder. Then, the molecular layer was grafted by electrochemical reduction of diazonium reagents with the same procedure used for fabrication of junctions. The absorbance of resulting chip (bottom contact + molecular layer) was recorded. Finally, absorbance measurement was repeated after deposition of top contact consisting of 10 nm of eC and 15 nm of Au.

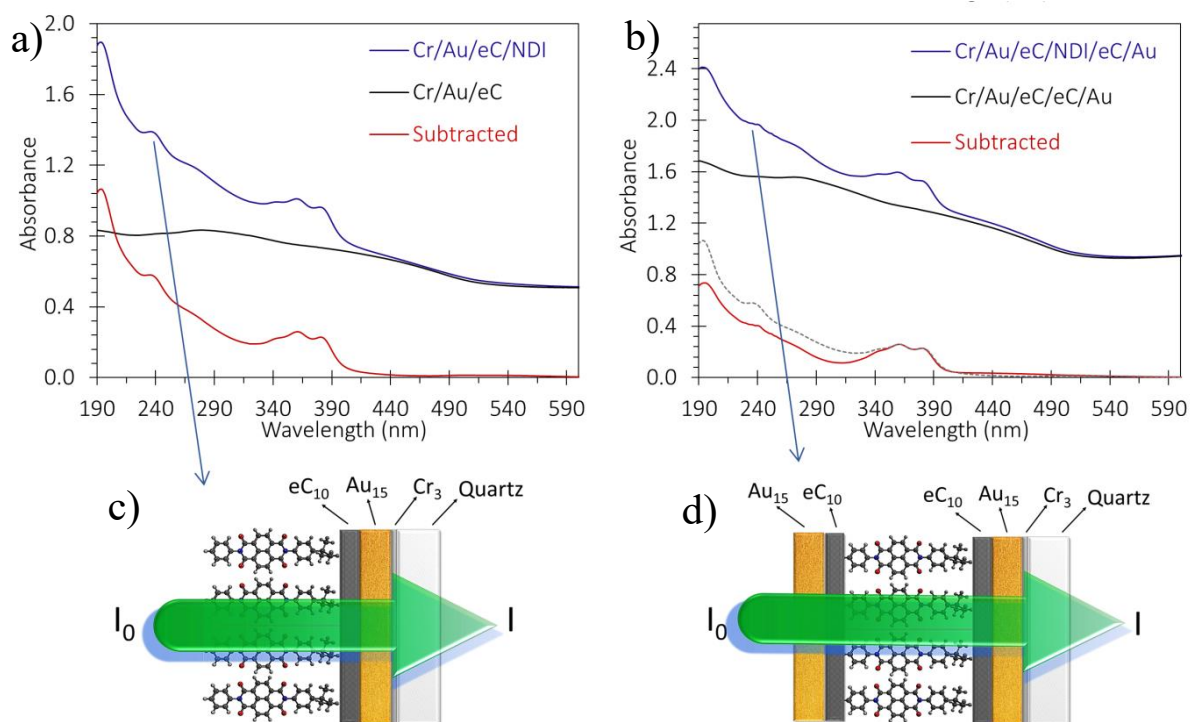
### **4.3 RESULTS**

#### **4.3.1 UV-Vis Absorption of molecular layer in different medium**

The partial transparency of the eC/Au contacts permits UV-Vis absorption spectroscopy of both the Au/eC/oligomer surface and the completed molecular junction. In-situ absorbance spectra provide direct indications of changes and broadening of molecular orbital energies in the local environment of completed, functioning MJ, and permit correlations with observed PCs (below). Figure 4.8a shows absorbance spectra (relative to air) of a 1.8x1.2 cm blanket Q/Cr<sub>4</sub>/Au<sub>20</sub>/eC<sub>10</sub> electrode, compared to the same electrode after electrochemical grafting of an NDI molecular multilayer. Subtraction of these two spectra clearly shows the absorbance of multilayer NDI molecules that are covalently grafted and



grown on the surface of eC (red line). Figure 4.8b shows the absorbance of the completed junction after deposition of top contact on the same device shown in panel c. Subtraction of the completed junction from the same electrode structure without molecular layer grafting (Q/Cr<sub>4</sub>/Au<sub>20</sub>/eC<sub>10</sub>/eC<sub>10</sub>/Au<sub>15</sub>), reveal the absorbance of NDI molecular layer in the transport environment (Red line).

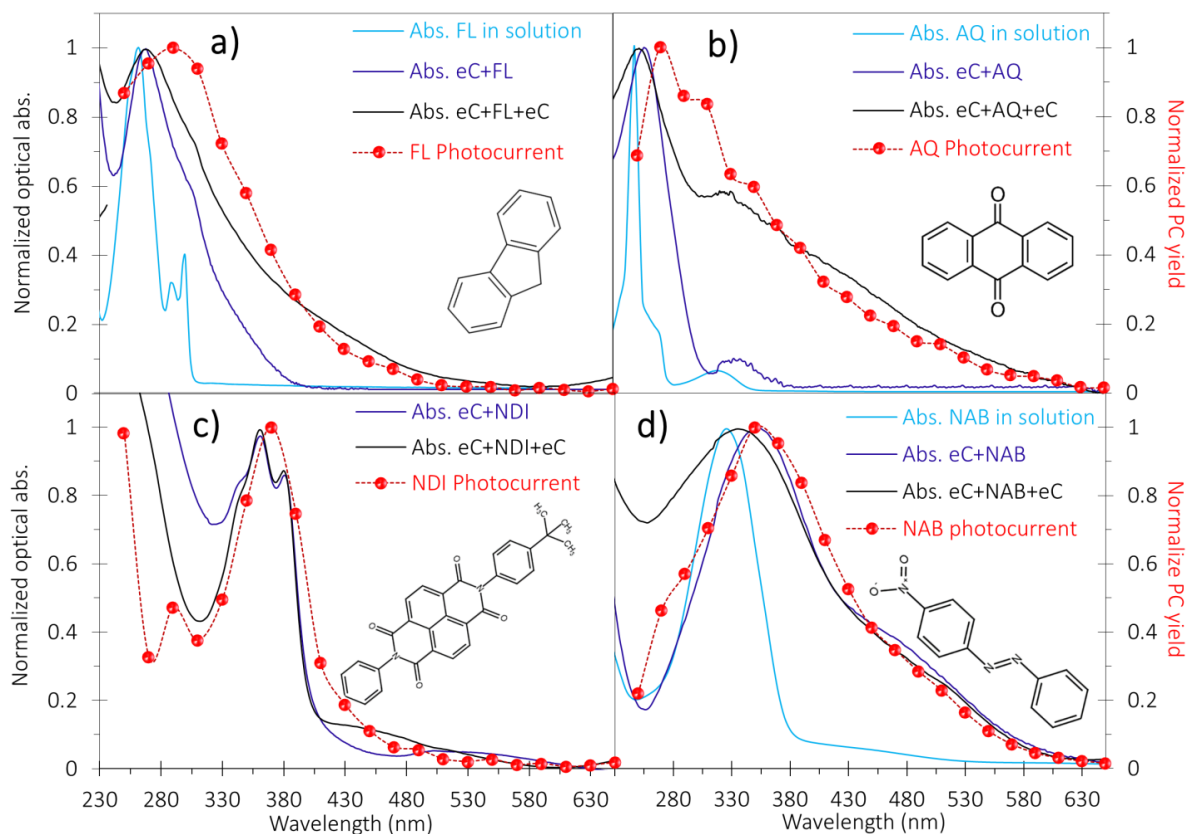


**Figure 4.8 a)** Overlay of optical absorbance of Quartz/Cr<sub>3</sub>/Au<sub>20</sub>/eC<sub>10</sub> (black curve) and the same electrode after NDI grafting on the surface (blue curve). Subtraction of the substrate spectrum yields the absorbance due to the NDI molecular layer shown as the red curve. **b)** Overlay of absorbance spectrum of “blank” Quartz/Cr<sub>3</sub>/Au<sub>20</sub>/eC<sub>10</sub>/eC<sub>10</sub>/Au<sub>15</sub> electrode (black curve) and complete junction *viz* Quartz/Cr<sub>3</sub>/Au<sub>20</sub>/eC<sub>10</sub>/NDI/eC<sub>10</sub>/Au<sub>15</sub> (blue curve). Subtraction of the “blank: spectrum from the MJ spectrum yields absorbance due to the NDI molecular layer in the full MJ stack (red curve). **c)** Schematic of the bottom contact electrode structure modified with NDI molecular layer. **d)** Schematic of the complete NDI MJ consisting of top contact.

### 4.3.2 Correlation of photocurrent with absorbance

When the molecules are covalently grafted on the eC surface and undergo oligomer formation, the energy levels of the molecules could significantly change from those of the isolated molecule. Intra- and inter-chain interactions, and more importantly electronic coupling with contacts are among the reasons for changes in energy levels in the solid state compared to the free molecules. We used the UV-Vis absorption spectrum to identify the wavelengths of maximum absorption in the complete junction, and to observe changes in orbital energies.

Figure 4.9 shows the optical absorbance of four molecules in different media: i) dilute acetonitrile solution, ii) multilayer grafted on the surface of eC, iii) multilayer between two contacts in the full stack of the junction. In the two latter cases, the spectrum of unmodified electrodes were subtracted to reveal the molecular layer spectrum, as shown in Figure 4.8a and **Figure 4.8b** for NDI. In all cases, bonding to eC and application of the top contact has minor effects ( $< 18$  nm) on the peak absorption wavelength, implying that the optical gap of the molecule is not strongly affected by the contacts and multilayer formation. However, there is a significant red shift in absorption onset for AQ, FL, and NAB upon bonding to eC, and a further red shift upon deposition of the top contact. We previously discussed the possible causes for these observations and concluded that they are due to strong coupling between the aromatic molecular layer and the contacts,<sup>101</sup> and are responsible for the small effects of molecular structure when  $d < 5$  nm.<sup>58</sup> However, the minor changes in the UV-Vis spectrum with increasing layer thickness implies relative weak coupling between molecular subunits, and a limited conjugation length within the layer interior.<sup>101</sup>



**Figure 4.9** Correlation of absorbance and photocurrent yield of molecules. Overlay of PC yield and absorption spectra for four molecules: **a** FL, **b** AQ, **c** NDI, **d** NAB. Absorption spectra of each molecule in different medium are shown: i) isolated monomer in solution, ii) Multilayer grafted on the surface of bottom contact (Cr/Au/eC/molecular layer), iii) Multilayer grafted on the surface in complete junction including top contact (Cr/Au/eC/molecular layer/eC/Au). All spectrums are corrected for the blank electrode absorption like the NDI shown in Figure 4.8 and normalized to the maximum peak of 1. PCs are shown in the secondary axis at the right side of the graphs with positive sign regardless of the actual measured polarity.

The main question in the current report is correlation of the absorption and PC spectra, to determine the origin of PC generation. Figure 4.9 shows overlays of the absorption and PC spectra for FL, AQ, NAB, NDI. The absorbance and PC spectra are normalized to a maximum value of 1.0 to permit direct comparison of spectrum shapes and maximum wavelengths. Note first that the PCs are negligible at wavelengths where the molecular layer

does not absorb significantly for eight different molecular layers, all with  $d > 4$  nm, the PC response tracks the absorbance of the molecules, as modified by interactions with the contacts. The maximum wavelengths and polarities of the PC and absorbance spectra are summarized in Table 4.1.

**Table 4.1** Summary of photocurrent results and DFT predicted energy levels of examined molecules

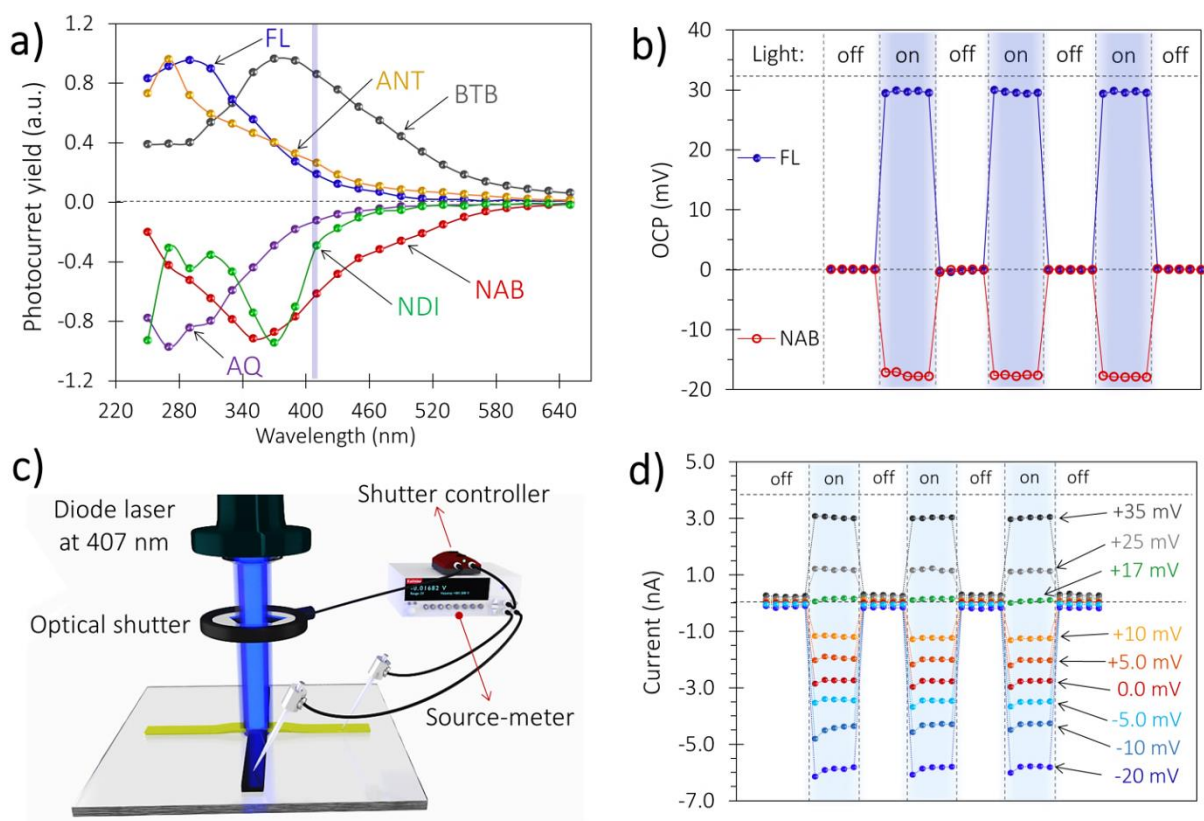
| Molecules | $\phi_h$ (eV) <sup>a</sup><br>$ E_{HOMO}  -  E_F $ | $\phi_e$ (eV) <sup>a</sup><br>$ E_F  -  E_{LUMO} $ | Smaller barrier | OCP sign at 407 nm | PC sign <sup>b</sup> | Max of PC (eV) | Max of Abs. (eV) <sup>c</sup> | Max of TD-DFT (eV) |
|-----------|--|--|-----------------|--------------------|----------------------|----------------|-------------------------------|--------------------|
| NAB       | 0.42   | 3.17   | $\phi_h$        | +                  | +                    | 4.59           | N/A                           | 3.26               |
| BTB       | 0.69   | 3.32   | $\phi_h$        | +                  | +                    | 3.35           | 3.46                          | 3.54               |
| FL        | 1.14   | 4.09   | $\phi_h$        | +                  | +                    | 4.59           | 4.62                          | 4.75               |
| TB        | 1.42   | 3.47   | $\phi_h$        | +                  | +                    | 3.76           | 4.24                          | 4.44               |
| NDI       | 2.32   | 1.45   | $\phi_e$        | -                  | -                    | 3.35           | 3.42                          | 3.40               |
| NAB       | 2.05   | 1.76   | $\phi_e$        | -                  | -                    | 3.54           | 3.56                          | 3.49               |
| AQ        | 2.40   | 2.01   | $\phi_e$        | -                  | -                    | 4.59           | 4.84                          | 5.10               |
| NP        | 2.99   | 2.37   | $\phi_e$        | -                  | -                    | 3.76           | N/A                           | 4.88               |

- a) Fermi-level of eC is measured by UPS at -4.8 eV  
b) The sign at the whole range of measured wavelength  
c) The absorbance of the molecule grafted on the surface.

### 4.3.3 Open-circuit potential and photocurrent polarity

Figure 4.10 compares the PCs of the four molecules in Figure 4.9 plus bis-thienyl-benzene (BTB) and anthracene (AN), plotted to indicate the PC polarity. FL, AN, and BTB are consistently positive provided  $d > 4$  nm, while AQ, NDI, and NAB are consistently negative. To further confirm the PC sign, we monitored the open circuit potential (OCP) during DC

illumination by a 6 mW, 407 nm diode laser, which could be interrupted by a mechanical aperture, as shown in Figure 4.10.



**Figure 4.10** Polarity of the photocurrent and OCP measurement. **a)** Overlay of the PC yield for six indicated molecules, with the sign of the yield indicating PC polarity. Maximum PC yield normalized to  $\pm 1.0$  for comparison. **b)** Observed OCP for three on/off light cycles for FL and NAB MJs. **c)** Schematic of OCP apparatus. **d)** Observed current for light on/off cycles with bias applied to a NAB MJ. Dark current is not subtracted; however, it is much smaller than the PC.

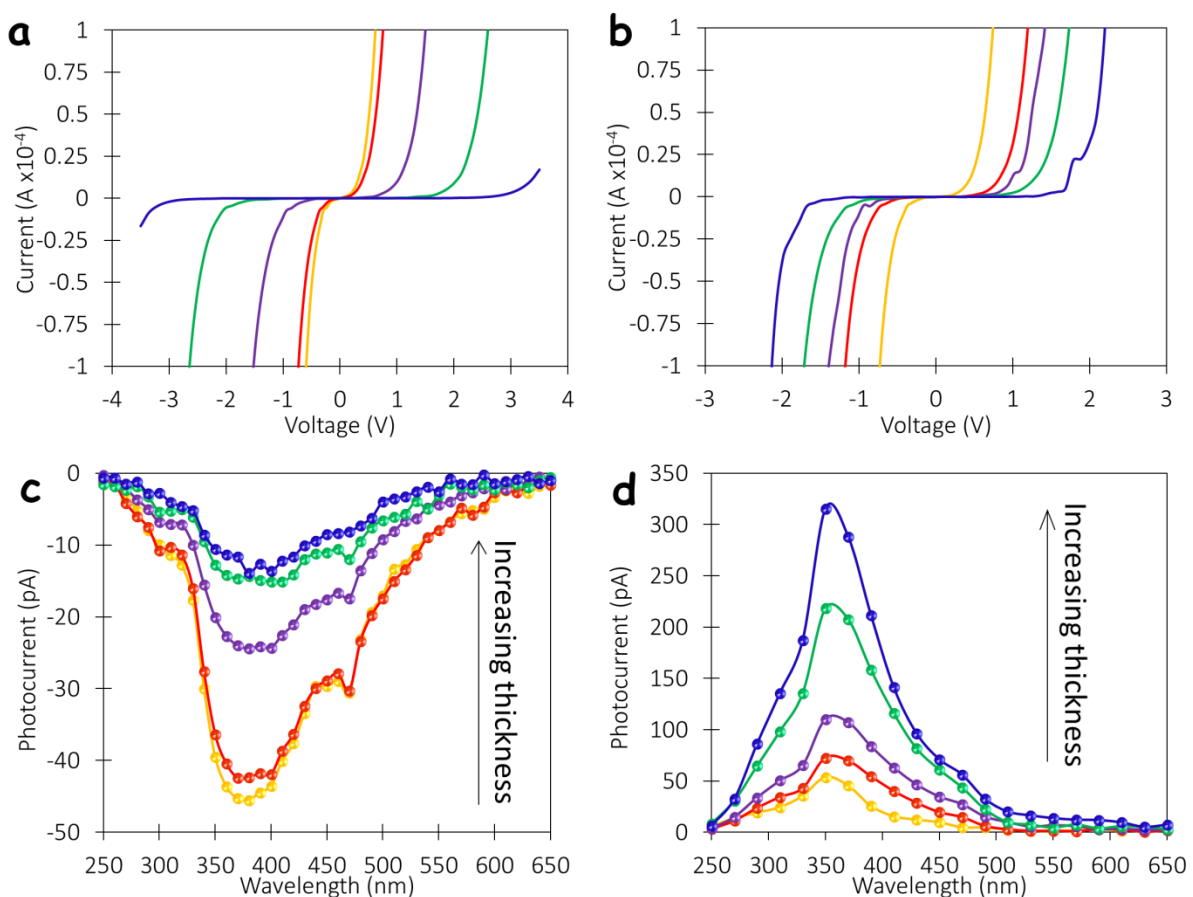
Figure 4.10c shows the OCP of FL and NAB junctions during several laser exposures lasting  $\sim 5$  seconds each. The significant, sign selective, and reversible photo-voltage generation upon exposure to laser radiation indicates that there is a light induced electric field in the MJ, in which the negative sign of OCP implies that the bottom contact becomes negative relative to the top contact. The polarity of this induced field is the same as the polarity of the

measured PC such that a negative OCP would drive the electrons to move from the bottom to top contact in the external circuit, thus generating a negative PC.

The polarities of the OCPs and PCs for eight molecular structures examined are summarized in Table 4.1, along with the DFT-predicted orbital energies and observed absorbance and PC peak energies. Note that in all cases the polarities of the OCP and PC match, and the peak absorbance photon energy is close to the maximum PC energy. Control of the PC sign by the OCP was confirmed by application of an external bias during exposure to laser light, as shown in Figure 4.10d for the case of NAB. Under constant external bias, there is a reversible rise in the current upon exposure to the laser light which returns to the initial dark current if the optical shutter is closed. The PC at zero external bias is negative and its magnitude can be increased with imposing external negative bias. However, a positive external bias decreases the PC, then cancels the PC when the bias equals +17 mV, which is equal and opposite to OCP observed without an external bias. Light absorption and photo-induced carrier generation still occur with the +17 mV bias applied, but there is no driving force for charge transport, and the carriers likely recombine. Applying a bias more positive than +17 mV reverses the polarity of the photoresponse to generate positive PC.

#### **4.3.4 Effect of the thickness**

Note that the PC sign and phaseshift are independent of the thickness of the molecular layer for the relatively thick MJs examined ( $d > 4$  nm). As shown in Figure 4.11 for the examples of FL and AQ, the PC magnitudes vary with molecular layer thickness, but polarity and maximum wavelength remain constant over all thicknesses examined.



**Figure 4.11** (a) Current vs bias voltage (*IV*) curves for Cr/Au/eC/AQ<sub>*d*</sub>/eC/Au. *d* is a thickness of Anthraquinone molecular layer: *d* = 4.1 → 10.5 nm. (b) *IV* curves for Cr/Au/eC/FL<sub>*d*</sub>/eC/Au. *d* = 4.6 → 8.1 nm. (c) Corresponding photocurrent spectrum for the AQ junctions shown in panel a. (d) Corresponding photocurrent spectrum for the FL junctions shown in panel b.

Various diazonium reduction scan ranges were used to produce different molecular layer thicknesses. As indicated in the last two columns of Table 4.2, all thicknesses for a given molecule produced the same sign and wavelength of maximum photocurrent. While sign and position were consistent for all samples of a given type, PC magnitudes varied, with examples shown in Figure 4.11. The dependence of PC on molecular layer thickness was not examined in detail, and no scientific conclusions were drawn from comparisons of relative intensities.

**Table 4.2** Scan ranges, PC statistics and number of samples for each junction type.

|     | No. of junctions <sup>a</sup> | Scan range ( <i>E</i> vs Ag/Ag <sup>+</sup> ) <sup>b</sup> | Thickness range (nm) <sup>c</sup> | PC and OCP sign <sup>d</sup>    | $\lambda_{max}$ in PC spectrum <sup>e</sup> |
|-----|-------------------------------|--|-----------------------------------|---------------------------------|---|
| AQ  | 12                            | +0.4 → (-0.45 to - 0.75)                                   | 4.1 – 10.5 nm <sup>f</sup>        | Negative<br>( <i>N</i> = 12/12) | 290 ± 20 nm                                 |
| FL  | 15                            | +0.4 → (-0.5 to - 1.2)                                     | 4.5 – 8.1 nm <sup>f</sup>         | Positive<br>( <i>N</i> = 15/15) | 290 ± 20 nm                                 |
| NAB | 11                            | +0.4 → (-0.4 to - 0.9)                                     | 4.5 – 12 nm                       | Negative<br>( <i>N</i> = 11/11) | 350 nm                                      |
| BTB | 10                            | +0.4 → (-0.3 to - 0.65)                                    | 5 – 13 nm                         | Positive<br>( <i>N</i> = 10/10) | 370 ± 20 nm                                 |
| NP  | 3                             | +0.4 → (-0.8 to - 1.1)                                     | 4 – 8 nm                          | Negative<br>( <i>N</i> = 3/3)   | 370 ± 60 nm <sup>g</sup>                    |
| AN  | 4                             | +0.4 → (-0.6 to - 1.2)                                     | 5 – 11 nm                         | Positive<br>( <i>N</i> = 4/4)   | 290 ± 20 nm                                 |
| TB  | 6                             | +0.4 → (-0.8 to - 1.7)                                     | 5 – 11 nm                         | Positive<br>( <i>N</i> = 6/6)   | 330 ± 20 nm                                 |
| NDI | 8                             | +0.4 → (-0.4 to - 0.7)                                     | 5 – 13 nm                         | Negative<br>( <i>N</i> = 8/8)   | 370 nm                                      |

**a)** Number of fabricated and examined junctions

**b)** Scanning potential range for electrochemical grafting of the diazonium species on the surface. All the grafting started at +0.4 V, but the end point for sweeping voltage is varied to change the thickness of the grafted molecular layer. Scan rates were 50 mV/s for all cases.

**c)** Thickness range estimated from the grafting procedure and *JV* curves

**d)** PC polarity over the entire examine wavelength (250-700 nm) and OCP polarity at 407 nm.

**e)** The wavelength at the maximum of the photocurrent yield. The increment of the PC measurement was 20 nm, and peak wavelengths for each samle type differed by at most ± one increment (20 nm) For NAB and NDI, no variation in  $\lambda_{max}$  was observed for the junctions examined.

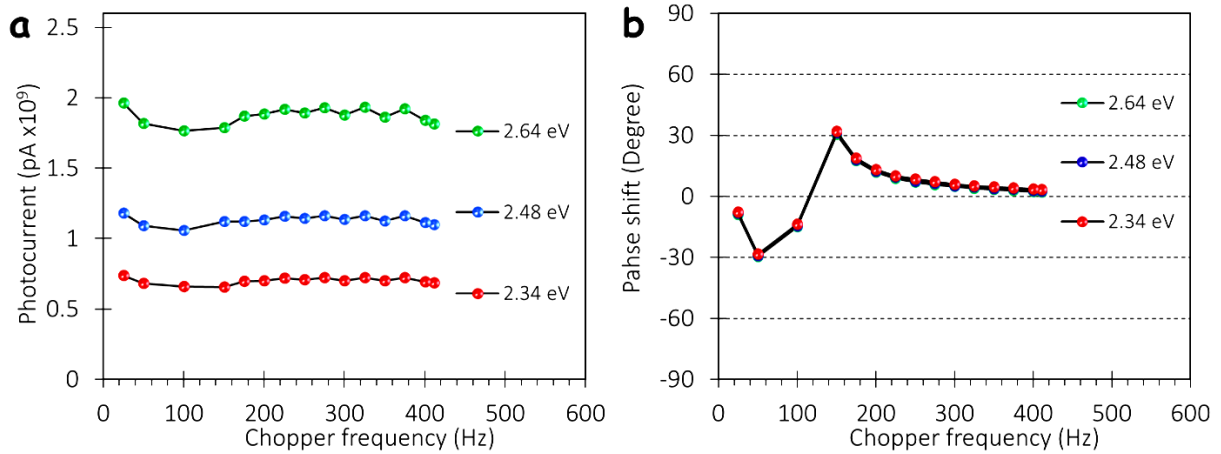
**f)** Verified by AFM procedure

**g)** Due to the low magnitude of the photocurrent in case of NP being comparable to the detection limit of the lock-in amplifier, the PC spectrum shape and  $\lambda_{max}$  of NP has significant error. However, the polarity of the OCP and PC were verified by laser illumination.



### 4.3.5 Heat-related photocurrent

Since incident light produces heat, we consider the possibility of the heat-induced or thermoelectric current in molecular junctions. As our measurement was done in AC mode with help of a chopper, apparent test to evaluate the heat effect is assessing the dependence of the photocurrent to the chopper frequency. Note that all results shown in this chapter were done at chopper frequency of 410 Hz. It is shown that the heat-related photocurrent decreases with increasing the frequency ( $PC \sim f^{-1.5}$ )<sup>216</sup>. Figure 4.12 clearly shows that the photocurrent at three different photon energy of incident light does not exhibit any dependence to the chopper frequency in a range of 25 to 410 Hz. BTB MJ result is shown as examples. Moreover, corresponding measured phase shift changes between -30 to 30 degree, which implies that the sign of photocurrent is constantly positive and it is independent of the chopper frequency. Also, we had shown that the time scale of photo-induced current response time in our molecular junction is  $< 250 \mu\text{s}$  and faster measurement was limited by the mechanical limits imposed by the chopper. This demonstrated fast photocurrent, and independent to the chopper frequency is not expected for any heat-related response.

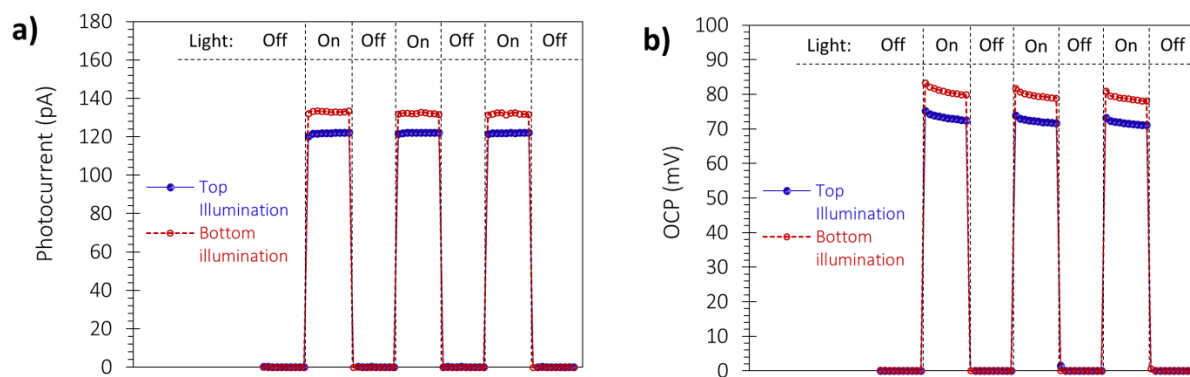


**Figure 4.12 (a)** Measured photocurrent by lock-in amplifier vs frequency of the optical chopper at three different energy of incident light for BTB molecular junction **(b)** Corresponding phase shift of the measured photocurrent vs chopper frequency.

If we assume that the heat is the driving force for the movement of the electron, maximum of the response should happen at the maximum of the absorption in the complete junction or at least at the maximum of the top contact absorption. In other words, since the heat production has the direct relation to the amount of the absorbed light in the system, any heat-related response should follow the spectrum of the absorption in the whole system (Abs. of top contact + Abs. of molecular layer + Abs. of bottom contact). However, as it is shown in section 4.3.2, the photocurrent response follows the subtracted absorption of the molecular layer (just absorption in the molecular layer), not the total absorption in MJs. Note that the absorption in the molecular layer is much weaker than the absorption in the contacts. Collectively, it is very unlikely that the thermoelectric effect would be a considerable contributing factor in this study.

### 4.3.6 Back illumination of the junctions

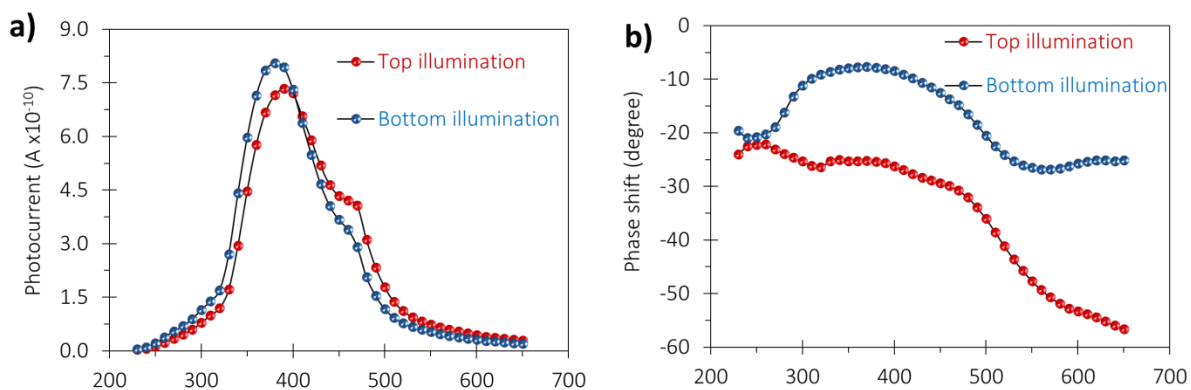
One of the significant advantages of MJ fabrication with eC electrode is partial transparency at both contacts (electrode), which enable us to illuminate the junction from both sides. Back Illumination becomes very important in order to determine the operating mechanism. Figure 4.13 shows the comparison of PC and OCP for top and back illumination in case of BTB MJ. As it is apparent from the Figure, there is no change in sign (polarity) of PC and OCP with changing the illumination side. The magnitude is not directly comparable due to the minor difference in thickness of Au layer in bottom and top contact, the presence of the quartz at the bottom and also uncertainty in the focusing of the laser spot on the junction. The same experiment was repeated for different molecules and similar independence of the PC to illumination side was obtained.



**Figure 4.13** (a) Observed photocurrent for three on/off light cycles for BTB MJ with top and bottom illumination (b) Observed OCP for three on/off light cycles for BTB MJ with top and bottom illumination. 405 nm diode laser and Keithley 6517 is used to the measurement.

For further validation of the results, we performed the AC photocurrent measurement to compare the PC spectrum for top and bottom illumination. The PC spectrum of BTB along with measured phase shift for top and bottom illumination is shown in Figure 4.14. The

spectrum is not changed with back illumination and phase shift between 0 to  $-90$  implies positive photocurrent for both cases.



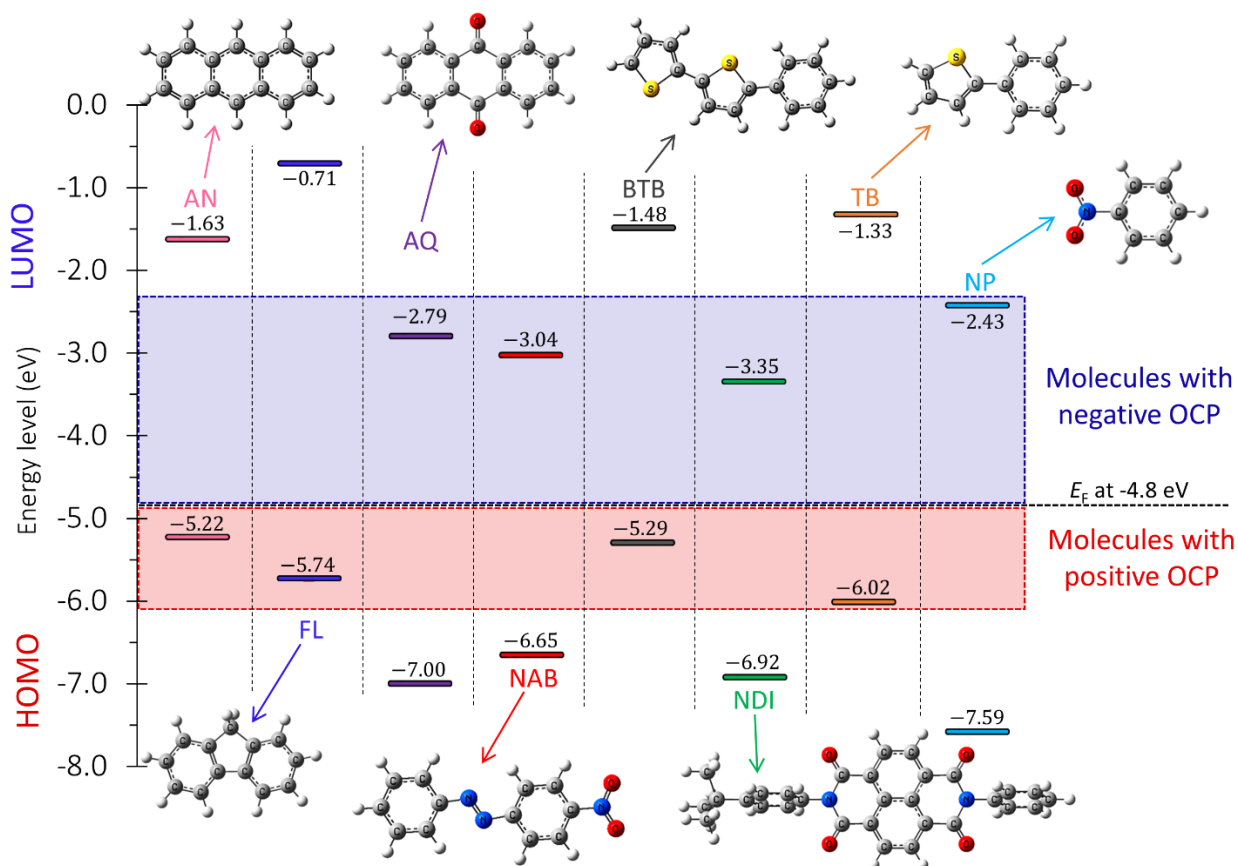
**Figure 4.14** (a) Photocurrent spectrum of BTB MJ for the top and bottom illumination. (b) Phase shift of the same junction in panel (a) for the bottom and top illumination.

## 4.4 DISCUSSION

### 4.4.1 Orbital control of the photocurrent polarity

The collection of results for eight aromatic junction structures summarized in Figure 4.10a and Table 4.1 indicates that the sign and wavelength maximum of PC, as well as the absorption maximum of the molecular layer, all vary with molecular structure. In all cases for junctions with  $d > 5$  nm, the PC spectrum is quite similar in shape to the UV-Vis absorption spectrum for the molecular layer in contact with the eC electrodes. A starting point for understanding how molecular structure affects PC response is the DFT-determined frontier orbital energy levels, shown in Figure 4.15. A common proposal for molecular tunnel junctions is based on a tunneling barrier height equal to the difference in energy between the electrode Fermi energy and the frontier orbital of the molecule (HOMO or LUMO) closest in energy.

The order in Table 4.1 is determined using this criterion, with AN having the smallest predicted barrier and NP the largest for HOMO-mediated tunneling. As indicated by the fourth column of Table 4.1, AN, BTB, FL, and TB have smaller barriers for hole tunneling ( $\phi_h$ ), while NDI, NAB, AQ, and NP have smaller electron tunneling barriers ( $\phi_e$ ) based on their DFT energies. The eight molecules cover a wide range of the HOMO (-5.3 to -7.6 vs vacuum) and LUMO (-0.8 to -3.4) energy levels, hence large variations in transport are expected based on this common model. A striking correlation is apparent in Figure 4.15 and Figure 4.10 between the OCP and PC polarities and the frontier orbitals close to the Fermi level ( $E_F$ ) of -4.8 V. Molecules with closer HOMO levels to  $E_F$  and smaller  $\phi_h$  than  $\phi_e$  (AN, BTB, FL and TB) have positive OCP and PCs, while those with closer LUMO levels and smaller  $\phi_e$  (NDI, NAB, AQ and NP) are negative. Although the free molecule DFT results are perturbed by electronic coupling with the contacts, they are consistent with the experiment in predicting whether the HOMO or LUMO energy is closest to the Fermi level. In addition, the predicted maximum absorption wavelength from TD-DFT is also close to the value observed experimentally in completed MJs. Similar sign selective currents have been reported for thermoelectric behavior in MJs;<sup>84, 217</sup> however, the mechanism is much different for the PCs reported here. As discussed in detail in Supporting Information section 5, a thermoelectric response should be dependent on chopping frequency (it is not) and should track optical power, contrary to the response shown in Figure 4.7.



**Figure 4.15** Correlation of the PC polarity and molecular orbitals. Frontier orbital energy diagram for the examined molecules relative to vacuum reference along with their Density Functional Theory (DFT) optimized molecular structure are shown. Orbital energies were calculated by DFT B3LYP 6-31G(d), in Gaussian 09. Fermi level of eC by UPS is  $-4.8$  V vs vacuum.<sup>38</sup> Blue shading indicates molecules negative PC and OCP and red shading indicates molecules with positive PC and OCP.

In addition, the OCP providing a clear indication of which frontier orbital is closer to the Fermi level, it also reflects the driving voltage for the PC. This conclusion is supported by Figure 4.10d, which shows that the PC polarity is readily reversed by an applied bias exceeding the OCP. Regarding the origin of the PC, we can rule out the IPE mechanism observed for thinner MJs ( $d < 5$  nm) in which the molecular absorption is weak.<sup>121, 209</sup> The IPE mechanism involves optical excitation in the contacts and further transport to the opposite contact through the barrier determined by either HOMO or LUMO offset from the

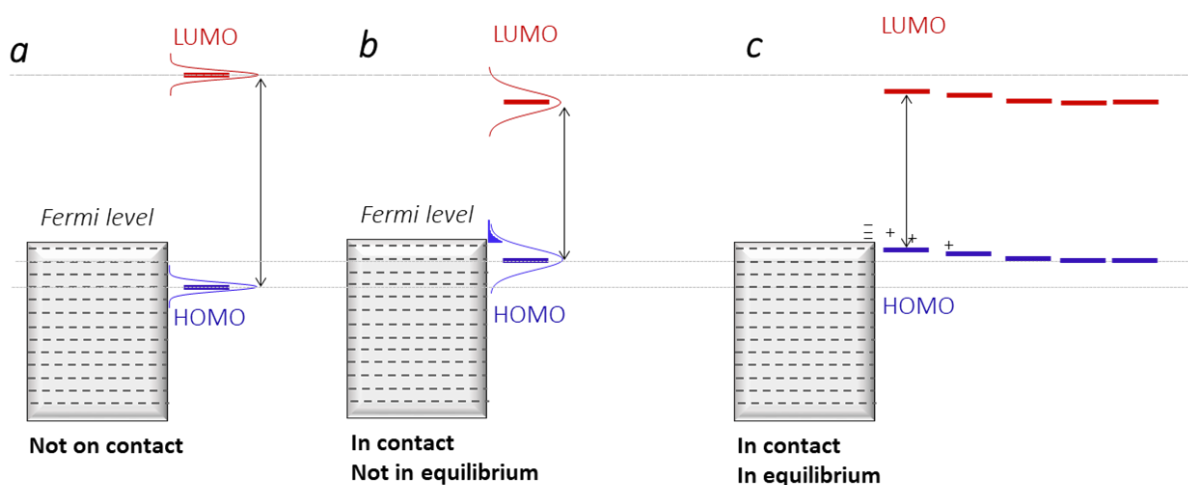
$E_F$ . IPE provided a direct probe of the hole or electron barrier for direct tunneling when  $d < 5$  nm, but was complicated when the molecule rather than the contact absorbed incident light<sup>121</sup>. In contrast, the current results for MJs with  $d > 5$  nm clearly show that the PC is negligible for photons not absorbed by the molecular layer (Figure 4.9, Figure 4.10a). The energy required for IPE is inherently smaller than the H-L gap, and the absence of PC for photon energies below the absorption onset of the molecular layer indicates that carriers excited in the contacts cannot traverse the thicker layers.

A critical observation is a strong correlation between the PC shape and the absorption spectrum of the molecular layer *as modified by electronic interactions with the contacts*. For each of the cases in Figure 4.9 and listed in Table 4.1, the onset and peak of the PC occur at similar wavelengths to those where molecular absorption occurs. As a consequence, the transport mechanism for the PC must involve the H-L gap, possibly by the photon-stimulated crossing of internal tunneling barriers, as discussed next.

#### 4.4.2 Molecule in contact with electrode

In solid state, whenever the molecule brought into the contact with the surface, the system experiences energy level alignment (ELA) in which the energy level of molecule and contact are modified relative to one another.<sup>218</sup> Several physical effects will contribute and influence the ELA.<sup>59, 67, 219</sup> Figure 4.16a shows the energy level of a molecule (Frontier molecular orbital) and electrode (eC) before contact with each other. Donor molecule with close HOMO level to the Fermi-level of contact (-4.8 in case of eC) is considered as an example. Broadening of the level is shown as a Gaussian distribution of density of states in energy axis. Although there may be a complex interplay between local charge rearrangements, bond dipoles, depolarization fields, Pauli pushback effects and interface

dipole formation; several theoretical and experimental studies agreed that the final consequence is the reduction of the HOMO-LUMO gap.<sup>59, 60, 67, 218, 219</sup> Electronic coupling of the molecule to extended states of the contact and formation of the hybridized molecule-contact interface will further reduce the gap and broaden discrete molecular energy levels. Reduction of the H-L gap, and broadening of the energy levels not only is predicted by theory, but also proved by the experimental measurements like the shift in the peak and a significant broadening of the UV-Vis absorption spectrum of molecules upon bonding to the surface. The resultant effects in energy levels of the molecule upon contacting with the surface are schematically shown in Figure 4.16b.



**Figure 4.16** Energy level alignment of the molecule in: **(a)** isolated molecule before contact with the electrode; **(b)** in contact with the surface of the electrode; **(c)** in contact and in electrostatic equilibrium for the molecular layer.

As it is shown in the schematic, after broadening of energy levels there is a possibility of charge transfer between the molecule and the contact. The direction of this charge transfer is dependent on which frontier molecular orbital is energetically closer to the Fermi-level of contact. After broadening of MOs, if the HOMO level is closer to the  $E_F$  there is a possibility



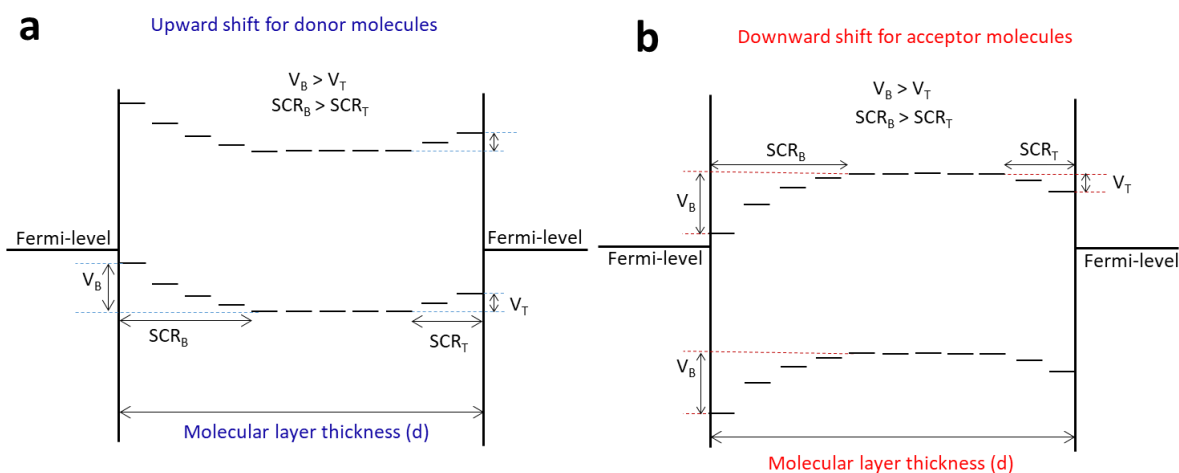
of overlapping the tail of HOMO energy level distribution with Fermi level of contact (As it is shown in Figure 4.16b). In this case, there would be charge transfer (electron flow) from the molecule to the contact. However, if the LUMO level of the molecule is closer to the  $E_F$ , there would be electron flow from the contact to the LUMO level of the molecule. Finally, this charge transfer leads to the shift in the energy level of molecules near to the surface due to electrostatic induction at the interfaces. The shifts in electrostatic potential and orbital energy levels in the molecular layer near the contact/molecule interface caused by interface charge transfer is analogous to the well-known band bending concept in semiconductors.<sup>66, 220</sup> The applicability of band bending to organic/metal interfaces has also been investigated and reviewed.<sup>63-68</sup> In addition, the concept of asymmetric coupling to the electrode was theoretically described by Galperin, et al, to explain how optical pumping can create an internal driving force for charge flow in the molecular layer.<sup>97, 221, 222</sup> The direction of the shift in energy levels can be envisioned by thinking about the electrostatic energy experienced by an electron as it moves through the interface. In case of a donor molecule with close HOMO level to contact, the image charge formed due to electronic screening in the contact stabilizes the added hole after charge transfer, making it easier to remove the electron, shifting the HOMO up. In opposite, downward shift happens in case of acceptor molecules with available LUMO levels.

#### **4.4.3 Molecular layer in contact with two interface**

As it is discussed in the previous section, the energy level alignment (ELA) becomes important and significant when the molecule is brought in contact with the surface (electrode). In complete molecular junction, there are two electrodes called bottom and top contact. The material of the contacts in our studied system for the bottom and top contact is

the same, which in turn reduces the complexity of the system (Au/eC at two sides). The molecular layer is covalently bonded to the bottom contact, however, the nature of the interface to the top contact is still unknown.

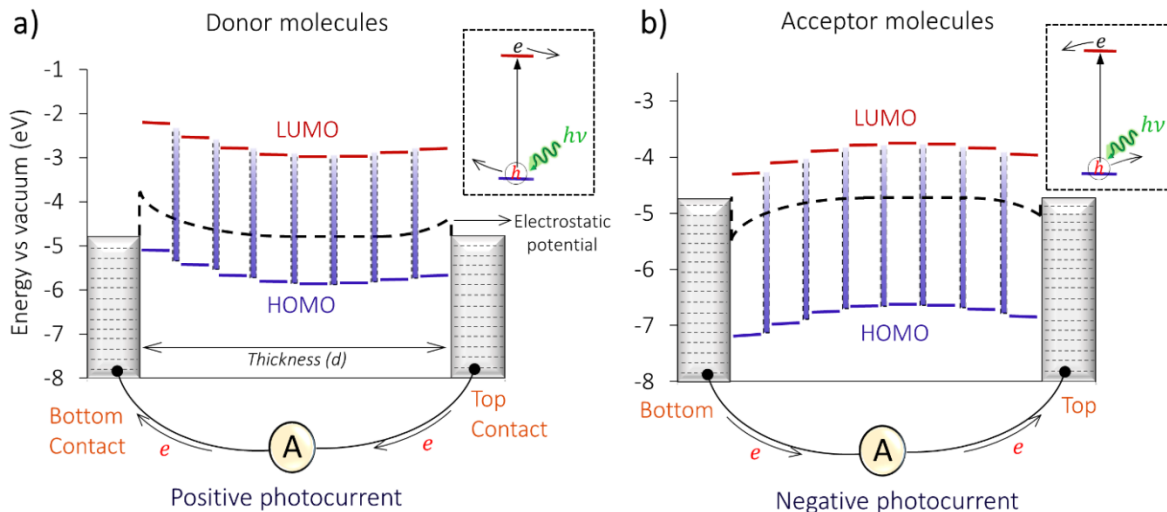
The shift in the energy level of molecular layers (upward or downward) is dependent on the amount of charge transfer and degree of coupling to the electrode.<sup>60</sup> Figure 4.17 shows the scenario for heterointerface nature, in which the coupling and charge transfer to the bottom contact is stronger. Covalent bonding to the bottom contact could be considered as the main reason for the asymmetric interface. In case of donor molecules, upward potential shift at bottom contact is larger than the one at top contact (Figure 4.17a) and for acceptor molecules, downward potential shift is larger in bottom contact (Figure 4.17b).



**Figure 4.17** Schematics of the energy level alignment at the heterointerface molecular junction in case of **(a)** donor molecules; **(b)** acceptor molecules.  $V_B$  : potential shift in energy levels of molecules at bottom contact interface,  $V_T$  : potential shift at top contact interface,  $SCR_B$ : space charge region near bottom contact interface,  $SCR_T$ : space charge region near top contact interface

#### 4.4.4 Photocurrent mechanism in thick molecular junction

We reported previously that bias-induced transport in carbon-based MJs ( $d > 5$  nm) containing FL, AQ, BTB, and NAB, conductance correlates better with the H-L gap rather than the offsets between  $E_F$  and either the HOMO or LUMO energies. We concluded that transport was limited by multi-step tunneling through the H-L barrier in the interior of the MJ, and the smaller barriers at the electrode interfaces were not controlling the current.<sup>101</sup> We proposed that the tunneling barriers are likely located between molecular subunits, where the electronic interactions between subunits of molecular layer are weak and delocalization length is limited to one or at most two attached molecules. In the current experiments with optical illumination, photon absorption permits carriers to traverse the H-L tunneling barrier and result in measurable PC from the small photo-induced OCP. The results shown in this chapter are all done with illumination from the top contact side (top illumination). However, the illumination from the other side (bottom illumination) did not change the polarity (sign) of PC and OCP. The fact that there is an measurable OCP (photovoltage) in the system regardless of the illumination side, clearly implies that there are some sorts of asymmetry in the studied junction which causes the charge separation after light absorption by the molecular layer. The specific photo-induced transitions and electron motions in a  $\sim 8$  nm thick molecular junctions are complex, and may involve multiple absorption, transport and recombination events, but the two important conclusions about OCP polarity and the strong correlation of molecular absorption with PC spectrum are manifested in the simplified schematic shown in Figure 4.18.



**Figure 4.18** Schematic of the proposed mechanism for photocurrent production in thick molecular junction. Energy level diagram at zero bias with eight pair of localized HOMO and LUMO states for: **a)** AN junction as an example of a molecule with smaller  $\phi_h$  **b)** NDI junction as an example with smaller  $\phi_e$ . Arrows indicate possible excitation and relaxation paths for the electron. Blue rectangles show the barrier between molecular subunits. Dashed line within the molecule layer is the electrostatic potential profile resulting from partial charge transfer between the electrodes and the oligomeric molecule. Top corner inset of each panel shows the direction of charge separation upon absorption of light by the molecular layer.

As it was discussed in section 4.4.2, depends on the closest MOs to the Fermi level, downward or upward shift in MO energy levels could happen near to the contacts. In section 4.4.3, we considered the introduction of asymmetry in the interfaces (heterointerface) due to strong coupling and covalent bonding to the bottom contact. Two cases are shown in Figure 4.18, one when the HOMO energy is closer to the electrode Fermi level (6a) and the other when the LUMO is closer (6b). Considering 6a first, there are upward shifts in MO energy levels near to the contacts due to electrostatic induction after charge transfer from the HOMO of molecules to the contacts. This shift is larger at bottom contact and drives the charge separation and generation of photo-voltage in the system. Molecular layer absorbs light and

photons excite the electron from the HOMO to LUMO levels. The result is a flow of the electrons from the top to bottom contact in the external circuit and positive PC and OCP. The polarity of the PC is independent of the illumination side and it is experimentally proved. When the LUMO is closer to the contact Fermi level (Figure 4.18b), downward shift leads to a negative PC and OCP opposite to that for the case of Figure 4.18a. Note that in both cases, unlike in semiconductors, the charges (electron and holes) are not free to move due to the lack of the conduction band and effective conjugation between molecular subunits. There may be multiple photoexcitation and recombination events to transverse the barriers within the molecular subunits and generating observable PC.

#### 4.5 CONCLUSION

In summary, photocurrents observed in relatively thick carbon-based molecular junctions at zero bias provide useful diagnostics of junction behavior, notably the relationship between frontier orbital energies and device electronic behavior. First, the sign of the PC and open-circuit potential are clear and direct indications of whether the HOMO or LUMO are closer in energy to the electrode Fermi level. Second, the correlation of absorbance spectrum with PC indicates that the optical gap is the main factor controlling transport in thick junctions ( $d > 5$  nm). Third, differences in electronic coupling at the top and bottom molecule/electrode interfaces are manifested as an observable OCP and PC polarity. Although asymmetric charge redistribution between the frontier molecular orbitals and the contacts is a prerequisite for the polarity of photo-voltage, the rate-limiting step for observable PC is charge transfer within the molecular layer when the thickness becomes greater than is possible with single-step (direct) tunneling. This point is consistent with a

previous conclusion of limited delocalization length within the molecular layer and H-L gaps as the effective barrier for proposed multistep tunneling mechanism dominant in thick MJ ( $d > 5$  nm). We anticipate that both the IPE mechanism reported previously and the PCs induced by molecular absorption will continue to be useful probes of molecular junction energetics and electronic behavior.

# CHAPTER 5

## Conclusion

## 5.1 Summary and final thoughts

After 30 years of extensive research in ME, it is the time to realize some promises and anticipated potential in molecular electronic devices, where the molecule act as an active circuit component. It is apparent that designing the device to show structure-function correlations is a required step for the realization of intended promises in ME. It is established through the thesis that the all-carbon thick molecular junction is a robust and stable device with behavior that depends in part on molecular orbital energies.

Chapter 2 described how electro-assisted evaporation of carbon (eC) provides a reliable interlayer buffer between metal electrodes and molecular layers. eC is an amorphous type of carbon with 30-40% sp<sup>3</sup> carbon hybridization and 3-6% oxygen to carbon ratio on its surface. eC shows outstanding flatness upon deposition and it can even improve the roughness of the deposited underlayer surface. Combining the desirable properties of eC with high conductivity of metal thin film (Au was studied here) provides suitable electrodes (top and bottom) for fabrication of cross-bar molecular junctions. Covalent attachment of molecules to the surface of eC and further covalent bonds between molecular subunits formed through electro-grafting of diazonium species assure the high stability, yield and reproducibility of finished MJs. In addition, semi-transparent and flexibility of completed junction have been examined and demonstrated. Fabricated MJ with eC electrodes enabled us to investigate the transport mechanism and associated characteristics in a platform which is suitable for scale-up fabrication and possible real-world applications.

Chapter 3 discussed the transport mechanism in thick all-carbon molecular junctions beyond the working range of direct tunneling. The results of fluorene (FL), anthraquinone



(AQ), nitro-azobenzene (NAB), and Bis-thienyl benzene (BTB) in range of 2-11 nm were compared in this chapter. Optical measurement shows that although changes in absorption maximum (wavelength of abs. peak) of examined molecules were insignificant upon deposition on the surface, the onset of absorption in longer wavelength shows substantial red shift upon bonding to the surface. In addition, further increasing the molecular layer thickness did not affect the shape of the absorption spectrum. It was concluded that the effective conjugation length for grafted molecular layer by means of electro-reduction of diazonium species is limited to one or a maximum of two monomers of the molecule. Fabricated junctions showed the high linearity of  $\ln J$  with  $V^{1/2}$  and  $T$ . Comparing the  $JV$  behavior of different molecular layer at the same thickness with the energy level of molecules, reveal the meaningful correlation between the DFT predicted H-L gap and conductivity of MJs. Furthermore, the conductivity of the MJs shows high correlation ( $R^2 > 0.95$ ) with experimentally measured peak maxima in UV-Vis absorption. Finally, we concluded that the charge transfer within localized states in the thick molecular layer is rate-limiting steps for the dominant transport rather than the charge injection at the interfaces. We proposed that multistep tunneling through the subunits of the molecular components with barrier height equal to the H-L gap is the most consistent mechanism with evidence and observations.

In Chapter 4, UV-vis light was used as a physical stimulus to gain deeper insight into the energy level alignments in completed MJ and subsequently into the charge transport mechanism in thick molecular layers ( $> 4$  nm). In order to make a reliable conclusion from the structure effect, eight different molecules with a wide range of energy were examined. In summary: i) The absorption spectrum of the molecular layers is dependent on the

environment of the molecules. The onset of the absorption spectrum of the molecular layer shows a significant red shift to longer wavelengths upon covalent bonding to the electrode surface and multilayer formation. However, increasing thickness of the molecular multilayer does not cause further red shift in the optical gap of the molecular layer. Subsequently, deposition of the top contact causes an additional red shift in the onset of the absorption spectra in most of the examined molecules. ii) Photocurrent spectrum closely follows the absorption of the molecular layer in the complete junction structure (full stack of the deposited layer). iii) There is a measurable and reversible induced field and OCP in the molecular junctions upon exposure to the light. iv) The sign of measured photocurrent and OCP can be either positive or negative based on the structure of the molecular layer. These polarities are characteristic of the tested molecule regardless of the thickness ( $>4$  nm). v) The sign and magnitude of the photocurrent can be tuned by the external bias across the junction. vi) There is a distinct correlation between the alignments of the frontier molecular orbital energy levels of the molecules and the sign of the photocurrent in the unbiased junction. Molecules with a HOMO closer to the electrode Fermi level than the LUMO show positive OCP. In contrast, the molecules with more a LUMO closer to  $E_F$  show negative OCP.

In chapter 3, we concluded that charge injection at electrode interfaces is not the rate-limiting step in transport, and in chapter 4 we demonstrated the presence of a hetero-interface character in all-carbon molecular junctions despite symmetric material at both electrodes. If the injection was relevant to the transport in the thick molecular junction, the junction should show rectification due to the demonstrated difference in interfaces. The absence of rectification and the conclusions from chapter 3 and 4 are consistent that transport in the molecular layer interior rather than at the electrode interfaces is controlling transport,

with the H-L gap as the effective barrier for charge transfer in localized orbitals in the molecular layer.

## 5.2 Outlook

Based on the results in each chapter, there are potentially important points to pursue in future. In chapter two, eC electrode was introduced for fabrication cross-bar molecular junctions. However, it was not systematically addressed the applicability of the proposed technique for fabrication of another type of nanodevices like inorganic Metal-Insulator-Metal devices. I made several batches of the junctions with electron-beam evaporated AlOx as an active component and eC electrodes. Initial results showed promising prospects regarding the high yield and stability of fabricated devices. I believe that eC electrodes are valuable with some remarkable advantages beyond the molecular electronics.

Chapter three investigated the region of transport in molecular junctions that exhibited structure controlled properties. In this region the localized states in molecular layer start to govern transport rather than the contact effects such as orbital energy offsets from the electrode Fermi levels. One may expect that when the charges reside in the energy level of the molecules, chemical changes in molecules (e.g. redox activity) should take place. However, the time scale of charge transfer is important in this process. If the charge transfer and relaxation in molecular layer are faster than the time scale of reorganization, redox chemistry is not expected. With attention to electrochemistry prospect, one approach is the motion and presence of ions at the interfaces and screen the field sharply near to the electrodes. In this way, the applied field would be enough to inject the charges directly from the Fermi level of electrodes into the MO of the molecular layer. The idea of screening at interfaces and redox activity in organic memory devices have followed and studied in RLM

group before. Nevertheless, I believe that the effective result of redox chemistry in the molecular junction is stabilization of charges on subunits of the molecular layer by counter ions motion within the molecular layer. I examined the idea of incorporating the solid electrolyte into the system and initial results clearly demonstrate the possibility of controlled redox chemistry in the solid-state molecular junction. Realization of redox chemistry in solid-state and at the molecular scale is a foundation of many promised applications of organic devices. Collectively, there is a great potential to follow the transport mechanism in the thick molecular junction and controlling redox chemistry in the molecular junction.

In chapter four, the interaction of light with thick molecular junction was investigated. We gained valuable insight into the energy level alignments in the molecular junctions, especially at the interfaces with measuring the photo-voltage and photocurrent at zero bias. It is clear that changes in energy level alignments under the applied bias across the junction is of great consequence to our understanding of dynamics of the molecular layer. Moreover, reversible photo-switching in conductivity of molecular junction in a very short time ( $\sim$ ns), without changes in the configuration of the molecular layer is of interest. We showed limited data about the PC current under the bias evidence in chapter four. However, the required setup and programs are prepared and PC under the bias for different thicknesses of two molecules have been measured. Some important controls and further experiments are needed before drawing a conclusion about the photoconductivity of molecular junction. Collectively, light interaction with molecular layer during transport and related photo-effects can be a valuable area for further research.

## References

1. Aradhya S. V., Venkataraman L. Single-molecule junctions beyond electronic transport. *Nat Nanotechnol* **8**, 399-410 (2013).
2. Bergren A. J., McCreery R. L. Analytical chemistry in molecular electronics. *Annu Rev Anal Chem (Palo Alto Calif)* **4**, 173-195 (2011).
3. Coskun A., *et al.* High hopes: Can molecular electronics realise its potential? *Chem. Soc. Rev.* **41**, 4827-4859 (2012).
4. Erbe A., Verleger S. Molecular electronics: A review of experimental results. *Acta Phys. Pol., A* **115**, 455-461 (2009).
5. Jeong H., Kim D., Xiang D., Lee T. High-yield functional molecular electronic devices. *ACS Nano* **11**, 6511-6548 (2017).
6. Liu Z., Ren S., Guo X. Switching effects in molecular electronic devices. *Top Curr Chem (Cham)* **375**, 56 (2017).
7. McCreery R. L., Bergren A. J. Progress with molecular electronic junctions: Meeting experimental challenges in design and fabrication. *Adv. Mater.* **21**, 4303-4322 (2009).
8. Metzger R. M. Unimolecular electronics. *Chem. Rev.* **115**, 5056-5115 (2015).
9. Su T. A., Neupane M., Steigerwald M. L., Venkataraman L., Nuckolls C. Chemical principles of single-molecule electronics. *Nature Reviews Materials* **1**, 16002 (2016).
10. Tyagi P. Multilayer edge molecular electronics devices: A review. *J. Mater. Chem.* **21**, 4733-4742 (2011).
11. Vilan A., Aswal D., Cahen D. Large-area, ensemble molecular electronics: Motivation and challenges. *Chem. Rev.* **117**, 4248-4286 (2017).
12. Vilan A., Cahen D. Chemical modification of semiconductor surfaces for molecular electronics. *Chem. Rev.* **117**, 4624-4666 (2017).
13. Xiang D., Wang X., Jia C., Lee T., Guo X. Molecular-scale electronics: From concept to function. *Chem. Rev.* **116**, 4318-4440 (2016).
14. Aviram A., Ratner M. Molecular rectifiers. *Chem. Phys. Lett.* **29**, 277-283 (1974).
15. Binnig G., Rohrer H., Gerber C., Weibel E. Surface studies by scanning tunneling microscopy. *Phys. Rev. Lett.* **49**, 57 (1982).

16. Reed M. A., Zhou C., Muller C. J., Burgin T. P., Tour J. M. Conductance of a molecular junction. *Science* **278**, 252-254 (1997).
17. Park J., *et al.* Coulomb blockade and the kondo effect in single-atom transistors. *Nature* **417**, 722-725 (2002).
18. Xiang J., *et al.* A controllable electrochemical fabrication of metallic electrodes with a nanometer/angstrom-sized gap using an electric double layer as feedback. *Angew. Chem. Int. Ed. Engl.* **44**, 1265-1268 (2005).
19. Bonifas A. P., McCreery R. L. 'Soft' au, pt and cu contacts for molecular junctions through surface-diffusion-mediated deposition. *Nat Nanotechnol* **5**, 612-617 (2010).
20. Haick H., Cahen D. Contacting organic molecules by soft methods: Towards molecule-based electronic devices. *Acc. Chem. Res.* **41**, 359-366 (2008).
21. Chabynyc M. L., *et al.* Molecular rectification in a metal-insulator-metal junction based on self-assembled monolayers. *J. Am. Chem. Soc.* **124**, 11730-11736 (2002).
22. Zhou C., Deshpande M. R., Reed M. A., Jones L., Tour J. M. Nanoscale metal/self-assembled monolayer/metal heterostructures. *Appl. Phys. Lett.* **71**, 611-613 (1997).
23. Loo Y. L., Lang D. V., Rogers J. A., Hsu J. W. P. Electrical contacts to molecular layers by nanotransfer printing. *Nano Lett.* **3**, 913-917 (2003).
24. Tang J., Wang Y., Klare J. E., Tulevski G. S., Wind S. J., Nuckolls C. Encoding molecular-wire formation within nanoscale sockets. *Angew. Chem. Int. Ed. Engl.* **46**, 3892-3895 (2007).
25. Chen X., *et al.* On-wire lithography-generated molecule-based transport junctions: A new testbed for molecular electronics. *J. Am. Chem. Soc.* **130**, 8166-8168 (2008).
26. Akkerman H. B., Blom P. W., de Leeuw D. M., de Boer B. Towards molecular electronics with large-area molecular junctions. *Nature* **441**, 69-72 (2006).
27. Kushmerick J. G., Naciri J., Yang J. C., Shashidhar R. Conductance scaling of molecular wires in parallel. *Nano Lett.* **3**, 897-900 (2003).
28. Lambert C. J. Basic concepts of quantum interference and electron transport in single-molecule electronics. *Chem. Soc. Rev.* **44**, 875-888 (2015).
29. Cao Y., *et al.* Building high-throughput molecular junctions using indented graphene point contacts. *Angew. Chem. Int. Ed. Engl.* **51**, 12228-12232 (2012).
30. Ashwell G. J., *et al.* Molecular bridging of silicon nanogaps. *ACS Nano* **4**, 7401-7406 (2010).

31. Okawa Y., *et al.* Chemical wiring and soldering toward all-molecule electronic circuitry. *J. Am. Chem. Soc.* **133**, 8227-8233 (2011).
32. Wang W., Lee T., Reed M. A. Mechanism of electron conduction in self-assembled alkanethiol monolayer devices. *Physical Review B* **68**, (2003).
33. Wang G., Kim T. W., Lee H., Lee T. Influence of metal-molecule contacts on decay coefficients and specific contact resistances in molecular junctions. *Physical Review B* **76**, (2007).
34. Chu C., Na J. S., Parsons G. N. Conductivity in alkylamine/gold and alkanethiol/gold molecular junctions measured in molecule/nanoparticle/molecule bridges and conducting probe structures. *J. Am. Chem. Soc.* **129**, 2287-2296 (2007).
35. Fracasso D., Valkenier H., Hummelen J. C., Solomon G. C., Chiechi R. C. Evidence for quantum interference in sams of aryldiethynylene thiolates in tunneling junctions with eutectic ga-in (egain) top-contacts. *J. Am. Chem. Soc.* **133**, 9556-9563 (2011).
36. Neuhausen A. B., Hosseini A., Sulpizio J. A., Chidsey C. E., Goldhaber-Gordon D. Molecular junctions of self-assembled monolayers with conducting polymer contacts. *ACS Nano* **6**, 9920-9931 (2012).
37. Wang G., Kim Y., Choe M., Kim T. W., Lee T. A new approach for molecular electronic junctions with a multilayer graphene electrode. *Adv. Mater.* **23**, 755-760 (2011).
38. Morteza Najarian A., Szeto B., Tefashe U. M., McCreery R. L. Robust all-carbon molecular junctions on flexible or semi-transparent substrates using "process-friendly" fabrication. *ACS Nano* **10**, 8918-8928 (2016).
39. Seo S., Min M., Lee J., Lee T., Choi S. Y., Lee H. Solution-processed reduced graphene oxide films as electronic contacts for molecular monolayer junctions. *Angew. Chem. Int. Ed. Engl.* **51**, 108-112 (2012).
40. Ceccato M., Bousquet A., Hinge M., Pedersen S. U., Daasbjerg K. Using a mediating effect in the electroreduction of aryldiazonium salts to prepare conducting organic films of high thickness. *Chemistry of Materials* **23**, 1551-1557 (2011).
41. Laurentius L., *et al.* Diazonium-derived aryl films on gold nanoparticles: Evidence for a carbon-gold covalent bond. *ACS Nano* **5**, 4219-4227 (2011).
42. Combellas C., Kanoufi F., Pinson J., Podvorica F. I. Time-of-flight secondary ion mass spectroscopy characterization of the covalent bonding between a carbon surface and aryl groups. *Langmuir* **21**, 280-286 (2005).

43. Chernyy S., *et al.* Elucidation of the mechanism of redox grafting of diazotated anthraquinone. *Langmuir* **28**, 9573-9582 (2012).
44. Bousquet A., Ceccato M., Hinge M., Pedersen S. U., Daasbjerg K. Redox grafting of diazotated anthraquinone as a means of forming thick conducting organic films. *Langmuir* **28**, 1267-1275 (2012).
45. Supur M., Smith S. R., McCreery R. L. Characterization of growth patterns of nanoscale organic films on carbon electrodes by surface enhanced raman spectroscopy. *Anal Chem* **89**, 6463-6471 (2017).
46. Amdursky N., Marchak D., Sepunaru L., Pecht I., Sheves M., Cahen D. Electronic transport via proteins. *Adv. Mater.* **26**, 7142-7161 (2014).
47. Choi S. H., Risko C., Delgado M. C., Kim B., Bredas J. L., Frisbie C. D. Transition from tunneling to hopping transport in long, conjugated oligo-imine wires connected to metals. *J. Am. Chem. Soc.* **132**, 4358-4368 (2010).
48. Finklea H. O. Electrochemistry of organized monolayers of thiols and related molecules on electrodes. In: *Electroanalytical chemistry* (ed<sup>^</sup>(eds Bard A. J.). Dekker (1996).
49. Li X., He J., Hihath J., Xu B., Lindsay S. M., Tao N. Conductance of single alkanedithiols: Conduction mechanism and effect of molecule-electrode contacts. *J. Am. Chem. Soc.* **128**, 2135-2141 (2006).
50. Chiechi R. C., Weiss E. A., Dickey M. D., Whitesides G. M. Eutectic gallium-indium (egain): A moldable liquid metal for electrical characterization of self-assembled monolayers. *Angew. Chem. Int. Ed. Engl.* **47**, 142-144 (2008).
51. Yang H.-H., McCreery R. L. Effects of surface monolayers on the electron transfer kinetics and adsorption of methyl viologen and phenothiazine derivatives on glassy carbon electrodes. *Anal. Chem.* **71**, 4081-4087 (1999).
52. Creager S., *et al.* Electron transfer at electrodes through conjugated "molecular wire" bridges. *J. Am. Chem. Soc.* **121**, 1059-1064 (1999).
53. Yamada R., Kumazawa H., Noutoshi T., Tanaka S., Tada H. Electrical conductance of oligothiophene molecular wires. *Nano Lett.* **8**, 1237-1240 (2008).
54. He J., *et al.* Electronic decay constant of carotenoid polyenes from single-molecule measurements. *J. Am. Chem. Soc.* **127**, 1384-1385 (2005).
55. Liu K., Li G., Wang X., Wang F. Length dependence of electron conduction for oligo(1,4-phenylene ethynylene)s: A conductive probe-atomic force microscopy investigation. *Journal of Physical Chemistry C* **112**, 4342-4349 (2008).



56. Choi S. H., Kim B., Frisbie C. D. Electrical resistance of long conjugated molecular wires. *Science* **320**, 1482-1486 (2008).
57. Stallinga P. Electronic transport in organic materials: Comparison of band theory with percolation/(variable range) hopping theory. *Adv. Mater.* **23**, 3356-3362 (2011).
58. Sayed S. Y., Fereiro J. A., Yan H., McCreery R. L., Bergren A. J. Charge transport in molecular electronic junctions: Compression of the molecular tunnel barrier in the strong coupling regime. *Proc Natl Acad Sci U S A* **109**, 11498-11503 (2012).
59. Chen Y. F., Tamblyn I., Quek S. Y. Energy level alignment at hybridized organic-metal interfaces: The role of many-electron effects. *Journal of Physical Chemistry C* **121**, 13125-13134 (2017).
60. Zheng Y. J., *et al.* Heterointerface screening effects between organic monolayers and monolayer transition metal dichalcogenides. *ACS Nano* **10**, 2476-2484 (2016).
61. Tang J. X., Lee C. S., Lee S. T. Electronic structures of organic/organic heterojunctions: From vacuum level alignment to fermi level pinning. *J. Appl. Phys.* **101**, 064504-064504 (2007).
62. Kim B., Beebe J. M., Jun Y., Zhu X. Y., Frisbie C. D. Correlation between homo alignment and contact resistance in molecular junctions: Aromatic thiols versus aromatic isocyanides. *J. Am. Chem. Soc.* **128**, 4970-4971 (2006).
63. Ishii H., Sugiyama K., Ito E., Seki K. Energy level alignment and interfacial electronic structures at organic/metal and organic/organic interfaces. *Adv. Mater.* **11**, 605-625 (1999).
64. Hill I. G., Makinen A. J., Kafafi Z. H. Initial stages of metal/organic semiconductor interface formation. *J. Appl. Phys.* **88**, 889-895 (2000).
65. Heimel G., Romaner L., Zojer E., Bredas J. L. Toward control of the metal-organic interfacial electronic structure in molecular electronics: A first-principles study on self-assembled monolayers of  $\pi$ -conjugated molecules on noble metals. *Nano Lett.* **7**, 932-940 (2007).
66. Zhang Z., Yates J. T., Jr. Band bending in semiconductors: Chemical and physical consequences at surfaces and interfaces. *Chem. Rev.* **112**, 5520-5551 (2012).
67. Flores F., Ortega J., Vazquez H. Modelling energy level alignment at organic interfaces and density functional theory. *Phys. Chem. Chem. Phys.* **11**, 8658-8675 (2009).

68. Hwang J., Wan A., Kahn A. Energetics of metal–organic interfaces: New experiments and assessment of the field. *Materials Science and Engineering: R: Reports* **64**, 1-31 (2009).
69. Ponce Ortiz R., Facchetti A., Marks T. J. High-k organic, inorganic, and hybrid dielectrics for low-voltage organic field-effect transistors. *Chem. Rev.* **110**, 205-239 (2010).
70. McCreery R. Molecular electronic junctions. *Chem. Mater.* **16**, 4477-4496 (2004).
71. Ho Choi S., Kim B., Frisbie C. D. Electrical resistance of long conjugated molecular wires. *Science* **320**, 1482-1486 (2008).
72. Metzger R. M., *et al.* Unimolecular electrical rectification in hexadecylquinolinium tricyanoquinodimethanide. *J. Am. Chem. Soc.* **119**, 10455-10466 (1997).
73. Chiu F.-C. A review on conduction mechanisms in dielectric films. *Advances in Materials Science and Engineering* **2014**, 1-18 (2014).
74. Tessler N., Preezant Y., Rappaport N., Roichman Y. Charge transport in disordered organic materials and its relevance to thin-film devices: A tutorial review. *Adv. Mater.* **21**, 2741-2761 (2009).
75. Lee P. A., Ramakrishnan T. V. Disordered electronic systems. *Rev. Mod. Phys.* **57**, 287-337 (1985).
76. Koughia C., Kasap S., Capper P. Springer handbook of electronic and photonic materials. (2007).
77. Joo J., Long S. M., Pouget J. P., Oh E. J., MacDiarmid A. G., Epstein A. J. Charge transport of the mesoscopic metallic state in partially crystalline polyanilines. *Physical Review B: Condensed Matter and Materials Physics* **57**, 9567-9580 (1998).
78. Borsenberger P. M., Pautmeier L., Bässler H. Charge transport in disordered molecular solids. *The Journal of Chemical Physics* **94**, 5447-5454 (1991).
79. Roberts G. G., Apsley N., Munn R. W. Temperature dependent electronic conduction in semiconductors. *Physics Reports* **60**, 59-150 (1980).
80. Roberts G. G., Polanco J. I. Thermally assisted tunnelling in dielectric films. *Physica Status Solidi (a)* **1**, 409-420 (1970).
81. Majumdar A. Materials science. Thermoelectricity in semiconductor nanostructures. *Science* **303**, 777-778 (2004).

82. Hochbaum A. I., *et al.* Enhanced thermoelectric performance of rough silicon nanowires. *Nature* **451**, 163-167 (2008).
83. Paulsson M., Datta S. Thermoelectric effect in molecular electronics. *Physical Review B* **67**, (2003).
84. Widawsky J. R., Darancet P., Neaton J. B., Venkataraman L. Simultaneous determination of conductance and thermopower of single molecule junctions. *Nano Lett.* **12**, 354-358 (2012).
85. Atwater H. A., Polman A. Plasmonics for improved photovoltaic devices. *Nat Mater* **9**, 205-213 (2010).
86. Jacob Z., Shalaev V. M. Physics. Plasmonics goes quantum. *Science* **334**, 463-464 (2011).
87. Wang T., Nijhuis C. A. Molecular electronic plasmonics. *Applied Materials Today* **3**, 73-86 (2016).
88. Du W., *et al.* On-chip molecular electronic plasmon sources based on self-assembled monolayer tunnel junctions. *Nature Photonics* **10**, 274-+ (2016).
89. Martinek J., *et al.* Kondo effect in single-molecule spintronic devices. *J. Magn. Magn. Mater.* **310**, e343-e345 (2007).
90. Naber W. J. M., Faez A. S., Wiel A. W. G. v. d. Organic spintronics. *J. Phys. D: Appl. Phys.* **40**, R205-R228 (2007).
91. Jang H.-J., Pernstich K. P., Gundlach D. J., Jurchescu O. D., Richter C. A. Observation of spin-polarized electron transport in alq<sub>3</sub> by using a low work function metal. *Appl. Phys. Lett.* **101**, 102412-102412-102415 (2012).
92. Jang H. J., *et al.* Interface engineering to control magnetic field effects of organic-based devices by using a molecular self-assembled monolayer. *ACS Nano* **8**, 7192-7201 (2014).
93. Rakhmievitch D., Sarkar S., Bitton O., Kronik L., Tal O. Enhanced magnetoresistance in molecular junctions by geometrical optimization of spin-selective orbital hybridization. *Nano Lett.* **16**, 1741-1745 (2016).
94. Schmaus S., *et al.* Giant magnetoresistance through a single molecule. *Nat Nanotechnol* **6**, 185-189 (2011).
95. Galperin M. Photonics and spectroscopy in nanojunctions: A theoretical insight. *Chem. Soc. Rev.* **46**, 4000-4019 (2017).

96. Nayak P. K., Narasimhan K. L., Cahen D. Separating charges at organic interfaces: Effects of disorder, hot states, and electric field. *J Phys Chem Lett* **4**, 1707-1717 (2013).
97. Galperin M., Nitzan A. Molecular optoelectronics: The interaction of molecular conduction junctions with light. *Phys. Chem. Chem. Phys.* **14**, 9421-9438 (2012).
98. Kondratenko M., Moiseev A. G., Perepichka D. F. New stable donor-acceptor dyads for molecular electronics. *J. Mater. Chem.* **21**, 1470-1478 (2011).
99. Pourhossein P., Vijayaraghavan R. K., Meskers S. C., Chiechi R. C. Optical modulation of nano-gap tunnelling junctions comprising self-assembled monolayers of hemicyanine dyes. *Nat Commun* **7**, 11749 (2016).
100. Liu Z., *et al.* Revealing the molecular structure of single-molecule junctions in different conductance states by fishing-mode tip-enhanced raman spectroscopy. *Nat Commun* **2**, 305 (2011).
101. Morteza Najarian A., McCreery R. L. Structure controlled long-range sequential tunneling in carbon-based molecular junctions. *ACS Nano* **11**, 3542-3552 (2017).
102. Sangeeth C. S., Demissie A. T., Yuan L., Wang T., Frisbie C. D., Nijhuis C. A. Comparison of dc and ac transport in 1.5-7.5 nm oligophenylene imine molecular wires across two junction platforms: Eutectic ga-in versus conducting probe atomic force microscope junctions. *J. Am. Chem. Soc.* **138**, 7305-7314 (2016).
103. Bayat A., Lacroix J. C., McCreery R. L. Control of electronic symmetry and rectification through energy level variations in bilayer molecular junctions. *J. Am. Chem. Soc.* **138**, 12287-12296 (2016).
104. Trasobares J., Vuillaume D., Theron D., Clement N. A 17 ghz molecular rectifier. *Nat Commun* **7**, 12850 (2016).
105. Yuan L., *et al.* Controlling the direction of rectification in a molecular diode. *Nat Commun* **6**, 6324 (2015).
106. Li Z., *et al.* Regulating a benzodifuran single molecule redox switch via electrochemical gating and optimization of molecule/electrode coupling. *J. Am. Chem. Soc.* **136**, 8867-8870 (2014).
107. Min M., Seo S., Lee S. M., Lee H. Voltage-controlled nonvolatile molecular memory of an azobenzene monolayer through solution-processed reduced graphene oxide contacts. *Adv. Mater.* **25**, 7045-7050 (2013).
108. Green J. E., *et al.* A 160-kilobit molecular electronic memory patterned at 10(11) bits per square centimetre. *Nature* **445**, 414-417 (2007).

109. Whalley A. C., Steigerwald M. L., Guo X., Nuckolls C. Reversible switching in molecular electronic devices. *J. Am. Chem. Soc.* **129**, 12590-12591 (2007).
110. Jia C., *et al.* Covalently bonded single-molecule junctions with stable and reversible photoswitched conductivity. *Science* **352**, 1443-1445 (2016).
111. Bergren A. J., Zeer-Wanklyn L., Semple M., Pekas N., Szeto B., McCreery R. L. Musical molecules: The molecular junction as an active component in audio distortion circuits. *J. Phys.: Condens. Matter* **28**, 094011 (2016).
112. Anariba F., Steach J. K., McCreery R. L. Strong effects of molecular structure on electron transport in carbon/molecule/copper electronic junctions. *J. Phys. Chem. B* **109**, 11163-11172 (2005).
113. Baldea I., Xie Z., Frisbie C. D. Uncovering a law of corresponding states for electron tunneling in molecular junctions. *Nanoscale* **7**, 10465-10471 (2015).
114. Nijhuis C. A., Reus W. F., Whitesides G. M. Mechanism of rectification in tunneling junctions based on molecules with asymmetric potential drops. *J. Am. Chem. Soc.* **132**, 18386-18401 (2010).
115. Nijhuis C. A., Reus W. F., Whitesides G. M. Molecular rectification in metal-sam-metal oxide-metal junctions. *J. Am. Chem. Soc.* **131**, 17814-17827 (2009).
116. Fluteau T., *et al.* Tuning the thickness of electrochemically grafted layers in large area molecular junctions. *J. Appl. Phys.* **116**, 114509 (2014).
117. Martin P., Della Rocca M. L., Anthore A., Lafarge P., Lacroix J. C. Organic electrodes based on grafted oligothiophene units in ultrathin, large-area molecular junctions. *J. Am. Chem. Soc.* **134**, 154-157 (2012).
118. Kim T., Liu Z. F., Lee C., Neaton J. B., Venkataraman L. Charge transport and rectification in molecular junctions formed with carbon-based electrodes. *Proc Natl Acad Sci U S A* **111**, 10928-10932 (2014).
119. Hong J.-Y., Jeon S. O., Jang J., Song K., Kim S. H. A facile route for the preparation of organic bistable memory devices based on size-controlled conducting polypyrrole nanoparticles. *Org. Electron.* **14**, 979-983 (2013).
120. Wu J., McCreery R. L. Solid-state electrochemistry in molecule/tio[sub 2] molecular heterojunctions as the basis of the tio[sub 2] ``memristor''. *J. Electrochem. Soc.* **156**, P29-P37 (2009).

121. Fereiro J. A., Kondratenko M., Bergren A. J., McCreery R. L. Internal photoemission in molecular junctions: Parameters for interfacial barrier determinations. *J. Am. Chem. Soc.* **137**, 1296-1304 (2015).
122. Banerjee P., Conklin D., Nanayakkara S., Park T. H., Therien M. J., Bonnell D. A. Plasmon-induced electrical conduction in molecular devices. *ACS Nano* **4**, 1019-1025 (2010).
123. Conklin D., *et al.* Exploiting plasmon-induced hot electrons in molecular electronic devices. *ACS Nano* **7**, 4479-4486 (2013).
124. Ivashenko O., Bergren A. J., McCreery R. L. Light emission as a probe of energy losses in molecular junctions. *J. Am. Chem. Soc.* **138**, 722-725 (2016).
125. Du W., *et al.* On-chip molecular electronic plasmon sources based on self-assembled monolayer tunnel junctions. *Nature Photonics* **10**, 274-280 (2016).
126. Marquardt C. W., *et al.* Electroluminescence from a single nanotube-molecule-nanotube junction. *Nat Nanotechnol* **5**, 863-867 (2010).
127. Kumar R., Pillai R. G., Pekas N., Wu Y., McCreery R. L. Spatially resolved raman spectroelectrochemistry of solid-state polythiophene/viologen memory devices. *J. Am. Chem. Soc.* **134**, 14869-14876 (2012).
128. Lacaze P. C., Lacroix J.-C. *Non-volatile memories*. ISTE Ltd (2014).
129. Migliore A., Nitzan A. Nonlinear charge transport in redox molecular junctions: A marcus perspective. *ACS Nano* **5**, 6669-6685 (2011).
130. Bergren A. J., McCreery R. L., Stoyanov S. R., Gusarov S., Kovalenko A. Electronic characteristics and charge transport mechanisms for large area aromatic molecular junctions. *Journal of Physical Chemistry C* **114**, 15806-15815 (2010).
131. Mahmoud A. M., Bergren A. J., Pekas N., McCreery R. L. Towards integrated molecular electronic devices: Characterization of molecular layer integrity during fabrication processes. *Adv. Funct. Mater.* **21**, 2273-2281 (2011).
132. Donner S., Li H. W., Yeung E. S., Porter M. D. Fabrication of optically transparent carbon electrodes by the pyrolysis of photoresist films: Approach to single-molecule spectroelectrochemistry. *Anal. Chem.* **78**, 2816-2822 (2006).
133. Tian H., Bergren A. J., McCreery R. L. Ultraviolet-visible spectroelectrochemistry of chemisorbed molecular layers on optically transparent carbon electrodes. *Appl. Spectrosc.* **61**, 1246-1253 (2007).

134. Mattson J. S., Smith C. A. Optically transparent carbon film electrodes for infrared spectroelectrochemistry. *Anal. Chem.* **47**, 1122-1125 (1975).
135. DeAngelis T. P., Hurst R. W., Yacynych A. M., Mark H. B., Jr., Heineman W. R., Mattson J. S. Carbon and mercury-carbon optically transparent electrodes. *Anal. Chem.* **49**, 1395-1398 (1977).
136. Blackstock J. J., Rostami A. A., Nowak A. M., McCreery R. L., Freeman M. R., McDermott M. T. Ultraflat carbon film electrodes prepared by electron beam evaporation. *Anal. Chem.* **76**, 2544-2552 (2004).
137. Ru J., Szeto B., Bonifas A., McCreery R. L. Microfabrication and integration of diazonium-based aromatic molecular junctions. *ACS Appl Mater Interfaces* **2**, 3693-3701 (2010).
138. Yan H., Bergren A. J., McCreery R. L. All-carbon molecular tunnel junctions. *J. Am. Chem. Soc.* **133**, 19168-19177 (2011).
139. Ramsey J. D., Ranganathan S., Zhao J., McCreery R. L. Performance comparison of conventional and line-focused surface raman spectrometers. *Appl. Spectrosc.* **55**, 767-773 (2001).
140. Robertson J. Diamond-like amorphous carbon. *Materials Science and Engineering: R: Reports* **37**, 129-281 (2002).
141. Ferrari A. C., Robertson J. Interpretation of raman spectra of disordered and amorphous carbon. *Physical Review B* **61**, 14095-14107 (2000).
142. Jackson S. Determining hybridization differences for amorphous carbon from the xps c 1s envelope. *Appl. Surf. Sci.* **90**, 195-203 (1995).
143. Jia J., *et al.* Structure and electrochemical properties of carbon films prepared by a electron cyclotron resonance sputtering method. *Anal. Chem.* **79**, 98-105 (2007).
144. Ambrosi A., Bonanni A., Sofer Z., Pumera M. Large-scale quantification of cvd graphene surface coverage. *Nanoscale* **5**, 2379-2387 (2013).
145. Ambrosi A., Chua C. K., Bonanni A., Pumera M. Electrochemistry of graphene and related materials. *Chemical Reviews* **114**, 7150-7188 (2014).
146. Brownson D. A. C., Banks C. E. Cvd graphene electrochemistry: The role of graphitic islands. *Physical Chemistry Chemical Physics* **13**, 15825-15828 (2011).
147. Velický M., *et al.* Electron transfer kinetics on mono- and multilayer graphene. *ACS Nano* **8**, 10089-10100 (2014).

148. Conley Jr J. F., Alimardani N. Rectenna solar cells. (ed<sup>^</sup>(eds). Springer Science (2013).
149. Cowell E. W., 3rd, *et al.* Advancing mim electronics: Amorphous metal electrodes. *Adv. Mater.* **23**, 74-78 (2011).
150. Yang S., Kymissis I., Leland E. S., Liu S., O'Brien S. Influence of electromigration on the maximum operating field of (ba, sr)tio<sub>3</sub>/parylene-c composite capacitors. *Journal of Vacuum Science & Technology B, Nanotechnology and Microelectronics: Materials, Processing, Measurement, and Phenomena* **31**, 60603 (2013).
151. Ranganathan S., McCreery R. L. Electroanalytical performance of carbon films with near-atomic flatness. *Anal. Chem.* **73**, 893-900 (2001).
152. Ranganathan S., McCreery R. L., Majji S. M., Madou M. Photoresist-derived carbon for microelectrochemical applications. *J. Electrochem. Soc.* **147**, 277 - 282 (2000).
153. Fairman C., Yu S. S. C., Liu G., Downard A. J., Hibbert D. B., Gooding J. J. Exploration of variables in the fabrication of pyrolysed photoresist. *J. Solid State Electrochem.* **12**, 1357-1365 (2008).
154. Yu S. S., Downard A. J. Photochemical grafting and activation of organic layers on glassy carbon and pyrolyzed photoresist films. *Langmuir* **23**, 4662-4668 (2007).
155. Wang S., Swain G. M. Spatially heterogeneous electrical and electrochemical properties of hydrogen-terminated boron-doped nanocrystalline diamond thin film deposited from an argon-rich ch<sub>4</sub>/h<sub>2</sub>/ar/b<sub>2</sub>h<sub>6</sub> source gas mixture. *Journal of Physical Chemistry C* **111**, 3986-3995 (2007).
156. Stotter J., Show Y., Wang S., Swain G. Comparison of the electrical, optical, and electrochemical properties of diamond and indium tin oxide thin-film electrodes. *Chem. Mater.* **17**, 4880-4888 (2005).
157. Swain G. M. Electrically conducting diamond thin films: Advanced electrode materials for electrochemical technologies. In: *Electroanalytical chemistry* (ed<sup>^</sup>(eds Bard A. J., Rubinstein I.). Dekker (2004).
158. Pleskov Y., Krotova M., Ralchenko V., Saveliev A., Bozhko A. Electrochemical behavior of nitrogenated nanocrystalline diamond electrodes. *Russ. J. Electrochem.* **43**, 827 (2007).
159. Yang N., Uetsuka H., Osawa E., Nebel C. E. Vertically aligned nanowires from boron-doped diamond. *Nano Lett.* **8**, 3572-3576 (2008).



160. Kamata T., Kato D., Ida H., Niwa O. Structure and electrochemical characterization of carbon films formed by unbalanced magnetron (ubm) sputtering method. *Diamond Relat. Mater.* **49**, 25-32 (2014).
161. Sekioka N., *et al.* Controllable electrode activities of nano-carbon films while maintaining surface flatness by electrochemical pretreatment. *Carbon* **46**, 1918-1926 (2008).
162. Rabache V., *et al.* Direct observation of large quantum interference effect in anthraquinone solid-state junctions. *J. Am. Chem. Soc.* **135**, 10218-10221 (2013).
163. Wan A., Jiang L., Sangeeth C. S. S., Nijhuis C. A. Reversible soft top-contacts to yield molecular junctions with precise and reproducible electrical characteristics. *Adv. Funct. Mater.* **24**, 4442-4456 (2014).
164. Nijhuis C. A., Reus W. F., Siegel A. C., Whitesides G. M. A molecular half-wave rectifier. *J. Am. Chem. Soc.* **133**, 15397-15411 (2011).
165. Xie Z., Baldea I., Smith C. E., Wu Y., Frisbie C. D. Experimental and theoretical analysis of nanotransport in oligophenylene dithiol junctions as a function of molecular length and contact work function. *ACS Nano* **9**, 8022-8036 (2015).
166. Cademartiri L., *et al.* Electrical resistance of  $\text{Ag}(\text{S}(\text{CH}_2)_n\text{CH}_3)/\text{Ga}_2\text{O}_3/\text{eAg}$  tunneling junctions. *The Journal of Physical Chemistry C* **116**, 10848-10860 (2012).
167. Dickey M. D., Chiechi R. C., Larsen R. J., Weiss E. A., Weitz D. A., Whitesides G. M. Eutectic gallium-indium (eGain): A liquid metal alloy for the formation of stable structures in microchannels at room temperature. *Adv. Funct. Mater.* **18**, 1097-1104 (2008).
168. Beebe J. M., Kim B., Frisbie C. D., Kushmerick J. G. Measuring relative barrier heights in molecular electronic junctions with transition voltage spectroscopy. *ACS Nano* **2**, 827-832 (2008).
169. Taherinia D., *et al.* Charge transport in 4 nm molecular wires with interrupted conjugation: Combined experimental and computational evidence for thermally assisted polaron tunneling. *ACS Nano* **10**, 4372-4383 (2016).
170. McCreery R., Yan H., Bergren A. J. A critical perspective on molecular electronic junctions: There is plenty of room in the middle. *PCCP* **15**, 1065-1081 (2013).
171. Song P., Sangeeth C. S., Thompson D., Du W., Loh K. P., Nijhuis C. A. Noncovalent self-assembled monolayers on graphene as a highly stable platform for molecular tunnel junctions. *Adv. Mater.* **28**, 631-639 (2016).

172. Seo S., Min M., Lee S. M., Lee H. Photo-switchable molecular monolayer anchored between highly transparent and flexible graphene electrodes. *Nat Commun* **4**, 1920 (2013).
173. Kim D., *et al.* Flexible molecular-scale electronic devices composed of diarylethene photoswitching molecules. *Adv. Mater.* **26**, 3968-3973 (2014).
174. Akinwande D., Petrone N., Hone J. Two-dimensional flexible nanoelectronics. *Nat Commun* **5**, 5678 (2014).
175. Cheng T., Zhang Y., Lai W. Y., Huang W. Stretchable thin-film electrodes for flexible electronics with high deformability and stretchability. *Adv. Mater.* **27**, 3349-3376 (2015).
176. Anariba F., DuVall S. H., McCreery R. L. Mono- and multilayer formation by diazonium reduction on carbon surfaces monitored with atomic force microscopy "scratching". *Anal. Chem.* **75**, 3837-3844 (2003).
177. Nowak A. M., McCreery R. L. In situ raman spectroscopy of bias-induced structural changes in nitroazobenzene molecular electronic junctions. *J. Am. Chem. Soc.* **126**, 16621-16631 (2004).
178. Bonifas A. P., McCreery R. L. Solid state spectroelectrochemistry of redox reactions in polypyrrole/oxide molecular heterojunctions. *Anal. Chem.* **84**, 2459-2465 (2012).
179. Bonifas A. P., McCreery R. L. In-situ optical absorbance spectroscopy of molecular layers in carbon based molecular electronic devices. *Chemistry of Materials* **20**, 3849-3856 (2008).
180. Moth-Poulsen K., Bjornholm T. Molecular electronics with single molecules in solid-state devices. *Nat Nanotechnol* **4**, 551-556 (2009).
181. McCreery R. L. The merger of electrochemistry and molecular electronics. *Chem Rec* **12**, 149-163 (2012).
182. Reus W. F., Nijhuis C. A., Barber J. R., Thuo M. M., Tricard S., Whitesides G. M. Statistical tools for analyzing measurements of charge transport. *The Journal of Physical Chemistry C* **116**, 6714-6733 (2012).
183. Bonifas A. P., McCreery R. L. "Soft" au, pt and cu contacts for molecular junctions through surface-diffusion-mediated deposition. *Nature Nanotechnology* **5**, 612-617 (2010).
184. Sedghi G., *et al.* Comparison of the conductance of three types of porphyrin-based molecular wires: Beta,meso,beta-fused tapes, meso-butadiyne-linked and twisted meso-meso linked oligomers. *Adv. Mater.* **24**, 653-657 (2012).

185. Sedghi G., *et al.* Long-range electron tunnelling in oligo-porphyrin molecular wires. *Nat Nanotechnol* **6**, 517-523 (2011).
186. Tuccitto N., *et al.* Highly conductive approximately 40-nm-long molecular wires assembled by stepwise incorporation of metal centres. *Nat Mater* **8**, 41-46 (2009).
187. Luo L., Choi S. H., Frisbie C. D. Probing hopping conduction in conjugated molecular wires connected to metal electrodes<sup>†</sup>. *Chem. Mater.* **23**, 631-645 (2011).
188. Lu Q., Liu K., Zhang H., Du Z., Wang X., Wang F. From tunneling to hopping: A comprehensive investigation of charge transport mechanism in molecular junctions based on oligo(p-phenylene ethynylene)s. *ACS Nano* **3**, 3861-3868 (2009).
189. Lee S. K., Yamada R., Tanaka S., Chang G. S., Asai Y., Tada H. Universal temperature crossover behavior of electrical conductance in a single oligothiophene molecular wire. *ACS Nano* **6**, 5078-5082 (2012).
190. Yan H., *et al.* Activationless charge transport across 4.5 to 22 nm in molecular electronic junctions. *Proc Natl Acad Sci U S A* **110**, 5326-5330 (2013).
191. Luo L., Balhorn L., Vlasisavljevich B., Ma D., Gagliardi L., Frisbie C. D. Hopping transport and rectifying behavior in long donor-acceptor molecular wires. *The Journal of Physical Chemistry C* **118**, 26485-26497 (2014).
192. Kondratenko M., Stoyanov S. R., Gusarov S., Kovalenko A., McCreery R. L. Theoretical modeling of tunneling barriers in carbon-based molecular electronic junctions. *The Journal of Physical Chemistry C* **119**, 11286-11295 (2015).
193. McCreery R. L. Effects of electronic coupling and electrostatic potential on charge transport in carbon-based molecular electronic junctions. *Beilstein J Nanotechnol* **7**, 32-46 (2016).
194. Gibbs J., Otero de la Roza A., Bergren A. J., DiLabio G. A. Interpretation of molecular device transport calculation. *Canadian Journal of Chemistry*, (2016).
195. Sze S. M. *Physics of semiconductor devices*, 2nd Edition edn. Wiley (1981).
196. Tsuda A., Osuka A. Fully conjugated porphyrin tapes with electronic absorption bands that reach into infrared. *Science* **293**, 79-82 (2001).
197. Yan H., McCreery R. L. Anomalous tunneling in carbon/alkane/tio(2)/gold molecular electronic junctions: Energy level alignment at the metal/semiconductor interface. *ACS Appl Mater Interfaces* **1**, 443-451 (2009).

198. Baranovskii S., Rubel O. Charge transport in disordered materials. In: *Springer handbook of electronic and photonic materials* (ed<sup>^</sup>(eds). Springer (2006).
199. Riben A. R., Feucht D. L. Electrical transport in nge-pgaas heterojunctions†. *International Journal of Electronics* **20**, 583-599 (1966).
200. Martinuzzi S., Mallem O. Dark-current conduction processes in cds–cu2s thin-film photocells. *Physica Status Solidi (a)* **16**, 339-344 (1973).
201. Karipidou Z., *et al.* Ultrarobust thin-film devices from self-assembled metal–terpyridine oligomers. *Advanced Materials* **28**, 3473-3480 (2016).
202. Braun S., Salaneck W. R., Fahlman M. Energy-level alignment at organic/metal and organic/organic interfaces. *Adv. Mater.* **21**, 1450-1472 (2009).
203. Vilan A., Yaffe O., Biller A., Salomon A., Kahn A., Cahen D. Molecules on si: Electronics with chemistry. *Adv. Mater.* **22**, 140-159 (2010).
204. Jia C., Ma B., Xin N., Guo X. Carbon electrode–molecule junctions: A reliable platform for molecular electronics. *Accounts of Chemical Research* **48**, 2565-2575 (2015).
205. Schwarz F., *et al.* Field-induced conductance switching by charge-state alternation in organometallic single-molecule junctions. *Nat Nanotechnol* **11**, 170-176 (2016).
206. Wagner S., *et al.* Switching of a coupled spin pair in a single-molecule junction. *Nat Nanotechnol* **8**, 575-579 (2013).
207. Ivashenko O., Bergren A. J., McCreery R. L. Monitoring of energy conservation and losses in molecular junctions through characterization of light emission. *Advanced Electronic Materials* **2**, 1600351 (2016).
208. Evangelini C., *et al.* Engineering the thermopower of c60 molecular junctions. *Nano Lett.* **13**, 2141-2145 (2013).
209. Fereiro J. A., McCreery R. L., Bergren A. J. Direct optical determination of interfacial transport barriers in molecular tunnel junctions. *J. Am. Chem. Soc.* **135**, 9584-9587 (2013).
210. Wang F., Melosh N. A. Power-independent wavelength determination by hot carrier collection in metal-insulator-metal devices. *Nat Commun* **4**, 1711 (2013).
211. Afanas'ev V. V. Internal photoemission spectroscopy methods. *sciencedirect*, 109-160 (2014).

212. Yoon H. J., Bowers C. M., Baghbanzadeh M., Whitesides G. M. The rate of charge tunneling is insensitive to polar terminal groups in self-assembled monolayers in Ag(tS)(CH<sub>2</sub>)<sub>n</sub>M(CH<sub>2</sub>)<sub>m</sub>/Ga<sub>2</sub>O<sub>3</sub>/EGaIn junctions. *J. Am. Chem. Soc.* **136**, 16-19 (2014).
213. Yoon H. J., Shapiro N. D., Park K. M., Thuo M. M., Soh S., Whitesides G. M. The rate of charge tunneling through self-assembled monolayers is insensitive to many functional group substitutions. *Angew. Chem. Int. Ed. Engl.* **51**, 4658-4661 (2012).
214. McCreery R., Bergren A., Morteza-Najarian A., Sayed S. Y., Yan H. Electron transport in all-carbon molecular electronic devices. *Faraday Discuss.* **172**, 9-25 (2014).
215. Sayed S. Y., Bayat A., Kondratenko M., Leroux Y., Hapiot P., McCreery R. L. Bilayer molecular electronics: All-carbon electronic junctions containing molecular bilayers made with "click" chemistry. *J. Am. Chem. Soc.* **135**, 12972-12975 (2013).
216. Lee C. H., Yu G., Heeger A. J. Persistent photoconductivity in poly(p-phenylenevinylene): Spectral response and slow relaxation. *Phys Rev B Condens Matter* **47**, 15543-15553 (1993).
217. Reddy P., Jang S. Y., Segalman R. A., Majumdar A. Thermoelectricity in molecular junctions. *Science* **315**, 1568-1571 (2007).
218. Garcia-Lastra J. M., Rostgaard C., Rubio A., Thygesen K. S. Polarization-induced renormalization of molecular levels at metallic and semiconducting surfaces. *Physical Review B* **80**, (2009).
219. Zelinsky Y., May V. Laser pulse induced transient currents in a molecular junction: Effects of plasmon excitations of the leads. *J. Chem. Phys.* **142**, 224701 (2015).
220. Hagfeldt A., Graetzel M. Light-induced redox reactions in nanocrystalline systems. *Chem. Rev.* **95**, 49-68 (1995).
221. Galperin M., Nitzan A. Current-induced light emission and light-induced current in molecular-tunneling junctions. *Phys. Rev. Lett.* **95**, 206802 (2005).
222. Galperin M., Nitzan A., Ratner M. A., Stewart D. R. Molecular transport junctions: Asymmetry in inelastic tunneling processes. *J. Phys. Chem. B* **109**, 8519 - 8522 (2005).